

**Synthesis, Structure, and Magnetic Properties of Spin-1/2 Kagomé
Antiferromagnets**

by

Emily A. Nytko

A.B. *Magna Cum Laude* Chemistry, 2001
Dartmouth College

SUBMITTED TO THE DEPARTMENT OF CHEMISTRY IN PARTIAL FULFILLMENT OF
THE REQUIREMENTS FOR THE DEGREE OF

DOCTOR OF PHILOSOPHY
AT THE
MASSACHUSETTS INSTITUTE OF TECHNOLOGY

September 2008

© 2008 Massachusetts Institute of Technology
All Rights Reserved

Signature of Author: _____
Department of Chemistry
July 3, 2008

Certified By: _____
Daniel G. Nocera
Henry Dreyfus Professor of Energy and Professor of Chemistry
Thesis Supervisor

Accepted By: _____
Robert W. Field
Haslam and Dewey Professor of Chemistry
Chairman, Departmental Committee on Graduate Students

This doctoral thesis has been examined by a Committee of the Department of Chemistry as follows:

Stephen J. Lippard
Arthur Amos Noyes Professor of Chemistry
Committee Chair

Daniel G. Nocera
Henry Dreyfus Professor of Energy and Professor of Chemistry
Thesis Supervisor

Young S. Lee
Mark Hyman Jr. Career Development Professor and Associate Professor of Physics

Synthesis, Structure, and Magnetic Properties of Spin-1/2 Kagomé Antiferromagnets

by

Emily A. Nytko

Submitted to the Department of Chemistry
on July 3, 2008 in Partial Fulfillment of the
Requirements for the Degree of Doctor of Philosophy in
Chemistry

Abstract

Stoichiometrically pure $S = \frac{1}{2}$ Cu^{2+} kagomé materials have been synthesized. Such materials provide an ideal venue for exploration of quantum states on a kagomé because they exhibit strong geometric spin frustration and are predicted to show no magnetic long-range ordering (LRO). The three broad classes of kagomé layered materials presented herein—covalently linked layers, hydrogen-bonded layers, and electrostatically linked layers—reflect optimization of structure to maximize frustration while simultaneously minimizing interlayer exchange to inhibit three-dimensional (3-D) LRO. The covalently linked layered system, $\text{Cu}(1,3\text{-benzenedicarboxylate})$, featuring in-plane monodentate μ -carboxylate bridges, is the first known structurally perfect $S = \frac{1}{2}$ metal-organic framework (MOF) kagomé and bears the shortest metal-metal distance of any such material. The frustrated material features antiferromagnetic nearest-neighbor exchange ($\Theta = -33$ K) but undergoes ferromagnetic ordering ($T_c = 2$ K), perhaps due to an out-of-plane spin polarization mechanism. The hydrogen-bonded layered system ($\text{CdCu}_3(\text{OH})_6(\text{NO}_3)_2 \cdot 0.5\text{H}_2\text{O}$), featuring in-plane μ -hydroxy bridges, shows even stronger antiferromagnetic exchange ($\Theta = -114 \pm 27$ K), but still exhibits magnetic ordering behavior ($T_c = 5$ K), likely arising from interlayer exchange through hydrogen bonds. Electrostatically linked systems featuring in-plane μ -hydroxy bridges—the rare minerals claringbullite ($\text{Cu}_4(\text{OH})_x\text{Cl}_y\text{F}_z$ where $x + y + z = 8$), clinoatacamite ($\text{Cu}_2(\text{OH})_3\text{Cl}$), and herbertsmithite ($\text{ZnCu}_3(\text{OH})_6\text{Cl}_2$)—have been prepared and characterized both structurally and magnetically. The former two minerals are frustrated systems but still show 3-D LRO arising from ferromagnetic interactions between the kagomé planes and interlayer copper(II) ions. Herbertsmithite, in contrast, features 2-D kagomé layers isolated by diamagnetic zinc(II) ions and exhibits no LRO to 50 mK, despite strong nearest-neighbor antiferromagnetic coupling ($\Theta = -314$ K). Herbertsmithite displays no spin gap in its excitation spectrum at low temperature, a signature of a spin liquid phase with long correlations. Continued efforts are directed at growth of large single crystals for probative neutron scattering studies. Current and future study of these stoichiometrically pure spin-frustrated systems will provide critical insight into the behavior of strongly correlated electrons.

Thesis Supervisor: Daniel G. Nocera

Title: Henry Dreyfus Professor of Energy and Professor of Chemistry

In loving memory of my grandparents, Jack and Rita Treacy, who always believed in me

Acknowledgments

First and foremost, I'd like to thank my advisor, Daniel Nocera, for giving me the opportunity to do research in his large and dynamic lab. Dan has supported my work and allowed me the freedom to pursue this project in directions I never dreamed it would take when I started five years ago. His charisma and love of science have been a continual source of inspiration. I would also like to thank the MIT inorganic faculty, most especially Professors Schrock and Lippard for serving on my thesis committee and taking time out of their busy schedules to meet with me and discuss my work.

I am grateful to the National Science Foundation and the MIT Presidential Fellows program for fellowship support.

I would like to thank Dimitris Papoutsakis and Daniel Grohol for laying the foundations of our spin frustration studies on jarosites. Although we only overlapped in lab for a brief period, over the years Daniel has been an invaluable resource for discussing hydrothermal reactions and safe usage of our largest vessels. The breadth of his work with jarosites impresses me to this day. We are also forever indebted to him for our lab rendition of "Happy Birthday," which is embarrassing when sung in public places. (Other people just stare and wonder what's wrong with us.)

Matt Shores taught me a lot about how to do science when I arrived in lab in late 2003. Shores introduced me to the chemistry of copper(II) minerals, always admonishing me to "figure it out." Bart Bartlett taught me how to use the SQUID and read/listened to countless incarnations of my second-year orals paper/talk (as did Shores). I am most grateful to these two people for helping me through my early years here. They are both wonderful scientists and share credit for much of the work in Chapters 4 and 5 of this Thesis.

I would like to thank our collaborators in the Physics Department at MIT, especially Young Lee, who is also a member of my committee. Young and his group (particularly Joel Helton and Kit Matan) have been immensely patient in explaining the results of their neutron scattering data and heat capacity measurements. I am also grateful to Andrea Prodi as well as Shaoyan Chu, who is now applying his ideas in crystal growth and engineering to the Zn-paratacamite/herbertsmithite system. Harry T.H. Han, one of Young's newest students, is also working on crystal growth, and I wish him the best of luck.

We have wonderful collaborators around the world, as well, and I thank them all for interesting and fruitful collaborations: Amit Keren and his student Oren Ofer for muon spin rotation (μ SR) work, and Takashi Imai for NMR measurements on herbertsmithite.

I must mention many people at MIT who have been committed to the upkeep of various instruments and the training of new users. Without help from the following people, this research would not have been possible: Scott Speakman, Joseph Adario, Peter Kloumann, Shaoyan Chu, Fangcheng Chou, and Tim McClure. I also thank Gretchen Guidess, Allison Kelsey, and Janet MacLaughlin for keeping the Nocera lab running over the years.

Peter Müller, our department crystallographer, merits special mention. In addition to the difficulty in distinguishing Cu from Zn in the Zn-paratacamite structures, this project has featured a number of difficult structures where Peter's expertise was invaluable. He has been endlessly patient in teaching me and has advanced this project immensely.

The following people have made MIT a better place for me, and I don't know what I would have done without them: the members of Women in Chemistry, Blanche Staton, Lynn Roberson, Susan Brighton, Jim Doughty, and Mary and Jeff Farbman. My good friends Pattie

Aron, Jim Flahive, Kevin Roth, and Shannon Locks have also been incredibly supportive through the years.

Montana Childress is one of the strongest people and most competent chemists that I know, and a wonderful friend as well. Becky Somers, my classmate, has been like a sister to me. I thank them both from the bottom of my heart. Thanks also to the following people for making the Nocera lab special during my time here:

Postdocs: Alex Krivokapic, Adam Veige, Shih-Yuan Liu (made the lab poker game fun, along with Adam), Thomas Gray, Dequiang An, Dino Villagrán (has been incredibly supportive and helpful), Sebastian Stoian (knows a lot about a lot of things), Matt Kanan (30!), Andrew Greytak, Alex Radosevich (has given me a lot of good advice over the past year), Rick Kelley (a voice of reason), Poul Petersen (we're still cool despite the misdirected e-mail and the fact that I thought he was Dutch), Preston "Dr. Chicken" Snee, and Jake Soper.

Undergraduates: Jillian Dempsey (a friend and fellow marathon runner), T. D. Lockett, Stephen Fried, Kris Tantillo (an esteemed second-floor sitter), Katie West, and Noah Rahman.

Graduate Students: Aetna Wun (always positive), Tim Cook (a talented chemist and artist), Kate Marckiewicz (a good friend), Jay Yang, Changhoon Lee, Tom Teets, Hannah Shafaat, Matt Chambers, Julien Bachmann (wonderfully supportive and optimistic), Arturo Pizano (a helpful ear and source of computer advice), Emily McLaurin, Mike Marshak, Yogi Surendranath, and Glen Alliger.

Graduate school has been an arduous and seemingly impossible journey at some times, punctuated by small victories and moments of accomplishment. It has been a period of reflection and vast personal growth for me. I am forever indebted to the Nytko, Treacy, and Lutz families for believing in me and seeing me through it; words cannot adequately express my gratitude. The love and reassurance of my parents and brother especially have sustained me throughout.

Finally, John Lutz, my husband, has been endlessly supportive and has inspired me to be a better person, both happier and kinder to others. A wonderful listener with his own special brand of humor, John has raised my spirits and not run screaming in the other direction when I've been at my worst. He's also been my biggest fan when I've been at my best. I have continually bounced ideas off of John, whose brilliance is only belied by some very refreshing humility and honesty. He is my love, my partner, and my best friend. I cherish the memories we have and look forward to our future together.

And so I begin my Thesis with a quotation:

"Few subjects in science are more difficult to understand than magnetism."

Encyclopedia Britannica, 1987.

(understatement of the century)

Table of Contents

Abstract	3
Dedication	5
Acknowledgments	7
Table of Contents	9
List of Tables	13
List of Figures	21
List of Schemes	35
Chapter 1. Spin Frustration on the Kagomé Lattice	37
1.1 Introduction	38
1.2 Spin Frustration	38
1.3 Bulk Magnetic Properties of Frustrated Systems	41
1.4 Frustrating Lattice Types and Long-Range Order	42
1.5 Resonating Valence Bond Theory	46
1.6 Experimental Realizations of Triangular and Kagomé Antiferromagnets	48
1.6.1 Triangular Antiferromagnets	48
1.6.2 Kagomé Antiferromagnets	49
1.6.2.1 $S > \frac{1}{2}$ Kagomé Antiferromagnets	49
1.6.2.2 $S = \frac{1}{2}$ Kagomé Antiferromagnets	58
1.7 The Jahn-Teller Effect / Peierls Distortion in the Structural Chemistry of Copper(II)	67
1.8 Outline and Scope of this Thesis	68
1.9 References	72
Chapter 2. Synthesis, Structure, and Magnetism of the First Structurally Perfect $S = \frac{1}{2}$ Metal-Organic Framework Kagomé Antiferromagnet	79
2.1 Introduction	80
2.2 Experimental	80
2.2.1 General Procedures	80
2.2.2 Synthesis of Cu(1,3-benzenedicarboxylate)	81
2.2.3 X-ray diffraction	82
2.2.4 Single-Crystal X-ray diffraction	82
2.2.5 Magnetic Measurements	83

2.2.6 Other Physical Measurements	83
2.3 Results	84
2.3.1 Synthetic Methodology	84
2.3.2 Structural Chemistry	85
2.3.3 Magnetic Properties	89
2.3.3.1 Preliminary Magnetoanisotropy Measurements	91
2.4 Discussion	91
2.5 Conclusions	95
2.6 References	96
Chapter 3. CdCu₃(OH)₆(NO₃)₂•xH₂O, An $S = \frac{1}{2}$ Kagomé Antiferromagnet with Hydrogen-Bonded Layers	99
3.1 Introduction	100
3.2 Experimental	101
3.2.1 General Procedures	101
3.2.2 Synthesis of CdCu ₃ (OH) ₆ (NO ₃) ₂ •xH ₂ O	101
3.2.3 Synthesis of Cu ₂ (OH) ₃ NO ₃ (rouaite, syn.)	103
3.2.4 X-ray diffraction	104
3.2.5 Magnetic Measurements	104
3.2.6 Other Physical Measurements	104
3.3 Results	105
3.3.1 Synthetic Methodology	105
3.3.2 Structural Chemistry	108
3.3.3 Magnetic Properties of Rouaite	114
3.3.4 Magnetic Properties of CdCu ₃ (OH) ₆ (NO ₃) ₂ •xH ₂ O	114
3.4 Discussion	117
3.5 Conclusions	123
3.6 References	124
Chapter 4. Synthesis, Structure, and Chemical Characterization of Copper(II) Hydroxychloride Minerals	127
4.1 Introduction	128
4.2 Experimental	131
4.2.1 General Procedures	131
4.2.2 Synthesis of Claringbullite	131

4.2.3 Synthesis of Clinoatacamite, $\text{Cu}_2(\text{OH})_3\text{Cl}$	132
4.2.4 Synthesis of Zn-paratacamites, $\text{Zn}_x\text{Cu}_{4-x}(\text{OH})_6\text{Cl}_2$ ($0.33 \leq x < 1$)	135
4.2.5 Synthesis of Herbertsmithite $\text{ZnCu}_3(\text{OH})_6\text{Cl}_2$	136
4.2.6 X-ray diffraction	136
4.2.7 Other Physical Measurements	138
4.3 Results	138
4.3.1 Synthetic Methodology	138
4.3.1.1 Synthesis of Claringbullite	138
4.3.1.2 Synthesis of Clinoatacamite, $\text{Cu}_2(\text{OH})_3\text{Cl}$	139
4.3.1.3 Synthesis of Zn-paratacamite and Herbertsmithite, $\text{Zn}_x\text{Cu}_{4-x}(\text{OH})_6\text{Cl}_2$ ($0.33 \leq x \leq 1$)	141
4.3.1.4 Thermal and Spectroscopic Characterization	146
4.3.1.5 $\text{M}_2(\text{OH})_3\text{Cl}$, $\text{ZnCu}_3(\text{OH})_6\text{Br}_2$, and other $\text{MCu}_3(\text{OH})_6\text{Cl}_2$ targets	146
4.3.1.6 Hydrothermal Zone Refinement Technique	149
4.3.2 General Structural Chemistry	150
4.3.2.1 Structure of Claringbullite, $\text{Cu}_4(\text{OH})_x\text{Cl}_y\text{F}_z$ ($x + y + z = 8$)	150
4.3.2.2 Structure of Clinoatacamite, $\text{Cu}_2(\text{OH})_3\text{Cl}$	152
4.3.2.3 Structure of Zn-paratacamite and Herbertsmithite, $\text{Zn}_x\text{Cu}_{4-x}(\text{OH})_6\text{Cl}_2$ ($0.33 \leq x \leq 1$)	154
4.3.2.4 Single-Crystal X-ray Diffraction of $\text{Zn}_x\text{Cu}_{4-x}(\text{OH})_6\text{Cl}_2$ ($0.33 \leq x \leq 1$)	159
4.4 Conclusions	165
4.5 References	166
Chapter 5. Magnetism of Copper(II) Hydroxychloride Minerals, Spin Liquid States, and the Search for RVB Superconductivity	169
5.1 Introduction	170
5.2 Experimental	170
5.2.1 Magnetic Measurements	170
5.2.2 Electrochemical Measurements	170
5.3 Results	171
5.3.1 Magnetic Properties of Claringbullite	171
5.3.2 Magnetic Properties of Clinoatacamite	172
5.3.3 Magnetic Properties of Zn-Paratacamites and Herbertsmithite	173

5.4 Discussion of Magnetic Properties	177
5.5 Summary of Neutron Scattering Results	180
5.6 Summary of Results of Local Probe Measurements: ^{63}Cu , ^{35}Cl , ^1H NMR and μSR (muon spin rotation)	180
5.7 Doping an $S = \frac{1}{2}$ Kagomé: RVB-Like Spin Liquid Phases and Superconductivity?	181
5.7.1 Redox Chemistry of Herbertsmithite	183
5.7.2 Electrochemistry of Herbertsmithite	185
5.8 Conclusions and Future Outlook	186
5.9 References	188
Appendix A. Structural Characterization of Compounds	193
Appendix A.1	194
Appendix A.2	219
Appendix A.3	222
Appendix B. Thermal and Spectroscopic Characterization of Compounds	279
Appendix B.1	280
Appendix B.2	282
Appendix B.3	285
<i>Curriculum Vitae</i>	295
Autobiographical Note	299

List of Tables

Table 1.1	A structural comparison of Cu^{2+} kagomé and pseudo-kagomé compounds. Potassium jarosite is also listed for comparison.	65
Table 3.1	Structural Comparison of $\text{CdCu}_3(\text{OH})_6(\text{NO}_3)_2 \cdot x\text{H}_2\text{O}$ and rouaite.	110
Table 4.1	Summary of Observed Reactivity for M-Paratacamite Syntheses. Reactions were run hydrothermally with temperatures ranging from 180 – 240 °C, with and without added HCl.	148
Table 4.2	Structural Comparison of claringbullite and clinoatacamite.	153
Table 4.3	Structural Comparison of claringbullite, clinoatacamite, and herbertsmithite.	157
Table 4.4	R-factor statistical data on clinoatacamite: c04042a, $\text{Cu}_2(\text{OH})_3\text{Cl}$ in $P2_1/n$. See also Appendix A.3, Figures A.3.3 and Tables A.3.8-A.3.13.	161
Table 4.5	R-factor statistical data on mps3a. See also Appendix A.3, Figure A.3.5 and Tables A.3.15-A.3.20.	161
Table 4.6	R-factor statistical data on $\text{Zn}_{0.42}$ -paratacamite: c04041a. See also Appendix A.3, Figures A.3.6 and Tables A.3.21-A.3.26.	162
Table 4.7	R-factor statistical data on $\text{Zn}_{0.76}$ -paratacamite: 08038_cu_mix. Synthesized from $\text{CuO} + \text{ZnCl}_2 + \text{HCl}$ in zone furnace. See also Appendix A.3, Tables A.3.27-A.3.32.	162
Table 4.8	R-factor statistical data on herbertsmithite: c05017a. See also Appendix A.3, Figures A.3.7 and Tables A.3.33-A.3.38.	163
Table 4.9	R-factor statistical data on herbertsmithite: 07036. See also Appendix A.3, Tables A.3.39-A.3.45.	163
Table 4.10	R-factor statistical data on herbertsmithite: 08039. Synthesized from $\text{CuO} + \text{ZnCl}_2$ in zone furnace. See also Appendix A.3, Tables A.3.53-A.3.58.	164
Table 4.11	R-factor statistical data on herbertsmithite: c04072b. Naturally occurring specimen from Sierra Gorde, Chile. See also Appendix A.3, Tables A.3.58-A.3.63.	164

Table 5.1	T_c , Θ , and f for clinoatacamite / Zn-paratacamite / herbertsmithite series.	174
Table 5.2	Summary of Redox Chemistry of $\text{ZnCu}_3(\text{OH})_6\text{Cl}_2$.	184
Table 5.3	T_c , Θ , and f for frustrated $S = \frac{1}{2}$ kagomé systems presented in this Thesis.	186
Table A.1.1.	Crystal data and structure refinement for Cu(1,3-bdc).	196
Table A.1.2	Atomic coordinates [$\times 10^4$] and equivalent isotropic displacement parameters [$\text{\AA}^2 \times 10^3$] for Cu(1,3-bdc). U_{eq} is defined as one third of the trace of the orthogonalized U_{ij} tensor.	197
Table A.1.3	Bond lengths [\AA] for Cu(1,3-bdc).	197
Table A.1.4	Bond angles [$^\circ$] for Cu(1,3-bdc).	198
Table A.1.5	Anisotropic displacement parameters [$\text{\AA}^2 \times 10^3$] for Cu(1,3-bdc). The anisotropic displacement factor exponent takes the form: $-2\pi^2[(ha^*)^2U_{11} + \dots + 2hka^*b^*U_{12}]$.	199
Table A.1.6	Hydrogen coordinates [$\times 10^4$] and isotropic displacement parameters [$\text{\AA}^2 \times 10^3$] for Cu(1,3-bdc).	199
Table A.1.7	Crystal data and structure refinement for Cu(1,3-bdc) $\cdot 0.11\text{H}_2\text{O}$.	201
Table A.1.8	Atomic coordinates [$\times 10^4$] and equivalent isotropic displacement parameters [$\text{\AA}^2 \times 10^3$] for Cu(1,3-bdc) $\cdot 0.11\text{H}_2\text{O}$. U_{eq} is defined as one third of the trace of the orthogonalized U_{ij} tensor.	202
Table A.1.9	Bond lengths [\AA] for Cu(1,3-bdc) $\cdot 0.11\text{H}_2\text{O}$.	202
Table A.1.10	Bond angles [$^\circ$] for Cu(1,3-bdc) $\cdot 0.11\text{H}_2\text{O}$.	203
Table A.1.11	Anisotropic displacement parameters [$\text{\AA}^2 \times 10^3$] for Cu(1,3-bdc) $\cdot 0.11\text{H}_2\text{O}$. The anisotropic displacement factor exponent takes the form: $-2\pi^2[(ha^*)^2U_{11} + \dots + 2hka^*b^*U_{12}]$.	204
Table A.1.12	Hydrogen coordinates [$\times 10^4$] and isotropic displacement parameters [$\text{\AA}^2 \times 10^3$] for Cu(1,3-bdc) $\cdot 0.11\text{H}_2\text{O}$.	204
Table A.1.13	Bragg reflections and Miller indices of pXRD pattern for Cu(1,3-bdc) matched to 07060 structure.	205

Table A.1.14	Crystal data and structure refinement for $C_{32}H_{24}Cu_6O_{26}$.	210
Table A.1.15	Atomic coordinates [$\times 10^4$] and equivalent isotropic displacement parameters [$\text{\AA}^2 \times 10^3$] for $C_{32}H_{24}Cu_6O_{26}$. U_{eq} is defined as one third of the trace of the orthogonalized U_{ij} tensor.	211
Table A.1.16	Bond lengths [\AA] for $C_{32}H_{24}Cu_6O_{26}$.	213
Table A.1.17	Bond angles [$^\circ$] for $C_{32}H_{24}Cu_6O_{26}$.	214
Table A.1.18	Anisotropic displacement parameters [$\text{\AA}^2 \times 10^3$] for $C_{32}H_{24}Cu_6O_{26}$. The anisotropic displacement factor exponent takes the form: $-2\pi^2[(ha^*)^2U_{11} + \dots + 2hka^*b^*U_{12}]$.	216
Table A.1.19	Hydrogen coordinates [$\times 10^4$] and isotropic displacement parameters [$\text{\AA}^2 \times 10^3$] for $C_{32}H_{24}Cu_6O_{26}$.	217
Table A.1.20	Hydrogen bond lengths [\AA] and angles [$^\circ$] for $C_{32}H_{24}Cu_6O_{26}$.	218
Table A.2.1	Selected interatomic distances [\AA] and angles [$^\circ$] for $Cu_2(OH)_3NO_3$, rouaite, from Chapter 3, Ref. [11].	219
Table A.2.2	Bragg reflections and Miller indices of pXRD pattern for $CdCu_3(OH)_6(NO_3)_2 \cdot xH_2O$, matched to PDF # 01-072-1433, $P\bar{3}m1$.	220
Table A.2.3	Bragg reflections and Miller indices of pXRD pattern for $CdCu_3(OH)_6(NO_3)_2 \cdot xH_2O$, matched to PDF # 01-070-1904, $P\bar{1}$.	220
Table A.2.4	Bragg reflections and Miller indices of pXRD pattern for $Cu_2(OH)_3NO_3$, rouaite, in $P2_1$, matched to PDF # 04-010-3058.	221
Table A.3.1	Crystal data and structure refinement for $Cu\{Cu_3(OH)_6\}ClF$, claringbullite, syn.	223
Table A.3.2	Atomic coordinates [$\times 10^4$] and equivalent isotropic displacement parameters [$\text{\AA}^2 \times 10^3$] for 08115, $Cu\{Cu_3(OH)_6\}ClF$, claringbullite, syn. U_{eq} is defined as one third of the trace of the orthogonalized U_{ij} tensor.	224
Table A.3.3	Bond lengths [\AA] for 08115, $Cu\{Cu_3(OH)_6\}ClF$, claringbullite, syn.	224
Table A.3.4	Bond angles [$^\circ$] for 08115, $Cu\{Cu_3(OH)_6\}ClF$, claringbullite,	225

	syn.	
Table A.3.5	Anisotropic displacement parameters [$\text{\AA}^2 \times 10^3$] for 08115, $\text{Cu}\{\text{Cu}_3(\text{OH})_6\}\text{ClF}$, claringbullite, syn. The anisotropic displacement factor exponent takes the form: $-2\pi^2[(ha^*)^2U_{11} + \dots + 2hka^*b^*U_{12}]$.	226
Table A.3.6	Hydrogen coordinates [$\times 10^4$] and isotropic displacement parameters [$\text{\AA}^2 \times 10^3$] for 08115, $\text{Cu}\{\text{Cu}_3(\text{OH})_6\}\text{ClF}$, claringbullite, syn.	226
Table A.3.7	Bragg reflections and Miller indices of pXRD pattern for claringbullite, syn matched to PDF # 01-086-0899.	227
Table A.3.8	Crystal data and structure refinement for $\text{Cu}\{\text{Cu}_3(\text{OH})_6\}\text{Cl}_2$, clinoatacamite, syn.	229
Table A.3.9	Atomic coordinates [$\times 10^4$] and equivalent isotropic displacement parameters [$\text{\AA}^2 \times 10^3$] for c04042a, $\text{Cu}\{\text{Cu}_3(\text{OH})_6\}\text{Cl}_2$, clinoatacamite, syn. U_{eq} is defined as one third of the trace of the orthogonalized U_{ij} tensor.	230
Table A.3.10	Bond lengths [\AA] for c04042a, $\text{Cu}\{\text{Cu}_3(\text{OH})_6\}\text{Cl}_2$, clinoatacamite, syn.	230
Table A.3.11	Bond angles [$^\circ$] for c04042a, $\text{Cu}\{\text{Cu}_3(\text{OH})_6\}\text{Cl}_2$, clinoatacamite, syn.	231
Table A.3.12	Anisotropic displacement parameters [$\text{\AA}^2 \times 10^3$] for c04042a, $\text{Cu}\{\text{Cu}_3(\text{OH})_6\}\text{Cl}_2$, clinoatacamite, syn. The anisotropic displacement factor exponent takes the form: $-2\pi^2[(ha^*)^2U_{11} + \dots + 2hka^*b^*U_{12}]$.	232
Table A.3.13	Hydrogen coordinates [$\times 10^4$] and isotropic displacement parameters [$\text{\AA}^2 \times 10^3$] for c04042a, $\text{Cu}\{\text{Cu}_3(\text{OH})_6\}\text{Cl}_2$, clinoatacamite, syn.	232
Table A.3.14	Bragg reflections and Miller indices of pXRD pattern for clinoatacamite, syn. matched to PDF # 00-50-1559.	233
Table A.3.15	Crystal data and structure refinement for $\text{Zn}_{0.33}\text{Cu}_{3.67}(\text{OH})_6\text{Cl}_2$.	235
Table A.3.16	Atomic coordinates [$\times 10^4$] and equivalent isotropic displacement parameters [$\text{\AA}^2 \times 10^3$] for mps3atest, $\text{Zn}_{0.33}\text{Cu}_{3.67}(\text{OH})_6\text{Cl}_2$. U_{eq} is defined as one third of the trace	236

of the orthogonalized U_{ij} tensor.

Table A.3.17	Bond lengths [\AA] for mps3atest, $\text{Zn}_{0.33}\text{Cu}_{3.67}(\text{OH})_6\text{Cl}_2$.	236
Table A.3.18	Bond angles [$^\circ$] for mps3atest, $\text{Zn}_{0.33}\text{Cu}_{3.67}(\text{OH})_6\text{Cl}_2$.	237
Table A.3.19	Anisotropic displacement parameters [$\text{\AA}^2 \times 10^3$] for mps3atest, $\text{Zn}_{0.33}\text{Cu}_{3.67}(\text{OH})_6\text{Cl}_2$. The anisotropic displacement factor exponent takes the form: $-2\pi^2[(ha^*)^2U_{11} + \dots + 2hka^*b^*U_{12}]$.	240
Table A.3.20	Hydrogen coordinates [$\times 10^4$] and isotropic displacement parameters [$\text{\AA}^2 \times 10^3$] for mps3atest, $\text{Zn}_{0.33}\text{Cu}_{3.67}(\text{OH})_6\text{Cl}_2$.	240
Table A.3.21	Crystal data and structure refinement for $\text{Zn}_{0.42}\text{Cu}_{3.58}(\text{OH})_6\text{Cl}_2$.	242
Table A.3.22	Atomic coordinates [$\times 10^4$] and equivalent isotropic displacement parameters [$\text{\AA}^2 \times 10^3$] for c04041a, $\text{Zn}_{0.42}\text{Cu}_{3.58}(\text{OH})_6\text{Cl}_2$. U_{eq} is defined as one third of the trace of the orthogonalized U_{ij} tensor.	243
Table A.3.23	Bond lengths [\AA] for c04041a, $\text{Zn}_{0.42}\text{Cu}_{3.58}(\text{OH})_6\text{Cl}_2$.	243
Table A.3.24	Bond angles [$^\circ$] for c04041a, $\text{Zn}_{0.42}\text{Cu}_{3.58}(\text{OH})_6\text{Cl}_2$.	244
Table A.3.25	Anisotropic displacement parameters [$\text{\AA}^2 \times 10^3$] for c04041a, $\text{Zn}_{0.42}\text{Cu}_{3.58}(\text{OH})_6\text{Cl}_2$. The anisotropic displacement factor exponent takes the form: $-2\pi^2[(ha^*)^2U_{11} + \dots + 2hka^*b^*U_{12}]$.	247
Table A.3.26	Hydrogen coordinates [$\times 10^4$] and isotropic displacement parameters [$\text{\AA}^2 \times 10^3$] for c04041a, $\text{Zn}_{0.42}\text{Cu}_{3.58}(\text{OH})_6\text{Cl}_2$.	247
Table A.3.27	Crystal data and structure refinement for 08038_cu_mix, $\text{Zn}_{0.76}\text{Cu}_{3.24}(\text{OH})_6\text{Cl}_2$.	248
Table A.3.28	Atomic coordinates [$\times 10^4$] and equivalent isotropic displacement parameters [$\text{\AA}^2 \times 10^3$] for 08038_cu_mix, $\text{Zn}_{0.76}\text{Cu}_{3.24}(\text{OH})_6\text{Cl}_2$. U_{eq} is defined as one third of the trace of the orthogonalized U_{ij} tensor.	249
Table A.3.29	Bond lengths [\AA] for 08038_cu_mix, $\text{Zn}_{0.76}\text{Cu}_{3.24}(\text{OH})_6\text{Cl}_2$.	249
Table A.3.30	Bond angles [$^\circ$] for 08038_cu_mix, $\text{Zn}_{0.76}\text{Cu}_{3.24}(\text{OH})_6\text{Cl}_2$.	250
Table A.3.31	Anisotropic displacement parameters [$\text{\AA}^2 \times 10^3$] for 08038_cu_mix, $\text{Zn}_{0.76}\text{Cu}_{3.24}(\text{OH})_6\text{Cl}_2$. The anisotropic displacement factor exponent takes the form: $-2\pi^2[(ha^*)^2U_{11}$	252

+ ... + $2hka^*b^*U_{12}$].

Table A.3.32	Hydrogen coordinates [$\times 10^4$] and isotropic displacement parameters [$\text{\AA}^2 \times 10^3$] for 08038_cu_mix, $\text{Zn}_{0.76}\text{Cu}_{3.24}(\text{OH})_6\text{Cl}_2$.	252
Table A.3.33	Crystal data and structure refinement for c05017a, $\text{ZnCu}_3(\text{OH})_6\text{Cl}_2$.	254
Table A.3.34	Atomic coordinates [$\times 10^4$] and equivalent isotropic displacement parameters [$\text{\AA}^2 \times 10^3$] for c05017a, $\text{ZnCu}_3(\text{OH})_6\text{Cl}_2$. U_{eq} is defined as one third of the trace of the orthogonalized U_{ij} tensor.	255
Table A.3.35	Bond lengths [\AA] for c05017a, $\text{ZnCu}_3(\text{OH})_6\text{Cl}_2$.	255
Table A.3.36	Bond angles [$^\circ$] for c05017a, $\text{ZnCu}_3(\text{OH})_6\text{Cl}_2$.	256
Table A.3.37	Anisotropic displacement parameters [$\text{\AA}^2 \times 10^3$] for c05017a, $\text{ZnCu}_3(\text{OH})_6\text{Cl}_2$. The anisotropic displacement factor exponent takes the form: $-2\pi^2[(ha^*)^2U_{11} + \dots + 2hka^*b^*U_{12}]$.	258
Table A.3.38	Hydrogen coordinates [$\times 10^4$] and isotropic displacement parameters [$\text{\AA}^2 \times 10^3$] for c05017a, $\text{ZnCu}_3(\text{OH})_6\text{Cl}_2$.	258
Table A.3.39	Crystal data and structure refinement for $\text{ZnCu}_3(\text{OH})_6\text{Cl}_2$.	259
Table A.3.40	Atomic coordinates [$\times 10^4$] and equivalent isotropic displacement parameters [$\text{\AA}^2 \times 10^3$] for 07036, $\text{ZnCu}_3(\text{OH})_6\text{Cl}_2$. U_{eq} is defined as one third of the trace of the orthogonalized U_{ij} tensor.	260
Table A.3.41	Bond lengths [\AA] for 07036, $\text{ZnCu}_3(\text{OH})_6\text{Cl}_2$.	260
Table A.3.42	Bond angles [$^\circ$] for 07036, $\text{ZnCu}_3(\text{OH})_6\text{Cl}_2$.	261
Table A.3.43	Anisotropic displacement parameters [$\text{\AA}^2 \times 10^3$] for 07036, $\text{ZnCu}_3(\text{OH})_6\text{Cl}_2$. The anisotropic displacement factor exponent takes the form: $-2\pi^2[(ha^*)^2U_{11} + \dots + 2hka^*b^*U_{12}]$.	262
Table A.3.44	Hydrogen coordinates [$\times 10^4$] and isotropic displacement parameters [$\text{\AA}^2 \times 10^3$] for 07036, $\text{ZnCu}_3(\text{OH})_6\text{Cl}_2$.	263
Table A.3.45	Hydrogen bond lengths [\AA] and angles [$^\circ$] for 07036, $\text{ZnCu}_3(\text{OH})_6\text{Cl}_2$.	263
Table A.3.46	Crystal data and structure refinement for $\text{ZnCu}_3(\text{OH})_6\text{Cl}_2$.	264

Table A.3.47	Atomic coordinates [$\times 10^4$] and equivalent isotropic displacement parameters [$\text{\AA}^2 \times 10^3$] for 08039, $\text{ZnCu}_3(\text{OH})_6\text{Cl}_2$. U_{eq} is defined as one third of the trace of the orthogonalized U_{ij} tensor.	265
Table A.3.48	Bond lengths [\AA] for 08039, $\text{ZnCu}_3(\text{OH})_6\text{Cl}_2$.	265
Table A.3.49	Bond angles [$^\circ$] for 08039, $\text{ZnCu}_3(\text{OH})_6\text{Cl}_2$.	266
Table A.3.50	Anisotropic displacement parameters [$\text{\AA}^2 \times 10^3$] for 08039, $\text{ZnCu}_3(\text{OH})_6\text{Cl}_2$. The anisotropic displacement factor exponent takes the form: $-2\pi^2[(ha^*)^2U_{11} + \dots + 2hka^*b^*U_{12}]$.	268
Table A.3.51	Hydrogen coordinates [$\times 10^4$] and isotropic displacement parameters [$\text{\AA}^2 \times 10^3$] for 08039, $\text{ZnCu}_3(\text{OH})_6\text{Cl}_2$.	268
Table A.3.52	Hydrogen bond lengths [\AA] and angles [$^\circ$] for 08039, $\text{ZnCu}_3(\text{OH})_6\text{Cl}_2$.	269
Table A.3.53	Crystal data and structure refinement for c04072b, $\text{ZnCu}_3(\text{OH})_6\text{Cl}_2$.	270
Table A.3.54	Atomic coordinates [$\times 10^4$] and equivalent isotropic displacement parameters [$\text{\AA}^2 \times 10^3$] for c04072b, $\text{ZnCu}_3(\text{OH})_6\text{Cl}_2$. U_{eq} is defined as one third of the trace of the orthogonalized U_{ij} tensor.	271
Table A.3.55	Bond lengths [\AA] for c04072b, $\text{ZnCu}_3(\text{OH})_6\text{Cl}_2$.	271
Table A.3.56	Bond angles [$^\circ$] for c04072b, $\text{ZnCu}_3(\text{OH})_6\text{Cl}_2$.	272
Table A.3.57	Anisotropic displacement parameters [$\text{\AA}^2 \times 10^3$] for c04072b, $\text{ZnCu}_3(\text{OH})_6\text{Cl}_2$. The anisotropic displacement factor exponent takes the form: $-2\pi^2[(ha^*)^2U_{11} + \dots + 2hka^*b^*U_{12}]$.	274
Table A.3.58	Hydrogen coordinates [$\times 10^4$] and isotropic displacement parameters [$\text{\AA}^2 \times 10^3$] for c04072b, $\text{ZnCu}_3(\text{OH})_6\text{Cl}_2$.	274
Table A.3.59	Bragg reflections and Miller indices of pXRD pattern for herbertsmithite, syn. matched to PDF # 01-87-0679.	276
Table A.3.60	Bragg reflections and Miller indices of pXRD pattern for herbertsmithite, syn. matched to PDF # 00-57-0595. Pattern calculated on Braithwaite <i>et al.</i> single-crystal structure, Chapter 4, Ref. [20].	277

Table B.3.1

Frequency (in wavenumbers) of FTIR absorption maxima for (a) $\text{Cu}\{\text{Cu}_3(\text{OH})_6\}\text{Cl}_2$ (b) $\text{Zn}_{0.50}\text{Cu}_{3.50}(\text{OH})_6\text{Cl}_2$ (c) $\text{Zn}_{0.66}\text{Cu}_{3.34}(\text{OH})_6\text{Cl}_2$ and (d) $\text{ZnCu}_3(\text{OH})_6\text{Cl}_2$. Data agree with those reported by Braithwaite and Martens for naturally occurring samples.

289

List of Figures

Figure 1.1	Types of magnetic coupling on a 1-D array: (a) ferromagnetism; (b) antiferromagnetism; (c) ferrimagnetism.	39
Figure 1.2	Frustration: (a) Spin glass state in doped cuprates. (b) Geometric spin frustration on a triangle.	41
Figure 1.3	Magnetic Jahn-Teller distortions in molecular triangles relieve spin frustration, making possible a {2 (coupled) + 1 (uncoupled)} ground state.	43
Figure 1.4	(a) Triangular lattice of edge-sharing equilateral triangles. (b) Kagomé lattice of corner-sharing equilateral triangles. Both lattices extend in two dimensions.	44
Figure 1.5	Degenerate non-collinear or compromised 120° spin arrangements on a triangular plaquette. (a) has positive vector chirality, while (b) has negative vector chirality.	44
Figure 1.6	Compromised or non-collinear ground states on portions of (a) edge-sharing (triangular) and (b) corner-sharing (kagomé) lattices. The kagomé is more frustrated than the triangular lattice because of its lower coordination number.	45
Figure 1.7	The kagomé lattice with spins in one possible ground-state configuration. Pairs of spins on the hexagons can be rotated into or out of the plane about the dotted ellipse without changing the energy, thus giving rise to an infinite number of degenerate ground states.	46
Figure 1.8	Parallels between Heisenberg antiferromagnets: the square lattice of high- T_c cuprate superconductors and the kagomé lattice.	47
Figure 1.9	The X-ray crystal structure of $\text{KFe}_3(\text{OH})_6(\text{SO}_4)_2$ showing (a) the magnetic subunit of a triangular μ -hydroxy metal trimer, (b) the in-plane segment of the kagomé layer and (c) side-on view of stacked kagomé layers.	50
Figure 1.10	A 48 mg crystal of pure $\text{KFe}_3(\text{OH})_6(\text{SO}_4)_2$ grown by redox-based hydrothermal methods.	52
Figure 1.11	Magnetic susceptibility plots of an oriented single crystal of $\text{KFe}_3(\text{OH})_6(\text{SO}_4)_2$.	52
Figure 1.12	A ferromagnetic transition can be observed for	54

$\text{KFe}_3(\text{OH})_6(\text{SO}_4)_2$ in high enough critical fields.

- Figure 1.13** Possible classical ground states on the kagomé. (a) $q = 0$ state and (b) $q = \sqrt{3} \times \sqrt{3}$. Note that these two states are two of many possibilities with global rotational symmetry. (Another $q = 0$ state with all negative chirality is possible for (a), and another $q = \sqrt{3} \times \sqrt{3}$ alternating ground state is possible for (b), for example.) 55
- Figure 1.14** Magneto-electronic correlation in jarosites, which emphasizes the need to go to late metals for nearest-neighbor antiferromagnetic coupling. 56
- Figure 1.15** Kagomé structure in $\text{Cu}_3(\text{titmb})_2(\text{OCOCH}_3)_6 \cdot \text{H}_2\text{O}$ in $R\bar{3}$ (left). Cu centers are far apart within the plane (7.769 Å), and any superexchange occurs through the unconjugated “bucket” structure provided by titmb, which is shown in the packing diagram (right). $d_{\text{kagomé}} = 7.050$ Å. Structure from Ref. [108]. 59
- Figure 1.16** Structure of pseudo-kagomé layer in volborthite, $\text{Cu}_3\text{V}_2\text{O}_7(\text{OH})_2 \cdot 2\text{H}_2\text{O}$ (left). Packing of the pyrovanadate decorated sheets (right). Pyrovanadate groups ($\text{O}_3\text{V}-\text{O}-\text{VO}_3$) link the layers, and two crystallographically located water molecules reside in the space between the layers. The kagomé layers stack AA. Structure from Ref. [47]. 60
- Figure 1.17** Structure of kagomé layer in $\text{Cs}_2\text{Cu}_3\text{ZrF}_{12}$ above 210 K (left). Packing of kagomé layers as viewed along the crystallographic b axis (right). Magnetic data show a singularity at 210 K due to a structural phase transition. Structure from Ref. [113]. 62
- Figure 1.18** Kagomé layer in kapellasite (left). Packing of kapellasite layers (right). Kapellasite layers are held together by hydrogen bonding between the Cl^- and OH^- of adjacent layers. Kapellasite is a polymorph of herbertsmithite and likely to be metastable. Structure from Ref. [118]. 63
- Figure 1.19** Schematic showing ABC packing of kagomé layers. Such packing is common to kagomé structures crystallizing in the space group $R\bar{3}m$. It occurs in jarosite and herbertsmithite structures. It also occurs in clinoatacamite, which crystallizes in $P2_1/n$. 66
- Figure 1.20** Stacking of adjacent layers in kagomé compounds. Squares represent the equatorial metal-ligand planes: the metal ion resides in the center of each square, with ligand atoms at the 66

corners. (a) Layers alternate up and down, packing is AB(C). Examples of this packing structure discussed in this Thesis include the $R\bar{3}m$ structures jarosite and herbertsmithite, and also clinoatacamite in $P2_1/n$. (b) Layers are both up, packing is AA. $P\bar{3}m1$. An example of this packing structure discussed in this Thesis is $\text{CdCu}_3(\text{OH})_6(\text{NO}_3)_2 \cdot x\text{H}_2\text{O}$. The minerals kapellasite and haydeelite also bear this packing structure. (c) Layers alternate up and down, packing is AA. $P6_3/m$, $P6_3/mmc$. Examples of this packing structure discussed in this Thesis are Cu(1,3-bdc) and claringbullite.

- Figure 1.21** Structural distortion to remove orbital electronic degeneracy is typical of the Jahn-Teller effect, which dominates the structural chemistry of cupric compounds. At left is an octahedrally coordinated Cu^{2+} ion, at right an ion with tetragonally elongated (4+2)-coordination. In extended solid-state structures, the effect is known as a Peierls distortion. 67
- Figure 1.22** A pictorial representation of the structure of this Thesis. We move from covalently linked layers with three-atom bridges in the kagomé plane (Chapter 2), to hydrogen-bonded layers (Chapter 3) and electrostatically linked layers (Chapters 4 and 5) with one-atom bridges in the kagomé plane. 69
- Figure 2.1** Large single crystals of Cu(1,3-bdc) prepared by hydrothermal methods. 84
- Figure 2.2** Crystal structure of Cu(1,3-bdc). (a) Interlayer coordination environment projected parallel to the crystallographic c axis. (b) The MOF kagomé lattice, projected perpendicular to the c axis. Phenyl ring atoms and guest water molecule have been omitted for clarity. Selected interatomic distances and angles: Cu(1)–O(1), 1.9265(9); Cu(1)–O(2), 1.9428(9); Cu(1A)⋯O(2B), 2.8396(9); Cu(1)–C(1A), 1.2685(15); O(2A)–C(1), 1.2689(14) Å; O(1)–Cu(1)–O(2), 92.14(4)°; O(2)–Cu(1)–O(1A), 87.86(4)°; Cu(1)–O(1)–C(1A), 115.67(8)°; Cu(1)–O(2A)–C(1), 132.42(8)°. 86
- Figure 2.3** FTIR of a crystalline sample of Cu(1,3-bdc) (a) before, and (b) after heating at 240 °C for 2 hours. Before heating, the sample shows an absorbance at 1693 cm^{-1} due to a bending mode of solvent water. After heating, this absorbance is largely absent. Data for (a): 3736(w), 3086(w), 3043(w), 2016(w), 1950(w), 1909(w), 1880(w), 1795(w), 1693(w), 1603(s), 1531(i, s), 1485(sh), 1456(sh), 1404(i, s), 1282(sh), 1165(s), 1088(s), 997(s), 957(sh), 943(s), 933(sh), 858(s), 87

839(s), 808(sh), 748(i, s), 687(w), 663(s), 594(s), 548(sh), 499(s), 453(s), 440(sh), 401(s). s = sharp, i = intense, w = weak, sh = shoulder.

- Figure 2.4** (a) TGDTA for a crystalline sample of solvated Cu(1,3-bdc) as prepared. (b) A differential plot shows the time profile of loss of solvent to 257 °C more clearly. (c) TGDTA for a crystalline sample of the title compound following further sample preparation (heating for 2 hours at 240 °C). No significant loss of mass occurs until decomposition of the sample at 292 °C, indicating desolvation by the heating process. (d) A differential plot shows the time profile for mass loss. 88
- Figure 2.5** Temperature dependence of χ^{-1} for a ground sample of Cu(1,3-bdc) (a) with no heating and (b) after heating crystals to 240 °C for 2 h prior to grinding them for SQUID measurement. Values for Θ were determined by fitting data in the temperature range $150 \leq T \leq 350$ K. Lines indicate best fit obtained. 88
- Figure 2.6** Temperature dependence of χ_M for a ground powder sample of Cu(1,3-bdc) as measured at 100 Oe under zero-field cooled (\circ) and field-cooled (\square) conditions. Inset: temperature dependence of $\chi_M T$ for the same powder sample. 89
- Figure 2.7** (a) Field dependence of the magnetization per mole of Cu for Cu(1,3-bdc), measured at 2 K, showing hysteresis indicative of a very soft ferromagnet. A ground sample of Cu(1,3-bdc) was measured after heating crystals to 240 °C for 2 h prior to grinding them for SQUID measurement. (b) Full range of measurement in (a). Lines are drawn to guide the eye. The magnetization saturates at $0.91 \mu_B / \text{mol Cu}$, which is consistent with 1 unpaired electron per Cu center. 90
- Figure 2.8** Temperature dependence of the specific heat for a single crystal of Cu(1,3-bdc) measured in magnetic fields of 0 T (\bullet), 1 T (\blacksquare), and 5 T (\blacktriangle). 90
- Figure 2.9** Magnetoanisotropy experiment on Cu(1,3-bdc) crystals with total mass 7 mg, stacked using petroleum jelly. ZFC data for (\circ) *ab* plane // to field and (\square) *c* axis // to field, taken in a 10 kOe measuring field. 92
- Figure 2.10** 1,3-bdc is likely to mediate ferromagnetic superexchange 93

between Cu(II) centers in different kagomé layers.

- Figure 2.11** Corrugation and stacking of layers in Cu(1,3-bdc). Cu is in the center of CuO₄ planes, represented by squares at right. 94
- Figure 2.12** View down (a) the Cu–O–C–O–Cu pathway in Cu(1,3-bdc) and (b) the Fe–O_H–Fe bond in K-jarosite. The Fe–O_H–Fe plane is a mirror plane in jarosite, another perpendicular mirror plane runs along the O–H bond, bisecting it. Cu(1,3-bdc) contains no such mirror planes. 95
- Figure 3.1** (a) Thermogravimetric and differential thermal analysis for a powder sample of CdCu₃(OH)₆(NO₃)₂•xH₂O. (b) A differential plot shows the time profile of the loss of mass more clearly. 108
- Figure 3.2** (a) The kagomé layer of CdCu₃(OH)₆(NO₃)₂•xH₂O. H atoms and NO₂ (from O–NO₂[−] groups) have been omitted. (b) View of the structure down the (100) axis in $P\bar{3}m1$: d_{001} 7.012 Å. H-bonding occurs between the nitrate groups and the protons of OW, the crystallographically located water molecule, to hold the layers together. (c) The basic magnetostructural unit of the kagomé is the triangle. 120° disorder of the nitrate group is shown. Selected bond distances and angles: Cu(1)–O(2)–Cu(1A), 84.5; Cu(1)–O(2)–N(1), 133.4; Cu(1)–O(2)–N(1A)/N(1B), 119.7°. Cu atoms are in teal, N in blue, Cd in green, O in red, with the exception of OW, in orange. From Ref. [7]. 111
- Figure 3.3** (a) A portion of the crystal structure of rouaite in $P2_1$, as viewed down the (001) axis. Tables 3.1 and A.2.1 provide selected interatomic distances and angles, as reported by Effenberger. (b) Schematic of interatomic distances (Å) showing the irregular geometry of the rouaite triangles. (c) The packing of rouaite showing interlayer hydrogen bonding, as viewed down the (100) axis. Cu atoms are shown in teal, N atoms in blue, O atoms in red, and H atoms in white. From Ref. [11]. 112
- Figure 3.4** (a) pXRD of CdCu₃(OH)₆(NO₃)₂•0.5H₂O as synthesized, matching patterns 01-072-1433 ($P\bar{3}m1$ structure) and 01-070-1904 ($P\bar{1}$ structure) in Jade 8. Miller indices are labeled for both space groups. (b) pXRD of rouaite, Cu₂(OH)₃NO₃ in $P2_1$, matched to pattern 04-010-3058 in Jade 8. Miller indices are labeled. 113
- Figure 3.5** (a) Magnetic susceptibility versus temperature for a ground 114

	powder sample of rouaite. Magnetic susceptibility times temperature versus temperature is shown in inset. (b) Curie-Weiss fit for a ground powder sample of rouaite.	
Figure 3.6	(a) ZFC (○) and FC (□) susceptibility of $\text{CdCu}_3(\text{OH})_6(\text{NO}_3)_2 \cdot 0.5\text{H}_2\text{O}$, measured with 100 Oe field. For FC, $H_C = 100$ Oe. Susceptibility times temperature (◆) versus temperature is shown as an inset. (b) Magnetization (○) versus field of $\text{CdCu}_3(\text{OH})_6(\text{NO}_3)_2 \cdot 0.5\text{H}_2\text{O}$ shows no measurable hysteresis at 2 K.	115
Figure 3.7	Temperature dependence of χ_M^{-1} for $\text{CdCu}_3(\text{OH})_6(\text{NO}_3)_2 \cdot 0.5\text{H}_2\text{O}$. The error range for Θ was obtained by fitting over different temperature ranges from $50 \leq T \leq 300$ K.	116
Figure 3.8	Frequency independence in the AC susceptibility of $\text{CdCu}_3(\text{OH})_6(\text{NO}_3)_2 \cdot 0.5\text{H}_2\text{O}$.	116
Figure 3.9	Stacking of adjacent layers in $\text{CdCu}_3(\text{OH})_6(\text{NO}_3)_2 \cdot x\text{H}_2\text{O}$. $\text{Cu}(\text{OH})_4$ planes are represented by squares.	122
Figure 4.1	Crystal of synthetic claringbullite.	139
Figure 4.2	Crystal of synthetic clinoatacamite, obtained from oxidation reaction with O_2 as an oxidant.	140
Figure 4.3	Comparison of pXRD pattern of (a) Zn-paratacamite and (b) clinoatacamite. Although the structures are similar, the most distinguishing feature is found at approximately $40^\circ 2\theta$, which occurs as a single peak in (a), but two peaks in (b) due to a difference in symmetry.	142
Figure 4.4	A single crystal of $\text{ZnCu}_3(\text{OH})_6\text{Cl}_2$ measuring $0.05 \times 0.04 \times 0.04$ mm.	143
Figure 4.5	Summary of observed reactivity for synthetic copper(II) hydroxychloride minerals.	145
Figure 4.6	Schematic of aqueous zone refinement technique for crystal growth in sealed quartz tubes.	149
Figure 4.7	(Left) X-ray crystal structure of the kagomé layer of claringbullite shown at 40% thermal ellipsoids, as viewed down the (0 0 1) axis and (right) view of the interlayer Cu^{2+} ion, which shows an unusual Jahn-Teller distortion and is statistically disordered over three sites.	150

Figure 4.8	X^- anion in claringbullite, showing hydrogen bonding to hydroxyl protons in two kagomé layers, as viewed down the (0 0 1) axis (left) and down the (1 1 0) axis (right). Cu(2) and Cl have been omitted for clarity. Cu atoms are in teal, O in red, H in white, and X in gray.	152
Figure 4.9	(Left) Distorted kagomé layer in clinoatacamite, with two crystallographically independent Cu centers. (Right) The interlayer Cu(3) ion shows is Jahn-Teller distorted in a (4+2)-octahedral coordination.	153
Figure 4.10	The interlayer copper ions in claringbullite (left) and clinoatacamite (center) exhibit different types of Jahn-Teller distortions. A “trigonal prismatic” coordination environment in claringbullite more closely approximates a square planar arrangement, while clinoatacamite exhibits a more typical (4+2)-Jahn-Teller-distorted octahedron. The Zn^{2+} interlayer ion in herbertsmithite (right) is unaffected by Jahn-Teller distortion because all degenerate orbitals have equal occupancy given its d^{10} electronic configuration.	154
Figure 4.11	Perfect kagomé layer of Zn-paratacamite/herbertsmithite (left). Interlayer Zn^{2+} ion in Zn-paratacamite/herbertsmithite (right) has equal bond lengths for all $M_{inter}-OH$ bonds, leading to regular kagomé geometry.	155
Figure 4.12	Atom labeling scheme for triangles of claringbullite, clinoatacamite, and herbertsmithite.	157
Figure 4.13	(Top left) AA packing of claringbullite, as viewed down the (1 1 0) axis. Cl^- ions (green) are shared between two layers. Cu(2) and Cl atoms are coplanar. X^- ions (not shown) are coplanar with Cu(2) and Cl as well, residing in the center of the hexagonal channel. (Top right) ABC packing of clinoatacamite, as viewed down the (1 1 2) axis, showing that each layer has its own Cl^- ions, above and below. (Bottom) Herbertsmithite, as viewed down its (1 1 0) axis, shows ABC packing and Cl^- ion positioning similar to that in clinoatacamite. In both herbertsmithite and clinoatacamite, Cl^- ions are not coplanar with the interlayer Zn and/or Cu.	158
Figure 5.1	(a) ZFC (\circ) and FC (\square) susceptibility of $Cu_4(OH)_xCl_yF_z$ ($x + y + z = 8$), measured with 100 Oe field. For FC, $H_C = 100$ Oe. (b) Magnetization of $Cu_4(OH)_xCl_yF_z$ ($x + y + z = 8$) showing hysteresis at 5 K.	171
Figure 5.2	Curie-Weiss plot for $Cu_4(OH)_xCl_yF_z$ ($x + y + z = 8$).	171

Figure 5.3	(a) ZFC (\circ) and FC (\square) susceptibility of $\text{Cu}_2(\text{OH})_3\text{Cl}$, measured with 100 Oe field. For FC, $H_C = 100$ Oe. (b) Magnetization of $\text{Cu}_2(\text{OH})_3\text{Cl}$ showing hysteresis at 2 K.	172
Figure 5.4	Frequency independent maximum in the AC susceptibility of $\text{Cu}_2(\text{OH})_3\text{Cl}$.	172
Figure 5.5	(a) Low temperature dependence of χ_M for compounds in the solid solution $\text{Zn}_x\text{Cu}_{4-x}(\text{OH})_6\text{Cl}_2$ for $x = 0$ (red, \blacktriangle), 0.50 (blue, \blacksquare), 0.66 (green, \blacklozenge), and 1.00 (black, \bullet) as measured under ZFC conditions at 100 Oe (inset, $x = 0$). Lines are shown to guide the eye. (b) Dependence of $ \Theta $ on interlayer site occupancy, the additional point is for $x = 0.80$ (\circ).	173
Figure 5.6	Temperature dependence of χ_M^{-1} for $\text{Zn}_x\text{Cu}_{4-x}(\text{OH})_6\text{Cl}_2$. Values for Θ were determined by fitting data in the temperature range $150 \leq T \leq 350$ K, except for $x = 0.8$, which was fit from 200 to 300 K. Red lines indicate best fits obtained.	175
Figure 5.7	(a) ZFC (\circ) and FC (\square) susceptibility of $\text{ZnCu}_3(\text{OH})_6\text{Cl}_2$, measured with 100 Oe field, and showing no transition to LRO. For FC, $H_C = 100$ Oe. (b) Magnetization (\circ) versus field of $\text{ZnCu}_3(\text{OH})_6\text{Cl}_2$ shows no measurable hysteresis at 2 K.	176
Figure 5.8	ZFC (\blacksquare , red) and FC (\bullet , blue) mass susceptibility of crystalline $\text{ZnCu}_3(\text{OH})_6\text{Cl}_2$ specimen from the San Francisco Mine in Sierra Gorda, Chile.	177
Figure 5.9	Tetragonal unit cell of La_2CuO_4 , showing square-planar CuO_2 layers. Cu atoms are in teal, O in red, and La in yellow.	182
Figure 5.10	Transport in hole-doped lanthanum cuprates. In (a), nearest-neighbor hole hopping mechanism would result in frustration, but in (b), transport through a singlet pair in an RVB spin liquid does not create frustration.	182
Figure 5.11	Cyclic voltammogram of ground powder sample of $\text{ZnCu}_3(\text{OH})_6\text{Cl}_2$, starting at an open circuit potential of 1 V and scanning cathodically. The peak current decays with successive cycles. The lowest line, shown here in black, corresponds to the measured background current.	185
Figure 5.12	ZFC magnetic susceptibility versus temperature for the compounds prepared in this Thesis. $H_{meas} = 100$ Oe. Inset: Enlargement of scale showing susceptibility behavior of	186

$\text{CdCu}_3(\text{OH})_6(\text{NO}_3)_2 \cdot 0.5 \text{H}_2\text{O}$ and $\text{ZnCu}_3(\text{OH})_6\text{Cl}_2$.

- Figure A.1.1** A portion of the crystal structure of $\text{Cu}(1,3\text{-bdc})$, with unit cell. 50% ellipsoids are shown. Symmetry equivalent atoms (shown but not labeled here) are given in Tables A.1.3 and A.1.4. Phenyl-ring carbon and hydrogen atoms are omitted for clarity. 195
- Figure A.1.2** A portion of the crystal structure of $\text{Cu}(1,3\text{-bdc}) \cdot 0.11\text{H}_2\text{O}$, with unit cell. 50% ellipsoids are shown. O(3) is the oxygen atom of a solvated water molecule statistically distributed over 1/9 of sites. Symmetry equivalent atoms (shown but not labeled here) are given in Tables A.1.9 and A.1.10. Phenyl-ring carbon atoms and all hydrogen atoms are omitted for clarity. The distances between O(3) and other atoms in the structure are as follows: O(3)–Cu(1), 4.5528(2) Å. O(3)–O(1A), 3.9405(8) Å. O(3)–C(1A), 3.5303(11) Å. O(3)–O(2B), 3.4166(8) Å. 200
- Figure A.1.3** pXRD pattern for $\text{Cu}(1,3\text{-bdc})$ matched to 07060 structure. 206
- Figure A.1.4** A portion of the crystal structure of $\text{C}_{32}\text{H}_{24}\text{Cu}_6\text{O}_{26}$. 50% ellipsoids are shown. Symmetry equivalent atoms (shown but not labeled here) are given in Tables A.1.15 and A.1.16. 207
- Figure A.1.5** Packing diagram for $\text{C}_{32}\text{H}_{24}\text{Cu}_6\text{O}_{26}$, as viewed down the crystallographic *a* axis. 50% thermal ellipsoids are shown. Cu atoms are shown in teal, O atoms in red, C atoms in gray, and H atoms in white. 208
- Figure A.1.6** Packing diagram for $\text{C}_{32}\text{H}_{24}\text{Cu}_6\text{O}_{26}$, as viewed down the crystallographic *c* axis. 50% thermal ellipsoids are shown. Cu atoms are shown in teal, O atoms in red, C atoms in gray, and H atoms in white. 209
- Figure A.3.1.** (a) A portion of the crystal structure of $\text{Cu}\{\text{Cu}_3(\text{OH})_6\}\text{ClF}$, claringbullite, syn. with 40% ellipsoids shown. Atoms labeled with letters correspond to symmetry equivalent atoms as found in Tables A.3.3 and A.3.4. Hydrogen atoms are not labeled. (b) A view of the structure down the *c* axis, highlighting the crystallographically disordered Cu(2) atom. 222

Figure A.3.2	pXRD of claringbullite, matched and indexed to PDF # 01-086-0899.	227
Figure A.3.3	A portion of the crystal structure of $\text{Cu}\{\text{Cu}_3(\text{OH})_6\}\text{Cl}_2$, clinoatacamite, syn. With 40% ellipsoids shown. Atoms labeled with letters correspond to symmetry equivalent atoms as found in Tables A.3.10 and A.3.11. Hydrogen atoms are not labeled.	228
Figure A.3.4	pXRD of clinoatacamite, matched and indexed to PDF # 00-050-1599.	233
Figure A.3.5	A portion of the crystal structure of $\text{Zn}_{0.33}\text{Cu}_{3.67}(\text{OH})_6\text{Cl}_2$. 50% ellipsoids are shown. Atoms labeled with letters correspond to symmetry equivalent atoms as found in tables A.3.17 and A.3.18. Hydrogen atoms are not labeled.	234
Figure A.3.6	A portion of the crystal structure of $\text{Zn}_{0.42}\text{Cu}_{3.58}(\text{OH})_6\text{Cl}_2$. 50% ellipsoids are shown. Atoms labeled with letters correspond to symmetry equivalent atoms as found in Tables A.3.25 and A.3.26. Hydrogen atoms are not labeled.	241
Figure A.3.7	A portion of the crystal structure of $\text{ZnCu}_3(\text{OH})_6\text{Cl}_2$. 50% ellipsoids are shown. Atoms labeled with letters correspond to symmetry equivalent atoms as found in Tables A.3.37 and A.3.38. Hydrogen atoms are not labeled.	253
Figure A.3.8	pXRD of herbertsmithite powder sample, matched and indexed to PDF # 01-087-0679.	275
Figure B.1.1	Raman spectrum of $\text{Cu}(1,3\text{-bdc})\cdot 0.11\text{H}_2\text{O}$. Data: 172.3 (sh), 199.6, 222.2, 302.4(sh), 329.4, 388.9, 432.9(sh), 452.2, 475.6, 570.9, 615.7, 662.5, 686.4, 741.4, 765.8, 799.5, 816.9(sh), 848.8, 941.4(vw), 955.8(vw), 994.8, 1012.1, 1087.9, 1113.3(vw), 1184.8, 1401.3, 1444.5(sh), 1459.3, 1493.4, 1511.4, 1575.1, 1594.3, 1609.2. sh = shoulder, v = very, w = weak.	280
Figure B.1.2	Diffuse reflectance UV-vis spectrum of $\text{Cu}(1,3\text{-bdc})\cdot 0.11\text{H}_2\text{O}$. The compound shows a maximum reflectance at 449 nm with weaker maxima at 613 and 718 nm.	281
Figure B.2.1	FTIR of samples of (a) $\text{CdCu}_3(\text{OH})_6(\text{NO}_3)_2\cdot 0.5\text{H}_2\text{O}$ and (b) rouaite. Data for (a): 3543(sh, O–H stretch), 3417(i, br, O–H stretch), 2459(w), 2351(w), 1763(w), 1610(br, w, δ H–O–H), 1413(i), 1384(s, w), 1329(i), 1049(s), 972(w), 945(w), 876(w), 816(s), 779(w), 679(w), 640(w, sh), 472(i). (b):	282

3743(w), 3545(i, br, O–H stretch), 3421(i, br, O–H stretch), 2464(w), 2426(w), 2343(w), 1763(w), 1421(i), 1384(s, i), 1346(i), 1047(s), 883(w), 852(w), 810(w, sh), 785(i), 717(w, sh), 677(i), 511(i, s), 457(w, sh), 428(i). s = sharp, i = intense, w = weak, sh = shoulder. The data agree with those reported in the literature for these compounds.

- Figure B.2.2** Raman spectra of samples of (a) $\text{CdCu}_3(\text{OH})_6(\text{NO}_3)_2 \cdot 0.5\text{H}_2\text{O}$ and (b) rouaite. Data for (a): 275.2, 330.9, 393.6, 476.9, 713.5, 1047.2(i), 1321.6, 1427.5. (b) 255.3, 331.2, 407.7, 456.0, 500.5, 713.7, 1046.7(i), 1320.7, 1423.2. i = intense. 283
- Figure B.2.3** Normalized diffuse reflectance UV-vis spectra of $\text{CdCu}_3(\text{OH})_6(\text{NO}_3)_2 \cdot 0.5\text{H}_2\text{O}$ (pale blue) and rouaite (pale green). Data were normalized on the maximum intensity of reflectance for each. The title compound has a maximum reflectance at 497, with weaker maxima at 615 and 687, and a shoulder at 410 nm. Rouaite has a maximum reflectance at 508, with weaker maxima at 615 and 673 nm. $\text{CdCu}_3(\text{OH})_6(\text{NO}_3)_2 \cdot 0.5\text{H}_2\text{O}$ is a pale blue powder, and rouaite is a pale green powder. 284
- Figure B.3.1** (a) TGDTA of claringbulite. The compound loses 13.9% of its mass between 260 °C and 360 °C, leaving 86.1%. (The calculated value for loss of $3\text{H}_2\text{O}$ from $\text{Cu}_4(\text{OH})_6\text{Cl}_2$ is 87.35% and from $\text{Cu}_4(\text{OH})_6\text{ClF}$ is 86.84%.) What upon initial examination appears to be a continuous loss of mass from 260 and 390 °C, upon closer examination of the endotherm in the DTA data is actually shown to be two different events (one from 260 to 360 °C and the other from 360 to 390 °C). Further decompositions occur at 390 °C and 440 °C. (b) A differential plot shows the loss of mass more clearly. 285
- Figure B.3.2** (a) TGDTA of clinoatacamite. The compound loses 12.65% of its mass between 270 °C and 380 °C, leaving 87.35% of the initial mass. (This value is theoretically expected for loss of $3\text{H}_2\text{O}$. Similarly to claringbullite, what initially appears as one loss of mass in the TGA is actually shown to be two in the DTA: one from 270 to 380 °C, another from 380 to 400 °C. At 400 °C another decomposition starts, and a final one starts at around 460 °C. (b) A differential plot shows the loss of mass more clearly. 286
- Figure B.3.3** (a) TGDTA of herbertsmithite. The compound loses 12.75% of its mass between 290 °C and 340 °C, leaving 87.25% of the initial mass. (12.6% mass loss is theoretically expected for 287

loss of 3H₂O.) Further mass losses occur at 375 °C and 425 °C, to leave a residue after heating to 550 °C of ZnO, CuO, CuCl, and Zn₅(OH)₈Cl₂ · H₂O by pXRD. (b) A differential plot shows the loss of mass more clearly. Braithwaite *et al.* also performed TGA but heated the compound to higher temperatures. They report similar results with a loss of 12.5% from 300 – 340 °C, followed by gradual weight loss that is complete by 620 °C leaving 50.0 % of the original mass (Cu₂O and ZnO by pXRD.)

- Figure B.3.4** FTIR spectra of, from top to bottom: herbertsmithite (black), Zn_{0.66}-paratacamite (green), Zn_{0.50}-paratacamite (blue), and clinoatacamite (red). 288
- Figure B.3.5** FTIR absorbance maximum in the 930 cm⁻¹ region for synthetic samples of herbertsmithite (black ●), Zn_{0.66}-paratacamite (green ◆), Zn_{0.50}-paratacamite (blue ■), and clinoatacamite (red ▲). Braithwaite *et al.* proposed that the position of this maximum (which is probably due to an in-plane M–OH deformation) can be used to assess the approximate composition of a sample in the paratacamite series. The change, however, is very subtle near the herbertsmithite end member, and therefore this method is only very useful near the clinoatacamite-paratacamite phase boundary. 290
- Figure B.3.6** FTIR spectra of, from top to bottom: claringbullite (blue), herbertsmithite (black), and clinoatacamite (red). Peak listing for claringbullite: 3133 br; 1067 sh; 1022; 855 s; 642 vw, sh; 565 s; 523 vw; 500 vw; 480 vw, sh; 453; 444 cm⁻¹ sh. s = sharp, br = broad, w = weak, v = very sh = shoulder. 291
- Figure B.3.7** Raman spectra for copper hydroxychloride minerals. Data are in agreement with those reported for naturally occurring samples. Data for (a), herbertsmithite: 360, 398, 498; 691, 937, 1146; 1350 cm⁻¹. (b), Zn_{0.66}-paratacamite: 296, 361, 388, 500, 600; 701, 825, 940, 1173, 1212, 1349 cm⁻¹. (c), Zn_{0.50}-paratacamite: 298, 362, 400, 455, 502, 585, 708, 762, 869, 939, 1166, 1338 cm⁻¹. (d), clinoatacamite: 261, 365, 408, 446, 509, 567, 678, 797, 875, 890, 927, 968, 1167, 1357 cm⁻¹. 292
- Figure B.3.8** Normalized Diffuse Reflectance UV-vis Spectra of herbertsmithite (black, bottom), Zn_{0.66}-paratacamite (green, second from top), Zn_{0.50}-paratacamite (blue, second from bottom), and clinoatacamite (red, top). Max. intensities for herbertsmithite: 499 nm. Zn_{0.66}-paratacamite: 508, 611, 662 nm. Zn_{0.50}-paratacamite: 507, 612, 667 nm. 293

Clinoatacamite: 528, 613, 665 nm. We observe, like Jambor *et al.*, that the color of the compounds shifts from green to blue-green with increasing zinc substitution. Qualitatively, the peak at around 500 nm generally follows this trend (though $Zn_{0.50}$ and $Zn_{0.66}$ do not follow it monotonically), with herbertsmithite showing maximum intensity at the shortest wavelength of any of the compounds. Herbertsmithite shows no additional bands at longer wavelengths, unlike the other compounds.

List of Schemes

Scheme 3.1	Decreasing the distance between metal centers in $S = \frac{1}{2}$ kagomé systems will increase the strength of nearest-neighbor superexchange.	100
Scheme 3.2	Structural disorder in the nitrate group might allow for subtle changes in the local electronic environment, altering one exchange pathway as opposed to the others.	119
Scheme 3.3	Protonation of a μ -hydroxy bridge may either (a) disrupt superexchange by forming a terminal aqua species or (b) introduce disparate (and possibly ferromagnetic) superexchange pathways into the lattice.	119
Scheme 3.4	Interlayer hydrogen bonding can lead to magnetic exchange between the layers.	121

Chapter 1.
Spin Frustration on the Kagomé Lattice

1.1 Introduction

This Thesis presents information on the synthesis, structure, and magnetism of frustrated $S = \frac{1}{2}$ antiferromagnets on the kagomé lattice. Experimental realization of such compounds has long been considered a holy grail of the condensed matter physics community, although before this work no stoichiometrically pure structurally perfect $S = \frac{1}{2}$ kagomé system had been synthesized or studied magnetically.¹ The research contained herein focuses on the preparation of pure materials containing the kagomé lattice to investigate magnetic ground states in an $S = \frac{1}{2}$ spin-frustrated system. The motivation for preparing such compounds is twofold: 1) the experimental study of geometric spin frustration and 2) the investigation of whether geometric spin frustration on the $S = \frac{1}{2}$ kagomé can be related to the quantum spin liquid state of the resonating valence bond and, by extension, high- T_c superconductivity. The first Chapter is organized as follows:

- 1.1 Introduction
- 1.2 Spin Frustration
- 1.3 Bulk Magnetic Properties of Frustrated Systems
- 1.4 Frustrating Lattice Types and Long-Range Order
- 1.5 Resonating Valence Bond (RVB) Theory
- 1.6 Experimental Realizations of Triangular and Kagomé Antiferromagnets
- 1.7 The Jahn-Teller Effect / Peierls Distortion in the Structural Chemistry of Copper(II)
- 1.8 Outline and Scope of This Thesis

1.2 Spin Frustration

We begin our discussion of magnetism by examining interactions between nearest-neighbor spins on a hypothetical one-dimensional array. Figure 1.1 illustrates three different varieties of magnetic coupling. Materials in which all nearest-neighbor spins are aligned parallel are ferromagnetic, as in array a. In array b, nearest-neighbor spins are aligned antiparallel to one another in an antiferromagnetic fashion. Finally, in array c, magnetic moments are

antiferromagnetically coupled but do not have the same magnitude, resulting in ferrimagnetism.

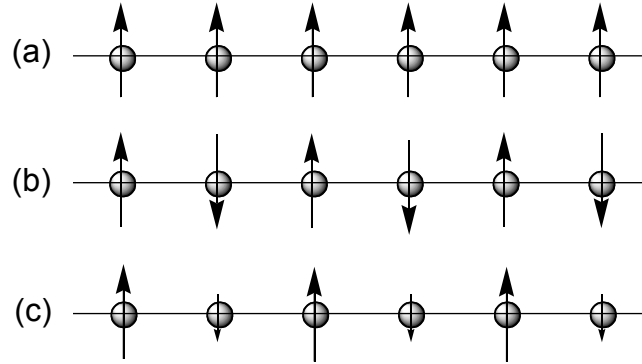


Figure 1.1. Types of magnetic coupling on a 1-D array: (a) ferromagnetism; (b) antiferromagnetism; (c) ferrimagnetism.

One of the greatest challenges in modern condensed matter physics is developing an understanding of the behavior of those systems, known as *frustrated* systems, with strong competing magnetic interactions between electrons.²⁻⁹ This challenge is made all the more salient with the advent of classes of frustrated materials that are superconducting at temperatures above 36 K, the high- T_c cuprates.¹⁰ Bednorz and Mueller discovered the archetypal high- T_c cuprate by adding chemical impurities to a La_2CuO_4 parent compound,¹¹ a process known as *doping*.

Undoped- La_2CuO_4 , which bears a square lattice of vertices of Cu^{2+} ions bridged by O^{2-} ligands, is not a frustrated material and undergoes antiferromagnetic long-range ordering above 300 K.¹² It behaves as what is known as a *Mott insulator*, a material that should be metallic according to band theory but is insulating due to strong electron-electron repulsion.^{13,14} The Cu^{2+} ions on lattice vertices have a d^9 electronic configuration, which, according to band theory, is a half-filled band and should therefore be metallic. However, the material is insulating due to a strong repulsive energy that arises when putting two electrons (or holes) on the same ion (a

Coulomb repulsion term). This Coulomb repulsion term (U) dominates over a kinetic energy, the intersite hopping energy, t_{ij} . An energy proportional to t_{ij}^2/U can be gained by antiferromagnetic superexchange.^{15,16}

Holes can be doped onto the CuO_2 lattice in order to form $\text{La}_{2-x}(\text{Ba,Sr})_x\text{CuO}_{4-y}$. This process occurs through removal of electrons from the bridging oxo ligands,¹⁷ leading to ferromagnetic interactions within the otherwise antiferromagnetic lattice.¹⁰ When doping causes ferromagnetic (F) exchange to compete with other antiferromagnetic (AF) interactions, an example of frustration known as a *spin glass* may emerge, as shown in Figure 1.2.a.² Spin glasses, studied extensively by Toulouse in some of the earliest known work on spin frustration,¹⁸ resist the tendency to show magnetic long-range order (LRO) because they have many nearly degenerate electronic configurations. A spin glass freezes into a particular configuration when the coupling energy between the spins exceeds the thermal energy, $k_B T$. This, however, is not a true long-range ordered state, because the spins introduced by doping orient themselves randomly with respect to one another in many short-range interactions. $\text{La}_{2-x}(\text{Ba,Sr})_x\text{CuO}_{4-y}$ has a rich and complex phase diagram, and at high enough hole concentrations and low enough temperatures, the material becomes superconducting.^{10,12,13}

In his review of spin frustration, Ramirez draws an important distinction between the two classes of frustrated materials: spin glasses and geometrically frustrated magnets.² In spin glasses, chemical disorder plays a role in suppressing long-range order, as discussed above with doped- La_2CuO_4 . In contrast, in *geometrically frustrated magnets*, frustration is induced exclusively by the arrangement of spins in space. Figure 1.2.b shows a basic unit of geometric frustration, the equilateral triangular plaquette with one-dimensional, or Ising, spins. Equal and competing nearest-neighbor interactions result in a paradox. In this picture, two of the three spins

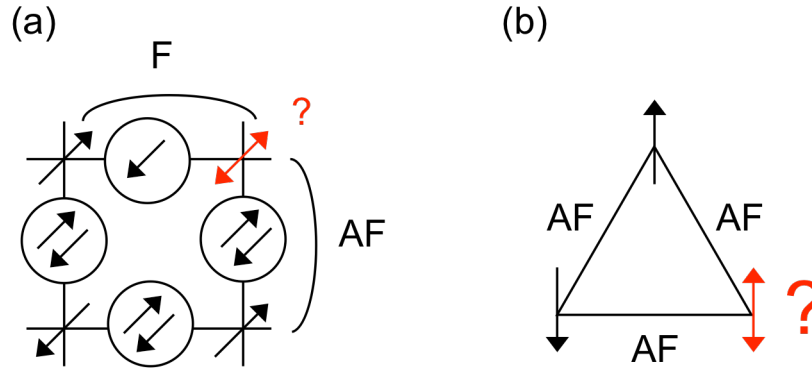


Figure 1.2. Frustration: (a) Spin glass state in doped cuprates. (b) Geometric spin frustration on a triangle.

on the triangle can couple antiferromagnetically, while a third cannot due to *geometric spin frustration*.

1.3 Bulk Magnetic Properties of Frustrated Systems

Study of frustrated systems relies mainly upon observation of their bulk properties, namely magnetic susceptibility and specific heat capacity. A critical point in either type of data indicates the transition to a long-range ordered state. Bulk magnetic interactions can be described by the Curie-Weiss Law:

$$\chi = \frac{C}{T - \Theta} \quad (1.1)$$

where χ is the molar magnetic susceptibility, C is the Curie constant, T is the temperature, and Θ is the Curie-Weiss constant. By fitting the inverse susceptibility versus temperature, one can extract values for the parameters Θ and C . A positive value of Θ is indicative of average ferromagnetic nearest-neighbor exchange within a system, while a negative value of Θ is indicative of average antiferromagnetic nearest-neighbor exchange. Treatment of a 3-D Heisenberg Hamiltonian¹⁹ ($H = -2J S_1 \cdot S_2$) with mean-field theory (which assumes that a given spin will be influenced isotropically only by its nearest neighbors) allows one to obtain values for the spin, S , from the Curie constant, C , and information on the nearest-neighbor

superexchange coupling constant, J , from the Curie-Weiss constant, Θ (Equations 1.2 and 1.3)^{2,20}

$$C = \frac{Ng^2\beta^2S(S+1)}{3k_B} \quad (1.2)$$

$$J = \frac{3\Theta k_B}{zS(S+1)} \quad (1.3)$$

Fitting the inverse susceptibility versus temperature for a non-frustrated antiferromagnet yields a value of Θ that is similar in magnitude to the observed Néel transition temperature, T_N . The material should order at $T_N = \Theta$, where the ground state configuration is achieved because the exchange energy between spins is larger than thermal fluctuations. In a spin-frustrated system, however, the observed T_N is significantly smaller relative to Θ because fluctuations among highly degenerate states suppress the transition to long-range order. Ramirez defines a frustration parameter, f , as an empirical means of quantifying frustration, with $f > 10$ in a frustrated system,² where T_c is a critical temperature for long-range ordering

$$f = \frac{|\Theta|}{T_c} \quad (1.4)$$

If spin fluctuations suppress conventional long-range order so far that it cannot be established, vastly degenerate two-dimensional geometrically frustrated systems are expected to give rise to exotic spin physics at low temperature, including the resonating valence bond, discussed in Section 1.5.^{9,21-27}

1.4 Frustrating Lattice Types and Long-Range Order

In order to target the synthesis of geometrically frustrated systems, we must first discuss the desired geometries of materials for studying spin frustration. As mentioned above and shown in Figure 1.2.b, the canonical illustration of geometric spin frustration is a triangular plaquette with Ising spins. Spin frustration has been explored in $S = 1/2$ triangular molecules, for instance,

which can be viewed as 0-D materials.²⁸⁻⁴⁴ However, these compounds undergo a magnetic Jahn-Teller distortion. Jahn and Teller showed that any non-linear polyatomic molecule with electronic orbital degeneracy is unstable and will distort spontaneously to lower the energy of one of its initially degenerate orbitals.⁴⁵ Although these triangular molecules have perfect D_3 symmetry with a 2E ground state at high temperature, symmetry lowering distortions at low temperature give a {2 (antiferromagnetically coupled) + 1 (uncoupled)} spin ground state, as depicted in Figure 1.3.²⁸⁻⁴⁴ These distortions inhibit the use of such molecules for studying geometric spin frustration as it relates to exotic spin physics, thus necessitating the use of 2-D systems with an extended array of spins.

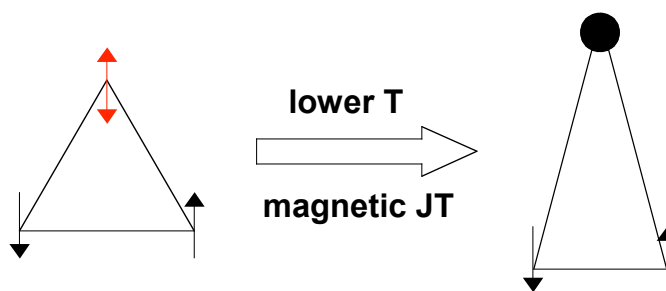


Figure 1.3. Magnetic Jahn-Teller distortions in molecular triangles relieve spin frustration, making possible a {2 (coupled) + 1 (uncoupled)} ground state.

The discussion here will therefore be limited to extended equilateral triangular arrays in two dimensions, the triangular lattice and the kagomé lattice. Real chemical systems are, of course, only quasi-two dimensional, and the 3-D packing of these lattices in space also becomes a consideration, as discussed in Section 1.6.2.2. The triangular lattice consists of edge-sharing triangles and the kagomé lattice consists of corner-sharing triangles, as shown in Figure 1.4. The

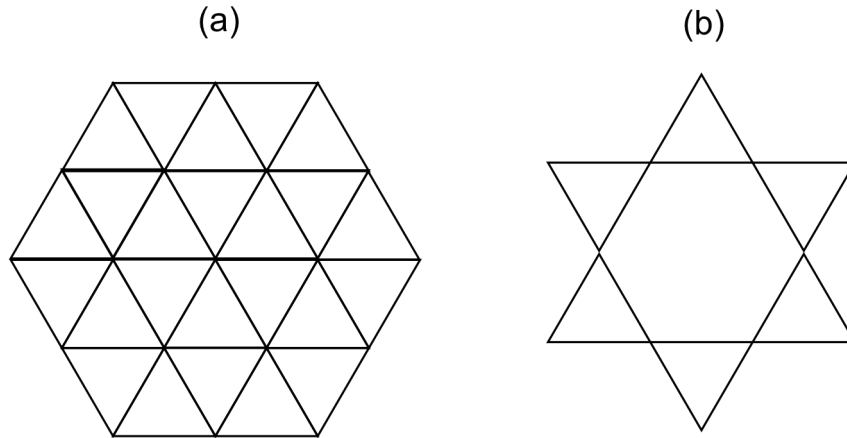


Figure 1.4. (a) Triangular lattice of edge-sharing equilateral triangles. (b) Kagomé lattice of corner-sharing equilateral triangles. Both lattices extend in two dimensions.

kagomé lattice, also known as the hexagonal tungsten bronze⁴⁶ or defect brucite layer,⁴⁷ is named after a form of Japanese weave (kago = basket, mé = eye or hole).

The dimensionality of the Hamiltonian used to describe spins in these systems is an important consideration. Hamiltonians can be one-dimensional (Ising spins, which are scalar and have no directionality beyond up or down), two-dimensional (XY spins, confined to a two-dimensional plane), or three-dimensional (Heisenberg spins).

Most frustrated systems that undergo true phase transitions to a long-range ordered state adopt what are known as compromised or non-collinear spin configurations. A 120° arrangement of spins for all triangular plaquettes within the lattice results in a vector sum of zero for the plaquette and the lattice, thus globally satisfying

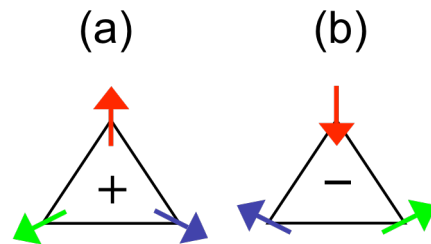


Figure 1.5. Degenerate non-collinear or compromised 120° spin arrangements on a triangular plaquette. (a) has positive vector chirality, while (b) has negative vector chirality.

antiferromagnetism on the lattice.^{5,22} Any such state is an energy minimum and therefore a ground state by definition.²² For a triangular lattice of Heisenberg spins, in addition to the degeneracy associated with globally rotating the spins, the 120° array has a degeneracy due to

handedness, or *chirality*.^{5,48} Positive (negative) vector chirality arises when the spins rotate by $+120^\circ$ (-120°) as one moves clockwise about the triangle, as shown in Figure 1.5.⁴⁹

Extensive theoretical study has been done on the antiferromagnetic triangular lattice. In a seminal paper on this subject, Wannier worked out the statistical mechanics on this lattice with an Ising Hamiltonian, predicting finite entropy for the system but no transition to long-range order. (As one of many possible energy minima, he predicted a state with alternating rows of up spins and down spins.)⁵⁰ The situation with Heisenberg spins is more complex. For $S > \frac{1}{2}$, a 120° ordered Néel state is believed to be the ground state,^{23,51-53} although there is still some debate over whether or not, in the quantum limit, the $S = \frac{1}{2}$ state will support a resonating valence bond ground state instead.²⁴⁻²⁷ The resonating valence bond state is described more extensively in Section 1.5.

Regardless of the situation on the triangular lattice, the kagomé lattice is expected to show more frustration and degeneracy than the triangular case because it has a lower coordination number and is therefore less constrained,^{9,22,54,55} as shown in Figure 1.6. As shown previously in Figure 1.4, each vertex on the triangular lattice is shared by six triangles, while in

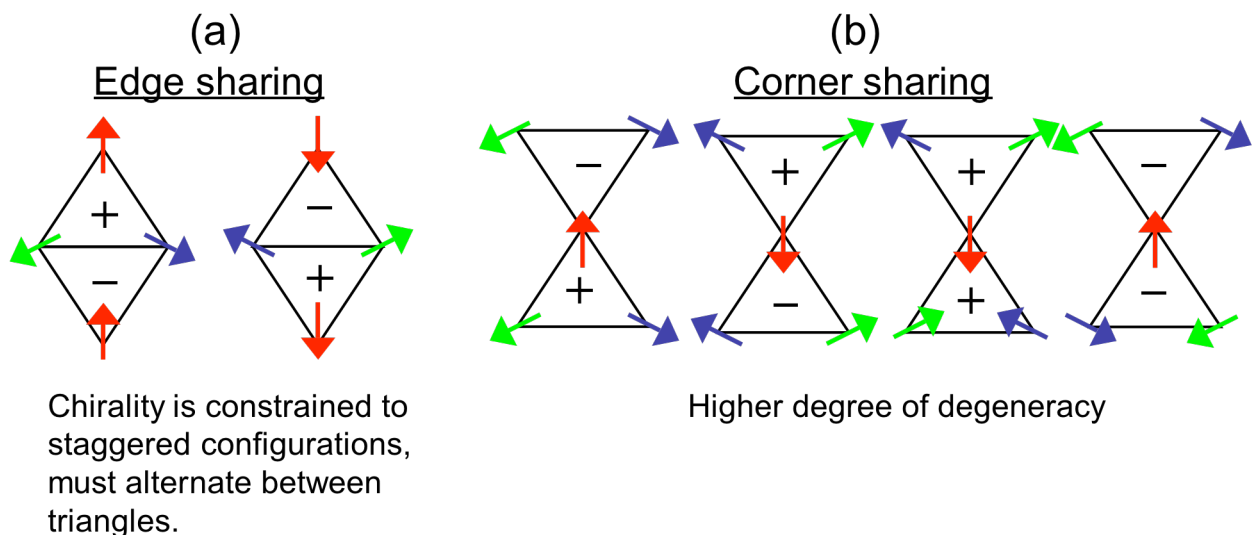


Figure 1.6. Compromised or non-collinear ground states on portions of (a) edge-sharing (triangular) and (b) corner-sharing (kagomé) lattices. The kagomé is more frustrated than the triangular lattice because of its lower coordination number.

the kagomé each vertex is shared by only two triangles. 120° chiral ground states, therefore, are constrained to be staggered to minimize the energy of each triangle in the edge-sharing case but not in the corner-sharing case, as shown in Figure 1.6.^{22,55}

A phase transition to long-range order, however, is not expected on the kagomé (and especially the $S = \frac{1}{2}$ kagomé) because of its infinite degeneracy: any spin configuration in which all spins are disposed at 120° to one another is a ground state by definition, and an infinite number of such states exist. In classical systems, unusual spin physics have been observed as thermal, quantum, or spatial fluctuations among spins suppress conventional long-range order.^{56,57} For quantum spins, different theoretical treatments have predicted a ground state that remains quantum disordered at zero temperature.^{21-23,54,58-63} Such disorder leaves open the possibility that the kagomé can support spin liquid states like the resonating valence bond (RVB), discussed in Section 1.5.⁶⁴⁻⁶⁷

1.5 Resonating Valence Bond (RVB) Theory

A resonating valence bond spin liquid state²⁴ has been proposed to explain the scatterless hole transport in high- T_c superconductors.^{16,68,69} In this state, spins spontaneously form singlet bonds, which fluctuate like a liquid between many different configurations. Such states are highly degenerate owing to the great number of spin configurations at the same energy. Similar high degeneracy in the kagomé leaves open the possibility that quantum fluctuations on the

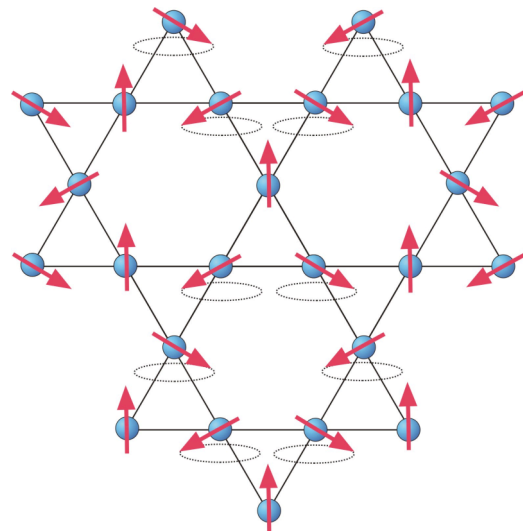


Figure 1.7. The kagomé lattice with spins in one possible ground-state configuration. Pairs of spins on the hexagons can be rotated into or out of the plane about the dotted ellipse without changing the energy, thus giving rise to an infinite number of degenerate ground states.

kagomé lattice are sufficiently strong to suppress long-range order^{21,54} and allow RVB to occur.⁶⁴⁻⁶⁷

Recall $\text{La}_{(2-x)}(\text{Ba,Sr})_x\text{CuO}_{4-y}$, which bears a Néel ordered state when undoped, but undergoes a transition to a superconducting phase at 37 K when doped with adequate hole concentrations.^{10,12} Crucial to understanding the mechanism of such high- T_c superconductivity is the as-yet unclear relationship between the antiferromagnetic interactions in the undoped state and the formation of singlet pairs in the superconducting state, as well as the role of frustration¹⁰ within such processes. According to theoretical predictions, the RVB quantum spin liquid phase is most likely to be found on a low-dimensional, low-spin magnetically frustrated lattice.¹⁶ In order to study the frustration associated with the RVB quantum spin liquid, one would ideally look at a material with no LRO at any temperature, as conventionally ordered states would destroy the RVB spin liquid phase.⁶⁸ Because quantum fluctuations on the Heisenberg antiferromagnet kagomé lattice, and particularly the $S = \frac{1}{2}$ kagomé lattice, are expected to prevent magnetic LRO, the lattice emerges as a prominent candidate for supporting an RVB state.⁶⁴⁻⁶⁷ Furthermore, the kagomé lattice and the high- T_c cuprate lattice bear several apparent similarities inviting such comparisons. As shown in Figure 1.8, both have four nearest-neighbor spins and antiferromagnetic nearest-neighbor exchange. The paramount distinction, however, lies in the difference between geometric frustration and spin glass, as discussed in Section 1.2. Kagomé materials, unlike the high- T_c cuprates, can reveal the low temperature physics of

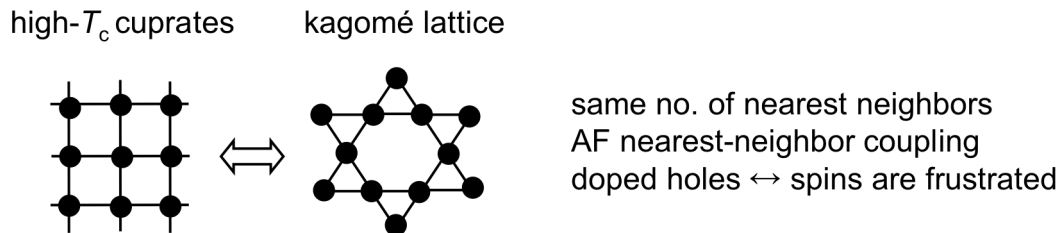


Figure 1.8. Parallels between Heisenberg antiferromagnets: the square lattice of high- T_c cuprate superconductors and the kagomé lattice.

frustration without the added complication of chemical disorder.

1.6 Experimental Realizations of Triangular and Kagomé Antiferromagnets

1.6.1 Triangular Antiferromagnets

Triangular antiferromagnets have been realized synthetically in the solid state in several forms.⁴ Because we are interested in the effects of geometrical frustration without structural disorder, we will limit our discussion here to stoichiometric compounds. The two most salient examples of frustrated triangular antiferromagnets in the recent literature are NiGa_2S_4 and NaTiO_2 . Significant quantum effects at low temperature are expected with such $S = 1$ and $S = \frac{1}{2}$ lattices.

NiGa_2S_4 , which crystallizes in $P\bar{3}m1$, bears a perfect equilateral triangle lattice of Ni^{2+} ions.⁷⁰ In this compound, NiS_6 octahedra comprise magnetic layers of edge-sharing triangles. Each Ni^{2+} layer is sandwiched between two layers of edge-sharing GaS_4 tetrahedra; the slabs are separated by van der Waals gaps giving a $\text{Ni}\cdots\text{Ni}$ interplane distance of 11.996 Å. The structure has AA packing. NiGa_2S_4 has moderate antiferromagnetic exchange, with $\Theta = -80$ K, and shows no magnetic LRO. Neutron measurements show gapless excitations, which may indicate that the compound has spin liquid behavior with coherence beyond nearest neighbor dimers.⁷¹

NaTiO_2 contains alternating layers of NaO_6 and TiO_6 octahedra in a delafossite structure.² The d^1 Ti^{3+} ions sit on the vertices of a perfect equilateral triangular lattice in the room temperature structure. While initial magnetic studies showed no ordering to 1.4 K despite $\Theta = -1000$ K, indicative of spin frustration, decomposition of NaTiO_2 samples occurs over the course of several hours.⁷² Magnetic and heat capacity data show a structural phase transition at 250 K, and crystallographic studies show a second-order Jahn Teller distortion which increases $\text{Ti}\cdots\text{Ti}$ bonding and results in isosceles triangles with two distinct $\text{Ti}\cdots\text{Ti}$ distances.⁷³ This

structural phase transition inhibits the use of NaTiO_2 for studying spin frustration on the 2-D triangular lattice.

1.6.2 Kagomé Antiferromagnets

1.6.2.1 $S > \frac{1}{2}$ Kagomé Antiferromagnets

A dearth of kagomé-based materials for a long time inhibited their systematic investigation, despite intense interest in their magnetic ground states.^{2,21-23,54,58-67,74} Existing materials, such the layered garnets, $\text{SrCr}_x\text{Ga}_{12-x}\text{O}_{19}$ (SCGO),⁷⁵⁻⁷⁹ are not ideal kagomé materials; despite showing strong frustration, they suffer from added structural complexities. For SCGO with $x = 0.89$, no transition to LRO is observed, although strong antiferromagnetic nearest-neighbor coupling is evidenced by $\Theta \approx -500$ K.⁸⁰ Non-stoichiometry issues and additional triangular-based layers interposed between kagomé layers complicate the interpretation of these magnetic properties, however, because metal ions reside in different magnetic environments with different coupling constants. A short spin correlation length in neutron studies indicates that the frustrated behavior is due to a spin glass, arising from site disorder instead of inherent geometry.

Difficulty of synthesis of kagomé-based compounds has hampered their magnetic study.^{81,82} For a long time such was the case with the jarosite family of compounds, notoriously difficult to prepare and plagued by variable magnetic properties arising from lattice disorder. A redox-based synthesis of jarosites, pioneered in the Nocera group, allowed for a systematic investigation of the magnetic properties of the largest group of isostructural and isoelectronic kagomé materials yet discovered.^{56,57,83-90} The jarosite family of compounds, based on the $\text{KFe}_3(\text{OH})_6(\text{SO}_4)_2$ parent, is composed exclusively of kagomé layers formed from $\text{Fe}^{\text{III}}_3(\mu\text{-OH})_3$ triangles (Figure 1.9.a). These triangles are capped by sulfate anions positioned alternately up and down about a hexagonal network shown in Figure 1.9.b.⁹¹ The kagomé layers are separated

by K^+ ions, which reside in the interlayer space in the same plane as the sulfur atoms of the capping tetrahedral groups (Figure 1.9.c). An extensive family of jarosite compounds arises from the substitution of the Fe^{3+} ions by other M^{3+} ions (Cr^{3+} , Al^{3+} , Ga^{3+} , In^{3+}) and from the substitution of the K^+ ion by other monovalent (Na^+ , Rb^+ , Ag^+ , Tl^+ , NH_4^+ , H_3O^+) or divalent ($\frac{1}{2}Pb^{2+}$, $\frac{1}{2}Hg^{2+}$) ions; more members of the jarosite family result from the replacement of the sulfate group by either SeO_4^{2-} or CrO_4^{2-} .^{91,92} The ability to systematically vary the intra- and interlayer metal ions and interlayer spacing in jarosite has provided our group with a unique framework for studies of spin frustration on the kagomé.

As shown in Figure 1.7, geometric considerations imposed by the spin arrangement of the kagomé engender an infinite number of degenerate ground states, and in theory, materials bearing this lattice should not display conventional long-range order (LRO).^{21-23,54,58-63}

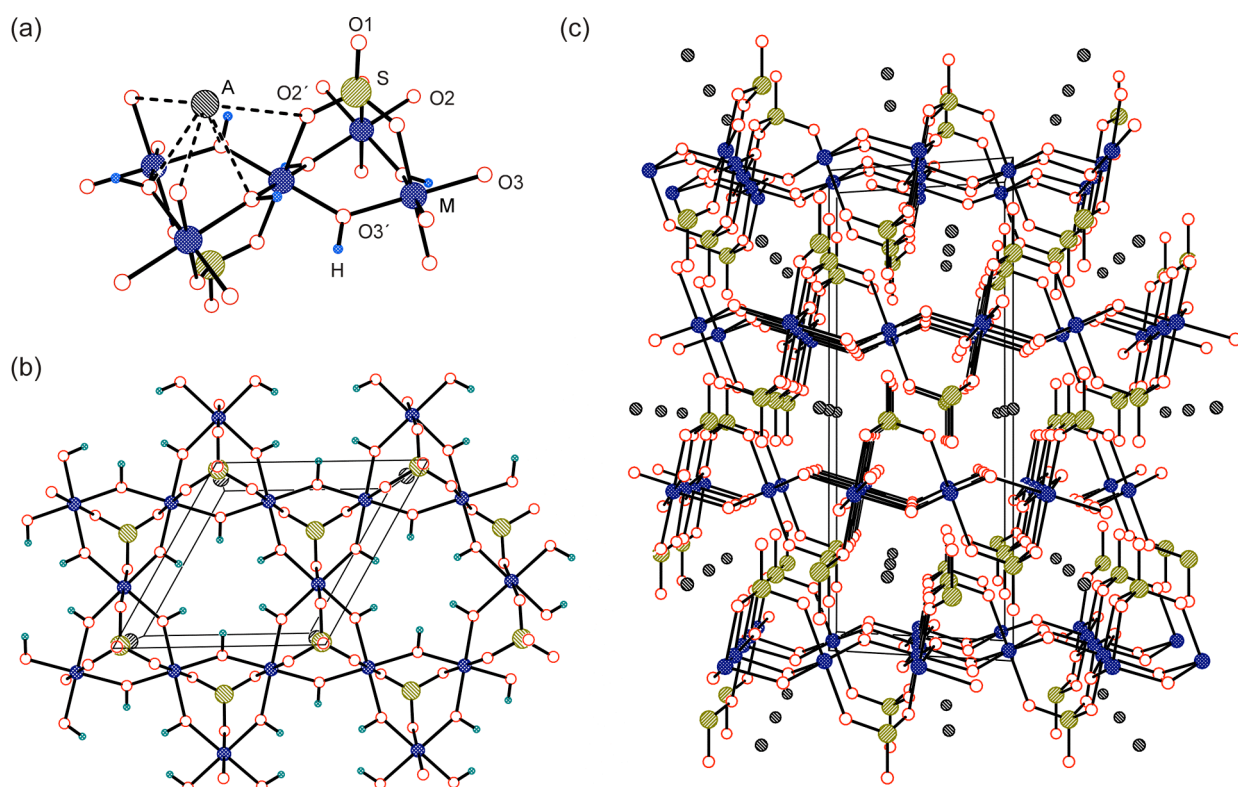
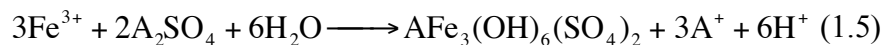


Figure 1.9. The X-ray crystal structure of $KFe_3(OH)_6(SO_4)_2$ showing (a) the magnetic subunit of a triangular μ -hydroxy metal trimer, (b) the in-plane segment of the kagomé layer and (c) side-on view of stacked kagomé layers.

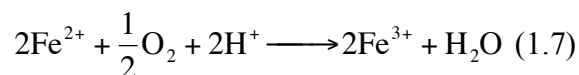
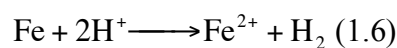
Nevertheless, in all but hydronium Fe^{3+} jarosite, LRO is observed. Three-dimensional (3-D) LRO may be established when the ground state-degeneracy created by spin frustration is lifted by the presence of anisotropy that can occur either within a two-dimensional plane or by virtue of interactions between neighboring planes, further-neighbor exchange interactions, or by lattice disorder. As mentioned above, this last perturbation is particularly relevant to jarosites, because they have been notoriously difficult to prepare in pure forms. The monovalent A^+ ions are susceptible to replacement by hydronium ions and/or the coverage of the Fe^{3+} lattice sites is incomplete; consequently samples with magnetic site occupancies of 70–94% are obtained. The presence of site defects in strongly correlated magnetic arrays may significantly affect the compounds' bulk behavior.^{55,92} Frustration on the kagomé is almost completely relaxed when magnetic site vacancies approach 30% that of a fully occupied lattice.

The importance of jarosites as experimental models of the strongly correlated kagomé antiferromagnet problem, coupled to the ambiguities associated with their magnetic properties owing to the nonstoichiometric coverage of the magnetic lattice, provided an imperative to develop new synthetic routes that afforded pure and crystalline jarosites. Before work pioneered in our group by Daniel Grohol, the most common method of preparing Fe^{3+} jarosites was a simple precipitation reaction under hydrothermal conditions (100 – 200 °C)^{93,94}



The drawback of this single-step reaction pathway is that the product precipitation is fast, leading to incorporation of hydronium ions in A^+ cation sites and persistent deficiencies in the Fe^{3+} site occupancy.^{95,96} Magnetic properties of iron jarosites are significantly affected by these site deficiencies, as well as proton transfer of hydronium ions to the hydroxide ions in the jarosite structure.^{55,90,92} Moreover, precipitation of product is so rapid that crystallites any larger than

$\sim 20 \mu\text{m}$ have not been obtained from this route.^{55,92,97} With the intent of preparing large crystals of high purity, our group developed a new method in which two kinetic steps are inserted prior to precipitation of the jarosite product, thus slowing down the reaction under hydrothermal conditions:⁸⁷



Control over the fast precipitation (Equation 1.5) is achieved by using this step-wise redox process to slowly generate Fe^{3+} throughout the course of the hydrothermal process. Using this method, pure crystals weighing up to 48 mg and 1 cm long grow from the solution (Figure 1.10). Grohol *et al.* performed detailed studies of the magnetism of pure samples with the following results.⁸⁷

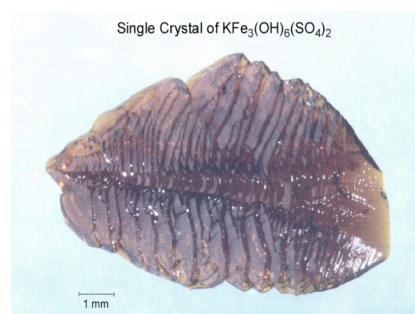


Figure 1.10. A 48 mg crystal of pure $\text{KFe}_3(\text{OH})_6(\text{SO}_4)_2$ grown by redox-based hydrothermal methods.

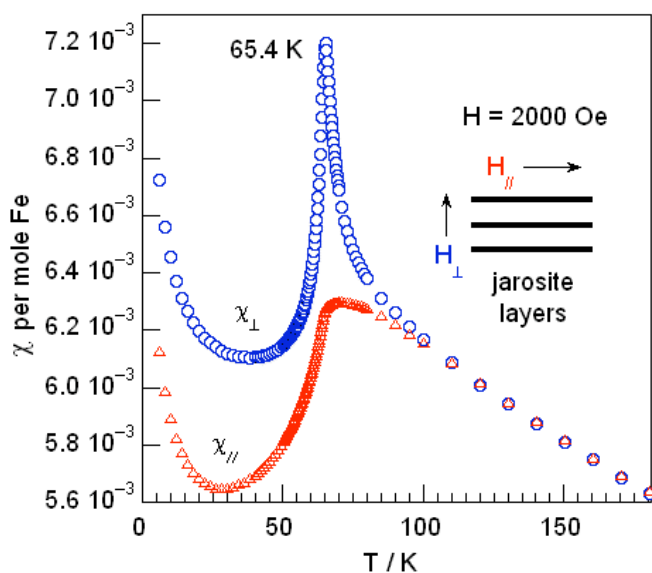


Figure 1.11. Magnetic susceptibility plots of an oriented single crystal of $\text{KFe}_3(\text{OH})_6(\text{SO}_4)_2$.

Stoichiometrically pure iron jarosites display LRO at finite temperature. Alkali metal jarosites all undergo long-range ordering behavior, characterized by a Néel transition at $T_N \sim 65 \text{ K}$, which is in accordance with the highest T_N values previously observed either by susceptibility or neutron diffraction measurements.^{48,55,98}

The maximum in the AC magnetic

susceptibility plot shows frequency independence, indicating the absence of spin-glass behavior. Unlike the inconsistent results observed in past studies of jarosites, the ordering temperature does not depend on sample preparation nor is it significantly altered by changing the size of the interlayer A^+ cation.

The absence of LRO in $(H_3O)Fe_3(OH)_6(SO_4)_2$, which has magnetic ion lattice coverages approaching 97%, is not due to intrinsic physics associated with a spin-frustrated lattice. Our group's detailed study of $K_x(H_3O)_{1-x}Fe_3(OH)_6(SO_4)_2$ ($0 < x < 1$) shows a monotonic decrease in ordering temperature with increasing H_3O^+ content, suggesting that the magnetic disorder arises from structural effects resulting from increased interlayer H_3O^+ .⁹⁰ Proton transfer from the interlayer hydronium ions to the μ -hydroxo ions to form μ -aqua bridges is manifested not only in structural disorder as observed by the presence of an H–O–H bending mode in the FTIR,⁸⁷ but in magnetic disorder as well, derived from unequal nearest-neighbor exchange coupling constants between metal centers bridged by water versus hydroxide.

The availability of large single crystals of pure potassium iron jarosite $KFe_3(OH)_6(SO_4)_2$ has made it possible to measure the susceptibility of single crystals oriented in the magnetic field along distinct axes (Figure 1.11), and to attribute the susceptibility maximum at $T_N \sim 65$ K to an out-of-plane canting of in-plane spins. Our results are consistent with LRO arising from coupling of jarosite layers exhibiting a net magnetization, which arises from anisotropy developed from the Dzyaloshinsky-Moriya (DM)^{99,100} interaction.

The DM interaction causes the spins on each triangle in the jarosite to form an 'umbrella' structure and gives each kagomé plane a net ferromagnetic moment. However, the interlayer coupling in iron jarosite causes the ferromagnetic moments to couple antiferromagnetically between layers in the absence of an applied field. In the presence of a high enough critical field,

a jump in magnetization versus field occurs when spins on layers that were previously oppositely canted are realigned in the same direction. For $\text{KFe}_3(\text{OH})_6(\text{SO}_4)_2$, this occurs at about $H_c = 14$ T when $T = 49$ K.⁵⁶ This transition is shown schematically in Figure 1.12.

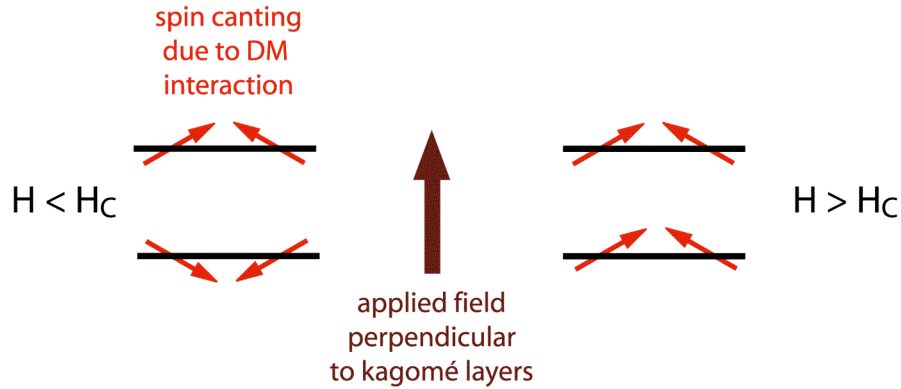


Figure 1.12. A ferromagnetic transition can be observed for $\text{KFe}_3(\text{OH})_6(\text{SO}_4)_2$ in high enough critical fields.

The DM interaction acts as a second-order perturbation term to isotropic exchange in a Heisenberg Hamiltonian

$$\sum_{\langle i,j \rangle} \mathbf{D}_{ij} \cdot (\mathbf{S}_i \times \mathbf{S}_j) \quad (1.8)$$

where \mathbf{D}_{ij} accounts for spin-orbit coupling of the magnetic ion, intersite hopping, Coulomb repulsion, and crystal-field splitting, and $(\mathbf{S}_i \times \mathbf{S}_j)$ is the cross product term of adjacent spins within the layer. Moriya's rules¹⁰¹ state that \mathbf{D}_{ij} is zero when an inversion center is located halfway between two sites in the crystal lattice, and since no such inversion center exists in jarosite, DM is allowed. Furthermore, if a mirror plane contains both metal centers, then \mathbf{D}_{ij} lies in a plane perpendicular to that plane between the metal centers. A mirror plane containing both metal centers exists in the potassium jarosite structure, coincident with the Fe—O_H—Fe bond and tilted $\sim 17.5^\circ$ from the plane of the kagomé. Moriya's rules further distinguish between the infinite number of perpendicular planes that fit this description by stating that \mathbf{D}_{ij} resides in the

perpendicular mirror plane between the two metal sites; thus the vector can reside anywhere in the mirror plane between the sites that is coincident with the O—H bond in jarosite.

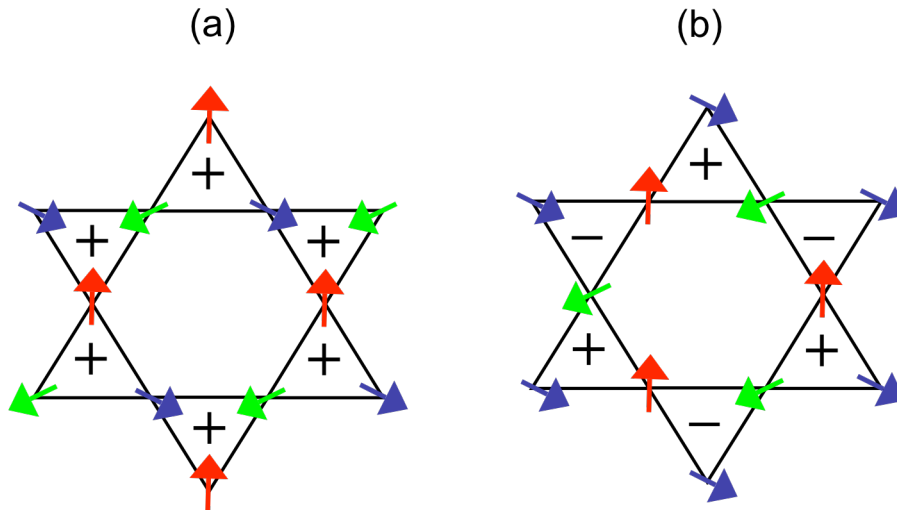


Figure 1.13. Possible classical ground states on the kagomé. (a) $q = 0$ state and (b) $q = \sqrt{3} \times \sqrt{3}$. Note that these two states are two of many possibilities with global rotational symmetry. (Another $q = 0$ state with all negative chirality is possible for (a), and another $q = \sqrt{3} \times \sqrt{3}$ alternating ground state is possible for (b), for example.)

The DM vector, \mathbf{D}_{ij} , has components that are both parallel ($D_{//}$) and perpendicular (D_z) to the plane of the kagomé. $D_{//}$ gives Ising-like anisotropy and results in spin canting out of the kagomé plane, and D_z gives XY -type anisotropy and selects the chirality of the system.^{101,102} The $q = 0$ and the $q = \sqrt{3} \times \sqrt{3}$ are possible classical ground states with different chirality on the kagomé, shown in Figure 1.13. Single crystals of sufficient dimensions have enabled inelastic neutron scattering to be undertaken for the study of spin-waves of the 2-D kagomé lattice. The results of these studies by Young Lee's group at MIT have shown that in iron jarosite, because of slight out-of-kagomé plane spin canting, completely free rotation of spins is destroyed, and the $q = 0$ ground state is very slightly energetically favored. The observation of spin waves with weakly dispersive zero energy modes between different chiral ground states was the first such observation in a geometrically frustrated spin system.⁵⁷

Because the Dzyaloshinsky-Moriya interaction leads to magnetic LRO in sulfate-capped iron jarosites, and because the easy-axis anisotropy arises due to the tilting of the FeO_6 octahedra relative to the kagomé plane, Bart Bartlett investigated DM at a synthetic level by preparing a series of selenate-capped jarosites, $\text{AFe}_3(\text{OH})_6(\text{SeO}_4)_2$, in an attempt to flatten the layers and attenuate the ordering behavior. However, he found that despite being able to flatten the canting angle to $\sim 14.5^\circ$, the metrics of the basic $\text{Fe}_3(\mu\text{-OH})_3$ structural unit were largely preserved and similar ordering behavior was observed.^{89,103} Because the DM interaction is proportional to S^2 , moving from an $S = 5/2$ to an $S = 1/2$ system should reduce the magnitude of the DM interaction 25-fold and suppress this classical ordering behavior. Systems with lower spin are also more likely to support quantum states,^{6,23,59,104} providing us with the potential to observe quantum effects and unusual spin physics. We therefore turned our attention to preparing $S = 1/2$ kagomé systems.

We used our previous work with jarosite systems to direct our choice of $S = 1/2$ metal ion.

Figure 1.14 presents the magnetic properties of the known jarosites and the d electron occupancy

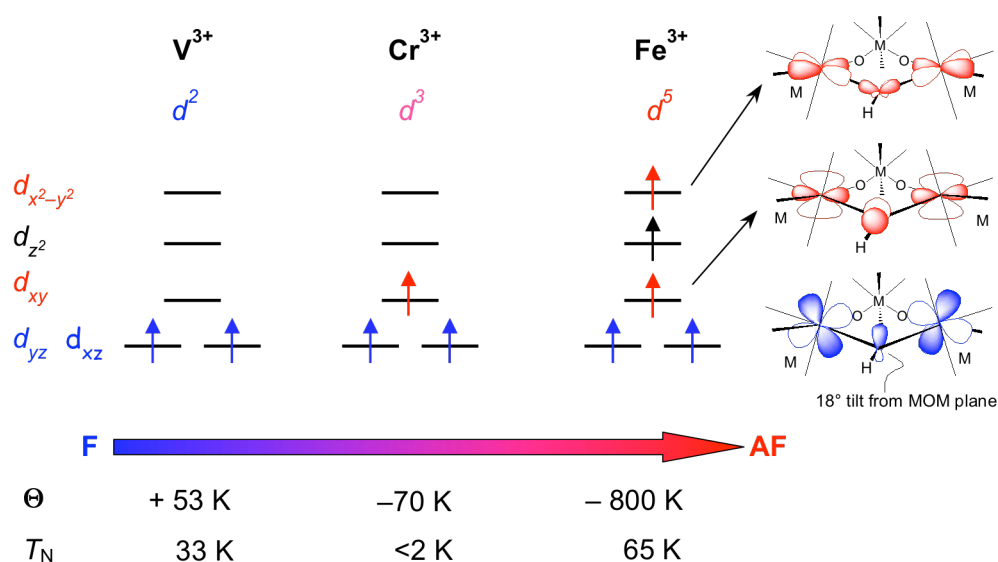


Figure 1.14. Magneto-electronic correlation in jarosites, which emphasizes the need to go to late metals for nearest-neighbor antiferromagnetic coupling.

of their crystal field splitting diagrams. The positive Weiss constant obtained from our magnetic studies of V^{3+} jarosite ($\Theta = + 53$ K) indicated superexchange was, on average, ferromagnetic.⁸⁵ The two d electrons of V^{3+} jarosite occupy the $e_g(d_{xz}, d_{yz})$ orbital set. Therefore, the π symmetry pathway, resulting from the interaction of the $e_g(d_{xz}, d_{yz})$ orbital set with the p orbital of the bridging hydroxide, leads to a ferromagnetic exchange interaction. Neutron diffraction studies on Fe jarosites show an 18° rotation of the O–H bond out of the Fe–O–Fe plane, a rotation apparently severe enough in the V^{3+} analog to decouple the $d\pi$ orbitals of neighboring V^{3+} metals to lead to a ferromagnetic ground state.

Adding one more d electron to the crystal field, we see that in Cr^{3+} jarosite, the sign of the nearest-neighbor magnetic coupling changes. Occupation of the metal d_{xy} orbitals in Cr^{3+} jarosites leads to a dominant antiferromagnetic exchange term through a $d_{xy}(\sigma)$ – $p(O)$ – $d_{xy}(\sigma)$ pathway that is capable of overwhelming the $d_{xz}(\pi)$ – $p(O)$ – $d_{xz}(\pi)$ pathway. Placement of two more electrons in the d_{z^2} and $d_{x^2-y^2}$ orbitals of Fe^{3+} jarosite increases this antiferromagnetic exchange interaction within the kagomé lattice by more than an order of magnitude. Since the overlap between the d_{z^2} and the p orbitals of the bridging hydroxide is small, it is the overlap between the $d_{x^2-y^2}$ orbitals with the μ -hydroxy p orbital that causes the large antiferromagnetic exchange interaction of Fe^{3+} jarosites. The observed properties of this exchange pathway concur with long-standing predictions of Goodenough and Kanamori,¹⁰⁵⁻¹⁰⁷ and account for the high degree of spin frustration observed in the d^5 ($S = 5/2$) spin system of iron jarosites.

Returning now to $S = 1/2$ systems, we see that an early metal $S = 1/2$ lattice, such as Ti^{3+} , would likely behave in a manner similar to V^{3+} . Even if the synthetic difficulty involved in stabilizing Ti^{3+} to oxidation in an oxygen-rich ligand environment were surmounted, the Ti^{3+} jarosite, with the same $d_{xz}(\pi)$ – $p(O)$ – $d_{xz}(\pi)$ pathway as in V^{3+} , would most likely be a kagomé

ferromagnet, inhibiting its use in the study of frustration. Our work with jarosites showed that Cu^{2+} , which would have a similarly strong $d_{x^2-y^2}(\sigma)-p(\text{O})-d_{x^2-y^2}(\sigma)$ pathway as in Fe^{3+} , would make the best candidate metal for an $S = \frac{1}{2}$ kagomé antiferromagnet in a μ -hydroxy framework.

1.6.2.2 $S = \frac{1}{2}$ Kagomé Antiferromagnets

No stoichiometrically pure structurally perfect $S = \frac{1}{2}$ kagomé system containing Cu(II) (or any other metal) had been synthesized prior to the inception of this Thesis work.¹ The most extensively studied materials, $[\text{Cu}_3(\text{titmb})_2(\text{OCOCH}_3)_6] \cdot \text{H}_2\text{O}$ ¹⁰⁸⁻¹¹² and the mineral volborthite,^{47,104} suffered from weak superexchange and imperfect geometry, respectively. Additionally, several $S = \frac{1}{2}$ materials synthesized by other groups after the inception of this Thesis work suffer from additional problems: $\text{CsCu}_3\text{MF}_{12}$ species (with $\text{M} = \text{Zr}$ and Hf) undergo a structural phase transition;^{113,114} $\text{Rb}_2\text{Cu}_3\text{SnF}_{12}$ bears a pseudo-kagomé lattice with distorted triangles and exhibits a rounded maximum in susceptibility at 70 K,¹¹⁵ which may be indicative of spin glassing; the doped lattice, $\text{La}_4\text{Cu}_{3-x}\text{Zn}_x\text{MoO}_{12}$ ($0.30 \leq x \leq 2.40$), has a triclinic structure with substitution of Zn onto the kagomé plane, resulting in one unpaired electron per three Cu atoms, and can be well described by independent Cu^{II}_3 clusters. The system shows weak bulk ferromagnetic interactions, and chemical disorder inhibits its use for studying frustration.¹¹⁶ (Another kagomé system in the literature, $\text{LiZn}_2\text{Mo}_3\text{O}_8$, can be described having $[\text{Mo}^{\text{IV}}_2\text{Mo}^{\text{III}}]$ clusters, with one unpaired electron per cluster.¹¹⁷) We will discuss many of these materials at greater length in this Section. Herbertsmithite, which is presented in Chapter 4, is the best realization of an $S = \frac{1}{2}$ kagomé system to date. Finally, this Thesis research has revealed other potential target $S = \frac{1}{2}$ systems, which bear mentioning here: kapellasite¹¹⁸ and haydeeite.^{119,120} The structures of Cu(II) containing candidate $S = \frac{1}{2}$ systems are summarized in Table 1.1.

The compound $[\text{Cu}_3(\text{titmb})_2(\text{OCOCH}_3)_6]\cdot\text{H}_2\text{O}$ (where $\text{titmb} = 1,3,5\text{-tris(imidazol-1-ylmethyl)-2,4,6-trimethylbenzene}$), crystallizing in space group $R\bar{3}$ and shown in Figure 1.15,¹⁰⁸ initially generated much interest as a frustrated $S = \frac{1}{2}$ kagomé system.^{109-112,121} Upon close examination, however, we see that this system has several structural shortcomings for studying geometric frustration. The $\text{Cu}\cdots\text{Cu}$ centers are separated within the kagomé plane by a distance of 7.769 Å. Superexchange interactions decay rapidly with distance, and at this distance superexchange, were it antiferromagnetic, would not be expected to be much greater than 10 cm^{-1} .¹²² Furthermore, the kagomé planes lie a shorter distance of 7.050 Å from one another, so out-of-plane interactions are potentially more significant than in-plane ones. Finally, rather than a structure in which it is coplanar with copper centers, the titmb ligand adopts a “bucket” configuration in the solid-state structure because the ligand is not completely conjugated. This lack of conjugation is unlikely to make for an efficient superexchange pathway. Initial magnetic study of the material gave $\Theta = -1.21\text{ K}$, indicating a weak mean nearest-neighbor

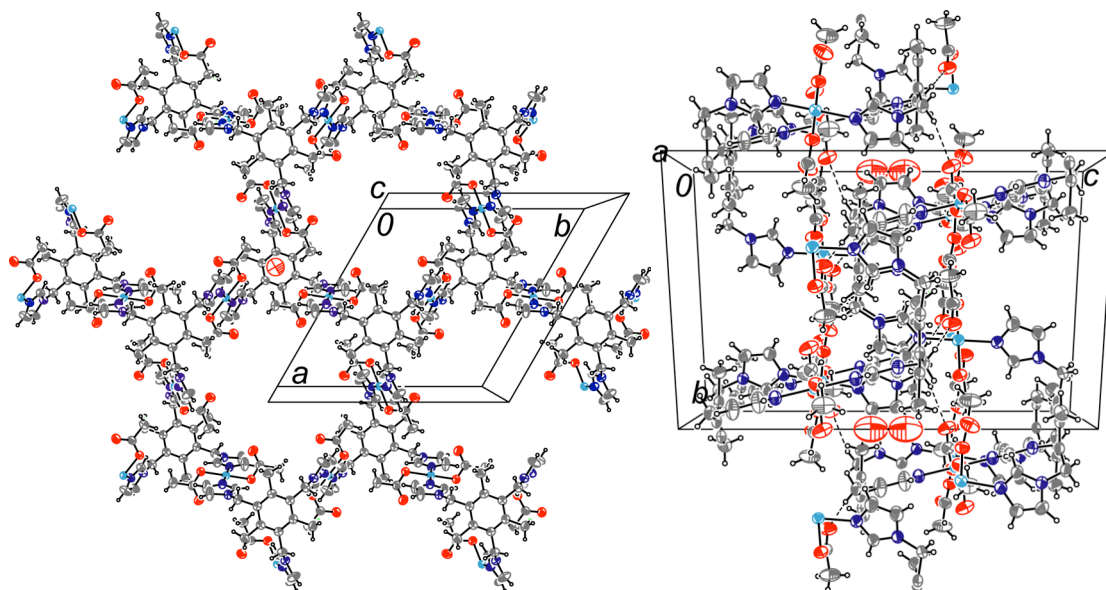


Figure 1.15. Kagomé structure in $\text{Cu}_3(\text{titmb})_2(\text{OCOCH}_3)_6\cdot\text{H}_2\text{O}$ in $R\bar{3}$ (left). Cu centers are far apart within the plane (7.769 Å), and any superexchange occurs through the unconjugated “bucket” structure provided by titmb , which is shown in the packing diagram (right). $d_{\text{kagomé}} = 7.050\text{ Å}$. Structure from Ref. [108].

antiferromagnetic exchange, and no LRO to 1.8 K, the limits of the SQUID instrument.¹²¹ Recently, ultra-low temperature magnetization and specific heat studies have shown a ferromagnetic ordering transition at 56 mK.¹¹² Because of the weak exchange and geometrical shortcomings of this system, better systems for studying frustration on the $S = \frac{1}{2}$ kagomé were needed.

The copper mineral volborthite, $\text{Cu}_3\text{V}_2\text{O}_7(\text{OH})_2 \cdot 2\text{H}_2\text{O}$, which bears a 2D pseudo-kagomé network, with isosceles triangles of Cu^{2+} centers,^{47,104} was the closest realization of a suitable $S = \frac{1}{2}$ system before this Thesis work was undertaken. The compound crystallizes in the monoclinic space group $C2/m$. In this compound, the superexchange pathway comprising the edge of each triangle is the pyrovanadate oxygen atom that bridges two Cu atoms. The center of each triangle contains a hydroxide ion that is shared between three Cu atoms. One of the

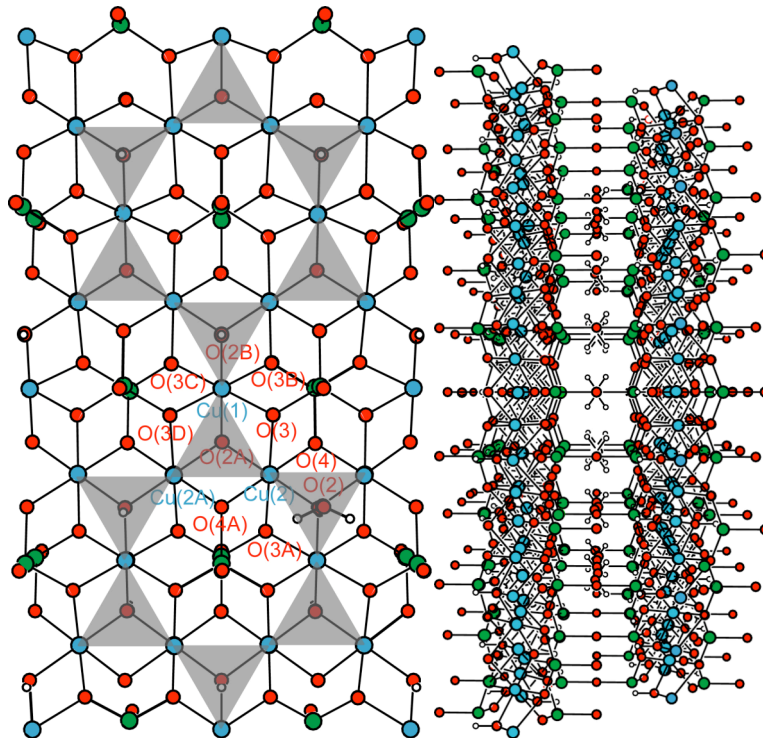


Figure 1.16. Structure of pseudo-kagomé layer in volborthite, $\text{Cu}_3\text{V}_2\text{O}_7(\text{OH})_2 \cdot 2\text{H}_2\text{O}$ (left). Packing of the pyrovanadate decorated sheets (right). Pyrovanadate groups ($\text{O}_3\text{V}-\text{O}-\text{VO}_3$) link the layers, and two crystallographically located water molecules reside in the space between the layers. The kagomé layers stack AA. Structure from Ref. [47].

crystallographically independent Cu(II) atoms shows (4+2)-coordination with four short equatorial bonds to pyrovanadate oxygens and two long axial bonds to hydroxide oxygens. ((4+2)-coordination, (2+4)-coordination, and other coordination modes resulting from the Jahn-Teller effect are discussed at length in Section 1.7.) The other Cu(II) ion displays approximately (2+4)-coordination with four long equatorial bonds to pyrovanadate and hydroxide oxygen atoms and two short axial bonds to pyrovanadate oxygens. Pyrovanadate ($\text{O}_3\text{V}-\text{O}-\text{VO}_3$) groups pillar the structure so the layers are separated by 7.214 Å, and water molecules are located between the layers. Despite showing evidence for strong average nearest-neighbor antiferromagnetism, with $\Theta = -115$ K, volborthite shows no evidence for LRO down to 1.8 K. (There is, however, a rounded maximum in its susceptibility at 20 K that may indicate short-range antiferromagnetic correlations.) The structure of volborthite is shown in Figure 1.16. The irregular geometry of isosceles triangles opposes geometrical frustration, thus limiting the utility of this compound for its study.

Recently, the magnetic properties of $\text{Cs}_2\text{Cu}_3\text{MF}_{12}$ (where $\text{M} = \text{Zr}, \text{Hf}$) have been studied.¹¹⁴ The room temperature structure of the Zr analog of this compound is shown in Figure 1.17.¹¹³ At room temperature, these compounds crystallize in the space group $R\bar{3}m$ with perfect kagomé symmetry. The structure comprises Cu (4+2)-coordinated to F^- anions in corner-sharing octahedrons that form perfect equilateral triangles. Cs^+ and Zr^{4+} reside above and below the kagomé layers to complete the structure. Large single crystals of these materials have been grown, but unfortunately both materials undergo a structural phase transition at 210 K and 175 K for $\text{M} = \text{Zr}, \text{Hf}$, respectively. Both materials show strong antiferromagnetic coupling above the transition temperature ($\Theta = -360$ and -540 K, respectively) and attenuated antiferromagnetic coupling below the transition temperature ($\Theta = -300$ and -450 K, respectively). Unfortunately

the structural phase transition at high temperature limits the compounds' utility for studying geometric frustration and novel spin physics at low temperatures.

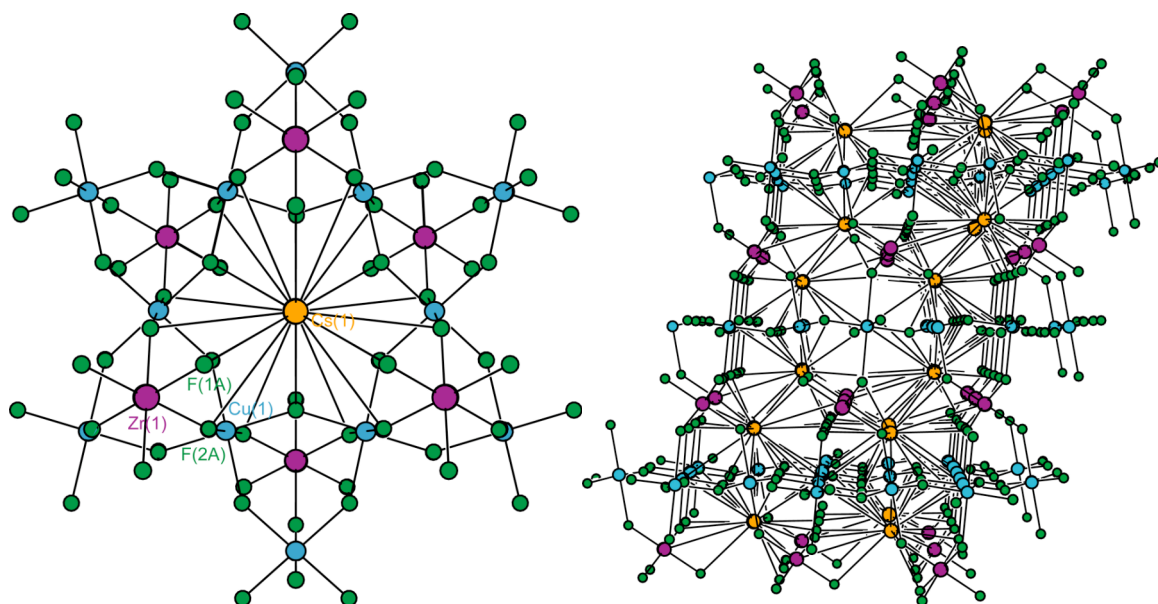


Figure 1.17. Structure of kagomé layer in $\text{Cs}_2\text{Cu}_3\text{ZrF}_{12}$ above 210 K (left). Packing of kagomé layers as viewed along the crystallographic b axis (right). Magnetic data show a singularity at 210 K due to a structural phase transition. Structure from Ref. [113].

This Thesis discusses the synthetic development and magnetic study of structurally perfect $S = \frac{1}{2}$ systems, culminating with a structurally perfect system known as herbertsmithite, $\text{ZnCu}_3(\text{OH})_6\text{Cl}_2$.¹²³ Herbertsmithite crystallizes in the $R\bar{3}m$ space group, and its structure is discussed at length in Section 4.3.2.3. A polymorph of herbertsmithite known as kapellasite, $\text{Cu}_3\text{Zn}(\text{OH})_6\text{Cl}_2$, has recently been discovered in nature, although it has not yet been realized synthetically (and may be metastable with respect to herbertsmithite).¹¹⁸ Shown in Figure 1.18, kapellasite may be a suitable synthetic target for future studies. The major structural differences between herbertsmithite and kapellasite lie in the location of the Zn^{2+} ions and the packing of kagomé layers. In the herbertsmithite structure, Zn^{2+} ions lie above and below the triangles in the kagomé plane, while in kapellasite, Zn^{2+} ions sit in the center of the hexagonal channels. Additionally, the herbertsmithite structure packs ABC, while the kapellasite structure packs AA.

Hydrogen bonding between chloride ions decorating the sheets and hydroxide ions on adjacent sheets is important in holding the kapellasite layers together. Naturally occurring samples of a magnesium analog of kapellasite named haydeeite, $\text{Cu}_3\text{Mg}(\text{OH})_6\text{Cl}_2$, have recently been mined.^{119,120}

In Table 1.1, we note that possible space groups for supporting structurally perfect kagomé geometry include the rhombohedral space group $R\bar{3}m$, the trigonal space group $P\bar{3}m1$, and hexagonal space groups with symmetry $P6_3/m$ or $P6_3/mmc$. (Several kagomé compounds presented in the discussion above have slightly distorted geometries and therefore crystallize in other space groups.) Rhombohedral (ABCABC) packing of kagomé layers is observed in compounds presented here crystallizing in the $R\bar{3}m$ space group. ABC packing is depicted in Figure 1.19. Compounds presented here crystallizing in $P\bar{3}m1$ and $P6_3/m$ or $P6_3/mmc$ space

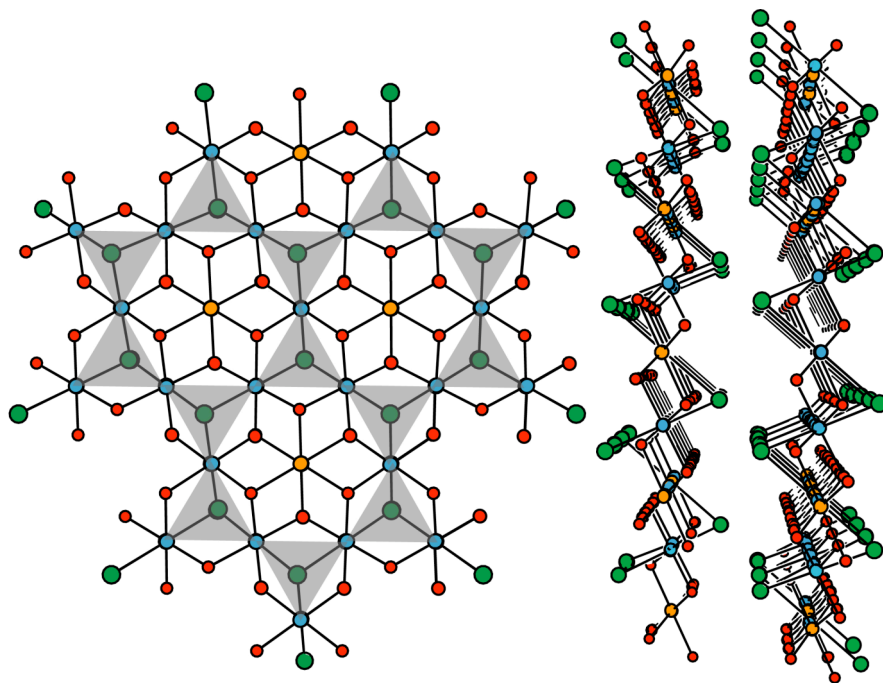


Figure 1.18. Kagomé layer in kapellasite (left). Packing of kapellasite layers (right). Kapellasite layers are held together by hydrogen bonding between the Cl^- and OH^- of adjacent layers. Kapellasite is a polymorph of herbertsmithite and likely to be metastable. Structure from Ref. [118].

Chapter 1

groups exhibit instead AA packing of kagomé layers. Additionally, the stacking of corrugated layers differs between the space groups presented here: it can be either alternating or the same from one layer to the next. Figure 1.20 demonstrates the stacking of corrugated layers: we represent the equatorial ligands around each metal as the vertices of a square (at the center of each square is the metal). Packing and stacking of layers might be of consequence to the magnitude of frustration in a system.⁵

Table 1.1. A structural comparison of Cu²⁺ kagomé and pseudo-kagomé compounds. Potassium jarosite is also listed for comparison.

Compound	Space group	M—M distance (Å)	M—L—M angles in plane (°)	M—L—M2 out-of-plane angle (°)	$d_{\text{kagomé}}$ (Å)	Packing	Stacking of corrugated layers	Tilt angle(°)	Ref
<i>potassium jarosite</i> KFe ₃ (OH) ₆ (SO ₄) ₂	$R\bar{3}m$	3.652	Fe—O—Fe 134.12	Fe—O _H —K 93.70 Fe—O _{SO3} —K 87.87	5.728	ABC	alternating	17.47	[87]
<i>volborthite</i> Cu ₃ V ₂ O ₇ (OH) ₂ ·2H ₂ O	$C2/m$	3.030 3.030 2.932 (Cu2—Cu2)	Cu1—O3 _{V2O4} —Cu2 83.66 Cu1—O2 _H —Cu2 105.57 Cu2—O4 _{V2O4} —Cu2 91.40 Cu2—O2 _H —Cu2 101.00	N/A	7.214	AA	same	50.5, 52.78 (Cu2—O2) 52.84(Cu1—O2)	[47]
Cs ₂ Cu ₃ ZrF ₁₂ (above 210 K)	$R\bar{3}m$	3.583	141.64	Cu—F2—Zr 133.78 Cu—F2—Cs 123.85 Cu—F1—Cs 108.81	6.821	ABC	alternating	8.71	[113]
Cu(1,3-bdc)	$P6_3/m$	4.554	N/A	N/A	7.978	AA	alternating	63.4	[124]
CdCu ₃ (OH) ₆ (NO ₃) ₂ ·xH ₂ O	$P\bar{3}m1$	3.261	Cu—O _H —Cu 106.4 Cu—O _{NO2} —Cu 84.5	N/A	7.012	AA	same	42.28	[125]
<i>claringbullite</i> Cu ₄ (OH) ₆ ClF	$P6_3/mmc$	3.335	Cu—O—Cu 117.77 Cu—Cl—Cu 67.70 (Cu—Cl 2.994)	87.63, 107.49	4.585	AA	alternating	33.85	This work
<i>Clinoatacamite</i> Cu ₂ (OH) ₃ Cl	$P2_1/n$	3.409 (1-1) 3.411 (1-O2-2) 3.423 (1-O1-2)	Cu—O—Cu 116.96 (1-1), 117.14 (1-O2-2), 124.15 (1-O1-2) Cu—Cl—Cu 75.51 (near O1) 75.40 (near O2) 76.32 (1-2)	Cu—O—Cu3 Cu1—O3 101.48 Cu1—O1 92.65 Cu1—O2 97.19 Cu1—O3 95.62 Cu2—O1 90.94 Cu2—O2 101.10	4.673	ABC	alternating	38.47/38.65 (Cu1) 37.04/38.39 (Cu2) 36.76/37.94 (Cu1)	[103]
<i>kapellasite</i> [‡] Cu ₃ Zn(OH) ₆ Cl ₂	$P\bar{3}m1$	3.150	Cu—O—Cu 105.87 Cu—Cl—Cu 69.53	N/A	5.7336	AA	same	34.76	[118]
<i>herbertsmithite</i> ZnCu ₃ (OH) ₆ Cl ₂	$R\bar{3}m$	3.417	Cu—O—Cu 119.06 Cu—Cl—Cu 76.17	97.05	4.678	ABC	alternating	38.08	[126]

Jarosite tilt angle defined as 90–(Fe...Fe–O2)^o, where O2 is the SO₄²⁻ base oxygen. Tilt angle in the Cu(II) systems is defined as 90–(Cu...Cu–L_{axial})^o. We note that the base of the SO₄²⁻ cap is a 3-atom bridge (O–S–O) between Fe centers in jarosite, while the axial ligands are 1-atom bridges in Cu(II) systems. Cu(1,3-bdc) has no axial ligands, and so the tilt angle is defined as the angle between the Cu...C...Cu plane (where C is from the bridging carboxylate) and the kagomé plane. [‡]Recently discovered haydeelite, Cu₃Mg(OH)₆Cl₂, bears a similar structure.^{119,120}

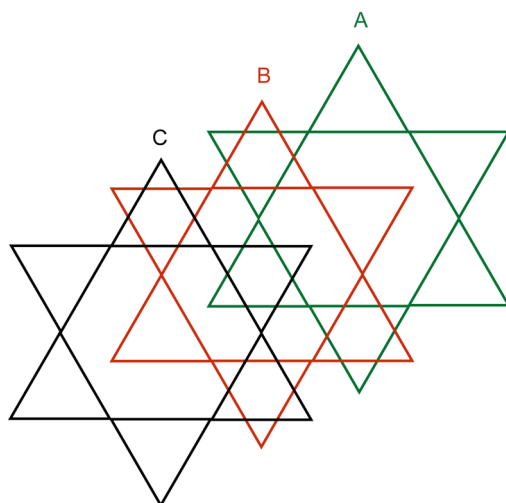


Figure 1.19. Schematic showing ABC packing of kagomé layers. Such packing is common to kagomé structures crystallizing in the space group $R\bar{3}m$. It occurs in jarosite and herbertsmithite structures. It also occurs in clinoatacamite, which crystallizes in $P2_1/n$.

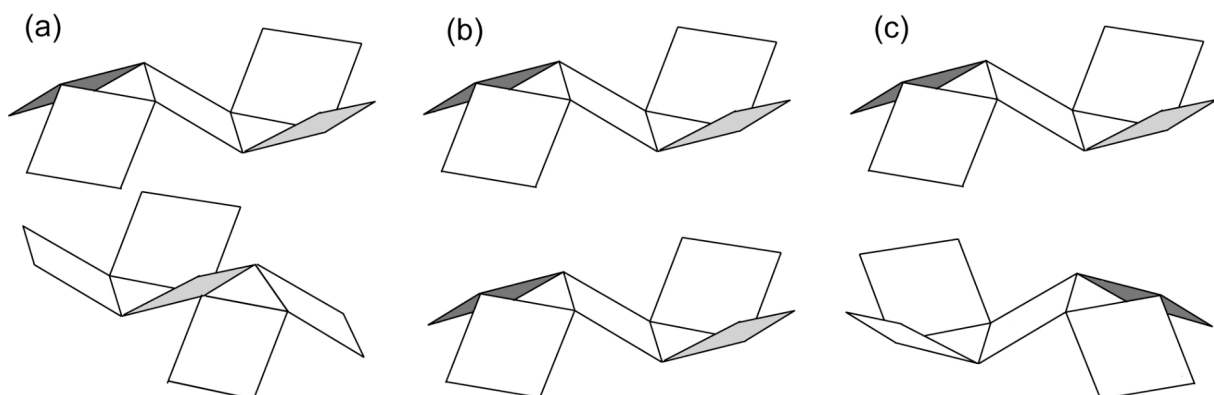


Figure 1.20. Stacking of adjacent layers in kagomé compounds. Squares represent the equatorial metal-ligand planes: the metal ion resides in the center of each square, with ligand atoms at the corners. (a) Layers alternate up and down, packing is AB(C). Examples of this packing structure discussed in this Thesis include the $R\bar{3}m$ structures jarosite and herbertsmithite, and also clinoatacamite in $P2_1/n$. (b) Layers are both up, packing is AA. $P\bar{3}m1$. An example of this packing structure discussed in this Thesis is $\text{CdCu}_3(\text{OH})_6(\text{NO}_3)_2 \cdot x\text{H}_2\text{O}$. The minerals kapellasite and haydeelite also bear this packing structure. (c) Layers alternate up and down, packing is AA. $P6_3/m$, $P6_3/mmc$. Examples of this packing structure discussed in this Thesis are $\text{Cu}(1,3\text{-bdc})$ and claringbullite.

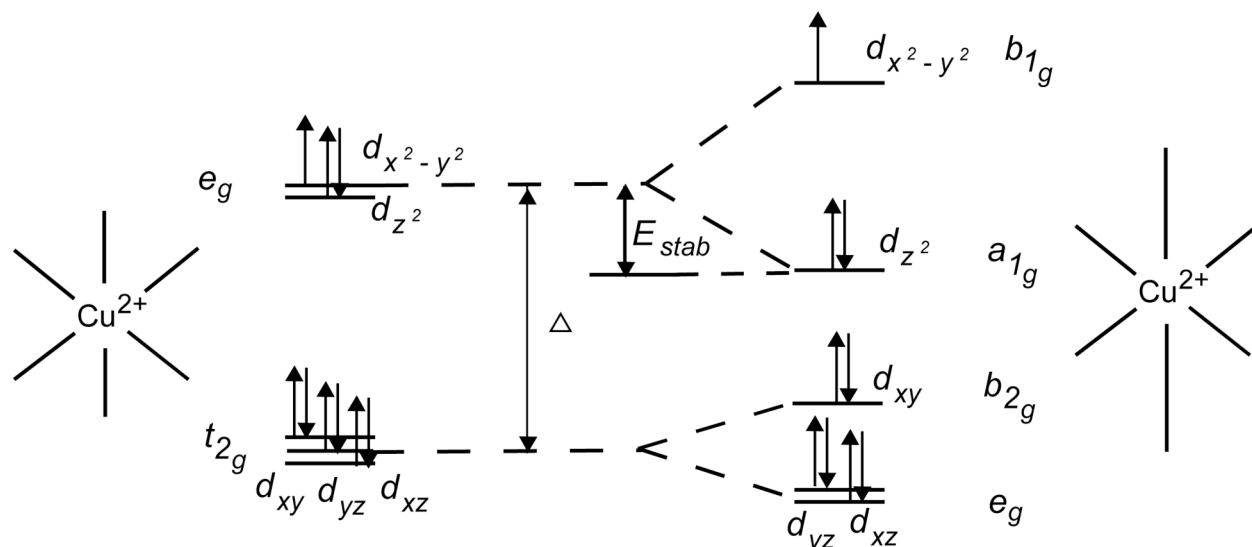


Figure 1.21. Structural distortion to remove orbital electronic degeneracy is typical of the Jahn-Teller effect, which dominates the structural chemistry of cupric compounds. At left is an octahedrally coordinated Cu^{2+} ion, at right an ion with tetragonally elongated (4+2)-coordination. In extended solid-state structures, the effect is known as a Peierls distortion.

1.7 The Jahn-Teller Effect / Peierls Distortion in the Structural Chemistry of Copper(II)

No discussion of the structural chemistry of cupric compounds would be complete without an initial mention of the Jahn-Teller effect⁴⁵ (discussed previously in Section 1.3) and the analogous effect for extended solid-state structures in band theory, known as a Peierls distortion.¹²⁷ Indeed, in his writings on the structural chemistry of cupric compounds, A. F. Wells writes, “This subject is of quite outstanding interest, for in one oxidation state this element shows a greater diversity in its stereochemical behaviour than any other element.”¹²⁸ In Cu^{2+} containing molecules, a d^9 electronic configuration in an octahedral ligand field results in an unequal occupancy of the e_g orbitals ($d_{x^2-y^2}$ and d_{z^2}), which leads, in turn, to a structural distortion to remove the degeneracy of these orbitals. The most prevalent Jahn-Teller distortion is the (4 + 2)-coordination, with four short equatorial metal-ligand bonds and two long axial ones. The ligand field of a tetragonally elongated (4 + 2)-coordination is shown in Figure 1.21. The effect of distortion on structure is readily apparent in the mineralogical literature; in a review

of the structures of Cu^{2+} -oxysalt minerals, for example, Eby and Hawthorne note that the Cu–O bond distances show a bimodal distribution, with an equatorial average of about 1.97 Å and axial distances ranging from 2.3 to 3.0 Å.^{127,129} Other possible but less common geometries for Cu^{2+} resulting from this distortion include (2+4)-octahedral, with two short axial bonds and 4 long equatorial bonds; and (4+1)-square pyramidal and square planar, both perturbations to the ligand field that result from pulling one or more ligands on the z axis to infinite distances.¹²⁸ Most of these structural variations are presented in this Thesis.

1.8 Outline and Scope of this Thesis

This Thesis examines the synthesis, structure, and magnetism of $S = \frac{1}{2}$ kagomé materials: a metal-organic framework compound known as Cu(1,3-bdc), a hydrogen-bonded layered kagomé, $\text{CdCu}_3(\text{OH})_6(\text{NO}_3)_2 \cdot x\text{H}_2\text{O}$, and a series of copper(II) hydroxychloride minerals. As the Chapters progress, we further optimize the geometry of the systems in our study of geometric spin frustration and our attempts to observe unusual spin physics. We sought in our synthetic systems simultaneously to maximize the strength of nearest-neighbor exchange and minimize the strength of interactions between neighboring planes for two reasons: first, because the magnitude of frustration is linked to the strength of nearest-neighbor exchange through mean-field theory (Equations 1.3 and 1.4); and second, because 3-D LRO (occurring at T_c in Equation 1.4) may inhibit frustration and the observation of unusual spin physics, and can arise from interactions between neighboring kagomé planes. This Thesis starts with a system of Cu^{2+} ions bridged by three-atom superexchange pathways with covalently linked layers, it then moves to systems with Cu^{2+} ions bridged by stronger one-atom superexchange pathways but with layers that are still not magnetically isolated, and it culminates in the synthesis and study of a compound with one-atom superexchange pathways and magnetically isolated layers (Figure 1.22). After we characterize

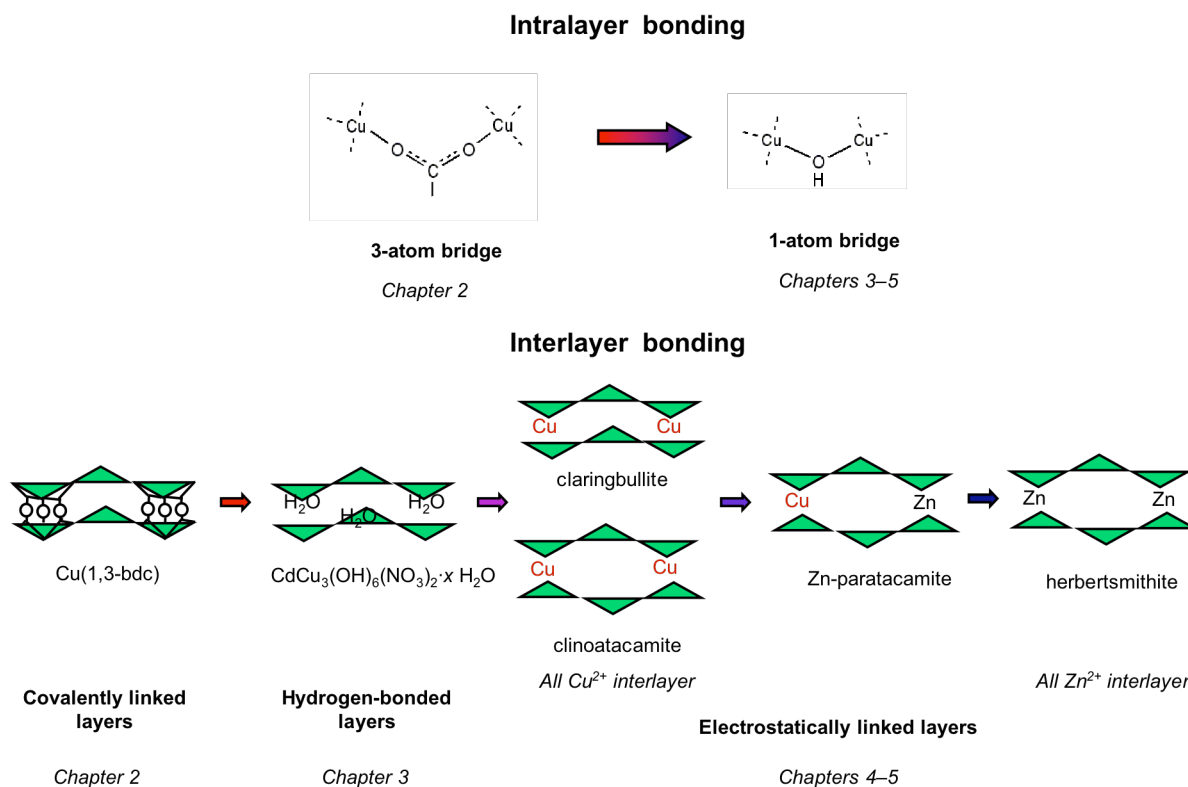


Figure 1.22. A pictorial representation of the structure of this Thesis. We move from covalently linked layers with three-atom bridges in the kagomé plane (Chapter 2), to hydrogen-bonded layers (Chapter 3) and electrostatically linked layers (Chapters 4 and 5) with one-atom bridges in the kagomé plane.

the ground states of pure frustrated systems, we turn to our attempts to dope electrons or holes into these kagomé systems in order to examine transport properties with the objective of experimentally probing the connection between RVB theory and spin frustration.

Chapter 2 discusses the synthesis, structure, and magnetic properties of Cu(1,3-bdc) (1,3-bdc = 1,3-benzenedicarboxylate), a novel structurally perfect $S = \frac{1}{2}$ metal-organic framework kagomé antiferromagnet exhibiting properties consonant with spin frustration. In the structure, each monodentate carboxylate ligand bridges two copper ions in the kagomé plane, and the three-atom bridge allows for the shortest known metal-metal distance in any metal-organic framework kagomé reported to date. The compound shows antiferromagnetic mean nearest-neighbor superexchange, as evidenced by $\Theta = -33$ K. The compound orders

Chapter 1

ferromagnetically at 2 K and has a frustration parameter, $f = 16.5$, indicative of a spin-frustrated compound.

Chapter 3 focuses on the synthesis and magnetic characterization of $\text{CdCu}_3(\text{OH})_6(\text{NO}_3)_2 \cdot 0.5\text{H}_2\text{O}$. The cadmium copper hydroxide nitrate, the synthesis and structure of which were first reported by Oswald,¹²⁵ bears the kagomé structural motif and shows no evidence of LRO to 5K, despite having $\Theta = -114 \pm 27$ K. A comparison of the structure and magnetic properties of the $\text{CdCu}_3(\text{OH})_6(\text{NO}_3)_2 \cdot 0.5\text{H}_2\text{O}$ is made with rouaite, a related monoclinic phase of $\text{Cu}_2(\text{OH})_3\text{NO}_3$. Possible explanations for the magnetic ordering behavior of $\text{CdCu}_3(\text{OH})_6(\text{NO}_3)_2 \cdot 0.5\text{H}_2\text{O}$ are discussed.

Chapter 4 discusses the synthesis, structure, and chemical characterization of the copper(II) hydroxychloride minerals: claringbullite, clinoatacamite, Zn-paratacamite, and herbertsmithite. Experimental difficulties encountered in the synthesis of large single crystals of monophasic $\text{ZnCu}_3(\text{OH})_6\text{Cl}_2$ are discussed, as are future directions for the growth of these crystals and other synthetic targets.

Chapter 5 focuses on the magnetism of the copper(II) hydroxychloride minerals. We find that for $\text{ZnCu}_3(\text{OH})_6\text{Cl}_2$, herbertsmithite, a structurally perfect stoichiometrically pure $S = \frac{1}{2}$ kagomé lattice, no magnetic ordering is observed to 50 mK although the superexchange is strongly antiferromagnetic ($\Theta = -314$ K). We discuss the implications of recent physical measurements on this material with respect to resonating valence bond theory. We also present attempts to dope electrons or holes into the herbertsmithite lattice, both chemically and electrochemically, in attempts to observe superconductivity.

Following the chapters are appendices of data that, while potentially useful for future researchers, would detract from the readability of this Thesis. Appendix A contains structural

Chapter 1

data for all of the compounds presented herein. Appendix B reports their thermal and spectroscopic characterization.

1.9 References

1. Lhuillier, C.; Misguich, G. *Lect. Notes Phys.* **2002**, *595*, 161-190.
2. Ramirez, A. P. *Annu. Rev. Mater. Sci.* **1994**, *24*, 453-480.
3. Schiffer, P.; Ramirez, A. P. *Comment. Cond. Mat. Phys.* **1996**, *18*, 21-50.
4. Collins, M. F.; Petrenko, O. A. *Can. J. Phys.* **1997**, *75*, 605-655.
5. Greedan, J. E. *J. Mater. Chem.* **2001**, *11*, 37-53.
6. Moessner, R. *Can. J. Phys.* **2001**, *79*, 1283-1294.
7. Dai, D.; Whangbo, M.-H. *J. Chem. Phys.* **2004**, *121*, 672-680.
8. Harrison, A. *J. Phys.: Condens. Matter* **2004**, *16*, S553-S572.
9. Moessner, R.; Ramirez, A. P. *Phys. Today* **2006**, *59*, 24-29.
10. Aharony, A.; Birgeneau, R. J.; Coniglio, A.; Kastner, M. A.; Stanley, H. E. *Phys. Rev. Lett.* **1988**, *60*, 1330-1333.
11. Bednorz, J. G.; Mueller, K. A. *Z. Phys. B: Condens. Matter* **1986**, *64*, 189-193.
12. Birgeneau, R. J.; Aharony, A.; Belk, N. R.; Chou, F. C.; Endoh, Y.; Greven, M.; Hosoya, S.; Kastner, M. A.; Lee, C. H.; et al. *J. Phys. Chem. Solids* **1995**, *56*, 1913-1919.
13. Lee, P. A.; Nagaosa, N.; Wen, X.-G. *Rev. Mod. Phys.* **2006**, *78*, 17-85.
14. Mott, N. F. *Proc. Phys. Soc., London* **1949**, *62A*, 416-422.
15. Anderson, P. W. *Physics Reviews* **1950**, *79*, 350-356.
16. Anderson, P. W. *Science* **1987**, *235*, 1196-1198.
17. Tranquada, J. M.; Heald, S. M.; Moodenbaugh, A. R. *Phys. Rev. B* **1987**, *36*, 5263-5274.
18. Toulouse, G. *Commun. Phys.* **1977**, *2*, 115-119.
19. Heisenberg, W. *Z. Phys.* **1928**, *49*, 619-636.
20. Kahn, O. *Molecular Magnetism*; VCH: New York, 1993, p. 10.
21. Misguich, G.; Lhuillier, C. In *Frustrated Spin Systems*; Diep, H. T., Ed.; World Scientific Publishing Co. Pte. Ltd.: Singapore, 2004, pp. 229-306.
22. Zeng, C.; Elser, V. *Phys. Rev. B* **1990**, *42*, 8436-8444.

Chapter 1

23. Singh, R. R. P.; Huse, D. A. *Phys. Rev. Lett.* **1992**, *68*, 1766-1769.
24. Anderson, P. W. *Mater. Res. Bull.* **1973**, *8*, 153-160.
25. Fazekas, P.; Anderson, P. W. *Philos. Mag.* **1974**, *30*, 423-440.
26. Yang, K.; Warman, L. K.; Girvin, S. M. *Phys. Rev. Lett.* **1993**, *70*, 2641.
27. Moessner, R.; Sondhi, S. L. *Phys. Rev. Lett.* **2001**, *86*, 1881-1884.
28. Beckett, R.; Colton, R.; Hoskins, B. F.; Martin, R. L.; Vince, D. G. *Aust. J. Chem.* **1969**, *22*, 2527-2533.
29. Butcher, R. J.; O'Connor, C. J.; Sinn, E. *Inorg. Chem.* **1981**, *20*, 537-545.
30. Kwiatkowski, M.; Kwiatkowski, E.; Olechnowicz, A.; Ho, D. M.; Deutsch, E. *Inorg. Chim. Acta* **1988**, *150*, 65-73.
31. Chaudhuri, P.; Karpenstein, I.; Winter, M.; Butzlaff, C.; Bill, E.; Trautwein, A. X.; Floerke, U.; Haupt, H. *J. Chem. Soc., Chem. Commun.* **1992**, 321-322.
32. Colacio, E.; Dominguez-Vera, J. M.; Escuer, A.; Klinga, M.; Kivekas, R.; Romerosa, A. *J. Chem. Soc., Dalton Trans.* **1995**, 343-348.
33. Padilla, J.; Gatteschi, D.; Chaudhuri, P. *Inorg. Chim. Acta* **1997**, *260*, 217-220.
34. Ferrer, S.; Haasnoot, J. G.; Reedijk, J.; Muller, E.; Cingi, M. B.; Lanfranchi, M.; Lanfredi, A. M.; Ribas, J. *Inorg. Chem.* **2000**, *39*, 1859-1867.
35. Clerac, R.; Cotton, F. A.; Dunbar, K. R.; Hillard, E. A.; Petrukhina, M. A.; Smucker, B. *W. C.R. Acad. Sci., Ser. IIc: Chim.* **2001**, *4*, 315-319.
36. Ferrer, S.; Lloret, F.; Bertomeu, I.; Alzuet, G.; Borrás, J.; Garcia-Granda, S.; Liu-Gonzalez, M.; Haasnoot, J. G. *Inorg. Chem.* **2002**, *41*, 5821-5830.
37. Cage, B.; Cotton, F. A.; Dalal, N. S.; Hillard, E. A.; Rakvin, B.; Ramsey, C. M. *J. Am. Chem. Soc.* **2003**, *125*, 5270-5271.
38. Liu, X.; de Miranda Marcelo, P.; McInnes Eric, J. L.; Kilner Colin, A.; Halcrow Malcolm, A. *Dalton Trans.* **2004**, 59-64.
39. Yoon, J.; Mirica, L. M.; Stack, T. D. P.; Solomon, E. I. *J. Am. Chem. Soc.* **2004**, *126*, 12586-12595.
40. Yoon, J.; Solomon, E. I. *Inorg. Chem.* **2005**, *44*, 8076-8086.
41. Stamatatos, T. C.; Vlahopoulou, J. C.; Sanakis, Y.; Raptopoulou, C. P.; Psycharis, V.; Boudalis, A. K.; Perlepes, S. P. *Inorg. Chem. Commun.* **2006**, *9*, 814-818.

Chapter 1

42. Stone, M. B.; Fernandez-Alonso, F.; Adroja, D. T.; Dalal, N. S.; Villagrán, D.; Cotton, F. A.; Nagler, S. E. *Phys. Rev. B* **2007**, *75*, 214427/214421-214427/214428.
43. Belinsky, M. I. *Inorg. Chem.* **2008**, *47*, 3521-3531.
44. Belinsky, M. I. *Inorg. Chem.* **2008**, *47*, 3532-3539.
45. Jahn, H. A.; Teller, E. *Proc. Roy. Soc. London, Ser. A* **1937**, *161*, 220-235.
46. Rusanov, E. B.; Ponomarova, V. V.; Komarchuk, V. V.; Stoeckli-Evans, H.; Fernandez-Ibanez, E.; Stoeckli, F.; Sieler, J.; Domasevitch, K. V. *Angew. Chem., Int. Ed.* **2003**, *42*, 2499-2501.
47. Lafontaine, M. A.; Le Bail, A.; Ferey, G. *J. Solid State Chem.* **1990**, *85*, 220-227.
48. Wills, A. S. *Phys. Rev. B* **2001**, *63*, 064430/064431-064430/064413.
49. Gaulin, B. D. *Nat. Mater.* **2005**, *4*, 269-270.
50. Wannier, G. H. *Phys. Rev.* **1950**, *79*, 357-364.
51. Huse, D. A.; Elser, V. *Phys. Rev. Lett.* **1988**, *60*, 2531-2534.
52. Bernu, B.; Lhuillier, C.; Pierre, L. *Phys. Rev. Lett.* **1992**, *69*, 2590-2593.
53. Capriotti, L.; Trumper, A. E.; Sorella, S. *Phys. Rev. Lett.* **1999**, *82*, 3899-3902.
54. Lecheminant, P.; Bernu, B.; Lhuillier, C.; Pierre, L.; Sindzingre, P. *Phys. Rev. B: Condens. Matter* **1997**, *56*, 2521-2529.
55. Wills, A. S.; Harrison, A.; Ritter, C.; Smith, R. I. *Phys. Rev. B* **2000**, *61*, 6156-6169.
56. Grohol, D.; Matan, K.; Cho, J.-H.; Lee, S.-H.; Lynn, J. W.; Nocera, D. G.; Lee, Y. S. *Nat. Mater.* **2005**, *4*, 323-328.
57. Matan, K.; Grohol, D.; Nocera, D. G.; Yildirim, T.; Harris, A. B.; Lee, S. H.; Nagler, S. E.; Lee, Y. S. *Phys. Rev. Lett.* **2006**, *96*, 247201/247201-247201/247204.
58. Harris, A. B.; Kallin, C.; Berlinsky, A. J. *Phys. Rev. B* **1992**, *45*, 2899-2919.
59. Chalker, J. T.; Eastmond, J. F. G. *Phys. Rev. B* **1992**, *46*, 14201-14204.
60. Sindzingre, P.; Misguich, G.; Lhuillier, C.; Bernu, B.; Pierre, L.; Waldtmann, C.; Everts, H. U. *Phys. Rev. Lett.* **2000**, *84*, 2953-2956.
61. Marston, J. B.; Zeng, C. *J. Appl. Phys.* **1991**, *69*, 5962-5964.
62. Sachdev, S. *Phys. Rev. B* **1992**, *45*, 12377-12396.

Chapter 1

63. Wang, F.; Vishwanath, A. *Phys. Rev. B* **2006**, *74*, 174423/174421-174423/174420.
64. Waldtmann, C.; Everts, H. U.; Bernu, B.; Lhuillier, C.; Sindzingre, P.; Lecheminant, P.; Pierre, L. *Eur. Phys. J. B* **1998**, *2*, 501-507.
65. Hastings, M. B. *Phys. Rev. B* **2001**, *63*, 014413/014411-014413/014416.
66. Mambrini, M.; Mila, F. *Eur. Phys. J. B* **2000**, *17*, 651-659.
67. Lhuillier, C. *LANL, Preprint Archive, Condens. Matt.* **2005**, 1-101, arXiv:cond-mat/0502464.
68. Anderson, P. W.; Lee, P. A.; Randeria, M.; Rice, T. M.; Trivedi, N.; Zhang, F. C. *J. Phys.: Condens. Matter* **2004**, *16*, R755-R769.
69. Baskaran, G.; Zou, Z.; Anderson, P. W. *Solid State Commun.* **1987**, *63*, 973-976.
70. Lutz, H. D.; Buchmeier, W.; Siwert, H. *Z. Anorg. Allg. Chem.* **1986**, *533*, 118-124.
71. Nakatsuji, S.; Nambu, Y.; Tonomura, H.; Sakai, O.; Jonas, S.; Broholm, C.; Tsunetsugu, H.; Qiu, Y.; Maeno, Y. *Science* **2005**, *309*, 1697-1700.
72. Hirakawa, K.; Kadowaki, H.; Ubukoshi, K. *J. Phys. Soc. Jpn.* **1985**, *54*, 3526-3536.
73. Clarke, S. J.; Fowkes, A. J.; Harrison, A.; Ibberson, R. M.; Rosseinsky, M. J. *Chem. Mater.* **1998**, *10*, 372-384.
74. Shender, E. F.; Holdsworth, P. C. W. In *Fluctuations and Order*; Millionas, M., Ed.; Springer-Verlag: Berlin, 1996, p. 259.
75. Lee, S. H.; Broholm, C.; Aeppli, G.; Perring, T. G.; Hessen, B.; Taylor, A. *Phys. Rev. Lett.* **1996**, *76*, 4424-4427.
76. Broholm, C.; Aeppli, G.; Espinosa, G. P.; Cooper, A. S. *Phys. Rev. Lett.* **1990**, *65*, 3173-3176.
77. Ramirez, A. P.; Espinosa, G. P.; Cooper, A. S. *Phys. Rev. Lett.* **1990**, *64*, 2070-2073.
78. Keren, A.; Mendels, P.; Horvatic, M.; Ferrer, F.; Uemura, Y. J.; Mekata, M.; Asano, T. *Phys. Rev. B* **1998**, *57*, 10745-10749.
79. Keren, A.; Uemura, Y. J.; Luke, G.; Mendels, P.; Mekata, M.; Asano, T. *Phys. Rev. Lett.* **2000**, *84*, 3450-3453.
80. Obradors, X.; Labarta, A.; Isalgue, A.; Tejada, J.; Rodriguez, J.; Pernet, M. *Solid State Commun.* **1988**, *65*, 189-192.
81. Van Loon, C. J. J.; Ijdo, D. J. W. *Acta Crystallogr. B* **1975**, *B31*, 770-773.

Chapter 1

82. Hinz, D. J.; Meyer, G.; Dedecke, T.; Umland, W. *Angew. Chem., Int. Ed. Engl.* **1995**, *34*, 71-73.
83. Grohol, D.; Papoutsakis, D.; Nocera, D. G. *Angew. Chem., Int. Ed.* **2001**, *40*, 1519-1521.
84. Grohol, D.; Nocera, D. G. *J. Am. Chem. Soc.* **2002**, *124*, 2640-2646.
85. Papoutsakis, D.; Grohol, D.; Nocera, D. G. *J. Am. Chem. Soc.* **2002**, *124*, 2647-2656.
86. Grohol, D.; Huang, Q.; Toby, B. H.; Lynn, J. W.; Lee, Y. S.; Nocera, D. G. *Phys. Rev. B* **2003**, *68*, 094404/094401-094404/094407.
87. Grohol, D.; Nocera, D. G.; Papoutsakis, D. *Phys. Rev. B* **2003**, *67*, 064401/064401-064401/064413.
88. Nocera, D. G.; Bartlett, B. M.; Grohol, D.; Papoutsakis, D.; Shores, M. P. *Chem. Eur. J.* **2004**, *10*, 3850-3859.
89. Bartlett, B. M.; Nocera, D. G. *J. Am. Chem. Soc.* **2005**, *127*, 8985-8993.
90. Grohol, D.; Nocera, D. G. *Chem. Mater.* **2007**, *19*, 3061-3066.
91. Jambor, J. L. *Can. Mineral.* **1999**, *37*, 1323-1341.
92. Wills, A. S.; Harrison, A. *J. Chem. Soc., Faraday Trans.* **1996**, *92*, 2161-2166.
93. Dutrizac, J. E.; Kaiman, S. *Can. Mineral.* **1976**, *14*, Pt. 2, 151-158.
94. Dutrizac, J. E. *Metall. Trans. B* **1983**, *14B*, 531-539.
95. Kubisz, J. *Mineral. Pol.* **1970**, *1*, 47-59.
96. Kubisz, J. *Mineral. Pol.* **1971**, *2*, 51-60.
97. Jambor, J. L.; Dutrizac, J. E. *Can. Mineral.* **1985**, *23*, 47-51.
98. Inami, T.; Nishiyama, M.; Maegawa, S.; Oka, Y. *Phys. Rev. B* **2000**, *61*, 12181-12186.
99. Dzyaloshinsky, I. E. *Phys. Chem. Sol.* **1958**, *4*, 241-255.
100. Moriya, T. *Phys. Rev.* **1960**, *120*, 91-98.
101. Elhajal, M.; Canals, B.; Lacroix, C. *Phys. Rev. B* **2002**, *66*, 014422/014421-014422/014426.
102. Ballou, R.; Canals, B.; Elhajal, M.; Lacroix, C.; Wills, A. S. *J. Magn. Magn. Mater.* **2003**, *262*, 465-471.
103. Bartlett, B. M. Ph.D. Thesis, Massachusetts Institute of Technology, 2005.

Chapter 1

104. Hiroi, Z.; Hanawa, M.; Kobayashi, N.; Nohara, M.; Takagi, H.; Kato, Y.; Takigawa, M. *J. Phys. Soc. Jpn.* **2001**, *70*, 3377-3384.
105. Goodenough, J. B. *Phys. Chem. Sol.* **1958**, *6*, 287-297.
106. Kanamori, J. *Phys. Chem. Sol.* **1959**, *10*, 87-98.
107. Ginsberg, A. P. *Inorg. Chim. Acta, Rev.* **1971**, *5*, 45-68.
108. Liu, H.-K.; Sun, W.-Y.; Tang, W.-X.; Yamamoto, T.; Ueyama, N. *Inorg. Chem.* **1999**, *38*, 6313-6316.
109. Honda, Z.; Katsumata, K.; Yamada, K. *J. Phys.: Condens. Matter* **2002**, *14*, L625-L629.
110. Honda, Z.; Katsumata, K.; Yamada, K. *Physica B* **2003**, *329-333*, 1032-1033.
111. Narumi, Y.; Honda, Z.; Katsumata, K.; Domenge, J. C.; Sindzingre, P.; Lhuillier, C.; Matsuo, A.; Suga, K.; Kindo, K. *J. Magn. Magn. Mater.* **2004**, *272-276*, 878-879.
112. Maegawa, S.; Kaji, R.; Kanou, S.; Oyamada, A.; Nishiyama, M. *J. Phys.: Condens. Matter* **2007**, *19*, 145250/145251-145250/145259.
113. Mueller, M.; Mueller, B. G. *Z. Anorg. Allg. Chem.* **1995**, *621*, 993-1000.
114. Yamabe, Y.; Ono, T.; Suto, T.; Tanaka, H. *J. Phys.: Condens. Matter* **2007**, *19*, 145253/145251-145253/145256.
115. Morita, K.; Yano, M.; Ono, T.; Tanaka, H.; Fujii, K.; Uekusa, H.; Narumi, Y.; Kindo, K. *arXiv.org, e-Print Archive, Condensed Matter* **2008**, 1-5, arXiv:0803 0205v0801 [cond-mat str-el].
116. Li, G.; You, L.; Wei, W.; Lu, Y.; Jing, J.; Wannberg, A.; Rundloef, H.; Zou, X.; Yang, T.; Tian, S.; Liao, F.; Toyota, N.; Lin, J. *J. Am. Chem. Soc.* **2005**, *127*, 14094-14099.
117. Torardi, C. C.; McCarley, R. E. *Inorg. Chem.* **1985**, *24*, 476-481.
118. Krause, W.; Bernhardt, H. J.; Braithwaite, R. S. W.; Kolitsch, U.; Pritchard, R. *Mineral. Mag.* **2006**, *70*, 329-340.
119. Malcherek, T.; Schlueter, J. *Acta Crystallogr. B.* **2007**, *B63*, 157-160.
120. Schluter, J.; Malcherek, T. *Neues Jahrb. Mineral., Abh.* **2007**, *184*, 39-43.
121. Kawahara, S.; Ueda, M.; Maegawa, S.; Fujita, K.; Yamaguchi, R. *J. Magn. Magn. Mater.* **2004**, *272*, E999-E1000.
122. Coffman, R. E.; Buettner, G. R. *J. Phys. Chem.* **1979**, *83*, 2387-2392.

Chapter 1

123. Braithwaite, R. S. W.; Mereiter, K.; Paar, W. H.; Clark, A. M. *Mineral. Mag.* **2004**, *68*, 527-539.
124. Nytko, E. A.; Helton, J. S.; Mueller, P.; Nocera, D. G. *J. Am. Chem. Soc.* **2008**, *130*, 2922-2923.
125. Oswald, H. R. *Helv. Chim. Acta* **1969**, *52*, 2369-2380.
126. Shores, M. P.; Nytko, E. A.; Bartlett, B. M.; Nocera, D. G. *J. Am. Chem. Soc.* **2005**, *127*, 13462-13463.
127. Eby, R. K.; Hawthorne, F. C. *Acta Crystallogr. B.* **1993**, *B49*, 28-56.
128. Wells, A. F. *Structural Inorganic Chemistry*; 5th ed.; Clarendon: New York, 1984, p. 1119.
129. Hawthorne, F. C.; Schindler, M. *Can. Mineral.* **2000**, *38*, 751-761.

Chapter 2.
Synthesis, Structure, and Magnetism of the First Structurally Perfect $S = \frac{1}{2}$ Metal-Organic Framework Kagomé Antiferromagnet

Portions of this work have been published as Nytko, E. A.; Helton, J. S.; Müller, P.; Nocera, D. *G. J. Am. Chem. Soc.* **2008**, *130*, 2922-2923.

2.1 Introduction

Although there have been recent reports of inorganic kagomé¹⁻³ and pseudo-kagomé structures with layers separated by organic moieties,⁴⁻⁸ such structures are relatively rare in metal-organic frameworks (MOFs), where an organic moiety is a structural constituent of the kagomé triangles.⁹⁻²⁹ Previous studies of spin frustration on MOF kagomé compounds have been complicated by long exchange pathways,¹⁵⁻¹⁹ triangulated or interpenetrating structures,²⁰⁻²³ and spin centers composed of dimers or clusters displaying intramolecular exchange interactions.²⁴⁻²⁸ There are some structurally distorted MOF kagomé with isolated metal ions on the vertices,^{9,29} but only a limited number of structurally perfect systems.^{10-12,15-19} Of relevance to the quest for quantum states on a kagomé, there is no MOF kagomé composed of $S = \frac{1}{2}$ ions with superexchange pathways short enough to be suitable for magnetic studies. We report here the synthesis and magnetic characterization of the first structurally perfect MOF kagomé with $S = \frac{1}{2}$ on lattice vertices. The compound has the shortest known metal-metal distance of any MOF kagomé, which allows for efficient superexchange between metal centers.

2.2 Experimental

2.2.1 General Procedures

Sample Preparation. Water was distilled and deionized with a Milli-Q filtering system. All other reagents were obtained from commercial vendors and used without further purification: Cu(OH)₂ (99.5+%, Noah Technologies); Cu(OH)F (99.999%, Alfa Aesar); imidazole (99+%, Aldrich); isophthalic acid (99%, Aldrich); isophthalic-2,4,5,6-d₄-acid (99%, 99.4 atom % D, C/D/N Isotopes), and deuterium oxide (99.9 atom % D, Cambridge Isotope). Hydrothermal reactions were carried out under autogeneous pressure in 23-mL Teflon-lined pressure vessels purchased from Parr Instruments; large-scale sample preparation was carried out in a custom-

built 1900-mL vessel. Fisher Isotemp programmable ovens with forced-air circulation were used to obtain the desired temperature profiles for the hydrothermal reactions. Elemental analysis was performed by H. Kolbe Mikroanalytisches Laboratorium.

2.2.2 Synthesis of Cu(1,3-benzenedicarboxylate)

A 1900-mL liner was charged with 6.04 g (61.9 mmol) of $\text{Cu}(\text{OH})_2$, 2.06 g (20.6 mmol) of $\text{Cu}(\text{OH})\text{F}$, 13.71 g (82.5 mmol) of isophthalic acid, 2.81 g (41.3 mmol) of imidazole, and 410 mL of water, capped and placed into a steel hydrothermal bomb. The bomb was heated to 150 °C at a rate of 1 °C/min, maintained at this temperature for 5 days, and cooled to room temperature at a rate of 0.1 °C/min. Blue hexagonal crystals of Cu(1,3-bdc) lined the walls of the vessel intimately covering a blue-green powder and were difficult to separate mechanically from the fine powder. The product mixture, therefore, was sonicated in its mother liquor in a 1000-mL glass bottle for 80 minutes. The suspension of powder was decanted, leaving behind blue hexagonal crystals of Cu(1,3-bdc), and the powder was separated from the mother liquor by vacuum filtration. The powder was identified by pXRD to consist of starting materials ($\text{Cu}(\text{OH})_2$, spertinite, PDF # 01-080-0656; $\text{Cu}(\text{OH})\text{F}$, PDF # 00-007-0306; and isophthalic acid, PDF #00-037-1920) and a green impurity, $\text{C}_{32}\text{H}_{24}\text{Cu}_6\text{O}_{26}$, whose structure is detailed in Appendix A.1 on pages 194 and 207-218. These reaction conditions were chosen in order to optimize the yield of crystalline Cu(1,3-bdc) relative to the above-mentioned impurities.

The filtrate mother liquor was recombined with the blue hexagonal crystals, sonicated for an additional 25 minutes, and the powder suspension was again decanted from the crystals. The blue hexagonal crystals of Cu(1,3-bdc) (13.3 g, ~ 71%) were then washed with deionized water, isolated by filtration, and dried in air. Impurities were further removed by physical separation

under a microscope. The purity of the crystalline Cu(1,3-bdc) sample was judged by pXRD. The crystal structure of Cu(1,3-bdc) contains a solvent-accessible void of 45 \AA^3 , which can be occupied by an incidental water molecule. Another crystal within the same batch refined as Cu(1,3-bdc) \cdot 0.11H₂O, with 1/9 of a water molecule per formula unit. Further crystallographic details are provided in Appendix A.1. Prior to magnetic measurements, samples were dried by heating them uncovered in a ceramic crucible at 10 °C/min, maintaining them at 240 °C for 2 h, and then cooling them to room temperature at 10 °C/min. No significant sample decomposition occurred, as judged by pXRD and elemental analysis. Anal. Calcd. for C₈H₄CuO₄: C, 42.21; H, 1.77; Cu, 27.91. Found: C, 41.90; H, 1.87; Cu, 27.74.

2.2.3 X-ray diffraction

Powder X-ray diffraction patterns were measured using a Rigaku RU300 rotating anode X-ray diffractometer with Cu K α radiation ($\lambda = 1.5405 \text{ \AA}$), which was wavelength-selected with a single-crystal graphite monochromator. Samples were spread onto a glass slide fixed with double-sided Scotch tape. Samples were rotated through $2\theta/\theta$ space and intensity was recorded as a function of 2θ from 10 to 60°. Patterns were indexed with MDI Jade software version 8.0 and referenced using the JCPDS powder diffraction database or dsp files calculated from single-crystal X-ray structures.

2.2.4 Single-Crystal X-ray diffraction

Structures were determined for Cu(1,3-bdc), Cu(1,3-bdc) \cdot 0.11H₂O, and C₃₂H₂₄Cu₆O₂₆. Single crystals were transferred onto a microscope slide coated with mineral oil. Crystals were affixed to a glass fiber or a cryoloop using the oil, frozen in a cold nitrogen gas stream, and optically centered. The data were collected on a Siemens three-circle platform goniometer equipped with a Bruker Smart Apex CCD detector with graphite-monochromated Mo K α

radiation ($\lambda = 0.71073 \text{ \AA}$), using both phi and omega scans at $-173 \text{ }^\circ\text{C}$. Data reduction and unit cell refinements were performed with the program SAINT,³⁰ and the program SADABS³¹ was used to perform scaling and absorption corrections. Space group assignments were based on systematic absences, E statistics, and successful refinement of the structures. The structures were solved by direct methods (SHELXS)³² and refined against F^2 on all data by full matrix least squares with SHELXL-97.³³ All non-hydrogen atoms were refined anisotropically; all hydrogen atoms were placed at idealized positions and refined using a riding model.

2.2.5 Magnetic Measurements

DC magnetic susceptibility data were collected on (ground-up) crystalline samples contained in gelatin capsules using Quantum Design MPMS-5S and MPMS-XL SQUID magnetometers at temperatures ranging from 2 to 350 K and field strengths varying from -50 to 50 kOe. For the magnetoanisotropy measurements, a cylindrical platform was made from Devcon epoxy, which was shaped to a straw and allowed to dry overnight. The epoxy was then removed from the straw and polished flat using sandpaper. Crystals were stacked on this platform using petroleum jelly to orient them relative to the field of the SQUID prior to measurement. The data were corrected for diamagnetic contributions of the sample holder by measurement of an empty capsule (or the capsule containing the epoxy sample holder, for the magnetoanisotropy measurements), and of the sample itself by use of constitutive corrections and Pascal's constants.³⁴

2.2.6 Other Physical Measurements

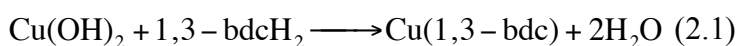
Infrared spectra of samples in KBr pellets were recorded on a Nicolet Magna-IR 860 spectrometer equipped with a KBr beam splitter and a DTGS detector. Raman spectra were recorded using a Kaiser Hololab 5000R Raman Spectrometer and Microprobe using an excitation

wavelength of 785 nm, large fibers, 10x objective, 8 minute exposure, 1 accumulation, and 3 mW laser power. Diffuse reflectance UV-vis spectra were recorded using a Varian Cary 5E with a Harrick Praying Mantis Accessory. An aluminum mirror was used as the 100% reflectance standard. Raman and diffuse reflectance UV-vis spectra are presented in Appendix B.1. Specific heat measurements were performed using a Quantum Design Model 6000 Physical Properties Measurement System with Helium-3 option. This system uses relaxation method calorimetry and determines specific heat by fitting the temperature response to a two exponential model. A single crystal of mass 0.999 ± 0.002 mg was held to the measurement platform using Apiezon N grease. The long time constant (τ_1) varied between 20 and 80 seconds for the temperature range measured. The sample coupling always exceeded 96%, implying that the ratio of the thermal conductance of the grease to that of the platform wires was at least 25. Thermogravimetric analysis measurements were performed using a Seiko Dual TG/DTA 320 Thermogravimetric/Differential Thermal Analyzer (SC). Samples were referenced and measured in aluminum pans, with N_2 as a purge gas flowing at 150 cc/min. Data were recorded at 0.2 s increments from 20 °C to 500 °C at a 5 °C/min heating rate.

2.3 Results

2.3.1 Synthetic Methodology

Initial treatment of $Cu(OH)_2$ with isophthalic acid (1,3-bdcH₂) under hydrothermal conditions led to the formation of a MOF kagomé, $Cu(1,3-bdc)$, according to the condensation reaction below:



The product mixture also contains 1,3-bdcH₂ and a copper-

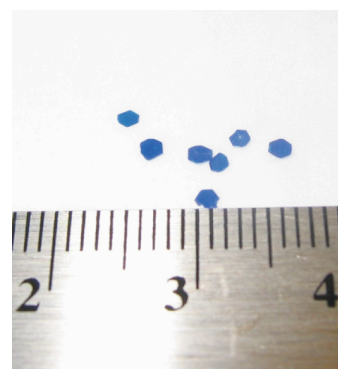


Figure 2.1. Large single crystals of $Cu(1,3-bdc)$ prepared by hydrothermal methods.

containing ligand oxidation byproduct. (Ligand oxidation of 1,3-bdcH₂ in Cu(II)-containing solutions has been previously reported.^{35,36}) To increase the solubility of 1,3-bdcH₂ and to buffer the reaction solution, imidazole was added to subsequent reactions. Additionally, Cu(OH)F was included as a mineralizing agent to promote crystallization. Without imidazole, product crystals were not well formed; without added F⁻ ion, product crystals were stacked and had little *c* dimension. F⁻ was not detected by ICP-AA in the product crystals. Large (up to 2 mm on an edge and 2.2 mg) dark blue hexagonal plates of Cu(1,3-bdc) were separated from a product mixture containing copper-containing starting materials, isophthalic acid, and a copper-containing ligand oxidation byproduct, C₃₂H₂₄Cu₆O₂₆. The structure of this byproduct is shown and discussed in Appendix A.1, pages 194 and 207-218. The structure of Cu(1,3-bdc) is discussed in Section 2.3.2. Solubility appears to play an important role in the formation of Cu(1,3-bdc) because related compounds Cu(H₂O)(1,3-bdc)•H₂O and Cu₂₄(1,3-bdc)₂₄(DMF)₁₄(H₂O)₁₀•(H₂O)₁₀(DMF)₆(C₂H₅OH)₆ can be obtained from reactions with cupric acetate and cupric nitrate, respectively.^{37,38} Attempts to prepare a non-magnetic analog of Cu(1,3-bdc) for heat capacity studies using Zn(OCOCH₃)₂•2H₂O or ZnO as Zn-based starting materials led to product mixtures containing isophthalic acid and a known Zn(1,3-bdc)•2H₂O phase (PDF # 00-38-1775) in the former case, and ZnO and Zn(1,3-bdc)•2H₂O in the latter. The PDF file for Zn(1,3-bdc)•2H₂O is unindexed, but the structure is not believed to be a hexagonal phase, thus making it unsuitable as a non-magnetic structural analog.

2.3.2 Structural Chemistry

The structure of Cu(1,3-bdc) is shown in Figure 2.2. Cu(1,3-bdc) may contain an incidental guest water molecule upon structural analysis, so crystals of Cu(1,3-bdc) were heated prior to magnetic measurements in order to remove the incidental solvent molecule. FTIR and

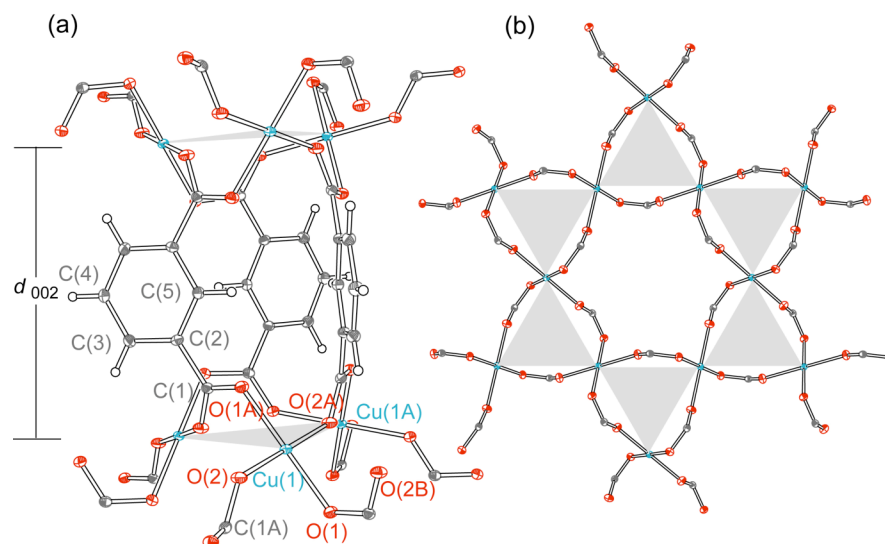


Figure 2.2. Crystal structure of Cu(1,3-bdc). (a) Interlayer coordination environment projected parallel to the crystallographic *c* axis. (b) The MOF kagomé lattice, projected perpendicular to the *c* axis. Phenyl ring atoms and guest water molecule have been omitted for clarity. Selected interatomic distances and angles: Cu(1)–O(1), 1.9265(9); Cu(1)–O(2), 1.9428(9); Cu(1A)···O(2B), 2.8396(9); Cu(1)–C(1A), 1.2685(15); O(2A)–C(1), 1.2689(14) Å; O(1)–Cu(1)–O(2), 92.14(4)°; O(2)–Cu(1)–O(1A), 87.86(4)°; Cu(1)–O(1)–C(1A), 115.67(8)°; Cu(1)–O(2A)–C(1), 132.42(8)°.

thermal analysis data both before and after heating are provided in Figures 2.3 and 2.4, respectively. Diffuse reflectance UV-vis data and Raman data were also recorded to further characterize the compound (Appendix B.1). The purity of Cu(1,3-bdc) was confirmed by similarities between simulated and experimental powder X-ray diffraction (Appendix A.1) and by elemental analysis.

The compound crystallizes in the hexagonal space group $P6_3/m$. The highly symmetric structure has only one-half crystallographically independent Cu(II) ion, which resides in a nearly square planar coordination environment with four monodentate carboxylate ligands. Each carboxylate group bridges two copper ions to form a kagomé lattice in the *ab* plane composed of $\{\text{Cu}_3(\text{OCO})_3\}$ triangles. The in-plane Cu—Cu distance is 4.5541(2) Å, (4.5528(3) Å for Cu(1,3-bdc)•0.11H₂O, the water containing species) and the distance between the kagomé planes (d_{002}) is 7.9716(3) Å (7.9775(6) Å for Cu(1,3-bdc)•0.11H₂O). The layers stack in AA fashion.

1,3-bdc ligands serve to link the layers together into a three dimensional metal-organic framework. The structure has hexagonal channels (Figure 2.2.b), with a solvent accessible void of 45 \AA^3 and a cross-channel Cu—Cu distance of $9.1081(2) \text{ \AA}$ ($9.1056(3) \text{ \AA}$ for $\text{Cu}(1,3\text{-bdc})\cdot 0.11\text{H}_2\text{O}$). The guest water molecule residing in the center of this channel in the kagomé plane can be removed by heating the crystals to $240 \text{ }^\circ\text{C}$ for 2 hours without significant decomposition. Desolvation of these crystals could be confirmed spectroscopically in the FTIR spectrum, as shown in Figure 2.3.

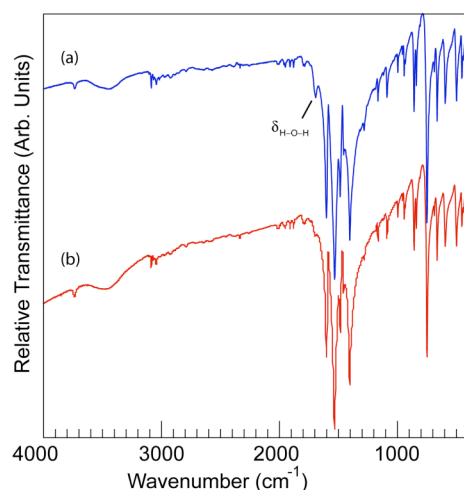


Figure 2.3. FTIR of a crystalline sample of $\text{Cu}(1,3\text{-bdc})$ (a) before, and (b) after heating at $240 \text{ }^\circ\text{C}$ for 2 hours. Before heating, the sample shows an absorbance at 1693 cm^{-1} due to a bending mode of solvent water. After heating, this absorbance is largely absent. Data for (a): $3736(\text{w})$, $3086(\text{w})$, $3043(\text{w})$, $2016(\text{w})$, $1950(\text{w})$, $1909(\text{w})$, $1880(\text{w})$, $1795(\text{w})$, $1693(\text{w})$, $1603(\text{s})$, $1531(\text{i, s})$, $1485(\text{sh})$, $1456(\text{sh})$, $1404(\text{i, s})$, $1282(\text{sh})$, $1165(\text{s})$, $1088(\text{s})$, $997(\text{s})$, $957(\text{sh})$, $943(\text{s})$, $933(\text{sh})$, $858(\text{s})$, $839(\text{s})$, $808(\text{sh})$, $748(\text{i, s})$, $687(\text{w})$, $663(\text{s})$, $594(\text{s})$, $548(\text{sh})$, $499(\text{s})$, $453(\text{s})$, $440(\text{sh})$, $401(\text{s})$. s = sharp, i = intense, w = weak, sh = shoulder.

Thermogravimetric analysis (TGA) of the crystalline sample (Figure 2.4.a) showed loss of 0.65% by mass (or $\sim 0.08 \text{ H}_2\text{O}$ per formula unit) to a temperature of $257 \text{ }^\circ\text{C}$, followed by decomposition of the sample at $300 \text{ }^\circ\text{C}$, leaving a residue (after heating to $550 \text{ }^\circ\text{C}$) of Cu_2O (PDF# 99-000-0865) and Cu metal (PDF # 00-004-0836) as determined by pXRD. TGA (Figure

2.4.c) of sample dried by heating the crystals to 240 °C showed no significant loss of mass before sample decomposition at 292 °C, indicating removal of the incidental solvent.

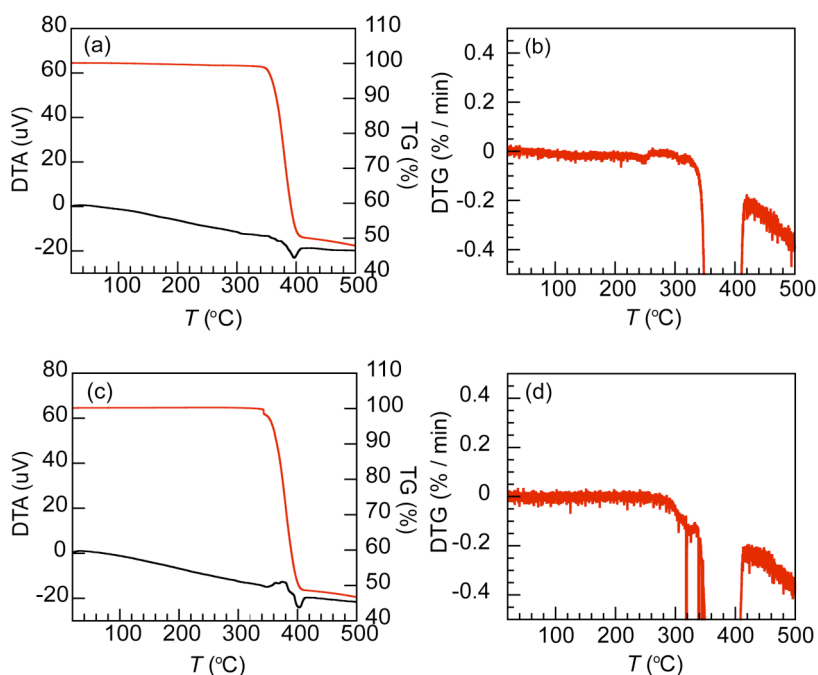


Figure 2.4. (a) TGDTA for a crystalline sample of solvated Cu(1,3-bdc) as prepared. (b) A differential plot shows the time profile of loss of solvent to 257 °C more clearly. (c) TGDTA for a crystalline sample of the title compound following further sample preparation (heating for 2 hours at 240 °C). No significant loss of mass occurs until decomposition of the sample at 292 °C, indicating desolvation by the heating process. (d) A differential plot shows the time profile for mass loss.

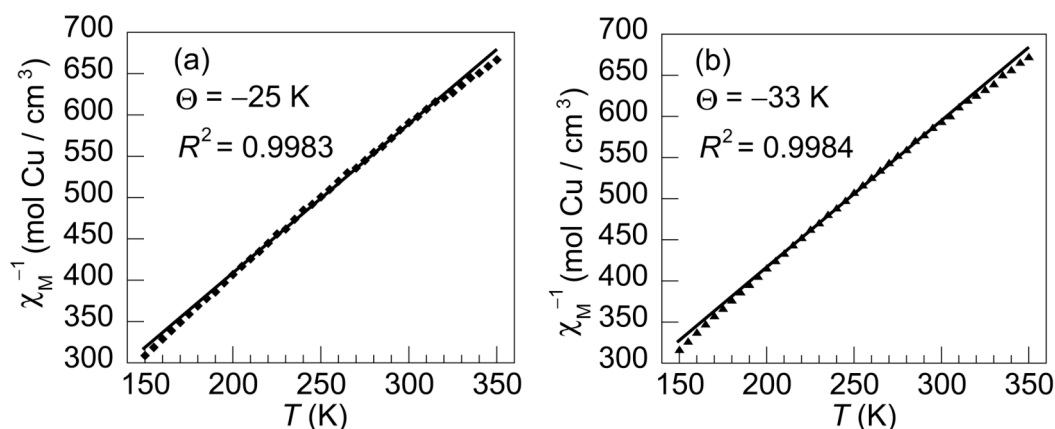


Figure 2.5. Temperature dependence of χ_M^{-1} for a ground sample of Cu(1,3-bdc) (a) with no heating and (b) after heating crystals to 240 °C for 2 h prior to grinding them for SQUID measurement. Values for Θ were determined by fitting data in the temperature range $150 \leq T \leq 350$ K. Lines indicate best fit obtained.

2.3.3 Magnetic Properties

Fitting the high temperature inverse susceptibility data (150 – 350 K) of ground powder of Cu(1,3-bdc) yields $\Theta = -33$ K, which suggests that the average nearest-neighbor superexchange interaction is antiferromagnetic (see Figure 2.5). From a mean-field analysis of Curie-Weiss law introduced in Section 1.2, the isotropic J value (assuming z , the number of nearest neighbors, is 4) is found to be -23 cm⁻¹. For comparison, Cotton, Dalal, and coworkers found $J = -75$ cm⁻¹ for a triangular di- μ -carboxylate molecule, with two bridging 2,4,6-tri-isopropyl-1-benzoate moieties between each pair of Cu(II) centers. These centers were only 3.131 Å apart, as opposed to 4.553 Å here.³⁹

The zero-field cooled and field cooled magnetic susceptibility of Cu(1,3-bdc) versus temperature are shown in Figure 2.6. A plot of χT vs. T is provided as an inset. Interestingly, both plots show an increase at low T , suggestive of the onset of a ferromagnetic ordering transition at the temperature limit of the SQUID susceptometer. The ferromagnetic ordering transition is likely due to an out-of-kagomé plane superexchange and will be discussed further in Section 2.4. Further evidence for a ferromagnetic ordering transition is provided by the

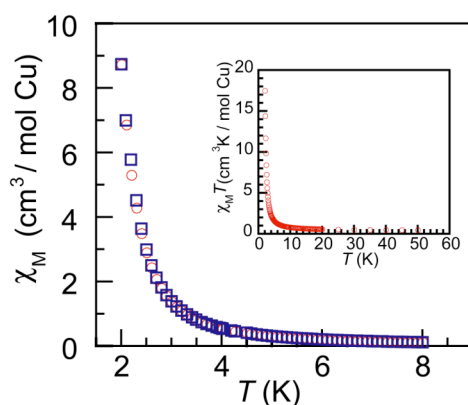


Figure 2.6. Temperature dependence of χ_M for a ground powder sample of Cu(1,3-bdc) as measured at 100 Oe under zero-field cooled (\circ) and field-cooled (\square) conditions. Inset: temperature dependence of $\chi_M T$ for the same powder sample.

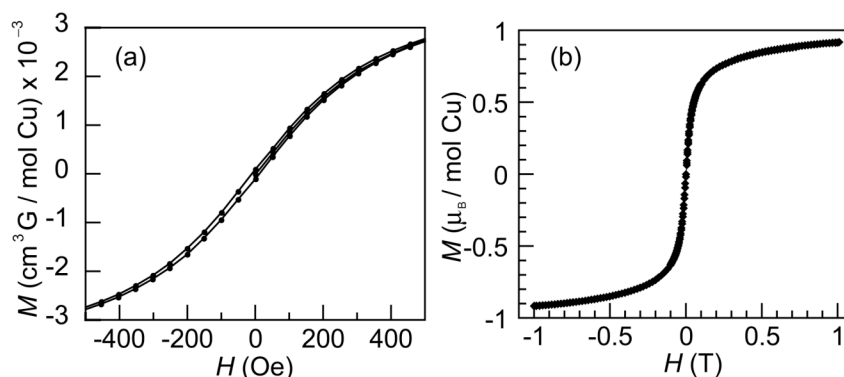


Figure 2.7. (a) Field dependence of the magnetization per mole of Cu for Cu(1,3-bdc), measured at 2 K, showing hysteresis indicative of a very soft ferromagnet. A ground sample of Cu(1,3-bdc) was measured after heating crystals to 240 °C for 2 h prior to grinding them for SQUID measurement. (b) Full range of measurement in (a). Lines are drawn to guide the eye. The magnetization saturates at $0.91 \mu_B / \text{mol Cu}$, which is consistent with 1 unpaired electron per Cu center.

magnetization versus field data measured at 2 K (Figure 2.7) and the specific heat versus temperature of a single crystal at variable magnetic fields, measured by Joel Helton (Figure 2.8).

Figure 2.7 shows the small hysteresis loop indicative of a very soft ferromagnet with a coercive field of 10.5 Oe and a remanence of 95.8 emu Oe / mol Cu. Figure 2.8 shows a singularity in the zero-field heat capacity at 2 K, consistent with the onset of magnetic ordering at that temperature in zero field. An ordering transition at 2 K is consistent to the same order of magnitude with literature values for J for Cu(II) centers across the seven-atom exchange pathway of the 1,3-bdc linker, which are on the order of $1\text{--}3 \text{ cm}^{-1}$ for distances of $10.4\text{--}10.8 \text{ \AA}$ (the distance here is 7.978 \AA).^{40,41}

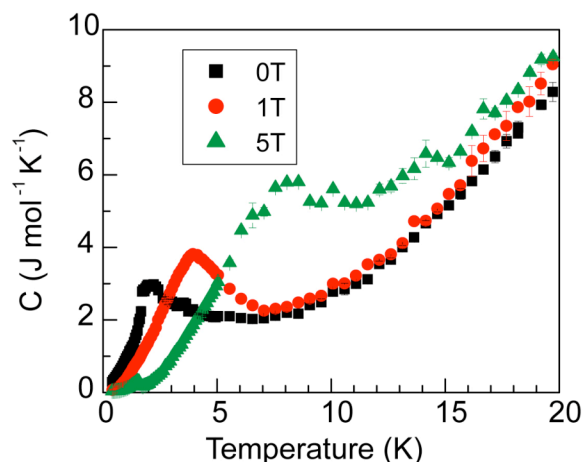


Figure 2.8. Temperature dependence of the specific heat for a single crystal of Cu(1,3-bdc) measured in magnetic fields of 0 T (●), 1 T (■), and 5 T (▲).

2.3.3.1 Preliminary Magnetoanisotropy Experiments

Preliminary magnetoanisotropy experiments were performed on Cu(1,3-bdc) crystals. A single-crystal X-ray diffraction experiment enabled us to index the crystals and to determine that (0 0 1), the kagomé plane, is a cleavage plane and the hexagonal face of the blue hexagonal prisms. Seven crystals (weighing approximately 1 mg each for a total mass of 7 mg) were stacked in petroleum jelly and coaligned with the kagomé plane first parallel and then perpendicular to the field of the SQUID magnet. Both zero-field cooled and field cooled measurements were performed at 10 KOe, as shown in Figure 2.9. However, the SQUID measurement failed to yield any observable magnetoanisotropy. Possible explanations for this failure include the small size of the crystals and the difficulty of aligning them with the magnetic field of the SQUID.

2.4 Discussion

The foregoing magnetic data suggest a spin-frustrated behavior of Cu(1,3-bdc). Using the frustration parameter defined by Ramirez, $f = |\Theta| / T_c$, with values of $f > 10$ signifying a strong effect,⁴² we find that Cu(1,3-bdc) is spin frustrated with a value of $f = |-33 \text{ K}| / 2 \text{ K} = 16.5$. The in-plane superexchange between copper centers bridged by the 1,3-bdc linker in Cu(1,3-bdc) is most likely antiferromagnetic. Copper centers bridged by monodentate carboxylates are typically coupled by antiferromagnetic superexchange interactions, as reported for paddlewheel complexes⁴³ and μ -carboxylate-bridged triangular molecules of Cu(II).^{39,44,45}

In Cu(1,3-bdc), the $d_{x^2-y^2}$ orbital has non-negligible spin density (an unpaired spin) and can participate in two possible superexchange pathways: an in-plane pathway from metal to metal through the μ -carboxylate, and a 7-atom out-of-plane superexchange pathway from metal

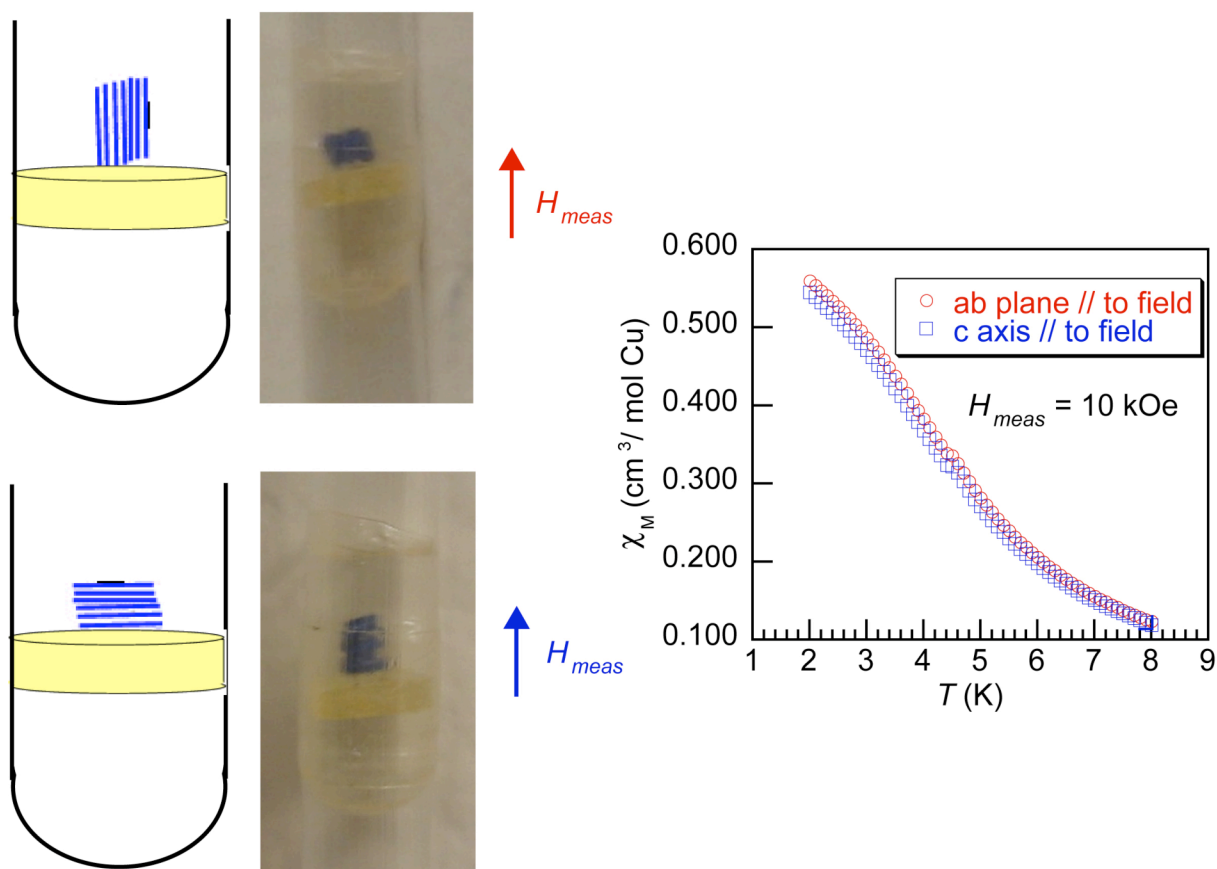


Figure 2.9. Magnetoanisotropy experiment on Cu(1,3-bdc) crystals with total mass 7 mg, stacked using petroleum jelly. ZFC data for (○) ab plane // to field and (□) c axis // to field, taken in a 10 kOe measuring field.

to metal through the 1,3-bdc linker (Figure 2.10). Therefore, if the out-of-kagomé plane superexchange is ferromagnetic, we would expect the compound to show ferromagnetic long-range ordering behavior once the coupling energy between the spins exceeds the thermal energy, $k_B T$. In a frustrated system such as this, however, this interaction competes with the 120° antiferromagnetic in-kagomé-plane constraint, and the temperature at which this ordering occurs is therefore suppressed.

1,3-bdc in particular, moreover, has been shown to mediate ferromagnetic superexchange in molecular dimers of Cu(II).^{40,41} These dimer systems with similar geometries to Cu(1,3-bdc) suggest that the origin of the observed ferromagnetic behavior is indeed derived from superexchange through the 1,3-bdc linker to Cu ions in different layers. In Cu dimer model complexes,^{40,41} Cu coupling is ferromagnetic and small in magnitude along a seven-atom superexchange pathway. The same pathway connects Cu ions in different layers of Cu(1,3-bdc). In fact, the *meta*- or 1,3-substituted benzene topology in general is well known to mediate ferromagnetic interactions through spin polarization mechanisms when the linker is planar and spin centers are separated by an odd number of atoms.^{40,41,46-53} This topology is

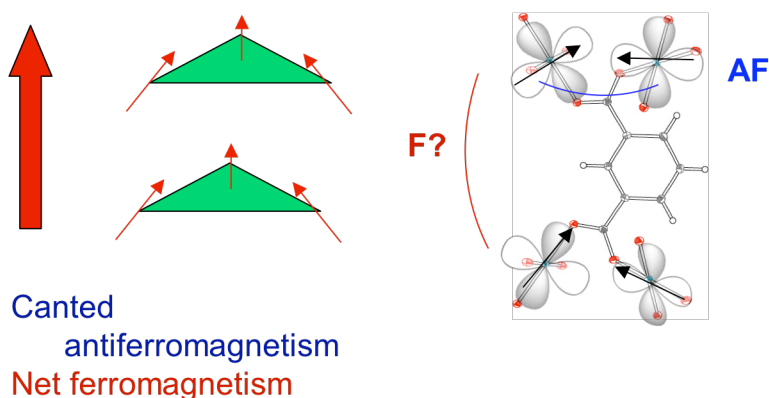


Figure 2.10. 1,3-bdc is likely to mediate ferromagnetic superexchange between Cu(II) centers in different kagomé layers.

frequently used in the design of high-spin organic molecules. If out-of-plane ferromagnetism is truly the case and limits the frustration of this system, future directions in the synthesis of frustrated MOF kagomés should avoid conjugated *m*-benzene topologies between kagomé layers.

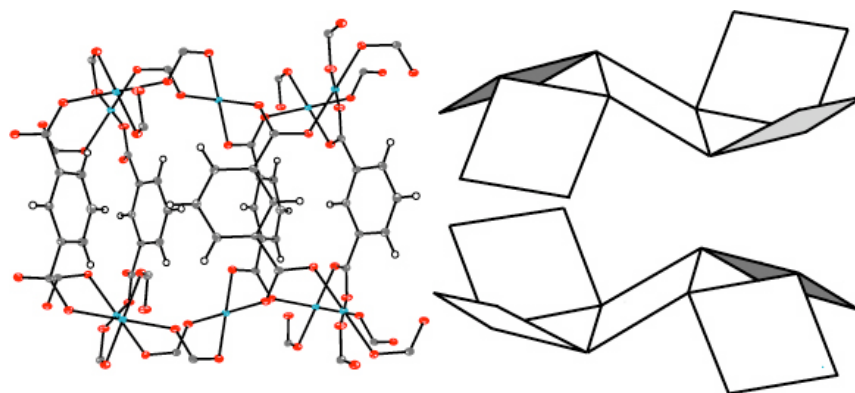


Figure 2.11. Corrugation and stacking of layers in Cu(1,3-bdc). Cu is in the center of CuO₄ planes, represented by squares at right.

On the other hand, if superexchange in both directions is indeed antiferromagnetic, we cannot, as of yet, rule out ordering through other mechanisms, such as a Dzyaloshinsky-Moriya interaction. A Dzyaloshinsky-Moriya interaction is allowed in this system, because the midpoint between Cu(II) centers in Cu(1,3-bdc) is not a center of inversion.⁵⁴ The kagomé layers of Cu(1,3-bdc) are highly corrugated, as shown in Figure 2.11. It is impossible, however, to predict a plane for the \mathbf{D}_{ij} vector in this system *a priori*. Unlike the situation in jarosite, this system lacks both a mirror plane containing the two metal centers (the M \cdots C \cdots M plane, which makes a 63.4° with the kagomé plane, is the closest approximation to such a mirror plane in this system; carboxylate oxygens are slightly out of this plane) or a mirror plane that bisects the bridging ligand in a perpendicular fashion (Figure 2.12).

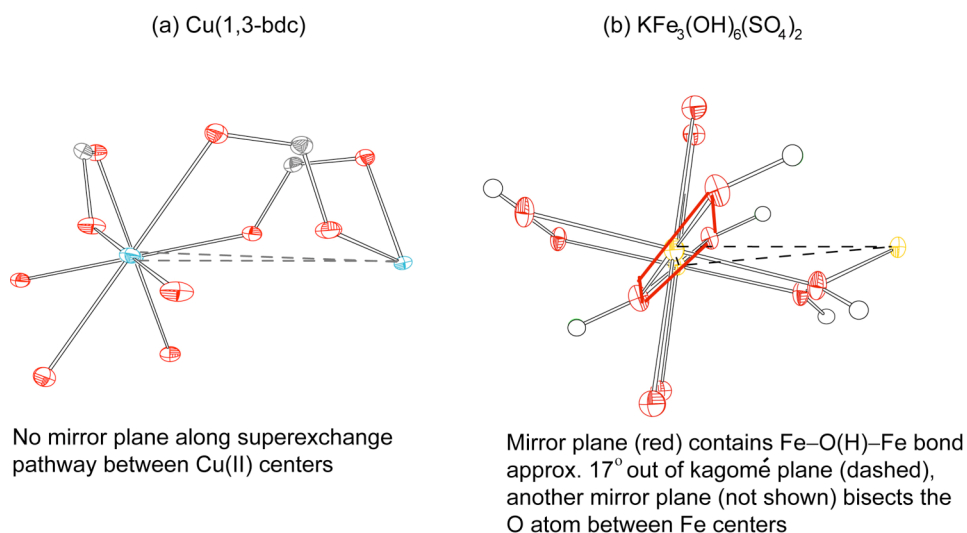


Figure 2.12. View down (a) the Cu–O–C–O–Cu pathway in Cu(1,3-bdc) and (b) the Fe–O_H–Fe bond in K-jarosite. The Fe–O_H–Fe plane is a mirror plane in jarosite, another perpendicular mirror plane runs along the O–H bond, bisecting it. Cu(1,3-bdc) contains no such mirror planes.

2.5 Conclusions

The metal-organic framework spin-frustrated material, Cu(1,3-bdc), is distinguished by its short three-atom bridge between Cu centers, which gives rise to the shortest known metal-metal distance in any MOF kagomé to date. The discovery of materials such as Cu(1,3-bdc) directs future synthetic efforts, paving the way for exploration of $S = \frac{1}{2}$ MOF kagomé with quantum disordered ground states. Neutron scattering studies are currently underway to probe the ordering behavior in this frustrated MOF system, the first MOF kagomé with $S = \frac{1}{2}$ and suitable M—M distances for studying geometric spin frustration.

2.6 References

1. Behera, J. N.; Rao, C. N. R. *Dalton Trans.* **2007**, 669-673.
2. Rao, C. N. R.; Sampathkumaran, E. V.; Nagarajan, R.; Paul, G.; Behera, J. N.; Choudhury, A. *Chem. Mater.* **2004**, *16*, 1441-1446.
3. Behera, J. N.; Rao, C. N. R. *J. Am. Chem. Soc.* **2006**, *128*, 9334-9335.
4. Behera, J. N.; Paul, G.; Choudhury, A.; Rao, C. N. R. *Chem. Commun.* **2004**, 456-457.
5. Paul, G.; Choudhury, A.; Sampathkumaran, E. V.; Rao, C. N. R. *Angew. Chem., Int. Ed.* **2002**, *41*, 4297-4300.
6. Rao, C. N. R.; Paul, G.; Choudhury, A.; Sampathkumaran, E. V.; Raychaudhuri, A. K.; Ramasesha, S.; Rudra, I. *Phys. Rev. B* **2003**, *67*, 134425/134421-134425/134425.
7. Paul, G.; Choudhury, A.; Rao, C. N. R. *Chem. Commun.* **2002**, 1904-1905.
8. Behera, J. N.; Rao, C. N. R. *Inorg. Chem.* **2006**, *45*, 9475-9479.
9. Rusanov, E. B.; Ponomarova, V. V.; Komarchuk, V. V.; Stoeckli-Evans, H.; Fernandez-Ibanez, E.; Stoeckli, F.; Sieler, J.; Domasevitch, K. V. *Angew. Chem., Int. Ed.* **2003**, *42*, 2499-2501.
10. Liu, Y.; Kravtsov, V. C.; Beauchamp, D. A.; Eubank, J. F.; Eddaoudi, M. *J. Am. Chem. Soc.* **2005**, *127*, 7266-7267.
11. Barthelet, K.; Marrot, J.; Ferey, G.; Riou, D. *Chem. Commun.* **2004**, 520-521.
12. Chun, H.; Moon, J. *Inorg. Chem.* **2007**, *46*, 4371-4373.
13. Perry, J. J.; McManus, G. J.; Zaworotko, M. J. *Chem. Commun.* **2004**, 2534-2535.
14. Eddaoudi, M.; Kim, J.; Vodak, D.; Sudik, A.; Wachter, J.; O'Keeffe, M.; Yaghi, O. M. *Proc. Natl. Acad. Sci. U. S. A.* **2002**, *99*, 4900-4904.
15. Liu, H.-K.; Sun, W.-Y.; Tang, W.-X.; Yamamoto, T.; Ueyama, N. *Inorg. Chem.* **1999**, *38*, 6313-6316.
16. Narumi, Y.; Honda, Z.; Katsumata, K.; Domenge, J. C.; Sindzingre, P.; Lhuillier, C.; Matsuo, A.; Suga, K.; Kindo, K. *J. Magn. Magn. Mater.* **2004**, 272-276, 878-879.
17. Maegawa, S.; Kaji, R.; Kanou, S.; Oyamada, A.; Nishiyama, M. *J. Phys.: Condens. Matter* **2007**, *19*, 145250/145251-145250/145259.
18. Honda, Z.; Katsumata, K.; Yamada, K. *Physica B* **2003**, 329-333, 1032-1033.
19. Honda, Z.; Katsumata, K.; Yamada, K. *J. Phys.: Condens. Matter* **2002**, *14*, L625-L629.

Chapter 2

20. Manson, J. L.; Ressouche, E.; Miller, J. S. *Inorg. Chem.* **2000**, *39*, 1135-1141.
21. Norman, R. E.; Rose, N. J.; Stenkamp, R. E. *J. Chem. Soc., Dalton Trans.* **1987**, 2905-2910.
22. Mekata, M.; Abdulla, M.; Asano, T.; Kikuchi, H.; Goto, T.; Morishita, T.; Hori, H. *J. Magn. Magn. Mater.* **1998**, *177-181*, 731-732.
23. Mekata, M.; Abdulla, M.; Kubota, M.; Oohara, Y. *Can. J. Phys.* **2001**, *79*, 1409-1413.
24. Moulton, B.; Lu, J.; Hajndl, R.; Hariharan, S.; Zaworotko, M. J. *Angew. Chem., Int. Ed.* **2002**, *41*, 2821-2824.
25. Atwood, J. L. *Nat. Mater.* **2002**, *1*, 91-92.
26. Furukawa, S.; Ohba, M.; Kitagawa, S. *Chem. Commun.* **2005**, 865-867.
27. Liu, B.; Li, Y.-Z.; Zheng, L.-M. *Inorg. Chem.* **2005**, *44*, 6921-6923.
28. Baudron, S. A.; Batail, P.; Coulon, C.; Clerac, R.; Canadell, E.; Laukhin, V.; Melzi, R.; Wzietek, P.; Jerome, D.; Auban-Senzier, P.; Ravy, S. *J. Am. Chem. Soc.* **2005**, *127*, 11785-11797.
29. Shin, D. M.; Lee, I. S.; Chung, Y. K.; Lah, M. S. *Inorg. Chem.* **2003**, *42*, 5459-5461.
30. SAINT; Bruker-AXS Inc.: Madison, Wisconsin, U.S.A., 2005.
31. Sheldrick, G. M. University of Goettingen, Germany, 2007.
32. Sheldrick, G. M. *Acta Crystallogr. A* **2008**, *A64*, 112-122.
33. Sheldrick, G. M. University of Goettingen, Germany, 2008.
34. Kahn, O. *Molecular Magnetism*; VCH: New York, 1993, p. 3.
35. Yang, S.-Y.; Long, L.-S.; Huang, R.-B.; Zheng, L.-S.; Ng, S. W. *Inorg. Chim. Acta* **2005**, *358*, 1882-1886.
36. Jiang, Y.-Q.; Zhou, Z.-H.; Wei, Z.-B. *Chin. J. Struct. Chem.* **2005**, *24*, 457-461.
37. Gao, L.; Zhao, B.; Li, G.; Shi, Z.; Feng, S. *Inorg. Chem. Commun.* **2003**, *6*, 1249-1251.
38. Eddaoudi, M.; Kim, J.; Wachter, J. B.; Chae, H. K.; O'Keeffe, M.; Yaghi, O. M. *J. Am. Chem. Soc.* **2001**, *123*, 4368-4369.
39. Stone, M. B.; Fernandez-Alonso, F.; Adroja, D. T.; Dalal, N. S.; Villagrán, D.; Cotton, F. A.; Nagler, S. E. *Phys. Rev. B* **2007**, *75*, 214427/214421-214427/214428.

Chapter 2

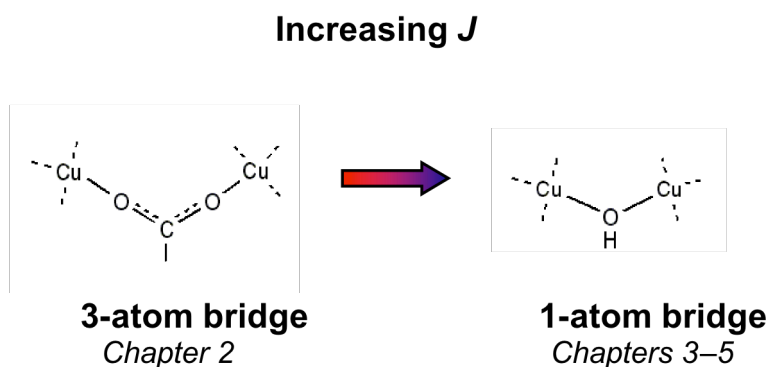
40. Cheng, P.; Yan, S.-P.; Xie, C.-Z.; Zhao, B.; Chen, X.-Y.; Liu, X.-W.; Li, C.-H.; Liao, D.-Z.; Jiang, Z.-H.; Wang, G.-L. *Eur. J. Inorg. Chem.* **2004**, 2369-2378.
41. Shen, W.-Z.; Chen, X.-Y.; Cheng, P.; Yan, S.-P.; Zhai, B.; Liao, D.-Z.; Jiang, Z.-H. *Eur. J. Inorg. Chem.* **2005**, 2297-2305.
42. Ramirez, A. P. *Annu. Rev. Mater. Sci.* **1994**, *24*, 453-480.
43. Jotham, R. W.; Kettle, S. F. A.; Marks, J. A. *J. Chem. Soc., Dalton Trans.* **1972**, 428-438.
44. Clerac, R.; Cotton, F. A.; Dunbar, K. R.; Hillard, E. A.; Petrukhina, M. A.; Smucker, B. W. *C.R. Acad. Sci., Ser. IIC: Chim.* **2001**, *4*, 315-319.
45. Cage, B.; Cotton, F. A.; Dalal, N. S.; Hillard, E. A.; Rakvin, B.; Ramsey, C. M. *J. Am. Chem. Soc.* **2003**, *125*, 5270-5271.
46. Pascu, M.; Lloret, F.; Avarvari, N.; Julve, M.; Andruh, M. *Inorg. Chem.* **2004**, *43*, 5189-5191.
47. Glaser, T.; Heidemeier, M.; Grimme, S.; Bill, E. *Inorg. Chem.* **2004**, *43*, 5192-5194.
48. Fernandez, I.; Ruiz, R.; Faus, J.; Julve, M.; Lloret, F.; Cano, J.; Ottenwaelder, X.; Journaux, Y.; Munoz, M. C. *Angew. Chem., Int. Ed.* **2001**, *40*, 3039-3042.
49. Paital, A. R.; Mitra, T.; Ray, D.; Wong, W. T.; Ribas-Arino, J.; Novoa, J. J.; Ribas, J.; Aromi, G. *Chem. Commun.* **2005**, 5172-5174.
50. Ung, V. A.; Thompson, A. M. W. C.; Bardwell, D. A.; Gatteschi, D.; Jeffery, J. C.; McCleverty, J. A.; Totti, F.; Ward, M. D. *Inorg. Chem.* **1997**, *36*, 3447-3454.
51. Mitani, M.; Yamaki, D.; Takano, Y.; Kitagawa, Y.; Yoshioka, Y.; Yamaguchi, K. *J. Chem. Phys.* **2000**, *113*, 10486-10504.
52. Yoshizawa, K.; Tanaka, K.; Yamabe, T. *J. Phys. Chem.* **1994**, *98*, 1851-1855.
53. Itoh, K.; Kinoshita, M. *Molecular Magnetism: New Magnetic Materials*; Taylor & Francis: London, 2004, p.28.
54. Elhajal, M.; Canals, B.; Lacroix, C. *Phys. Rev. B* **2002**, *66*, 014422/014421-014422/014426.

Chapter 3.

$\text{CdCu}_3(\text{OH})_6(\text{NO}_3)_2 \cdot x\text{H}_2\text{O}$, An $S = \frac{1}{2}$ Kagomé Antiferromagnet with Hydrogen-Bonded Layers

3.1 Introduction

In our quest to observe quantum states on the kagomé, we would like to optimize $S = \frac{1}{2}$ kagomé systems to maximize their frustration. Ramirez's frustration parameter, $f = |\Theta| / T_c$, indicates that one way to increase frustration in a system is to increase the magnitude of the Curie-Weiss constant, Θ . Because the isotropic J value is directly proportional to Θ from mean-field theory (Equation 1.3), to synthesize a more frustrated $S = \frac{1}{2}$ kagomé we must increase the magnitude of mean antiferromagnetic nearest-neighbor exchange. Superexchange interactions are a complicated function of several variables, including orbital symmetry, electronic occupation of both metals and ligands, and bridging angles;¹⁻⁵ it is well known, however, that superexchange interactions generally decay rapidly with distance.^{4,6} (Coffman and Buettner, for instance, collected empirically determined values of J in many inorganic compounds in order to define a limiting function for such values at various distances.⁶) Although the MOF kagomé presented in Chapter 2 has the shortest M—M distance of any known MOF kagomé, the distance is still quite long at 4.553 Å. In order to increase the strength of frustration in an $S = \frac{1}{2}$ kagomé, therefore, we needed to maintain nearest-neighbor antiferromagnetism while simultaneously increasing the strength of superexchange; we sought to do so by decreasing the distance between



Scheme 3.1. Decreasing the distance between metal centers in $S = \frac{1}{2}$ kagomé systems will increase the strength of nearest-neighbor superexchange.

metal centers (Scheme 3.1). The foregoing Chapter focused on a μ -carboxylate bridged system, while this Chapter and those following it will focus on μ -hydroxy bridged systems with shorter Cu—Cu distances.

3.2 Experimental

3.2.1 General Procedures

Sample Preparation

Water was distilled and deionized with a Milli-Q filtering system. All other reagents were obtained from commercial vendors and used without further purification: CuO (Strem Chemicals, 99.999+%); Cu(NO₃)₂•2.5H₂O (Aldrich, 99.99+%); NaOH (Mallinckrodt, 98+%); Cu₂O (Strem Chemicals, 99.9%); Cd(NO₃)₂•4H₂O (Strem Chemicals, 98%); O₂ (Airgas). Elemental analysis was performed by H. Kolbe Mikroanalytisches Laboratorium.

3.2.2 Synthesis of CdCu₃(OH)₆(NO₃)₂•0.5H₂O

Method 1. A 250-mL Schlenk flask was charged with 3.53 g (24.7 mmol) of Cu₂O, 15.45 g (50.09 mmol) of Cd(NO₃)₂•4H₂O, 12.5 mL of water, and a magnetic stirbar. A rubber septum was used to seal the flask with a needle to vent, and magnetic stirring was begun. Oxygen was introduced into the flask in order to saturate the cadmium nitrate solution and fill the headspace above the reaction slurry, before the flask was quickly sealed with a greased glass stopper and Keck clip. A gradual color change from red to purple was noted over the course of the next two months, indicating the occurrence of a reaction. To ensure the presence of adequate oxygen for the oxidation, additional oxygen was introduced after those two months to saturate the cadmium nitrate solution and fill the headspace above the slurry using the same procedure before the flask was again sealed. (According to Equation 3.4, 12.5 mmol of O₂ are needed to react with 25 mmol

Chapter 3

of Cu_2O ; a 250-mL Schlenk flask holds approximately 11 mmol O_2 at STP.) The reaction was allowed to proceed for approximately five more months, over which time a gradual color change from purple to pale green was noted in the reaction mixture. To assess the completion of the reaction, the pale green powder was vacuum filtered, rinsed with three 15-mL aliquots of dH_2O , and left on the Büchner funnel to dry overnight under suction, yielding 8.17 g of pale green solid. Purity was assessed with pXRD and elemental analysis by ICP (H. Kolbe). These assessments indicated the presence of unreacted Cu_2O along with the desired $\text{CdCu}_3(\text{OH})_6(\text{NO}_3)_2 \cdot x\text{H}_2\text{O}$ product (matching both PDF # 01-072-1433 for the $P\bar{1}$ structure and 01-070-1904 for the $P\bar{3}m1$ structure), so the 8.17 g of pale green solid was again placed in a 250-mL Schlenk flask with 15.45 g (50.09 mmol) of $\text{Cd}(\text{NO}_3)_2 \cdot 4\text{H}_2\text{O}$, 12.5 mL of water, and a magnetic stirbar. Oxygen was introduced to saturate the solution and fill the headspace above the slurry using the above procedure, after which the flask was again sealed with a greased glass stopper and Keck clip. A gradual color change from pale green to pale blue was noted in the reaction mixture as it stirred under oxygen for approximately three additional months. At the end of this time period, the pale blue powdered product was again vacuum filtered, rinsed with three 15-mL aliquots of dH_2O , and left on the Büchner funnel to dry overnight under suction, yielding 8.13 g (90 % based on starting Cu) of pale blue solid. Total reaction time: 42 weeks (322 days). Purity was again assessed with pXRD (Section 3.3) and elemental analysis by ICP (H. Kolbe). Anal. Calcd. for $\text{Cu}_3\text{CdH}_8\text{O}_{13}\text{N}_2$ ($\text{CdCu}_3(\text{OH})_6(\text{NO}_3)_2 \cdot \text{H}_2\text{O}$): Cu, 34.84; Cd, 20.55; H, 1.47; N, 5.12. Found: Cu, 34.71; Cd, 20.48; H, 1.45; N, 5.15.

Thermogravimetric analysis (TGA) of the powder sample (Section 3.3) showed loss of 1.64% by mass (or $\sim 0.5 \text{ H}_2\text{O}$ per formula unit) to 226 °C, followed by a loss of an additional

10.08% by mass (consistent with 3 H₂O) by 240 °C. The compound loses an additional 20.07% by mass by 500 °C, which is likely volatile oxides of nitrogen, to leave a residue of 69.09% of the original mass. The residue contains CuO (tenorite, PDF # 01-080-0076) and CdO (PDF # 03-065-2908, also known as monteponite, 01-073-2245) by pXRD.

Method 2. The following preparation is based on Oswald's procedure.⁷ 3.96 g (50.0 mmol) CuO and 15.5 g (50.0 mmol) Cd(NO₃)₂•4H₂O and 25 mL dH₂O were placed in a 50-mL Erlenmeyer flask. The flask was covered with several layers of Kimwipes to allow diffusion of atmospheric oxygen while blocking dust. The flask was placed in the back of a fume hood without disturbance for 588 days before the blue-gray solid was vacuum filtered, rinsed with three 15-mL aliquots of dH₂O, and left on the Büchner funnel to dry overnight under suction, yielding 3.51 g of blue-gray solid. pXRD with phase weighting indicated roughly 10% by mass unreacted CuO (tenorite, PDF # 01-080-0076). A portion of this powder was reacted with 2 M aqueous Cd(NO₃)₂•4H₂O in the same manner as above but with magnetic stirring for an additional month. The product was washed and dried as above. pXRD with phase weighting indicated approximately 6% by mass unreacted CuO (tenorite, PDF # 01-080-0076). The reaction was ultimately abandoned (after over 20 months total reaction time) in favor of the more kinetically accessible Method 1.

3.2.3 Synthesis of Cu₂(OH)₃NO₃ (rouaite, syn.)

The following procedure is modified from Tanaka and Terada.⁸ 4.67 g of Cu(NO₃)₂•2.5 H₂O (20.1 mmol) was placed in a 200-mL volumetric flask and brought to volume with water. 1.14 g (28.5 mmol) of NaOH was placed in a 100-mL volumetric flask and brought to volume with water. The Cu(NO₃)₂ solution was added to a 500-mL round-bottomed flask with

magnetic stirring. The NaOH solution was subsequently added, and a blue-green precipitate formed. The reaction mixture was allowed to age for one day prior to vacuum filtration and drying under suction on a Büchner funnel to yield 1.80 g (75 % based on starting Cu) pale blue-green solid, which matched PDF # 04-010-3058 for rouaite.

3.2.4 X-ray diffraction

Powder X-ray diffraction patterns were measured using a Rigaku RU300 rotating anode X-ray diffractometer with Cu K α radiation ($\lambda = 1.5405 \text{ \AA}$), which was wavelength-selected with a single-crystal graphite monochromator. Samples were spread onto a glass slide fixed with double-sided Scotch tape. Samples were rotated through $2\theta/\theta$ space and intensity was recorded as a function of 2θ from 10 to 60°. Patterns were indexed with MDI Jade software version 8.0 and referenced using the JCPDS powder diffraction database.

3.2.5 Magnetic Measurements

DC magnetic susceptibility data were collected on (ground-up) crystalline samples contained in gelatin capsules using Quantum Design MPMS-5S and MPMS-XL SQUID magnetometers at temperatures ranging from 2 to 350 K and field strengths varying from -50 to 50 kOe. The data were corrected for diamagnetic contributions of the sample holder by measurement of an empty capsule, and of the sample itself by use of Pascal's constants.

3.2.6 Other Physical Measurements

Infrared spectra of samples in KBr pellets were recorded on a Nicolet Magna-IR 860 spectrometer equipped with a KBr beam splitter and a DTGS detector. Raman spectra were recorded using a Kaiser Hololab 5000R Raman Spectrometer and Microprobe using an excitation wavelength of 785 nm, large fibers, 10x objective, 8 minute exposure, 1 accumulation, and 3 mW laser power. Diffuse reflectance UV-vis spectra were recorded using a Varian Cary 5E

with a Harrick Praying Mantis Accessory. An aluminum mirror was used as the 100% reflectance standard. FTIR, Raman and diffuse reflectance UV-vis spectra are presented in Appendix B.2. Thermogravimetric analysis (Section 3.3.1) measurements were performed using a Seiko Dual TG/DTA 320 Thermogravimetric/Differential Thermal Analyzer (SC). Samples were referenced and measured in aluminum pans, with N₂ as a purge gas flowing at 150 cc/min. Data were recorded at 0.2 s increments from 20 °C to 500 °C at a 5 °C/min heating rate.

3.3 Results

3.3.1 Synthetic Methodology

The initial synthesis of CdCu₃(OH)₆(NO₃)₂•*x*H₂O with *x* = 0.5 – 3 was reported by Oswald and took 15 years.⁷ A copper metal sheet in a saturated solution of aqueous cadmium nitrate was oxidized by atmospheric oxygen, which slowly diffused through a rubber stopper. Oswald also reports the synthesis of microcrystalline powders of the same material through the rapid corrosion of copper under excess oxygen in 2 *M* aqueous cadmium nitrate, or from the copper(II) precursors CuO or Cu(OH)₂ in 2 *M* aqueous cadmium nitrate. The kinetics of these last three reactions were not reported in the original paper, but the reactions presumably took several years. We initially set out to modify these last three routes hydrothermally in order to accelerate the formation of CdCu₃(OH)₆(NO₃)₂•*x*H₂O, which bears a kagomé lattice, as shown in Figure 3.2.⁹

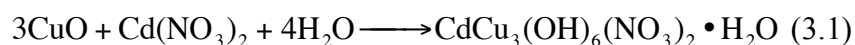
Our hydrothermal attempts to accelerate this reaction, however, were unsuccessful. The use of Cu(OH)₂ and aqueous cadmium nitrate as precursors both with and without added HNO₃ resulted in product mixtures of CuO and Cu₂(OH)₃NO₃, rouaite (PDF # 04-010-3058),^{10,11} a monoclinic dimorph of the orthorhombic mineral gerhardtite,¹²⁻¹⁵ under all hydrothermal

conditions attempted. Rouaite bears a distorted triangular lattice with Cu—Cu distances ranging from 3.045 to 3.236 Å, as shown in Figure 3.3.¹¹

Under our hydrothermal conditions, the use of CuO and aqueous cadmium nitrate as precursors both with and without added HNO₃ resulted in no apparent reaction. Use of other copper starting materials such as malachite (Cu₂(OH)₂CO₃) with aqueous cadmium nitrate both with and without added HNO₃ yielded product mixtures of CuO and rouaite. Under hydrothermal conditions at the lowest temperatures (130 °C) and pHs studied, this reaction yielded exclusively rouaite after 60 hours.

We then prepared rouaite⁸ in an attempt to use it as a synthon for hydrothermal reaction with different cadmium sources (cadmium nitrate, Cd(OH)₂) both with and without added HNO₃, which resulted in no apparent reaction under all hydrothermal conditions attempted. Attempts to precipitate CdCu₃(OH)₆(NO₃)₂•xH₂O from a basic aqueous solution of copper nitrate and cadmium nitrate at room temperature also yielded rouaite. Reaction of Cu metal with aqueous solutions of cadmium nitrate with added HNO₃ at room temperature yielded rouaite yet again. Given the timescale of the initial synthesis and the results of our reactions attempting to accelerate the formation of CdCu₃(OH)₆(NO₃)₂•xH₂O, we concluded that this compound is likely to be metastable.

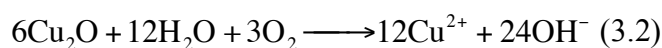
Simultaneously, we sought to replicate Oswald's syntheses of CdCu₃(OH)₆(NO₃)₂•xH₂O.⁷ The reaction of CuO with 2 M aqueous cadmium nitrate yielded blue powder that was analyzed after 588 days. It was found to contain 10% by mass CuO along with the desired product, of CdCu₃(OH)₆(NO₃)₂•xH₂O, as determined by pXRD (Figure 3.4.a). This reaction presumably proceeds according to the equation



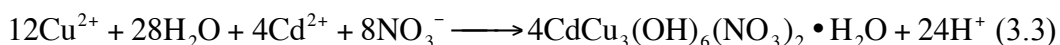
Chapter 3

Upon examination after 452 days of reaction, a sheet of Cu metal submerged in a saturated solution of aqueous cadmium nitrate also appeared to have a microscopic amount of a blue powder on its surface above some red corrosion, presumably Cu_2O . Having made this observation, we decided to attempt an oxidation of Cu_2O in a solution of aqueous cadmium nitrate, which ultimately yielded the desired product.

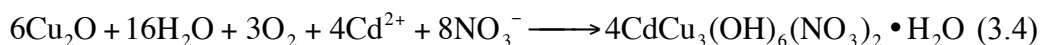
Our sample was produced by a gradual oxidation of Cu_2O over 42 weeks under an oxygen atmosphere in 4 M aqueous solution of CdNO_3 . The oxidation of Cu_2O (cuprite) presumably proceeds according to



Lattice assembly could proceed according to



and an overall reaction could be written as



Reaction 3.4 is thermodynamically favored under standard conditions, with E° of 0.481 V.

The product was characterized by pXRD and ICP-AA (H. Kolbe). Thermogravimetric analysis (TGA) of the powder sample (Figure 3.1) showed loss of 1.64% by mass (or $\sim 0.5 \text{ H}_2\text{O}$ per formula unit) starting at 47 °C and lasting to 226 °C, followed by a loss of an additional 10.08% by mass (consistent with the decomposition of the six hydroxyl groups to 3 H_2O and nonvolatile oxides) by 240 °C. The compound loses an additional 20.07% by mass by 500 °C, which is likely volatile oxides of nitrogen, to leave a residue of 69.09% of the original mass. The residue contains CuO (tenorite, PDF # 01-080-0076) and CdO (PDF # 03-065-2908, also known

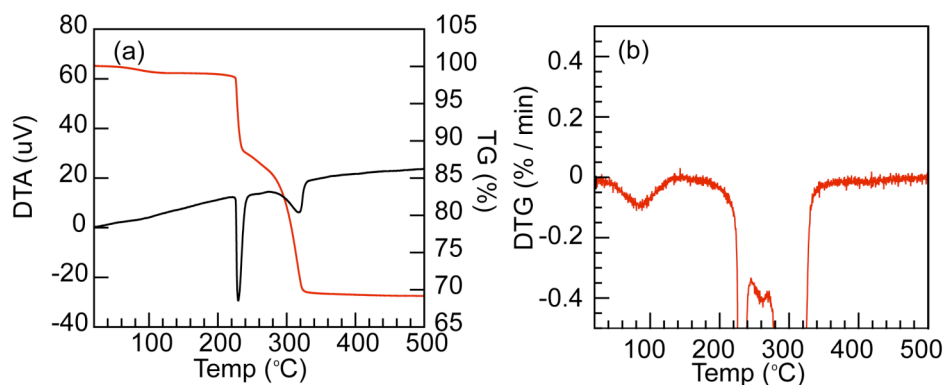


Figure 3.1. (a) Thermogravimetric and differential thermal analysis for a powder sample of $\text{CdCu}_3(\text{OH})_6(\text{NO}_3)_2 \cdot x\text{H}_2\text{O}$. (b) A differential plot shows the time profile of the loss of mass more clearly.

as monteponite, 01-073-2245) by pXRD. These results are in agreement with the data reported by Oswald.⁷

3.3.2 Structural Chemistry

The structure of $\text{CdCu}_3(\text{OH})_6(\text{NO}_3)_2 \cdot x\text{H}_2\text{O}$ was reported by Oswald⁷ and is shown in Figure 3.2, with relevant bond lengths and angles given in Table 3.1. $\text{CdCu}_3(\text{OH})_6(\text{NO}_3)_2 \cdot x\text{H}_2\text{O}$ crystallizes in $P\bar{1}$ with $P\bar{3}m1$ superstructure if disorder in the nitrate groups is taken into account. The structure comprises Jahn-Teller distorted octahedra of $\text{Cu}(\text{OH})_4(\text{NO}_3)_2$, which share edges to make up a kagomé lattice of corner-sharing $\text{Cu}_3(\mu\text{-OH})_3$ triangles. The three Cu^{2+} ions of each triangle share apical nitrate oxygen atoms, and the nitrate groups of adjacent triangles alternate above and below the decorated sheet. The pendant nitrate groups (with the exception of the apical oxygen atom) are statistically disordered over three positions at 120° to one another (Figure 3.2.c). The Cd^{2+} ion is coplanar with the Cu^{2+} ions of a given sheet and resides in the hexagonal channel of the kagomé. Cd^{2+} is in an angle-distorted octahedral environment with 6 equidistant OH^- groups and $\text{O}-\text{Cd}-\text{O}$ angles of 76.3 and 103.7° . Hydrogen bonding of adjacent kagomé planes occurs between nitrate groups and interlayer water molecules; the interlayer water, therefore, plays a crucial role in holding the structure together. Oswald reports

the most crystalline material containing up to 3 H₂O molecules, one of which was located in the crystal structure.⁷ The layers stack in AA fashion, and in this structure, the Cu(OH)₄(NO₃)₂ octahedra are at a tilt angle of 42.3° from the kagomé plane. The distance between the kagomé planes is 7.012 Å.

The structure of rouaite was initially solved in $P2_1/m$ by Nowacki and Scheidegger.¹² In later work, Effenberger was able to refine the structure anisotropically, which resulted in a lower symmetry space group ($P2_1$) and a considerable decrease in R factors.¹¹ The Effenberger structure is shown in Figure 3.3. Rouaite features two crystallographically independent Cu(II) ions. Cu(1) sits in a Jahn-Teller distorted octahedral environment, with four equatorial hydroxides at an average distance of 1.960 Å and two axial O—NO₂ groups at 2.434 Å. Cu(2) has four equatorial hydroxides at an average distance of 2.000 Å, an axial hydroxide at 2.308 Å, and an axial O—NO₂ group at 2.392 Å. Like CdCu₃(OH)₆(NO₃)₂•xH₂O, rouaite, too, bears a layered structure. In the structure of rouaite, however, the oxygen atoms of the nitrate groups show hydrogen-bonding interactions directly with the hydroxy protons in the adjacent layer, resulting in a smaller interlayer distance (d_{001}) of 6.929 Å. Rouaite bears a triangular lattice that is distorted from ideal geometry, as shown in Figure 3.3.b. The effect of this distortion on its magnetism will be discussed in Section 3.3.3.

Both our CdCu₃(OH)₆(NO₃)₂•0.5H₂O and our rouaite samples were characterized by pXRD, the results of which are shown in Figure 3.4.

Table 3.1. Structural Comparison of $\text{CdCu}_3(\text{OH})_6(\text{NO}_3)_2 \cdot x\text{H}_2\text{O}$ and rouaite

Bond	$\text{CdCu}_3(\text{OH})_6(\text{NO}_3)_2 \cdot x\text{H}_2\text{O}$	rouaite
		Bond distances (Å)
Cu—O _H	2.036	1.919 Cu(1)—O(1) x 2 1.994 Cu(1)—O(2) 2.007 Cu(1)—O(3) 2.047 Cu(2)—O(2) x 2 1.953 Cu(2)—O(3) x 2 2.308 Cu(2)—O(1)
Cu—O _{NO2}	2.424	2.434 Cu(1)—O(4) 2.392 Cu(2)—O(4)
Cd—O	2.263	N/A
M—M	3.261 Cu—Cu 3.261 Cd—Cu	3.045 Cu(1)—Cu(1) 3.046 Cu(2)—Cu(2) 3.154 Cu(1A)—Cu(2A)/Cu(1A)—Cu(2A) 3.236 Cu(1A)—Cu(2B)/Cu(2A)—Cu(1B) 3.236 Cu(1C)—Cu(2A) 3.134 Cu(1C)—Cu(2B)
		Bond angles (°)
Cu—O _H —Cu	106.4	104.2 Cu(1)—O(1)—Cu(1) 110.4 Cu(1B)—O(2AZ)—Cu(2A) 110.4 Cu(1A)—O(2W)—Cu(2B) 99.4 Cu(2)—O(2)—Cu(2) 99.9 Cu(2)—O(3)—Cu(2) 104.6 Cu(1C)—O(3Z)—Cu(2B) 106.7 Cu(1C)—O(3Z)—Cu(2A) 102.6 Cu(1D)—O(2BM)—Cu(2B) 102.6 Cu(1A)—O(2W)—Cu(2A)

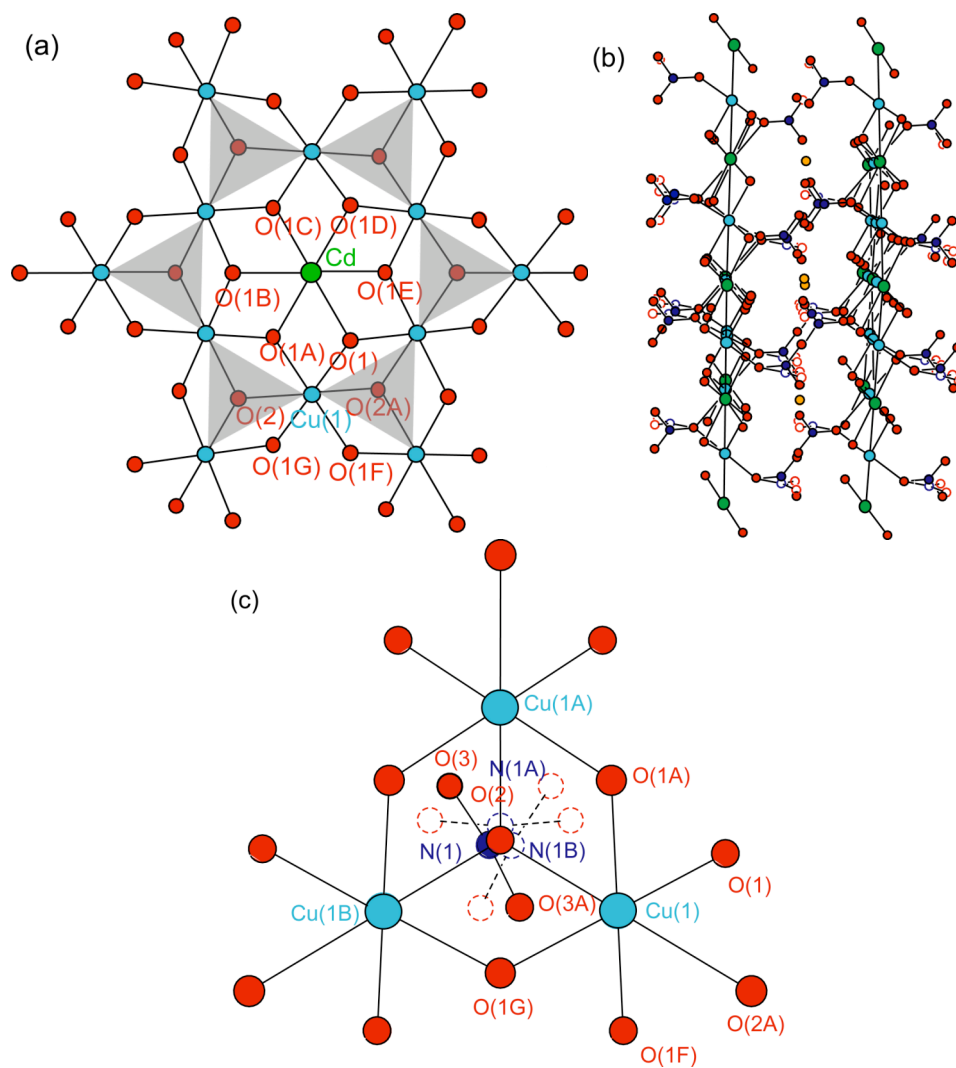


Figure 3.2. (a) The kagomé layer of $\text{CdCu}_3(\text{OH})_6(\text{NO}_3)_2 \cdot x\text{H}_2\text{O}$. H atoms and NO_2 (from $\text{O}-\text{NO}_2^-$ groups) have been omitted. (b) View of the structure down the (100) axis in $P\bar{3}m1$: d_{001} 7.012 Å. H-bonding occurs between the nitrate groups and the protons of OW, the crystallographically located water molecule, to hold the layers together. (c) The basic magnetostructural unit of the kagomé is the triangle. 120° disorder of the nitrate group is shown. Selected bond distances and angles: $\text{Cu}(1)-\text{O}(2)-\text{Cu}(1\text{A})$, 84.5° ; $\text{Cu}(1)-\text{O}(2)-\text{N}(1)$, 133.4° ; $\text{Cu}(1)-\text{O}(2)-\text{N}(1\text{A})/\text{N}(1\text{B})$, 119.7° . Cu atoms are in teal, N in blue, Cd in green, O in red, with the exception of OW, in orange. From Ref. [7].

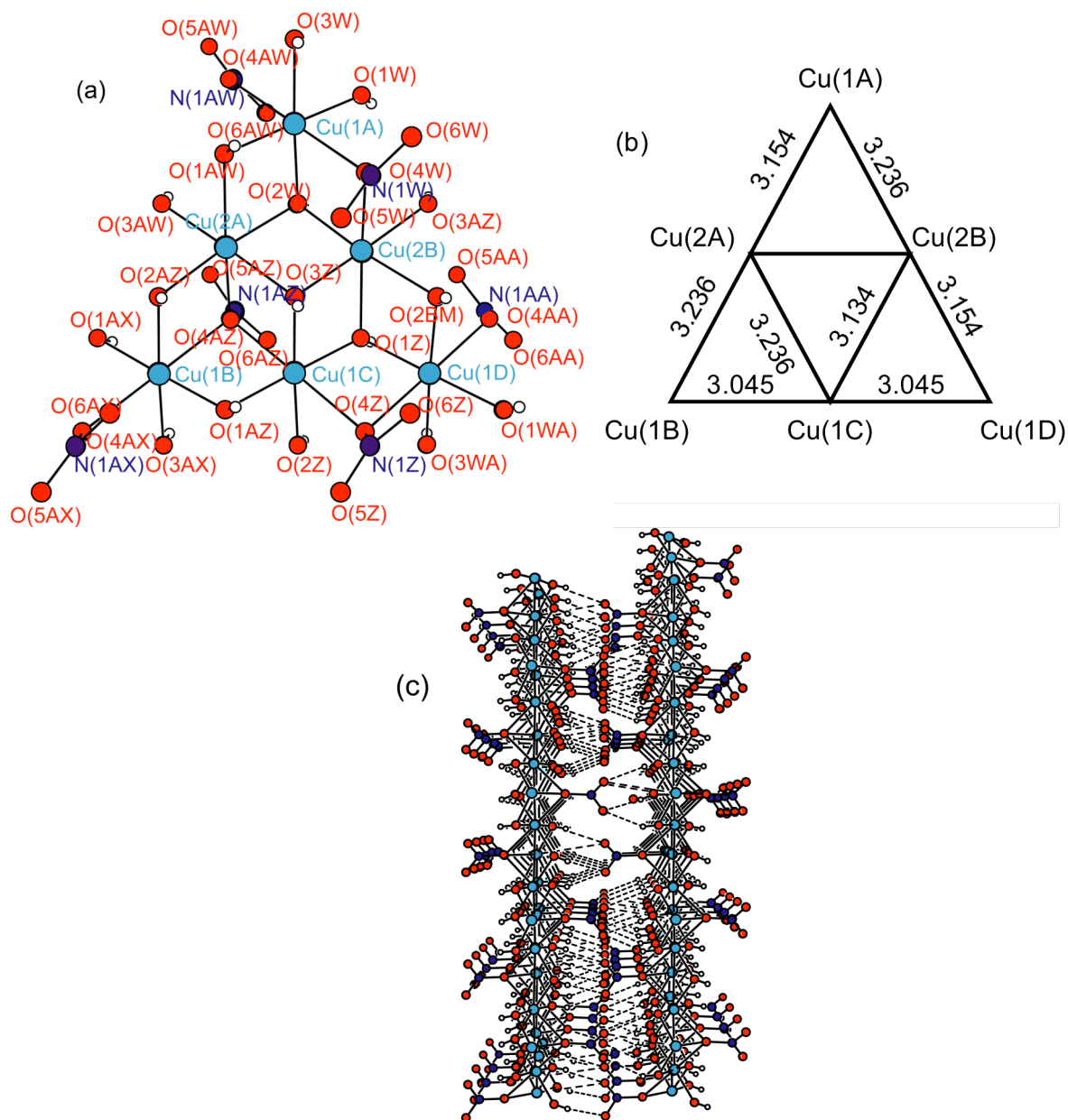


Figure 3.3. (a) A portion of the crystal structure of rouaite in $P2_1$, as viewed down the (001) axis. Tables 3.1 and A.2.1 provide selected interatomic distances and angles, as reported by Effenberger. (b) Schematic of interatomic distances (Å) showing the irregular geometry of the rouaite triangles. (c) The packing of rouaite showing interlayer hydrogen bonding, as viewed down the (100) axis. Cu atoms are shown in teal, N atoms in blue, O atoms in red, and H atoms in white. From Ref. [11].

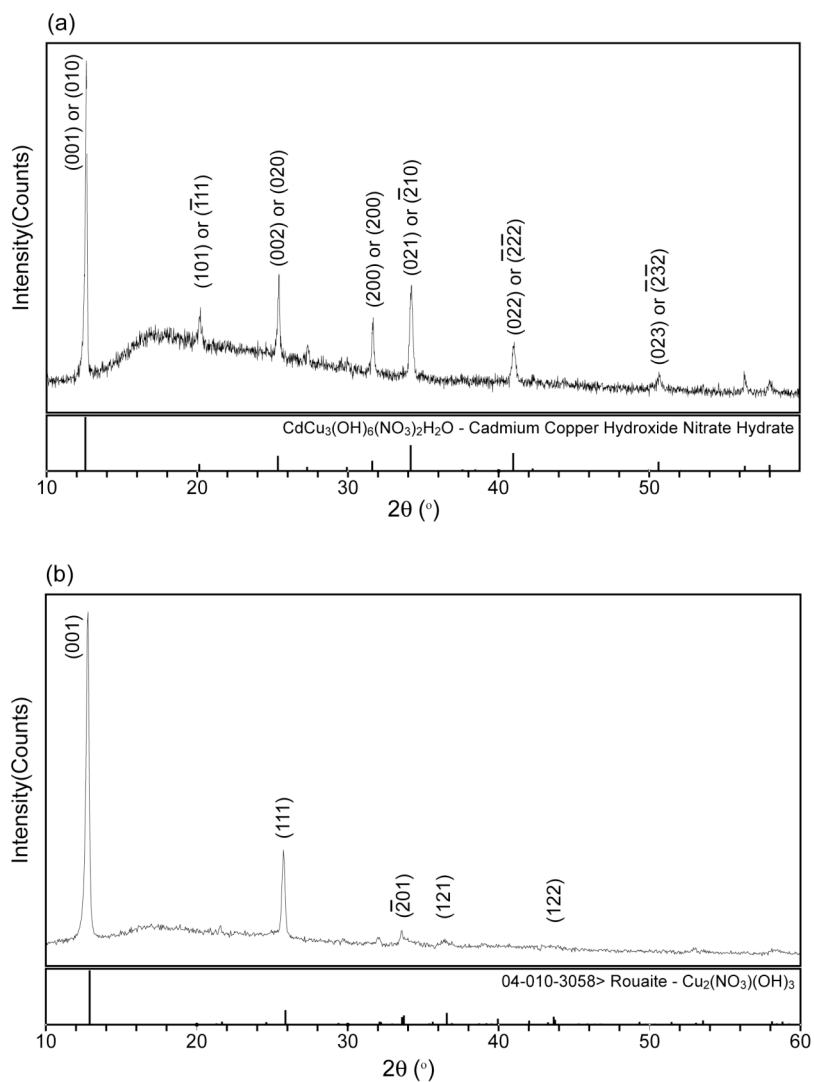


Figure 3.4. (a) pXRD of $\text{CdCu}_3(\text{OH})_6(\text{NO}_3)_2 \cdot 0.5\text{H}_2\text{O}$ as synthesized, matching patterns 01-072-1433 ($P\bar{3}m1$ structure) and 01-070-1904 ($P\bar{1}$ structure) in Jade 8. Miller indices are labeled for both space groups. (b) pXRD of rouaite, $\text{Cu}_2(\text{OH})_3\text{NO}_3$ in $P2_1$, matched to pattern 04-010-3058 in Jade 8. Miller indices are labeled.

3.3 Magnetic Properties of Rouaite

The magnetic properties of rouaite have also been studied by other groups,¹⁶⁻¹⁸ and our data are in agreement with those reported.^{17,18} Rouaite shows Néel ordering behavior at 11 K, as evidenced by a critical point in the susceptibility at that temperature and a continually decreasing value for χT as temperature is lowered (Figure 3.5.a). Curie-Weiss analysis (Figure 3.5.b) of χ^{-1} from 150 – 350 K yields $\Theta = -12$ K. With $f = |\Theta| / T_c = 1.1$, rouaite does not bear the hallmark of spin frustration.¹⁹

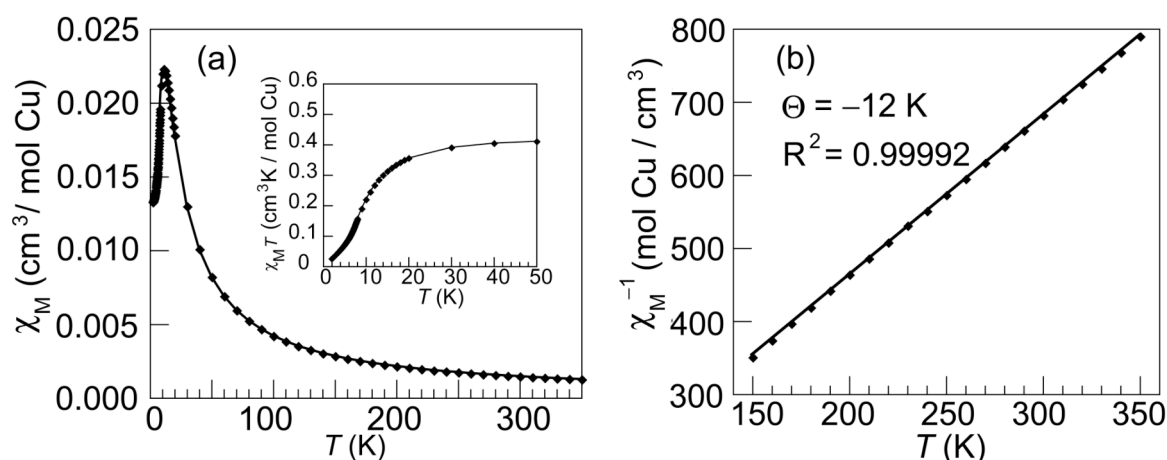


Figure 3.5. (a) Magnetic susceptibility versus temperature for a ground powder sample of rouaite. Magnetic susceptibility times temperature versus temperature is shown in inset. (b) Curie-Weiss fit for a ground powder sample of rouaite.

3.3.4 Magnetic Properties of $\text{CdCu}_3(\text{OH})_6(\text{NO}_3)_2 \cdot 0.5\text{H}_2\text{O}$

The DC susceptibility plot of $\text{CdCu}_3(\text{OH})_6(\text{NO}_3)_2 \cdot 0.5\text{H}_2\text{O}$, shown in Figure 3.6, exhibits an ordering transition at 5 K. Analysis of χT (Figure 3.6.a inset) reveals that, as the temperature is decreased from 300 K, χT also decreases, indicating that the dominant magnetic interactions are antiferromagnetic in nature. Between 5 K and 2.9 K, with χT increasing, the dominant magnetic interactions in this system are ferromagnetic. Antiferromagnetic exchange again dominates below 2.9 K. Magnetization versus field shows no measurable hysteresis at 2 K

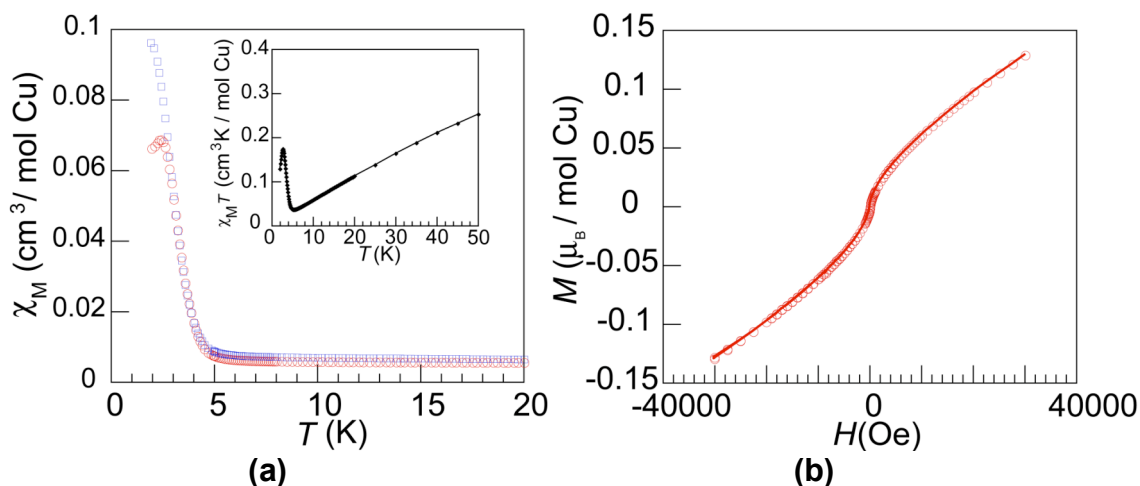


Figure 3.6. (a) ZFC (\circ) and FC (\square) susceptibility of $\text{CdCu}_3(\text{OH})_6(\text{NO}_3)_2 \cdot 0.5\text{H}_2\text{O}$, measured with 100 Oe field. For FC, $H_c = 100$ Oe. Susceptibility times temperature (\blacklozenge) versus temperature is shown as an inset. (b) Magnetization (\circ) versus field of $\text{CdCu}_3(\text{OH})_6(\text{NO}_3)_2 \cdot 0.5\text{H}_2\text{O}$ shows no measurable hysteresis at 2 K.

(Figure 3.6.b), consistent with antiferromagnetic interactions dominating below 2.9 K. Curie-Weiss analysis of χ^{-1} was performed over four different temperature ranges: 50 – 300 K, 100 – 300 K, 150 – 300 K, and 200 – 300 K. (300 K was the maximum temperature studied to avoid the potential loss of water above 325 K.) The R^2 values obtained for fitting a Weiss constant over 50 – 300 K only differ in the fifth decimal place from those obtained from fitting over 200 – 300 K, which statistically justifies the inclusion of the broader range. The measurement presented was taken on four separate occasions and fit over each of the four ranges. One such measurement is shown in Figure 3.7. The range of values obtained in this manner is $\Theta = -114 \pm 27$ K, revealing strong antiferromagnetic mean nearest-neighbor exchange. $\text{CdCu}_3(\text{OH})_6(\text{NO}_3)_2 \cdot 0.5\text{H}_2\text{O}$ is therefore a frustrated system, with $f = |\Theta| / T_c = |-114 \text{ K}| / 5 \text{ K} = 22.8$. The AC susceptibility data (Figure 3.8) shows no frequency-dependent temperature shift in its maximum, precluding spin-glass behavior to the low-temperature limit of the SQUID. Heat capacity measurements are currently underway.

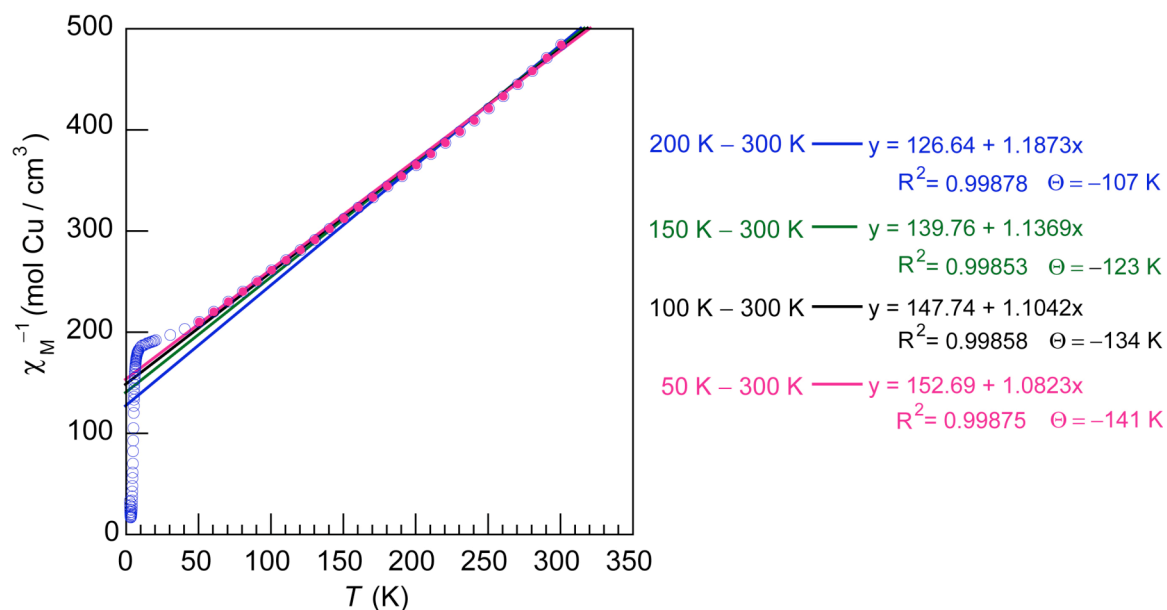


Figure 3.7. Temperature dependence of χ_M^{-1} for CdCu₃(OH)₆(NO₃)₂·0.5H₂O. The error range for Θ was obtained by fitting over different temperature ranges from $50 \leq T \leq 300$ K.

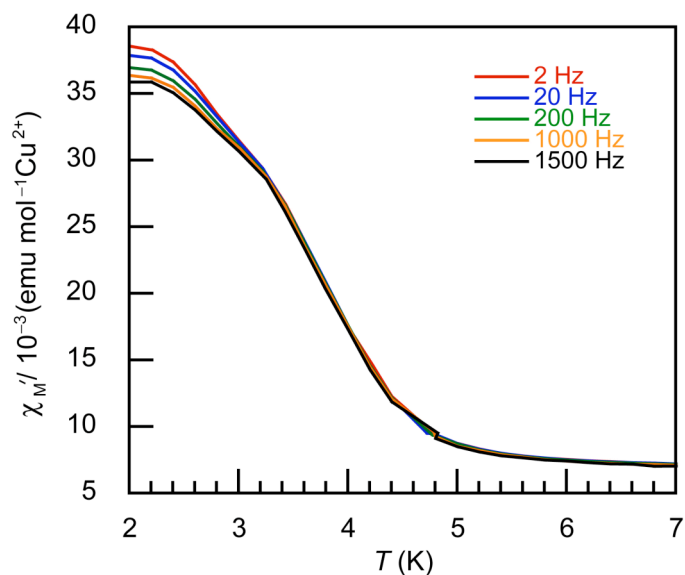


Figure 3.8. Frequency independence in the AC susceptibility of CdCu₃(OH)₆(NO₃)₂·0.5H₂O.

3.4 Discussion

The magnetic properties of rouaite, with Cu—Cu distances that deviate from one another by no more than 6% (Figure 3.3.b), show the profound effect of irregular geometry in alleviating frustration on a triangular lattice. Recall Section 1.4, where we discussed how Jahn-Teller distortions limit the use of triangular molecules for studying geometric spin frustration because they bring about unequal exchange pathways. Such unequal exchange pathways can lead to a {2 (antiferromagnetically coupled) + 1 (uncoupled)} ground state in these systems.²⁰⁻³⁶ Ruiz *et al.* did a careful density functional study of rouaite, accounting for six unequal in-plane Cu—O_H—Cu exchange pathways due to the compound's irregular triangular geometry.¹⁸ Such inequalities provide mechanisms for long-range ordering, thereby inhibiting frustration.

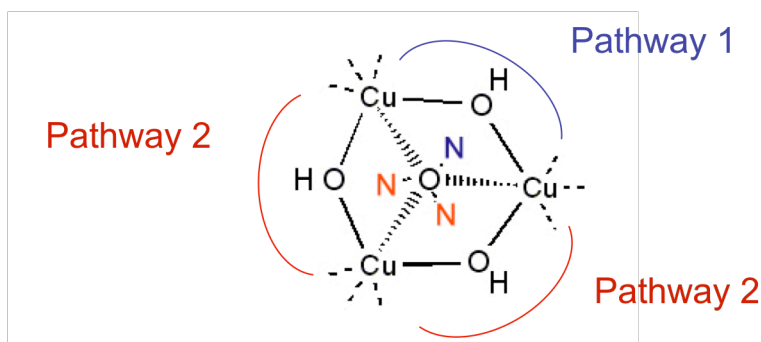
Out-of-plane interactions in rouaite are also possible due to hydrogen bonding between hydroxide protons and nitrate groups on adjacent layers separated by distances of 2.2 to 2.3 Å, though such interactions should be weak, both because the participating nitrate groups are bonded to d_{z^2} orbitals with little unpaired spin density and because the interlayer distance approaches 7 Å. Nonetheless, several groups have reported anion exchange of nitrate groups to produce layer-expanded analogs of rouaite with both aliphatic³⁷⁻³⁹ and aromatic⁴⁰ carboxylates; some groups argue that these compounds show evidence of enhanced frustration, glassiness, and canted antiferromagnetism.³⁷⁻³⁹ It should be noted that, by and large, these compounds maintain the irregular triangular intralayer geometry of rouaite with multiple in-plane exchange pathways (and should show similar antiferromagnetic ordering behavior to the extent that interlayer coupling is negligible). The enhanced frustration observed, therefore, is not likely to be the result

of increased geometric frustration and might come about due to structural disorder introduced by the anion exchange reaction, consistent with glassing behavior.

$\text{CdCu}_3(\text{OH})_6(\text{NO}_3)_2 \cdot 0.5\text{H}_2\text{O}$ has a regular geometry of equilateral triangles and, in contrast to the situation in rouaite, its magnetic behavior shows evidence of strong geometric frustration. With $\Theta = -114 \pm 27$ K, $\text{CdCu}_3(\text{OH})_6(\text{NO}_3)_2 \cdot 0.5\text{H}_2\text{O}$ shows strong nearest-neighbor antiferromagnetic exchange within the kagomé planes, which arises from the strong σ -symmetry pathway $\text{Cu}(d_{x^2-y^2})-\text{O}_\text{H}(sp^3)-\text{Cu}(d_{x^2-y^2})$. The bridging angle, 106.4° , falls within the expected range for antiferromagnetic coupling, as predicted by Goodenough-Kanamori rules^{1-3,5} and the magnetostructural analysis of Crawford et al., which predicts antiferromagnetic superexchange for μ -hydroxo-bridged Cu(II) centers with bridge angles larger than a critical angle of 97.54° .⁴ A mean-field theory analysis of the Curie-Weiss Law (Equation 1.3), assuming z , the number of nearest neighbors per Cu(II) center, is 4, yields $J = -79 \pm 19 \text{ cm}^{-1}$ based on $\Theta = -114 \pm 27$ K.

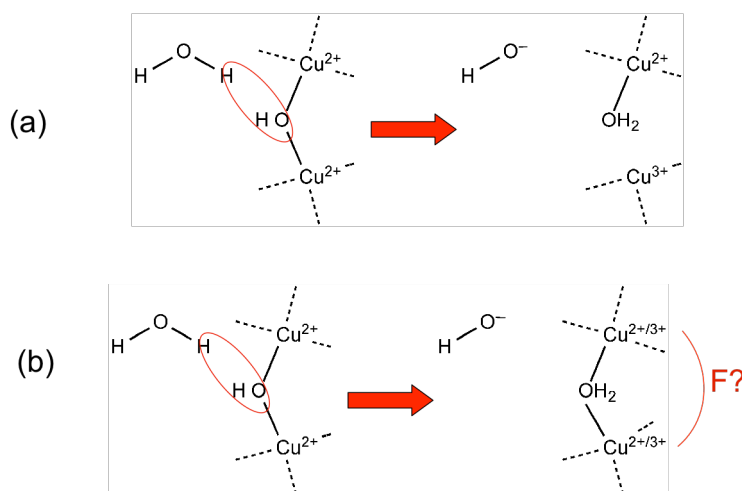
Turning our attention now to the low temperature behavior of $\text{CdCu}_3(\text{OH})_6(\text{NO}_3)_2 \cdot 0.5\text{H}_2\text{O}$, one can imagine a number of possible scenarios that might account for magnetic ordering in this system. We will now discuss three possible scenarios in $\text{CdCu}_3(\text{OH})_6(\text{NO}_3)_2 \cdot 0.5\text{H}_2\text{O}$ and the magnetic behavior expected if each were the dominant effect at low temperature. We will compare these predicted behaviors to the observed behavior of the system below 5 K.

One possible scenario that might cause magnetic ordering in this system is nitrate disorder (Scheme 3.2). Recall from Section 3.3.2 that the nitrate groups are disordered over three positions at 120° relative to one another. This disorder would allow for a very subtle electronic difference in exchange pathways between Cu(II) centers. However, any effect on superexchange is expected



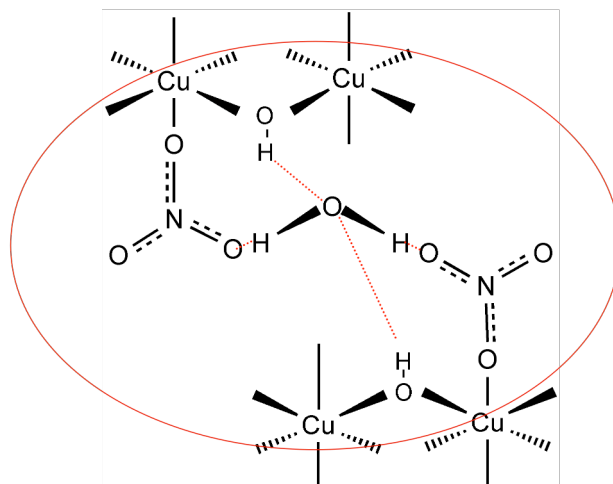
Scheme 3.2. Structural disorder in the nitrate group might allow for subtle changes in the local electronic environment, altering one exchange pathway as opposed to the others.

to be minimal for two reasons: 1) the displacement of the nitrate group is small because the apical oxygen remains in the same place (according to Oswald's structure),⁷ thus giving rise to the same Cu–O–Cu bridge angle regardless of the disorder; and 2) the magnetic orbital of Cu(II) involved in this interaction is the d_{z^2} orbital, which should have little unpaired spin density in the first place. At best, this interaction might lead to spin glassing or favor a particular antiferromagnetically ordered state. We do not observe glassing in our system to 2 K, and this interaction, moreover, does not explain the ferromagnetism that we observe below 5 K.



Scheme 3.3. Protonation of a μ -hydroxy bridge may either (a) disrupt superexchange by forming a terminal aqua species or (b) introduce disparate (and possibly ferromagnetic) superexchange pathways into the lattice.

A second possible scenario exists in protonation of the intralayer hydroxide bridge by the interlayer water molecule, as in Scheme 3.3. The crystallographically located OW atom is within 3.283 Å of the bridging hydroxyl oxygen. Because O–H bond distances typically range from 0.8 – 1 Å, an O•••H distance here of ~ 2.2 Å means that proton transfer is possible in this system. The water could become a proton donor and the bridging hydroxyl group a proton acceptor. Recall the discussion in Section 1.6.2.1 of the disordered magnetic behavior in hydronium jarosite, wherein the O•••O distance between the interlayer hydronium ion and bridging hydroxyl moiety is roughly 2.8 Å. Spin glass behavior in this compound may be attributed to such proton transfers between the interlayer hydronium ions and the intralayer hydroxide bridges, which change certain in-kagomé-plane exchange pathways relative to others.⁴¹ The protonation reaction in the jarosite system is favored because of the large pK_a difference between the interlayer hydronium ions and the hydroxide bridges. (A similar protonation reaction in the Cd system would be driven by the pK_a difference between the interlayer water molecule and the μ -hydroxy group.) In Fe^{3+} systems, successive protonations of oxo-bridged compounds have been shown to increase bond lengths and to decrease the strength of antiferromagnetic exchange in the order oxo > hydroxo > aqua.⁴²⁻⁴⁴ Density functional studies of protonation in μ -hydroxy-bridged Cu(II) systems indicate subtle differences in geometry may have a significant impact: in addition to the dependence on the bridge angle originally described in μ -hydroxy systems by Hatfield and Hodgson,⁴ the nature of hydrogen bonding⁴⁵ to counterions present may play a role.⁴⁶ Protonation, then, to the extent that it contributes to the magnetism of this system, might induce glassing or ordering behavior, depending on the strength and nature of the magnetic interactions it causes (Scheme 3.3).



Scheme 3.4. Interlayer hydrogen bonding can lead to magnetic exchange between the layers.

A third possible scenario, and an interesting explanation of the data, consists of hydrogen bonding effecting magnetic superexchange between the layers. Our data shows antiferromagnetic superexchange predominating at high T , with ferromagnetic interactions developing below 5 K. This behavior is consistent with a 120° ground state and canted antiferromagnetism, perhaps due to a Dzyaloshinsky-Moriya interaction. Indeed this system, too, lacks an inversion center between Cu(II) ions, making such an interaction possible. Below 2.9 K, antiferromagnetic interactions again dominate, which perhaps indicates the antiferromagnetic stacking of layers with a net ferromagnetism due to canting (a Néel ordering as is the case in the alkali iron jarosites). How can the layers communicate antiferromagnetic stacking? There are previous known examples of hydrogen bonding mediating magnetic exchange.⁴⁷ As shown in Scheme 3.4, there are various hydrogen-bonding interactions that can occur in the system. The sp^3 orbital of the μ -hydroxy can interact with both the $d_{x^2-y^2}$ orbitals of the Cu^{2+} centers and the sp^3 orbitals of an interlayer water molecule. This interlayer water molecule can mediate superexchange with the orbitals of the same symmetry in the adjacent kagomé plane, in a super-superexchange interaction. In this manner, magnetic exchange can be conveyed by hydrogen bonding across an interlayer distance of

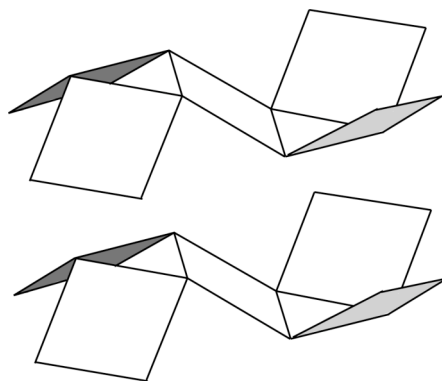


Figure 3.9. Stacking of adjacent layers in $\text{CdCu}_3(\text{OH})_6(\text{NO}_3)_2 \cdot x\text{H}_2\text{O}$. $\text{Cu}(\text{OH})_4$ planes are represented by squares.

7.012 Å, as shown in Scheme 3.4. Hydrogen bonding also occurs through water molecules between the nitrate groups on adjacent layers and may mediate weak magnetic exchange through a pathway involving d_{z^2} ; spins in d_{z^2} , however, are paired and this effect is expected to be weak. The corrugated layers pack AA and stack all in the same direction (Figure 3.9), which might be of relevance to additive effects between Dzyaloshinsky-Moriya vectors on adjacent layers.

In order to assess the effects of interlayer hydrogen bonding (Scheme 3.4) on the magnetism of $\text{CdCu}_3(\text{OH})_6(\text{NO}_3)_2 \cdot 0.5\text{H}_2\text{O}$, we attempted anion exchange reactions to expand the interlayer distance and possibly attenuate hydrogen bonding effects. We modeled the conditions of these reactions after those reported by Newman for rouaite:⁴⁰ room temperature reaction of aqueous 1 M sodium acetate, benzoate or 0.5 M sodium terephthalate with powder samples. A color change of the powder from pale blue to dark gray was noted in the reaction of $\text{CdCu}_3(\text{OH})_6(\text{NO}_3)_2 \cdot 0.5\text{H}_2\text{O}$ with sodium acetate after 24 hours; however, pXRD showed only starting material. (Presumably the product powder was a biphasic mixture containing black CuO , as impurity phases of up to 5% by mass can go undetected pXRD.) The other reactions showed decomposition products, indicating that the structural integrity of the lattice was not maintained. After 2 weeks reaction of $\text{CdCu}_3(\text{OH})_6(\text{NO}_3)_2 \cdot 0.5\text{H}_2\text{O}$ with sodium benzoate, the product

mixture contained $\text{CdCu}_3(\text{OH})_6(\text{NO}_3)_2 \cdot 0.5\text{H}_2\text{O}$ and $\text{Cd}(\text{OH})_2$ by pXRD. Reacting $\text{CdCu}_3(\text{OH})_6(\text{NO}_3)_2 \cdot 0.5\text{H}_2\text{O}$ for 2 weeks with sodium terephthalate yielded a cadmium hydroxynitrate, $\text{Cd}_5(\text{OH})_8(\text{NO}_3)_2 \cdot 2\text{H}_2\text{O}$, as the only identifiable phase in the product mixture by pXRD. (The powder product was pale blue and presumably some Cu-containing species were also present, though they could not be identified.) Finally, from other layer expansion attempts, we note that exposure of $\text{CdCu}_3(\text{OH})_6(\text{NO}_3)_2 \cdot 0.5\text{H}_2\text{O}$ to amine bases produces CuO and/or soluble aminocopper(II) species.

3.5 Conclusions

The hydrogen-bonded layered $S = \frac{1}{2}$ kagomé system, $\text{CdCu}_3(\text{OH})_6(\text{NO}_3)_2 \cdot 0.5\text{H}_2\text{O}$, features in-plane μ -hydroxy bridges and shows strong nearest-neighbor antiferromagnetic exchange within the kagomé planes, as evidenced by $\Theta = -114 \pm 27$ K. This coupling arises from the strong σ -symmetry pathway $\text{Cu}(d_{x^2-y^2})-\text{O}_\text{H}(sp^3)-\text{Cu}(d_{x^2-y^2})$. The increased frustration in this system relative to Cu(1,3-bdc) from Chapter 2 reflects further optimization of exchange geometry in our studies of frustration. We now seek to minimize two possible ordering mechanisms of this system: magnetic disorder and out-of-plane exchange through hydrogen bonding. To further optimize our studies of frustration in our quest to observe quantum disordered states on an $S = \frac{1}{2}$ kagomé, we targeted systems where both magnetic disorder and interlayer exchange would be less prevalent than in the $\text{CdCu}_3(\text{OH})_6(\text{NO}_3)_2 \cdot 0.5\text{H}_2\text{O}$ material presented in this Chapter. We sought to maintain strong antiferromagnetic superexchange by keeping μ -hydroxy bridges as a structural motif, but wanted to move from this hydrogen-bonded system to electrostatically linked systems that could better magnetically isolate the layers. These results are presented in Chapters 4 and 5.

3.6 References

1. Goodenough, J. B. *Phys. Chem. Sol.* **1958**, *6*, 287-297.
2. Kanamori, J. *Phys. Chem. Sol.* **1959**, *10*, 87-98.
3. Ginsberg, A. P. *Inorg. Chim. Acta, Rev.* **1971**, *5*, 45-68.
4. Crawford, V. H.; Richardson, H. W.; Wasson, J. R.; Hodgson, D. J.; Hatfield, W. E. *Inorg. Chem.* **1976**, *15*, 2107-2110.
5. Kahn, O. *Molecular Magnetism*; VCH: New York, 1993, pp. 190-191.
6. Coffman, R. E.; Buettner, G. R. *J. Phys. Chem.* **1979**, *83*, 2387-2392.
7. Oswald, H. R. *Helv. Chim. Acta* **1969**, *52*, 2369-2380.
8. Tanaka, H.; Terada, S. *J. Therm. Anal.* **1993**, *39*, 1011-1018.
9. Eby, R. K.; Hawthorne, F. C. *Acta Crystallogr. B.* **1993**, *B49*, 28-56.
10. Jambor, J. L.; Roberts, A. C. *Am. Mineral.* **2002**, *87*, 996-999.
11. Effenberger, H. *Z. Kristallogr.* **1983**, *165*, 127-135.
12. Nowacki, W.; Scheidegger, R. *Helv. Chim. Acta* **1952**, *35*, 375-390.
13. Kohler, K. *Z. Kristallogr. Krist.* **1955**, *106*, 474-475.
14. Oswald, H. R. *Z. Kristallogr. Krist.* **1961**, *116*, 210-219.
15. Bovio, B.; Locchi, S. *J. Crystallogr. Spectrosc. Res.* **1982**, *12*, 507-517.
16. Pillet, S.; Souhassou, M.; Lecomte, C.; Rabu, P.; Drillon, M.; Massobrio, C. *Phys. Rev. B* **2006**, *73*.
17. Linder, G. G.; Atanasov, M.; Pebler, J. *J. Solid State Chem.* **1995**, *116*, 1-7.
18. Ruiz, E.; Llunell, M.; Cano, J.; Rabu, P.; Drillon, M.; Massobrio, C. *J. Phys. Chem. B* **2006**, *110*, 115-118.
19. Ramirez, A. P. *Annu. Rev. Mater. Sci.* **1994**, *24*, 453-480.
20. Beckett, R.; Colton, R.; Hoskins, B. F.; Martin, R. L.; Vince, D. G. *Aust. J. Chem.* **1969**, *22*, 2527-2533.
21. Butcher, R. J.; O'Connor, C. J.; Sinn, E. *Inorg. Chem.* **1981**, *20*, 537-545.

Chapter 3

22. Kwiatkowski, M.; Kwiatkowski, E.; Olechnowicz, A.; Ho, D. M.; Deutsch, E. *Inorg. Chim. Acta* **1988**, *150*, 65-73.
23. Chaudhuri, P.; Karpenstein, I.; Winter, M.; Butzlaff, C.; Bill, E.; Trautwein, A. X.; Floerke, U.; Haupt, H. J. *J. Chem. Soc., Chem. Commun.* **1992**, 321-322.
24. Colacio, E.; Dominguez-Vera, J. M.; Escuer, A.; Klinga, M.; Kivekas, R.; Romerosa, A. *J. Chem. Soc., Dalton Trans.* **1995**, 343-348.
25. Padilla, J.; Gatteschi, D.; Chaudhuri, P. *Inorg. Chim. Acta* **1997**, *260*, 217-220.
26. Ferrer, S.; Haasnoot, J. G.; Reedijk, J.; Muller, E.; Cingi, M. B.; Lanfranchi, M.; Lanfredi, A. M.; Ribas, J. *Inorg. Chem.* **2000**, *39*, 1859-1867.
27. Clerac, R.; Cotton, F. A.; Dunbar, K. R.; Hillard, E. A.; Petrukhina, M. A.; Smucker, B. W. *C.R. Acad. Sci., Ser. IIC: Chim.* **2001**, *4*, 315-319.
28. Ferrer, S.; Lloret, F.; Bertomeu, I.; Alzuet, G.; Borrás, J.; Garcia-Granda, S.; Liu-Gonzalez, M.; Haasnoot, J. G. *Inorg. Chem.* **2002**, *41*, 5821-5830.
29. Cage, B.; Cotton, F. A.; Dalal, N. S.; Hillard, E. A.; Rakvin, B.; Ramsey, C. M. *J. Am. Chem. Soc.* **2003**, *125*, 5270-5271.
30. Liu, X.; de Miranda Marcelo, P.; McInnes Eric, J. L.; Kilner Colin, A.; Halcrow Malcolm, A. *Dalton Trans.* **2004**, 59-64.
31. Yoon, J.; Mirica, L. M.; Stack, T. D. P.; Solomon, E. I. *J. Am. Chem. Soc.* **2004**, *126*, 12586-12595.
32. Yoon, J.; Solomon, E. I. *Inorg. Chem.* **2005**, *44*, 8076-8086.
33. Stamataatos, T. C.; Vlahopoulou, J. C.; Sanakis, Y.; Raptopoulou, C. P.; Psycharis, V.; Boudalis, A. K.; Perlepes, S. P. *Inorg. Chem. Commun.* **2006**, *9*, 814-818.
34. Stone, M. B.; Fernandez-Alonso, F.; Adroja, D. T.; Dalal, N. S.; Villagran, D.; Cotton, F. A.; Nagler, S. E. *Phys. Rev. B* **2007**, *75*, 214427/214421-214427/214428.
35. Belinsky, M. I. *Inorg. Chem.* **2008**, *47*, 3521-3531.
36. Belinsky, M. I. *Inorg. Chem.* **2008**, *47*, 3532-3539.
37. Girtu, M. A.; Wynn, C. M.; Fujita, W.; Awaga, K.; Epstein, A. J. *J. Appl. Phys.* **1998**, *83*, 7378-7380.
38. Girtu, M. A.; Wynn, C. M.; Fujita, W.; Awaga, K.; Epstein, A. J. *Phys. Rev. B* **1998**, *57*, R11058-R11061.
39. Girtu, M. A.; Wynn, C. M.; Fujita, W.; Awaga, K.; Epstein, A. J. *Phys. Rev. B* **2000**, *61*, 4117-4130.

Chapter 3

40. Newman, S. P.; Jones, W. *J. Solid State Chem.* **1999**, *148*, 26-40.
41. Grohol, D.; Nocera, D. G. *Chem. Mater.* **2007**, *19*, 3061-3066.
42. Kurtz, D. M., Jr. *Chem. Rev.* **1990**, *90*, 585-606.
43. Armstrong, W. H.; Lippard, S. J. *J. Am. Chem. Soc.* **1984**, *106*, 4632-4633.
44. Chen, Z.; Xu, Z.; Zhang, L.; Yan, F.; Lin, Z. *J. Phys. Chem. A* **2001**, *105*, 9710-9716.
45. Ruiz, E.; Alemany, P.; Alvarez, S.; Cano, J. *J. Am. Chem. Soc.* **1997**, *119*.
46. Rodriguez-Forteza, A.; Ruiz, E.; Alvarez, S.; Alemany, P. *Dalton Trans.* **2005**, 2624-2629.
47. Papoutsakis, D.; Kirby, J. P.; Jackson, J. E.; Nocera, D. G. *Chem. Eur. J.* **1999**, *5*, 1474-1480.

Chapter 4.
Synthesis, Structure, and Chemical Characterization of Copper(II) Hydroxychloride Minerals

Portions of this work have been published as Shores, M. P.; Nytko, E. A.; Bartlett, B. M.; Nocera, D. G. *J. Am. Chem. Soc.* **2005**, *127*, 13462-13463.

4.1 Introduction

Chapter 2 presented the first structurally perfect metal-organic framework (MOF) kagomé bearing $S = \frac{1}{2}$ on lattice vertices. This system contains copper(II) centers bridged by monodentate μ -carboxylates, and although it has the shortest known metal-metal distance of any MOF kagomé, it suffers from the structural shortcoming that this distance (4.553 Å) is still quite long. Chapter 3 presented a layered copper(II) kagomé system with μ -hydroxy bridges, $\text{CdCu}_3(\text{OH})_6(\text{NO}_3)_2 \cdot 0.5\text{H}_2\text{O}$, which has shorter distances between metal centers but suffers from structural disorder brought about by interlayer water molecules. We now turn our attention to the syntheses, structures, and chemical characterization of some rare naturally occurring μ -hydroxy bridged copper(II) minerals bearing the kagomé lattice motif: claringbullite, clinoatacamite, Zn-paratacamite, and herbertsmithite. These compounds have short metal-metal distances and minimal structural disorder.

The discovery of the mineral claringbullite was first reported in 1977 by Fejer *et al.*, who also indexed its powder diffraction pattern.¹ The mineral, named for Sir Frank Claringbull of the British Museum of Natural History, is known to occur in deposits in mines in Zambia, Zaire, and Arizona. The first naturally occurring samples were analyzed by electron microprobe analysis (EMPA). From this analysis and a measured density of 3.9 g/cm³, the ideal formula was identified as $\text{Cu}_4\text{Cl}(\text{OH})_7 \cdot \frac{1}{2}\text{H}_2\text{O}$. A number of possible hexagonal space groups were proposed based on systematic absences in the powder diffraction data. The single-crystal structure of a specimen from Arizona was later reported by Burns *et al.*² Claringbullite crystallizes in the hexagonal space group $P6_3/mmc$. Burns *et al.* formulated the compound as $\text{Cu}\{\text{Cu}_3(\text{OH})_6\}\text{Cl}[\text{Cl}_{0.29}(\text{OH})_{0.71}]$. In claringbullite, $\text{Cu}_3(\text{OH})_6$ comprises ideal kagomé layers based on perfect equilateral triangles.³ A Cu^{2+} ion resides between the kagomé layers in a

distorted trigonal prismatic environment. The structure of synthetic samples of claringbullite will be discussed at length in Section 4.3.2.1.

The atacamite family of minerals consists of orthorhombic (atacamite) and monoclinic (botallackite, clinoatacamite) polymorphs of $\text{Cu}_2(\text{OH})_3\text{Cl}$ and the rhombohedral paratacamite minerals, $\text{MCu}_3(\text{OH})_6\text{Cl}_2$ ($\text{M} = \text{Co}, \text{Ni}, \text{or Zn}$, in solid solution with Cu).⁴⁻²⁰ These materials have interesting magnetic properties: clinoatacamite and the paratacamite minerals contain slightly distorted and ideal kagomé layers, respectively. Naturally occurring samples of clinoatacamite have been found in Chile, Iran, U.S.A., and the U.K.¹⁹ Clinoatacamite, so named for its monoclinic symmetry, contains (1 0 1) planes of nearly isosceles triangles of $\text{Cu}_3(\text{OH})_6$. (The longest edge of each triangle deviates by only 0.4% of the length of the shortest edge, which is much less than the comparable 3.3% difference in volborthite.²¹) Furthermore, clinoatacamite contains interlayer $\text{Cu}(\text{II})$ ions that comprise an out-of-plane $\text{Cu}_{\text{intra}}-\text{O}_{\text{H}}-\text{Cu}_{\text{inter}}$ pathway, and for this reason it has also been studied as a pyrochlore.²²⁻²⁴

Substitution of this interlayer Cu^{2+} ion in the clinoatacamite structure to form a paratacamite structure with a perfect kagomé lattice of equilateral triangles is known for various metal ions.¹⁴⁻²⁰ Rhombohedral phases (in the same $R\bar{3}m$ space group as paratacamites) of $\text{Co}_2(\text{OH})_3\text{Cl}$ and $\text{Fe}_2(\text{OH})_3\text{Cl}$ are known,^{9,25} which would suggest Co^{2+} and Fe^{2+} as good metals for substitution into a paratacamite framework. Jambor *et al.* attempted to effect substitution to form cobalt paratacamite, $\text{Co}_x\text{Cu}_{4-x}(\text{OH})_6\text{Cl}_2$; their experiments, however, led to a maximum Co composition of $x = 0.17$, and higher compositions were found to contain phase mixtures of clinoatacamite and $\text{Co}_2(\text{OH})_3\text{Cl}$.¹⁹ Our attempts at Fe^{2+} substitution into the paratacamite framework, discussed later in Section 4.3.1.5 of this chapter, were unsuccessful. Feitknecht described the syntheses of solid solutions of substituted $\text{MCu}_3(\text{OH})_6\text{Cl}_2$, where $\text{M} = \text{Ni}, \text{Co}, \text{Mg}$,

Zn, or Cd, in solid solution with Cu.¹⁴ Although a rhombohedral phase of $\text{Ni}_2(\text{OH})_3\text{Cl}$ is not known (a $P\bar{3}m1$ phase, however, is),^{9,19} nickel paratacamite ($\text{Ni}_x\text{Cu}_{4-x}(\text{OH})_6\text{Cl}_2$) has been mined in Australia, and recently solid solutions with compositions of approximately $x = 0.9$ have been found. The end member ($x = 1$) nickel mineral has been named gillardite and is a structural analog of herbertsmithite, $\text{ZnCu}_3(\text{OH})_6\text{Cl}_2$.¹⁷ In their attempts to synthesize Ni-paratacamite, Jambor *et al.* were unable to effect the uptake of Ni into a paratacamite structure under all conditions studied, forming instead phase mixtures of clinoatacamite and $\text{Ni}(\text{OH})_2$.¹⁹ Additionally, although they are not interlayer substituted but rather bear a $P\bar{3}m1$ structure with M^{2+} residing in the hexagonal channel of the kagomé plane (shown in Figure 1.18), two minerals isostructural to one another known as haydeeite ($\text{Cu}_3\text{Mg}(\text{OH})_6\text{Cl}_2$) and kapellasite ($\text{Cu}_3\text{Zn}(\text{OH})_6\text{Cl}_2$) have recently been discovered. Haydeeite was found in a mine in Chile,^{26,27} and kapellasite, a polymorph of herbertsmithite that is likely to be metastable, was discovered in Greece and Germany.²⁸

Turning our attention now to Zn-substituted paratacamite frameworks, it is known that a solid solution exists for naturally occurring $\text{Zn}_x\text{Cu}_{4-x}(\text{OH})_6\text{Cl}_2$ specimens, such that even macroscopically “single” crystals may exhibit variable Cu/Zn composition at the interlayer site.¹⁹ For $x < 0.33$, the crystal symmetry is monoclinic, resulting in the distorted kagomé lattice of clinoatacamite. At $x = 0.33$, the crystal symmetry increases to rhombohedral, and the Cu triangular plaquettes become equilateral. This high symmetry phase of intermediate Zn occupancy ($0.33 \leq x < 1$) is known as Zn-paratacamite. The compositional end member with $x = 1$ has been named herbertsmithite, after Herbert Smith of the British Museum of Natural History.²⁰ An all Zn compound, $\text{Zn}_4(\text{OH})_6\text{Cl}_2$, is not known; the known zinc hydroxychloride, simonkolleite ($\text{Zn}_5(\text{OH})_8\text{Cl}_2 \cdot \text{H}_2\text{O}$), does not bear a kagomé lattice structure.²⁹ In Zn-paratacamite

and herbertsmithite, although it is difficult to differentiate Cu and Zn by standard X-ray analysis, the two sites' distinct coordination environments suggest that the Jahn–Teller distorted Cu(II) ion should rest on the tetragonally elongated interlayer site, whereas the d^{10} Zn(II) ion should reside on the higher symmetry site. In support of this contention, several refinements of our synthetic crystals were carried out in which either Zn or a Cu/Zn mixture was included on the intralayer site; all resulted in a significant increase in refinement residuals (the Hamilton R-factor test).³⁰ These statistics are provided at the end of this Chapter in Section 4.3.2.4.

This Chapter describes the synthesis, structure, and chemical characterization of claringbullite, clinoatacamite, Zn-paratacamite, and herbertsmithite. Magnetic properties of these minerals, as well as an investigation of their redox chemistry to search for RVB superconductivity, will be described in Chapter 5.

4.2 Experimental

4.2.1 General Procedures

All chemicals of reagent or analytical grade were obtained from Aldrich or Strem, and they were used without purification. Hydrothermal reactions were carried out in Teflon-lined pressure vessels, which were purchased from Parr Instruments. A Fisher Isotemp programmable oven with forced-air circulation was used to obtain the desired temperature profiles for hydrothermal reactions. Chemical analyses were conducted by the H. Kolbe Mikroanalytisches Laboratorium.

4.2.2 Synthesis of Claringbullite

Method 1. A 125-mL liner was charged with 2.22 g of $\text{Cu}_2(\text{OH})_2\text{CO}_3$ (10.0 mmol), 0.36 g of NaCl (6.2 mmol), 50 mL of water, and 1.0 mL of 48 % tetrafluoroboric acid (7.7 mmol), capped and placed into a steel hydrothermal bomb. The bomb was heated to 180 °C at a rate of

1 °C/min, maintained for 48 h, and cooled to room temperature at a rate of 0.1 °C/min. Blue hexagonal prismatic crystals were isolated from the liner by filtration, washed with deionized water, and dried in air to afford 1.82 g (88 %) of product. Powder X-ray diffraction (pXRD) analysis of the product was consistent with that obtained for claringbullite (PDF 01-086-0899).

Method 2. A 125-mL liner was charged with 2.22 g of $\text{Cu}_2(\text{OH})_2\text{CO}_3$ (10.0 mmol), 0.29 g of NaCl (4.96 mmol), 50 mL of water, and 1.5 mL of 48 % tetrafluoroboric acid (11.6 mmol), capped and placed into a steel hydrothermal bomb. The bomb was heated to 180 °C at a rate of 1 °C/min, maintained for 60 h, and cooled to room temperature at a rate of 0.1 °C/min. Blue hexagonal prismatic crystals were isolated from the liner by filtration, washed with deionized water (2×50 mL), and dried in air to afford 1.56 g (76 %) of product. Powder X-ray diffraction (pXRD) analysis of the product was consistent with that obtained for claringbullite (PDF 01-086-0899).

4.2.3 Synthesis of Clinoatacamite, $\text{Cu}_2(\text{OH})_3\text{Cl}$

Method 1. A 23-mL liner was charged with 0.448 g of basic copper carbonate (2.03 mmol), 0.3 mL of conc. HCl (3.7 mmol), and 10 mL of deionized water. The liner was capped and placed into a steel hydrothermal bomb under ambient room atmosphere. The bomb was heated at a rate of 5 °C/min. to 210 °C, which was maintained for 60 h. The oven was then cooled to room temperature at a rate of 0.1 °C/min. A blue-green microcrystalline powder was isolated from the walls and bottom of the liner, and was washed with deionized water and dried in air. The product was identified as clinoatacamite by powder X-ray diffraction. Yield: 0.139 g (32.0% based on starting $\text{Cu}_2(\text{OH})_2\text{CO}_3$).

Method 2. An 800-mL liner was charged with 11.9 g of copper(I) chloride (0.120 mol) and 390 mL of deionized water. Into this mixture, 2.33 g of sodium chloride (0.040 mol) and

6.8 mL of hydrochloric acid (0.08 mol) were added. The liner was capped and placed into a steel hydrothermal bomb under an atmosphere of oxygen using an Aldrich AtmosbagTM. The tightened bomb was heated at a rate of 5 °C/min. to 210 °C, which was maintained for 9 d. The oven was then cooled to room temperature at a rate of 0.1 °C/min. Crystals were isolated as green plates from the walls of the liner. More green plates and a microcrystalline blue-green powder were isolated from the bottom of the liner. Sieves were employed to physically separate the plates and powder. The green crystals were washed with deionized water and dried in air. The product was identified as clinoatacamite by powder X-ray diffraction. Yield: 0.905 g (7.05% based on starting CuCl).

Method 3. A 23-mL liner was charged with 0.294 g of copper(I) chloride (2.97 mmol) and 10 mL of deionized water. Into this mixture, 0.09 mL of perchloric acid (1.0 mmol) was added via Mohr pipet. The liner was capped and placed into a steel hydrothermal bomb under ambient room atmosphere. The tightened bomb was heated at a rate of 5 °C/min to 210 °C, which was maintained for 72 h. The oven was then cooled to room temperature at a rate of 0.1 °C/min. Crystals were isolated as green plates from the walls and base of the liner. The green crystals were washed with deionized water and dried in air. The product was identified as clinoatacamite by powder X-ray diffraction. Yield: 0.089 g (28.1% based on starting CuCl). Anal. calcd. for H₃Cu₂ClO₃: H, 1.41; Cu, 59.51; Cl, 16.60. Found: H, 1.39; Cu, 59.48; Cl, 16.63.

Method 4. A 23-mL liner was charged with 0.662 g of Cu₂(OH)₂CO₃ (2.99 mmol), 0.426 g CuCl₂•2H₂O (2.50 mmol), and 10 mL of water. The liner was capped and placed into a steel hydrothermal bomb under ambient room atmosphere. The tightened bomb was heated at a rate of 1 °C/min to 210 °C, which was maintained for 48 h. The oven was then cooled to 40 °C at a rate of 0.1 °C/min. The resulting powder was washed with deionized water and dried in air to

Chapter 4

afford 0.717 g (84 %) of product. A small amount of a dark colored phase (CuO by pXRD) was also present in the sample but isolated to large flakes. The flakes were separated from the bulk powder with a #60 sieve (250 μm pore size) after weighing the entire sample. The remaining green powder gave a pXRD pattern consistent with clinoatacamite (PDF 01-050-1559). Anal. calcd. for $\text{H}_6\text{Cu}_4\text{O}_6\text{Cl}_2$: H, 1.42; Cu, 59.51; Cl, 16.60 Found: H, 1.41; Cu, 59.55; Cl, 16.54.

Method 5. A 23-mL liner was charged with 0.441 g of basic copper carbonate (1.99 mmol), 0.3 mL of conc. HCl (3.7 mmol), 0.121 g NaCl (2.07 mmol), and 10 mL of deionized water. The liner was capped and placed into a steel hydrothermal bomb under ambient room atmosphere. The tightened bomb was heated in a Fisher IsotempTM programmable oven at a rate of 1 $^\circ\text{C}/\text{min}$. to 180 $^\circ\text{C}$, which was maintained for 60 h. The oven was then cooled to room temperature at a rate of 0.1 $^\circ\text{C}/\text{min}$. A blue-green microcrystalline powder was isolated from the walls and bottom of the liner, and was washed with deionized water and dried in air. The product was identified as clinoatacamite by powder X-ray diffraction. Yield: 0.244 g (57.4% based on starting $\text{Cu}_2(\text{OH})_2\text{CO}_3$).

Method 6. A 23-mL liner was charged with 0.200 g of claringbullite, syn. (0.487 mmol), 0.041 g of NaCl (0.70 mmol), 10 mL of water, and 0.05 mL of conc. HCl (0.6 mmol), capped and placed into a steel hydrothermal bomb. The tightened bomb was heated at a rate of 1 $^\circ\text{C}/\text{min}$ to 180 $^\circ\text{C}$, which was maintained for 2 h. The oven was then cooled to 40 $^\circ\text{C}$ at a rate of 0.1 $^\circ\text{C}/\text{min}$. The resulting powder was washed with deionized water and dried in air to afford 0.152 g (73 %) of green microcrystalline powder, which gave a pXRD pattern consistent with clinoatacamite (PDF 01-050-1559).

4.2.4 Synthesis of Zn-paratacamites, $\text{Zn}_x\text{Cu}_{4-x}(\text{OH})_6\text{Cl}_2$ ($0.33 \leq x < 1$)

$\text{Zn}_{0.50}\text{Cu}_{3.50}(\text{OH})_6\text{Cl}_2$ $\text{Zn}_{0.50}$ -paratacamite, syn. This sample was prepared in a manner similar to *Method 4* for clinoatacamite, syn., except that the liner was charged with 0.663 g of $\text{Cu}_2(\text{OH})_2\text{CO}_3$ (3.00 mmol), 0.204 g anhydrous ZnCl_2 (1.50 mmol), 0.170 g of $\text{CuCl}_2 \cdot 2\text{H}_2\text{O}$ (1.00 mmol), and 10 mL of water. Yield: 0.684 g (80 %). The sieved powder gave a pXRD pattern consistent with the Zn-paratacamite substructure (PDF 01-087-0679). Anal. calcd. for $\text{H}_6\text{Cu}_{3.50}\text{Cl}_2\text{O}_6\text{Zn}_{0.50}$: H, 1.41; Cu, 51.96; Cl, 16.57; Zn, 7.64. Found: H, 1.41; Cu, 52.02; Cl, 16.45; Zn, 7.63.

$\text{Zn}_{0.66}\text{Cu}_{3.34}(\text{OH})_6\text{Cl}_2$ $\text{Zn}_{0.66}$ -paratacamite, syn. This sample was prepared in a manner similar to *Method 4* for clinoatacamite, syn., except that the liner was charged with 0.662 g of $\text{Cu}_2(\text{OH})_2\text{CO}_3$ (2.99 mmol), 0.271 g anhydrous ZnCl_2 (1.99 mmol), 0.085 g of $\text{CuCl}_2 \cdot 2\text{H}_2\text{O}$ (0.50 mmol), and 10 mL of water. Yield: 0.762 g (89 %). The sieved powder gave a pXRD pattern consistent with the Zn-paratacamite substructure (PDF 01-087-0679). Anal. calcd. for $\text{H}_6\text{Cu}_{3.34}\text{Cl}_2\text{O}_6\text{Zn}_{0.66}$: H, 1.41; Cu, 49.55; Cl, 16.55; Zn, 10.07. Found: H, 1.38; Cu, 49.53; Cl, 16.46; Zn, 10.18.

$\text{Zn}_{0.80}\text{Cu}_{0.20}\{\text{Cu}_3(\text{OH})_6\}\text{Cl}_2$ $\text{Zn}_{0.80}$ -paratacamite, syn. An 800-mL liner was charged with 1.00 g of claringbullite, syn. (2.4 mmol), 25.13 g of ZnCl_2 (0.18 mol), 400 mL of water, and 0.6 mL of concentrated HCl (6.0 mmol). The liner was capped and placed in a steel hydrothermal bomb under ambient room atmosphere. The tightened vessel was heated at a rate of 1 °C/min to 240 °C, which was maintained for 24 h. The oven was cooled to room temperature at a rate of 0.1 °C/min. Green triangular plate crystals and a green powder were isolated from the base of the liner by filtration, washed with deionized water and dried in air to afford 1.03 g (80 %) of product. Both the crystals and powder gave pXRD patterns consistent

with the Zn-paratacamite substructure (PDF 01-087-0679). The powder was separated from the crystals by sieving prior to chemical analysis. Anal. calcd. for $\text{H}_6\text{Cu}_{3.20}\text{Cl}_2\text{O}_6\text{Zn}_{0.80}$: H, 1.41; Cu, 47.44; Cl, 16.54; F, 0.00; Zn, 12.20. Found: H, 1.25; Cu, 47.19; Cl, 16.61; F, 0.08; Zn, 11.98.

4.2.5 Synthesis of Herbertsmithite, $\text{ZnCu}_3(\text{OH})_6\text{Cl}_2$

A 23-mL liner was charged with 0.66 g of $\text{Cu}_2(\text{OH})_2\text{CO}_3$ (2.98 mmol), 0.31 g of ZnCl_2 (2.27 mmol), and 10 mL of water, capped and placed into a steel hydrothermal bomb under ambient room atmosphere. The tightened bomb was heated at a rate of 1 °C/min to 210 °C, which was maintained for 24 h. The oven was cooled to room temperature at a rate of 0.1 °C/min. A light blue powder was isolated from base of the liner by filtration, washed with deionized water, and dried in air to afford 0.80 g (94 %) of product. The powder gave a pXRD pattern consistent with the Zn-paratacamite substructure (PDF 01-087-0679); no CuO was detected by pXRD. Anal. calcd. for $\text{H}_6\text{Cu}_3\text{Cl}_2\text{O}_6\text{Zn}$: H, 1.41; Cu, 44.44; Cl, 16.53; Zn, 15.24. Found: H, 1.42; Cu, 44.38; Cl, 16.46; Zn, 15.18.

4.2.6 X-ray diffraction

Powder X-ray diffraction patterns were measured using a Rigaku RU300 rotating anode X-ray diffractometer with Cu $K\alpha$ radiation ($\lambda = 1.5405 \text{ \AA}$), which was wavelength-selected with a single-crystal graphite monochromator. Samples were spread onto a glass slide fixed with double-sided Scotch tape. Samples were rotated through $2\theta/\theta$ space and intensity was recorded as a function of 2θ from 10 - 60°. Patterns were indexed with MDI Jade software version 8.0 and referenced using the JCPDS powder diffraction database.

Single-crystal X-ray diffraction data were collected using a fixed-chi three-circle diffractometer equipped with a Bruker SMART APEX CCD area detector. Data were acquired at 100, 130, or 150 K (see Appendix A.3 Tables) using Mo $K\alpha$ radiation ($\lambda = 0.71073 \text{ \AA}$), which

was wavelength-selected with a single-crystal graphite monochromator. For each crystal, four sets of frames were collected over a hemisphere of reciprocal space using ϕ and/or ω scans. The data frames were integrated to hkl /intensity, and final unit cells were calculated using the SAINT program.³¹ Semi-empirical absorption correction for all datasets was performed with the program SADABS.³² Space group assignments were based on systematic absences, E^2 statistics, and successful refinement of the structures. Structures were solved by Patterson methods with the aid of successive difference Fourier maps and were refined against all data with SHELXL.³³ Thermal parameters for all heavy atoms were refined anisotropically. Details regarding the refined data and cell parameters are provided in Appendix A.3.

In the structure of claringbullite, several refinement scenarios were carried out to aid in the identification of the anion not directly bound to any other atom in the structure. After consideration of OH^-/Cl^- , $\text{O}(\text{H})^-$, Cl^-/F^- , and F^- , the best residuals were found for fluoride as the sole anion on that site. The hydrogen atom of the hydroxide ligand was found in the difference-Fourier map, restrained to maintain an O-H bond distance of 0.83(2) Å, and refined using a riding model with an isotropic thermal parameter 1.2 times that of U_{eq} of the attached oxygen atom.

Details of the data collection and structural refinement of $\text{Zn}_x\text{Cu}_{4-x}(\text{OH})_6\text{Cl}_2$ ($x = 0, 0.33, 0.42, 1.00$) are presented in Section 4.3.2.4 of this Chapter.

4.2.7 Other Physical Measurements

Thermogravimetric analysis measurements were performed using a Seiko Dual TG/DTA 320 Thermogravimetric/Differential Thermal Analyzer (SC). Samples were referenced and measured in aluminum pans, with N₂ as a purge gas (with the exception of the herbertsmithite sample, for which Ar was the purge gas) flowing at 150 cc/min. Data were recorded at 0.2 s increments from 20 °C to 500 °C at a 5 °C/min heating rate. Infrared spectra of samples in KBr pellets were recorded on a Nicolet Magna-IR 860 spectrometer equipped with a KBr beam splitter and a DTGS detector. Raman spectra were recorded using a Kaiser Hololab 5000R Raman Spectrometer and Microprobe using an excitation wavelength of 785 nm, large fibers, 10× objective, 16-minute exposure (except herbertsmithite, which underwent an 8-minute exposure), 1 accumulation, and 3 mW laser power. Diffuse reflectance UV-vis were recorded on ground powder samples using a Varian Cary 5E with a Harrick Praying Mantis Accessory. An aluminum mirror was used as the 100% reflectance standard. These results are presented in Appendix B.3 and discussed in Section 4.3.1.4 of this Chapter.

4.3 Results

4.3.1 Synthetic Methodology

4.3.1.1 Synthesis of Claringbullite

Initial hydrothermal attempts to prepare a tetrafluoroborate-capped Cu(II) analog of jarosite resulted in the formation of the first synthetic samples of the mineral claringbullite



A 4:1 stoichiometry of Cu:Cl produces claringbullite as the sole product. A 2:1 ratio of Cu:Cl produces a mixture of claringbullite and clinoatacamite, suggesting that the presence of higher concentrations of aqueous Cl⁻ lead to the formation of clinoatacamite. Attempts to run

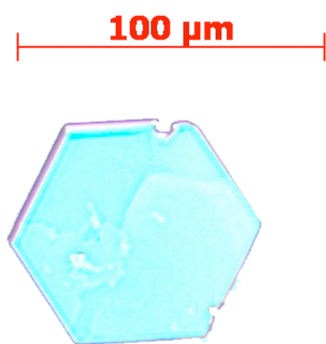


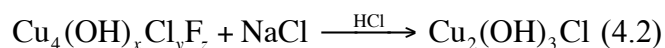
Figure 4.1. Crystal of synthetic claringbullite.

Reaction 4.1 with aqueous HF instead of HBF₄ lead to a mixture of claringbullite and Cu(OH)F. The reaction to form claringbullite likely requires the presence of F⁻, derived from HBF₄, as claringbullite has yet to be produced without an exogenous source of F⁻ ions. Furthermore, F⁻ has been located in the crystal structure, as discussed in Section 4.3.2.1. This suggests that claringbullite is better formulated as Cu₄(OH)_xCl_yF_z ($x + y + z = 8$), and we will adopt this

convention for the remainder of this Thesis.

4.3.1.2 Synthesis of Clinoatacamite, Cu₂(OH)₃Cl

The product mixtures obtained from varying the stoichiometry of Reaction 4.1 suggest that claringbullite is not stable relative to clinoatacamite in aqueous solutions containing excess acid and excess chloride ions. Indeed, claringbullite can be interconverted cleanly to clinoatacamite through reaction with HCl or a mixture of NaCl/HCl.



This reaction leads to the formation of a microcrystalline powder containing small single crystals of clinoatacamite. Running Reaction 4.2 without any HCl results in a mixture of clinoatacamite and CuO. Addition of a proton source (HBF₄) and no exogenous Cl⁻ ions to aqueous suspensions of claringbullite at 90 °C and ambient pressure effects some conversion of claringbullite to clinoatacamite, suggesting that claringbullite is not stable to excess acid. Furthermore, Frost³⁴ has suggested that aqueous suspensions of claringbullite with no exogenous ions will decompose to clinoatacamite. Attempts at converting clinoatacamite to claringbullite through addition of an

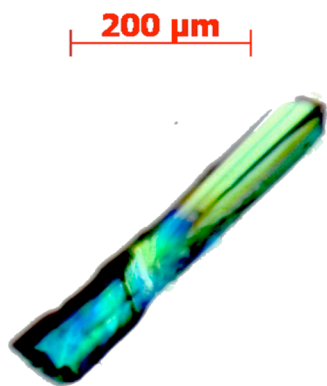
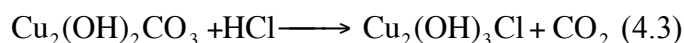


Figure 4.2. Crystal of synthetic clinoatacamite, obtained from oxidation reaction with O_2 as an oxidant.

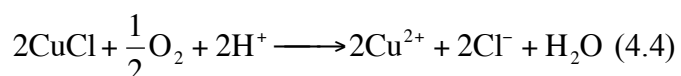
F^- source (BF_4^-) have not been successful at effecting a conversion. A summary of this reactivity is presented in Figure 4.5.

A number of other synthetic routes to clinoatacamite have also been discovered. Literature preparations of clinoatacamite consist of precipitation of aqueous copper(II) chloride under basic conditions through titration with $NaOH$.¹⁹ Under acidic conditions, we observe that treatment of malachite with HCl or a mixture

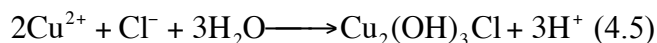
of $NaCl/HCl$ leads to the formation of clinoatacamite, according to the equation



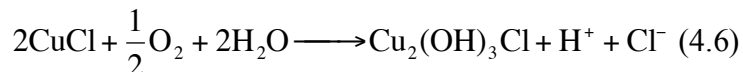
Slowing the process of nucleation relative to crystal growth by adding redox steps afforded us the kinetic control necessary for growth of large single crystals in our work with jarosites. Seeking to extend this redox chemistry to clinoatacamite, we used cuprous chloride as a reactant.³⁵



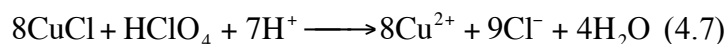
The low solubility of $CuCl$ limits Cl^- concentration, thus a separate source of Cl^- ($NaCl$) must be added to assemble the lattice. The slow dissolution of O_2 and $CuCl$ in this heterogeneous reaction results in reaction times of 9 days. Shorter reaction times yield unreacted $CuCl$ in the product. Reaction 4.4 is thermodynamically favored under standard conditions, with E° of 1.076 V. Gradual precipitation of aqueous Cu^{2+} occurs as it appears in solution



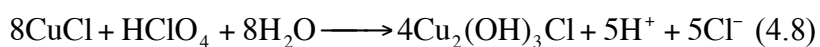
yields clinoatacamite according to the balanced equation



A solution-based oxidant eliminates the O₂ dissolving step, allowing us to achieve faster reaction times. Perchlorate, ClO₄⁻, is the oxidant of choice because its reduction yields Cl⁻,



which then precipitates (Reaction 4.5) to yield, overall



Reaction 4.8 proceeds in 4 days, much faster than Reaction 4.5 because of the elimination of the heterogeneous O₂ dissolving step. Reaction 4.8 is thermodynamically favored under standard conditions, with E° of 1.236 V. Attempts to effect a conversion of clinoatacamite to Zn-paratacamite/herbertsmithite have yielded, at best, phase mixtures of Zn-paratacamite and clinoatacamite, even under the harshest forcing conditions (hydrothermal reactions for several days at 240 °C both with and without added H⁺). Phase mixtures can be most easily identified by pXRD by looking at the shape of the peak at approximately 40°2θ; mixtures show some doubling or asymmetry in the shape of this peak (Figure 4.10). We note that impurities of up to 5% by mass may go undetected in pXRD, and for this reason, have used the results of magnetic susceptibility measurements (Chapter 5) as well as ICP-AA to assess the success of some of these reactions.

4.3.1.3 Synthesis of Zn-Paratacamites and Herbertsmithite, Zn_xCu_{4-x}(OH)₆Cl₂ (0.33 ≤ x ≤ 1)

We turn now to the preparation of samples of Zn-paratacamite and herbertsmithite. Precipitation of aqueous ZnCl₂/CuCl₂ mixtures with NaOH at 95 °C to yield Zn-paratacamite phases has been reported by Jambor, among others.¹⁹ Herbertsmithite cannot be made by this route because, in these reactions, swamping excesses of aqueous Zn²⁺ are required to effect

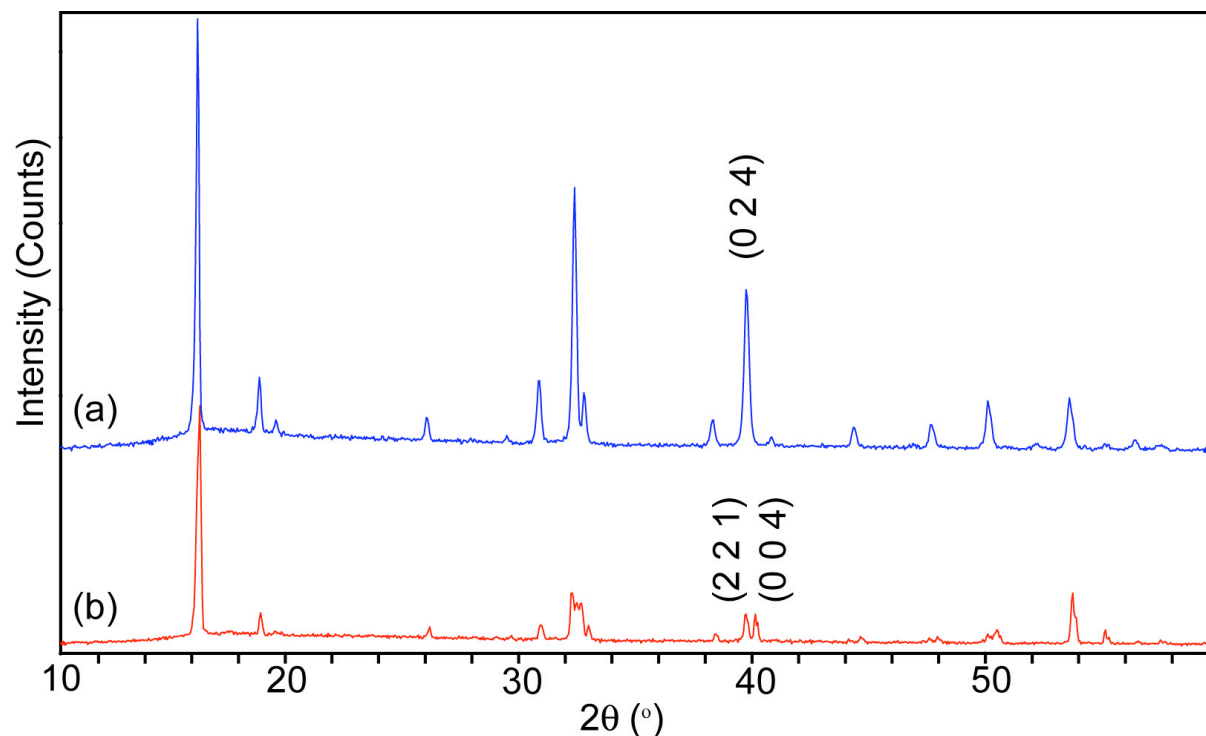


Figure 4.3. Comparison of pXRD pattern of (a) Zn-paratacamite and (b) clinoatacamite. Although the structures are similar, the most distinguishing feature is found at approximately $40^\circ 2\theta$, which occurs as a single peak in (a), but two peaks in (b) due to a difference in symmetry.

modest uptake of Zn^{2+} into the paratacamite structure; a concentration ratio of 40:1 ZnCl_2 to CuCl_2 resulted in a product that contained only 10% Zn by mass (bulk $\text{Zn}_{0.66}$ -paratacamite). Lowering the Cl^- concentration through addition of aqueous $\text{Zn}(\text{NO}_3)_2$ instead of ZnCl_2 resulted in more uptake of Zn^{2+} into a structure relative to an equimolar control with ZnCl_2 (although metal hydroxynitrate phases eventually precipitate at high concentrations). These results suggest that all other things (pH, temperature, pressure) being equal, for a given concentration of Cu^{2+} in aqueous solution, maximum Zn^{2+} uptake into the paratacamite structure may be achieved by minimizing Cl^- concentration above the threshold required to form the paratacamite phase. We note that bulk characterization of these samples through pXRD and ICP-AA, as used by Jambor *et al.*, may be insufficient to assess the presence of Zn-paratacamite phase mixtures within these powders, as discussed above.

We note that attempts to prepare herbertsmithite directly through the redox chemistry presented in Equations 4.7 and 4.8 have been unsuccessful, presumably due to the presence of excess aqueous Cu^{2+} and Cl^- ions in solution. Reaction 4.2, however, for converting claringbullite to clinoatacamite using excess aqueous Cl^- ions suggested a method to obtain crystalline Zn-paratacamite phases and herbertsmithite through the use of ZnCl_2 in the following reaction



Crystals isolated from the bulk product (which analyzed to $\text{Zn}_{0.8}$ -paratacamite under the conditions reported in Section 4.2.4) showed variable compositions over the range $0.33 \geq x \geq 1$. Running this reaction under similar conditions without added HCl gave similar results, but we noted the presence of unreacted claringbullite in the product mixture. Using zinc triflate as a Zn^{2+} source with stoichiometric amounts of Cl^- resulted in some aggregated crystalline material mixed with CuO as the major phase. Although claringbullite is a promising starting material for growth of monophasic crystalline herbertsmithite, we have yet to grow crystals with consistent compositions throughout a given bulk sample and have always isolated our crystals from paratacamite phase mixtures. The major obstacle in using claringbullite as a starting material lies in keeping Cu^{2+} and Cl^- concentrations in solution low enough to prevent the formation of low-Zn paratacamite phases. This task might be all the more challenging because there may, in fact, be a concentration gradient of Cu^{2+} ions above the solid in the aqueous phase (the result of dissolution of our starting material), which might lead to nucleation and crystal growth of phases

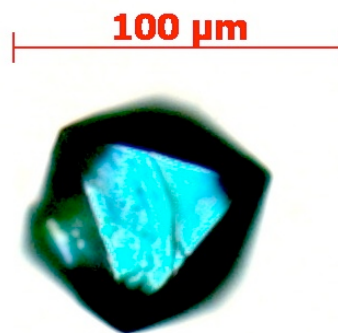
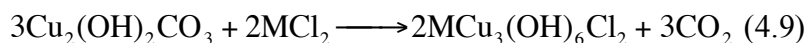


Figure 4.4. A single crystal of $\text{ZnCu}_3(\text{OH})_6\text{Cl}_2$ measuring $0.05 \times 0.04 \times 0.04$ mm.

of variable and lower interlayer Zn composition. This problem might be remedied through the spatial separation of reactants from products with an aqueous zone-refinement method, which will be discussed further in Section 4.3.1.6.

We also used hydrothermal synthesis to prepare a series of Zn-paratacamites according to the reaction below



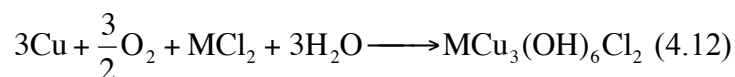
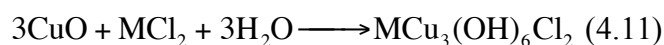
where M = Cu and/or Zn. By varying the Cu/Zn stoichiometry, microcrystalline samples of the entire $0 \leq x \leq 1$ series can be prepared, with the end members ($x = 0$ and $x = 1$) formed by the exclusive use of $\text{MCl}_2 = \text{CuCl}_2$ and ZnCl_2 , respectively. Running Reaction 4.9 in the presence of aqueous hydrochloric acid resulted in phase mixtures that presumably contained some clinoatacamite, according to SQUID measurements and ICP-AA. We note that Reaction 4.9 requires a slight excess of ZnCl_2 (1.1 – 1.5 fold); otherwise some small amount of tenorite (CuO) is observed under our conditions. We also note that reactions with mixed $\text{CuCl}_2/\text{ZnCl}_2$ as starting materials produced some small amount of tenorite, which was removed by sieving prior to analysis. Without metal salts and under similar hydrothermal conditions to the ones employed in Reaction 4.9, $\text{Cu}_2(\text{OH})_2\text{CO}_3$ decomposes to CuO , which presumably occurs through loss of CO_2 and water



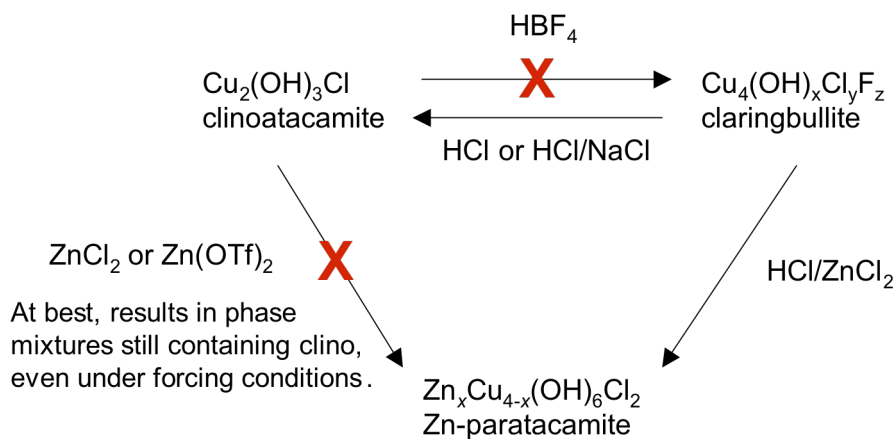
In Reaction 4.9, the bubbling of CO_2 probably disrupts the crystal growth process relative to nucleation, which may be why this reaction has yielded only herbertsmithite powder as a product. Such decomposition may produce CuO *in situ*, which might then dissolve slowly to serve as a reactant. The low solubility of $\text{Cu}_2(\text{OH})_2\text{CO}_3/\text{CuO}$ limits the concentration of Cu^{2+} in

solution, helping to keep the Zn^{2+} to Cu^{2+} ratio in solution high, and resulting in the production of herbertsmithite.

Indeed, Feitknecht and Maget¹⁴ studied the formation of $\text{MCu}_3(\text{OH})_6\text{Cl}_2$ (with $\text{M} = \text{Ni}, \text{Co}, \text{Zn}, \text{Cd}, \text{Mg}$) phases according to the two reactions below



For $\text{M} = \text{Zn}$, they report using Equation 4.12 to produce analytically pure (by elemental analysis) $\text{ZnCu}_3(\text{OH})_6\text{Cl}_2$ from Cu powder in boiling aqueous solutions of ZnCl_2 under oxygen after 1 day. Their analysis shows a pXRD pattern that corresponds to a paratacamite phase. Although single-crystal X-ray studies could not be done, they report highly aggregated small light blue crystals of this material. Furthermore, they report observation of an unstable intermediate phase with a hexagonal C6 structure, which they claim to isolate purely. Presumably this other structure, for which they also report small crystals, is kapellasite. Exploration of Reaction 4.11 by Shaoyan Chu using zone furnace techniques presented in Section 4.3.1.6 has yielded, to date, mixtures of Zn-paratacamite crystals of variable compositions.



Summary of Observed Reactivity

Figure 4.5. Summary of observed reactivity for synthetic copper(II) hydroxychloride minerals.

4.3.1.4 Thermal and Spectroscopic Characterization

These data are reported in Appendix B.3. In summary, the thermal data show that the decomposition of the ground powder synthetic samples occurs at 260 °C for claringbullite, 270 °C for clinoatacamite, and 290 °C for herbertsmithite (Figures B.3.1, B.3.2, and B.3.3, respectively). Braithwaite *et al.* report a monotonic increase in the frequency of an FTIR stretch at around 930 cm^{-1} , which they assign to an in-plane M–OH deformation.²⁸ We see a similar trend in the data for our synthetic samples (Figure B.3.5). Finally, Jambor notes that paratacamite phases with higher Zn contents appear bluer.¹⁹ We note a shift in a maximum in the diffuse reflectance UV-vis to bluer wavelengths with increasing interlayer Zn substitution (although the trend is not entirely monotonic). We also observe that the paratacamites and clinoatacamite show three bands in its UV-vis spectrum, while herbertsmithite only shows one band (Figure B.3.8).

4.3.1.5 $M_2(OH)_3Cl$, $ZnCu_3(OH)_6Br_2$, and other $MCu_3(OH)_6Cl_2$ targets

In our investigation of the chemistry of $ZnCu(OH)_6Cl_2$, we also sought to explore other related targets. We targeted $M_2(OH)_3Cl$, (with $M = Co, Fe$), $ZnCu_3(OH)_6X_2$ (with $X = Br, F$) and $MCu_3(OH)_6Cl_2$ with $M = Ni, Co, Mn, Fe, Ca, Mg, Cd, Hg,$ and Pb .

In the literature, known $R\bar{3}m$ $M_2(OH)_3Cl$ phases include $M = Co$ and Fe .^{9,19} $Ni_2(OH)_3Cl$ is known as a $P\bar{3}m1$ phase.^{9,15} Oswald and Feitknecht report the synthesis of $Co_2(OH)_3Cl$ through precipitation of aqueous $CoCl_2$ solutions under basic conditions with urea, followed by recrystallization from heated $CoCl_2$ solutions.⁹ Jambor *et al.* report the precipitation of aqueous $CoCl_2$ under basic conditions with $NaOH$ at elevated temperatures.¹⁹ Our attempts to prepare $Co_2(OH)_3Cl$ hydrothermally from various stoichiometries of $Co(OH)_2$ and/or $CoCO_3$ with $CoCl_2$ gave mixtures of $Co_2(OH)_3Cl$ and Co_3O_4 under all conditions attempted. Oswald and Feitknecht report the preparation of $Fe_2(OH)_3Cl$ under air-free conditions from reaction of $Fe(CO)_5$ and

aqueous FeCl_2 at $80\text{ }^\circ\text{C}$.⁹ Our attempts to replicate this chemistry failed to yield isolable product. Finally, Oswald and Feitknecht report obtaining a $P\bar{3}m1$ phase that analyzes to $\text{Ni}_{2.93-5.27}(\text{OH})_{3.86-8.54}\text{Cl}_2$ from the precipitation of aqueous NiCl_2 under basic conditions with NaOH at elevated temperatures.⁹ Jambor reports that similar chemistry yields substantial amounts of $\text{Ni}(\text{OH})_2$ in the product mixtures, and so these reactions were not attempted.¹⁹ Interestingly, too, Oswald and Feitknecht review the synthesis of $\text{Mg}_2(\text{OH})_3\text{Cl}\cdot 7-8\text{H}_2\text{O}$ from MgO and aqueous MgCl_2 , with a structure in $P\bar{3}m1$ (a possible non-magnetic analog of haydeeite/kapellasite).⁹

The known $\text{MCu}_3(\text{OH})_6\text{Cl}_2$ paratacamite phases include $\text{M} = \text{Zn}, \text{Ni}, \text{Co}, \text{Mg},$ and Cd in solid solution with Cu .¹⁴⁻²⁰ $\text{M} = \text{Mg}$ is also known to exist in a hexagonal $P\bar{3}m1$ structure as the naturally occurring mineral haydeeite.^{26,27} Feitknecht and Maget report that their attempts to prepare $\text{MgCu}_3(\text{OH})_6\text{Cl}_2$ at room temperature from Cu powder and different concentrations of aqueous MgCl_2 under O_2 yielded different phases, one rhombohedral and another hexagonal, depending on the concentration of MgCl_2 and the reaction time.¹⁴ They also report the production of $\text{NiCu}_3(\text{OH})_6\text{Cl}_2$ upon cooling of heated aqueous mixtures of NiCl_2 and CuCl_2 with NaOH , although they acknowledge that this route might also produce some CuO .¹⁴ Jambor *et al.* report that similar chemistry results in the production of mixtures of clinoatacamite and $\text{Ni}(\text{OH})_2$.¹⁹ Feitknecht and Maget report the production of $\text{CoCu}_3(\text{OH})_6\text{Cl}_2$ at room temperature from Cu powder in aqueous CoCl_2 under O_2 .¹⁴ Jambor *et al.* attempted to form cobalt paratacamite, $\text{Co}_x\text{Cu}_{4-x}(\text{OH})_6\text{Cl}_2$ from aqueous CoCl_2 and CuCl_2 with the addition of NaOH ; their experiments, however, led to a maximum Co composition of $x = 0.17$. Higher compositions were found to contain phase mixtures of clinoatacamite and $\text{Co}_2(\text{OH})_3\text{Cl}$.¹⁹ Finally, Feitknecht and

Maget report the preparation of $\text{Cd}_{0.96}$ -paratacamite from Cu powder and aqueous CdCl_2 under oxygen.¹⁴

Our exploration of the chemistry of M-paratacamites is outlined in Table 4.1. The notable reactions are those with Ni, Co, and Cd. In summary, we were able to obtain Ni-paratacamite, Co-paratacamite, or Cd-paratacamite by pXRD from hydrothermal reactions of NiCl_2 , CoCl_2 , or CdCl_2 with $\text{Cu}_2(\text{OH})_2\text{CO}_3$ and HCl. However, examination of all of these products through SQUID measurement appeared to indicate the presence of clinoatacamite phase impurities. Without HCl, we obtained phase mixtures of Ni- or Co-paratacamite with CuO (though we did not attempt an analogous reaction for Cd). We were able to obtain Ni-paratacamite from hydrothermal reaction of claringbullite with NiCl_2 and HCl; similar attempts at Co-paratacamite yielded phase mixtures of Co-paratacamite and Co_3O_4 .

Table 4.1. Summary of Observed Reactivity for M-Paratacamite Syntheses. Reactions were run hydrothermally with temperatures ranging from 180 – 240 °C, with and without added HCl.

	Claringbullite	$\text{Cu}_2(\text{OH})_2\text{CO}_3$
FeCl_2	Fe_2O_3 + unknowns (w/ acid)	Not attempted
CaCl_2	Clino. + CaF_2 (w/ acid)	Clino. + CuO
MnCl_2	Clino. + MnO (w/ acid)	Not attempted
SrCl_2	Not attempted	CuO + SrCO_3 (w/ acid)
PbCl_2	Clino. + PbClF (w/ acid)	Not attempted
HgCl_2	Clino. (w/ acid)	Clino. + CuO (w/ acid)
MgCl_2	Clino. + MgCl_2 + unknown (w/ acid)	Clino. + CuO (w/ or w/o acid)
NiCl_2	Ni-para. (w/ acid)	Ni-para. + Clino.(?) (w/ acid) Ni-para. + CuO (w/o acid)
CoCl_2	Co-para. + Co_3O_4 (w/ acid)	Co-para + Clino (?) (w/ acid) Co-para + CuO (w/o acid)
CdCl_2	Cd-para (w/ acid)	Cd-para + Clino (?) (w/ acid)

Finally, we attempted to prepare $\text{ZnCu}_3(\text{OH})_6\text{X}_2$ with X = Br, F. Hydrothermal reaction of claringbullite with aqueous ZnBr_2 and HCl yielded claringbullite and an unknown phase. Braithwaite *et al.* reports the synthesis of $\text{Cu}_{2.8}\text{Zn}_{1.1}(\text{OH})_6\text{Br}_{1.9}$ from $\text{Cu}_2(\text{OH})_2\text{CO}_3$ and aqueous

ZnBr₂. They report it to have a $P\bar{3}m$ -type structure, which would make it structurally similar to kapellasite.^{20,28} Our hydrothermal attempts at ZnCu₃(OH)₆F₂ from Cu₂(OH)₂CO₃ and aqueous ZnF₂ yielded CuO, Cu(OH)₂, and Zn(OH)F.

4.3.1.6 Hydrothermal Zone Refinement Technique

Shaoyan Chu of the MIT Physics Department has engineered a hydrothermal zone refinement technique for the growth of large crystals. The technique utilizes a sealed quartz-glass tube as a hydrothermal reaction vessel. A zone furnace provides a temperature gradient so that reactants diffuse from the source end of the vessel at high temperature to the product end at low temperature. This technique is advantageous because it allows for spatial separation of reactants and products, which could potentially allow for a more uniform concentration of metal ions at the product end, and therefore, a more uniform composition of product crystals than can be achieved with conventional stainless steel Teflon-lined pressure vessels. Exploration of the chemistry presented in this Chapter with this technique is currently underway.

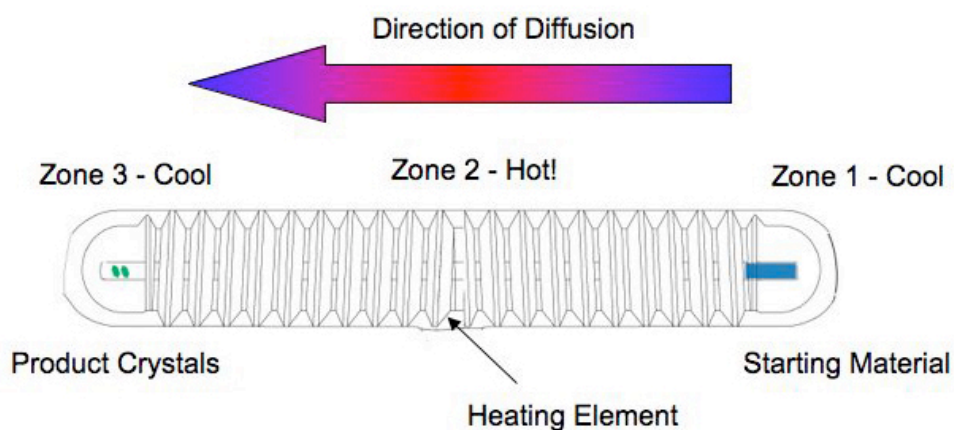


Figure 4.6. Schematic of aqueous zone refinement technique for crystal growth in sealed quartz tubes.

4.3.2 General Structural Chemistry

4.3.2.1 Structure of Claringbullite, $\text{Cu}_4(\text{OH})_x\text{Cl}_y\text{F}_z$ ($x + y + z = 8$)

The compounds claringbullite, clinoatacamite, and Zn-paratacamite/herbertsmithite are all structurally related. These compounds bear kagomé lattices of $\text{Cu}_3(\mu\text{-OH})_6$ triangles. Figure 4.7 shows the single-crystal X-ray structure of synthetic claringbullite. Claringbullite crystallizes in the space group $P6_3/mmc$, with two crystallographically distinct Cu^{2+} ions. The intralayer Cu—O distance is 1.9478(19) Å, and Cl^- ions complete a distorted (4+2)-octahedral coordination sphere for Cu(1) at a long Cu—Cl distance of 2.9939(4) Å. The Cu(1)—O—Cu(1) bond angle is $117.77(18)^\circ$. This coordination environment gives rise to corner sharing equilateral triangles of $\{\text{Cu}_3(\text{OH})_6\}$, with $\text{Cu}\cdots\text{Cu}$ distances of 3.335 Å, which extend to form a kagomé layer. The layers of $[\text{Cu}_3(\text{OH})_6\text{Cl}]^+$ are positively charged. To maintain charge balance, then, an additional anion is needed. An X^- anion sits in the center of the hexagonal channel of the kagomé, centered

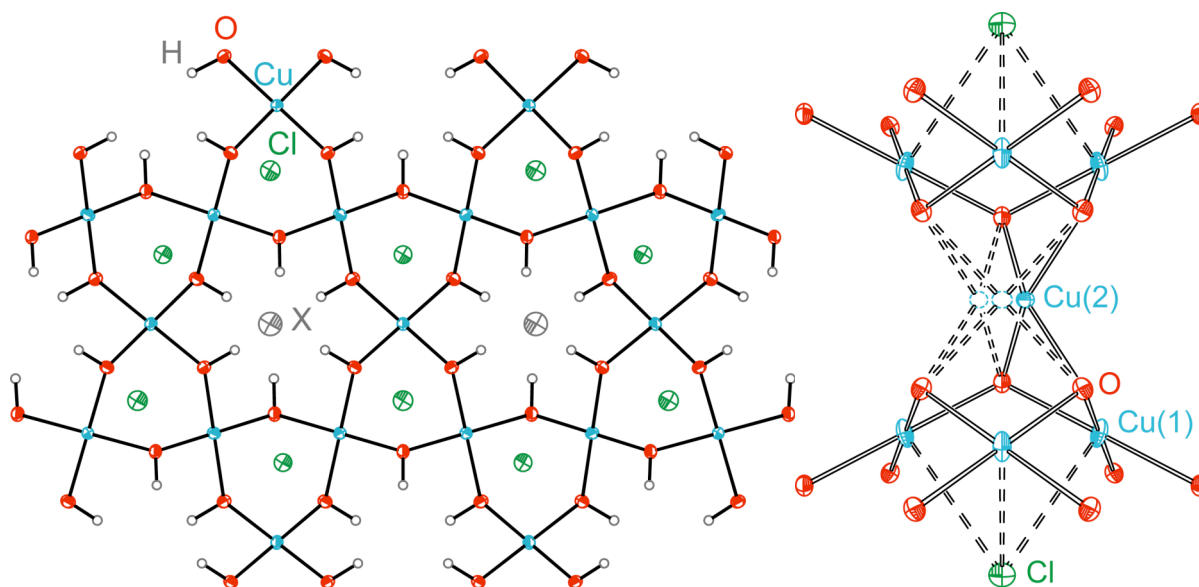


Figure 4.7. (Left) X-ray crystal structure of the kagomé layer of claringbullite shown at 40% thermal ellipsoids, as viewed down the (0 0 1) axis and (right) view of the interlayer Cu^{2+} ion, which shows an unusual Jahn-Teller distortion and is statistically disordered over three sites.

between the layers, as shown in Figure 4.8. Burns *et al.* refined the structure of natural claringbullite from Arizona with the atom labeled X^- as a Cl^-/OH^- solid solution with 29% Cl^- and 71% OH^- . The authors suggest that there is no reason why this site should not have a complete solid solution with compositions ranging from $Cu_4(OH)_6Cl_2$ to $Cu_4(OH)_7Cl$.² The lowest R-factors obtained on refinement of our synthetic crystal structure, however, show this site occupied exclusively by an F^- anion, with $R_1 = 0.0332$ and $wR_2 = 0.0731$.

The interlayer Cu^{2+} ion in claringbullite shows the effects of a very unusual Jahn-Teller distortion, as depicted in Figure 4.7 and again in Figure 4.10. To maintain a regular kagomé lattice in claringbullite, the “trigonal prismatic” interlayer cation is disordered over three crystallographically equivalent sites, affording something more akin to a square planar ligand arrangement. Statistical disorder places Cu(2) closer to two Cu(1) atoms in a given triangle in the plane than to the third. The coordination of Cu(2) to six hydroxyl groups in this distorted trigonal prismatic environment also gives rise to AA packing of layers in the claringbullite structure. Four Cu—O distances of 1.984(4) Å and two Cu—O distances of 2.454(4) Å make up this approximately square planar environment. This unusual arrangement allows for shorter Cu—O bond lengths than an octahedral arrangement. Consequently the Cu···Cu distances, both in and out of plane, are shorter in claringbullite than in clinoatacamite or herbertsmithite. Of relevance to the magnetic properties of claringbullite, the $Cu_{intra}-O-Cu_{inter}$ angles vary from 87.63(11)° to 107.49(17)°, as shown in Table 4.3.

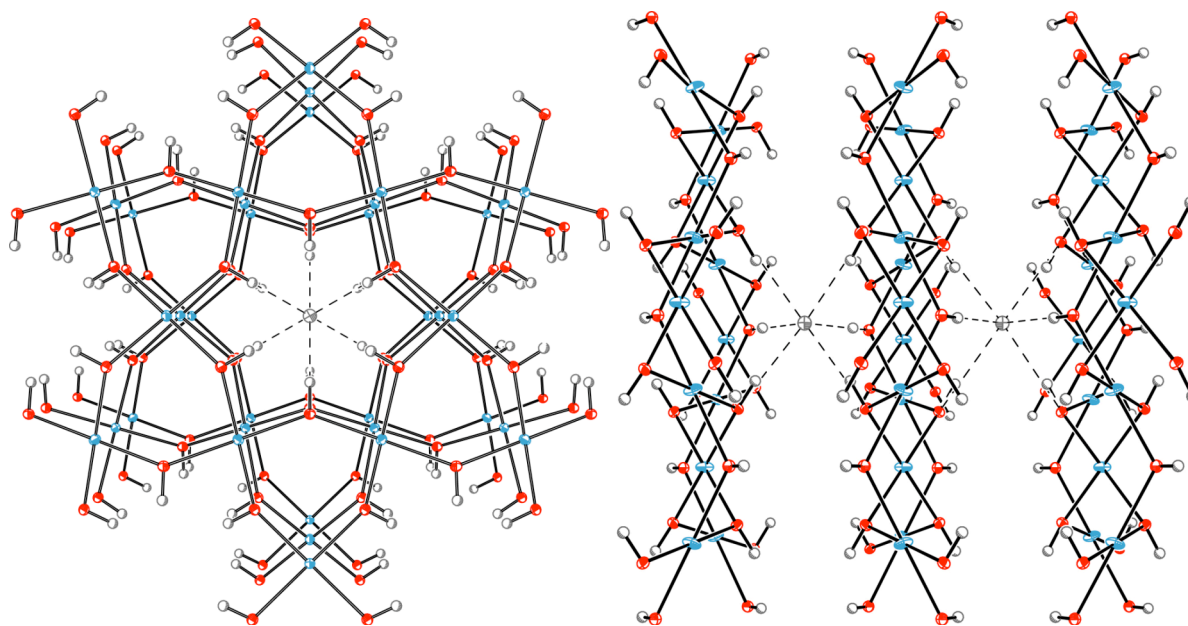


Figure 4.8. X^- anion in claringbullite, showing hydrogen bonding to hydroxyl protons in two kagomé layers, as viewed down the (0 0 1) axis (left) and down the (1 1 0) axis (right). Cu(2) and Cl have been omitted for clarity. Cu atoms are in teal, O in red, H in white, and X in gray.

4.3.2.2 Structure of Clinoatacamite, $Cu_2(OH)_3Cl$

Clinoatacamite crystallizes in the monoclinic space group $P2_1/n$ with three crystallographically distinct Cu^{2+} ions, as shown in Figure 4.9. Two of these crystallographically distinct Cu^{2+} ions reside within a distorted kagomé plane, while the third resides between kagomé layers. In clinoatacamite, the interlayer cation displays a Jahn-Teller distorted (4+2)-octahedral coordination, which results in a distortion of the kagomé layers. This interlayer Cu^{2+} ion has longer axial bonds (2.356(3) Å) and shorter equatorial bonds (1.980(3) and 2.022(3) Å) to hydroxyl groups, as shown in Figure 4.9 and 4.10. Each in-plane Cu^{2+} ion is coordinated equatorially to four oxygen atoms, with two axial Cl^- ions at longer distances. The intralayer Cu—O distance ranges from 1.932(3) to 2.006(3) Å. Cu(1) is coordinated to Cl^- ions at a short distance of 2.7514(10) Å and a longer distance of 2.822(10) Å, while Cu(2) is coordinated to two Cl^- ions at a distance of 2.7685(11) Å. The Cl^- ions, therefore, reside above and below the kagomé layers and form two shorter contacts and one longer contact to any given triangle. A

structural comparison of clinoatacamite and claringbullite is presented in Table 4.2, detailing differences in their packing structure, the coordination environments of their interlayer cations and Cl^- anions, and distances relevant to the kagomé planes. Finally, and perhaps most importantly for the magnetism of clinoatacamite, the $\text{Cu}_{\text{intra}}\text{—O—Cu}_{\text{intra}}$ angles range from $116.96(14)^\circ$ to $124.15(14)^\circ$, while the $\text{Cu}_{\text{intra}}\text{—O—Cu}_{\text{inter}}$ angles range from $90.94(11)^\circ$ to $101.48(12)^\circ$, as presented in Table 4.3.

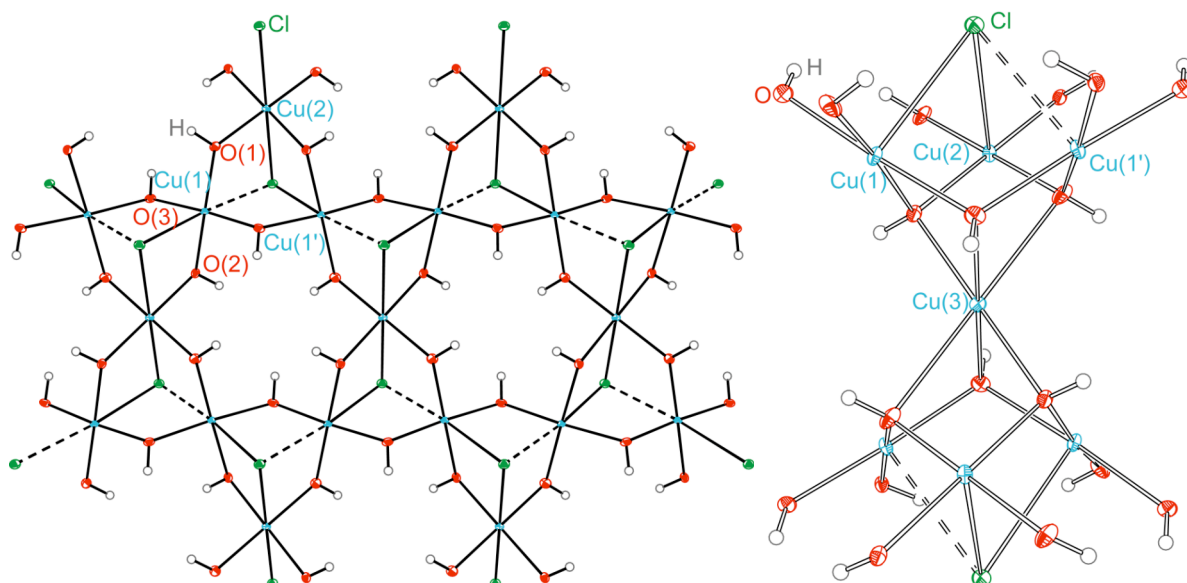


Figure 4.9. (Left) Distorted kagomé layer in clinoatacamite, with two crystallographically independent Cu centers. (Right) The interlayer Cu(3) ion shows is Jahn-Teller distorted in a (4+2)-octahedral coordination.

Table 4.2. Structural Comparison of claringbullite and clinoatacamite.

	claringbullite	clinoatacamite
Packing	AA	ABC
Triangles	Equilateral, $\text{Cu}\cdots\text{Cu}$ 3.335 Å	Approximately isosceles, $\text{Cu}\cdots\text{Cu}$ 3.409, 3.411, 3.423 Å
Jahn-Teller distortion of interlayer cation	Distorted trigonal prismatic approximating square planar. Cu(2) is disordered over 3 sites.	(4 + 2)-octahedral
Cu—Cu in-plane distances	Shorter, $\text{Cu}\cdots\text{Cu}$ 3.335 Å	Longer, avg. $\text{Cu}\cdots\text{Cu}$ 3.414 Å
$d_{\text{kagomé}}$	Shorter (4.585 Å)	Longer (4.673 Å)
Interlayer Cl^-	Shared between layers at a long distance (Cu—Cl 2.994 Å)	Each layer has its own, above and below (Cu(2)—Cl 2.769 Å, Cu(1)—Cl 2.751 Å, 2.822 Å)

4.3.2.3 Structure of Zn-paratacamite and Herbertsmithite, $\text{Zn}_x\text{Cu}_{4-x}(\text{OH})_6\text{Cl}_2$ ($0.33 \leq x \leq 1$)

The structural chemistry of Cu(II) hydroxychloride minerals is dominated by the Jahn-Teller effect, or more precisely, a Peierls distortion. (The Jahn-Teller effect is by definition a local, molecular effect. In solid state structures with translational symmetry, the effect is called a Peierls distortion, because local arguments in themselves are insufficient to explain the complexity of such periodic structures, as discussed in Section 1.7.⁸) Figure 4.10 demonstrates the profound effect of such distortion on the interlayer cations of the Cu(II) hydroxychloride minerals described herein. In the clinoatacamite-Zn-paratacamite series, at $x \geq 0.33$, the symmetry increases from monoclinic to rhombohedral and the minerals crystallize in the space group $R\bar{3}m$. In the rhombohedral arrangement, the interlayer ion sits on a $\bar{3}$ site with six equal $\text{M}^{2+}\text{-OH}$ bond lengths. Again, the effects of an extended solid-state structure take over: the energetic advantage of this highly symmetric structural arrangement presumably more than compensates for the energetic penalty of lacking the stabilization induced by a (4+2)-distortion on those Cu^{2+} -containing interlayer sites. The regular interlayer geometry leads to a perfect kagomé lattice. The in-plane site still shows the (4+2)-coordination of equatorial hydroxides

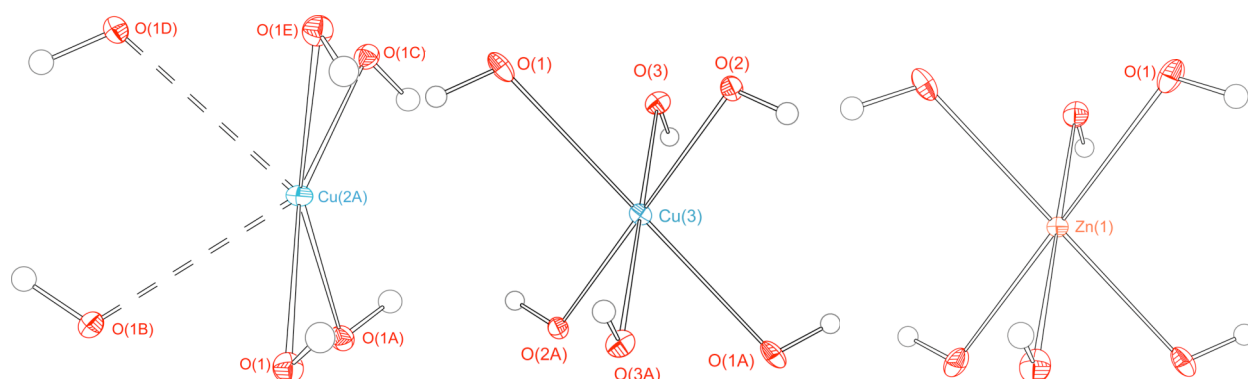


Figure 4.10. The interlayer copper ions in claringbullite (left) and clinoatacamite (center) exhibit different types of Jahn-Teller distortions. A “trigonal prismatic” coordination environment in claringbullite more closely approximates a square planar arrangement, while clinoatacamite exhibits a more typical (4+2)-Jahn-Teller-distorted octahedron. The Zn^{2+} interlayer ion in herbertsmithite (right) is unaffected by Jahn-Teller distortion because all degenerate orbitals have equal occupancy given its d^{10} electronic configuration.

(1.982(2) Å) and axial chlorides (2.7697(17) and 2.7698(17) Å), which reside above and below the layers. The $x = 1$ end member, herbertsmithite, has in-plane $\text{Cu}\cdots\text{Cu}$ distances of 3.417 Å and $\text{Cu}_{\text{intra}}\text{—O—Cu}_{\text{intra}}$ angles of $119.1(2)^\circ$. The structure of herbertsmithite is shown in Figure 4.10. Figure 4.12 and Table 4.3 summarize the structural parameters of the minerals.

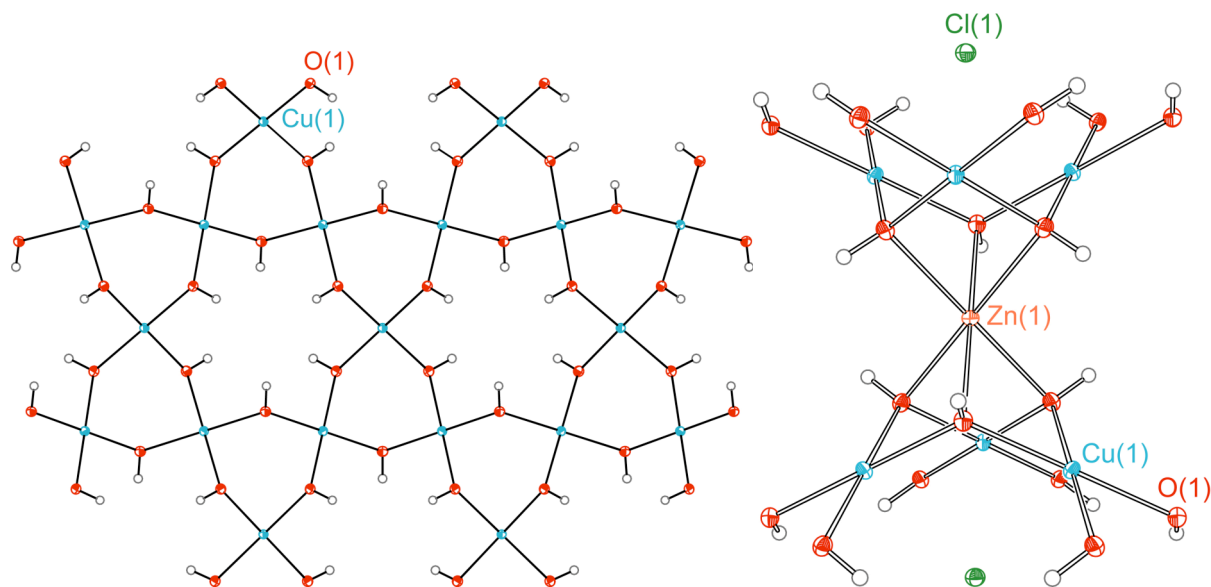


Figure 4.11. Perfect kagomé layer of Zn-paratacamite/herbertsmithite (left). Interlayer Zn^{2+} ion in Zn-paratacamite/herbertsmithite (right) has equal bond lengths for all $\text{M}_{\text{inter}}\text{—OH}$ bonds, leading to regular kagomé geometry.

Figure 4.13 presents the packing structures of the three minerals. These packing structures might provide some insight into the chemistry of these synthetic minerals and their magnetic properties. The Cl^- ion is shared between layers in the structure of claringbullite. In clinoatacamite and herbertsmithite, on the other hand, two Cl^- ions (above and below) are unique to each layer. In this respect, the structure of claringbullite is “deficient” in Cl^- relative to the other two minerals; indeed, adding Cl^- to claringbullite under the right synthetic conditions can effect a conversion to either clinoatacamite or Zn-paratacamite/herbertsmithite, depending on whether or not Zn^{2+} is also present in solution. Because of its packing, too, claringbullite has small hexagonal cavities (occupied by X^- , 6.670 Å in $\text{Cu}\cdots\text{Cu}$ diameter), which might account

Chapter 4

for its enhanced reactivity to Zn^{2+} -substitution relative to clinoatacamite, which has no such cavities. (Shorter $\text{Cu}\cdots\text{Cu}$ distances all-around might make claringbullite less stable thermodynamically, as well.) Finally, the packing in claringbullite is AA, but in the other two minerals it is ABC. Although both undergo a ferromagnetic ordering transition, the minerals claringbullite and clinoatacamite show slightly different magnetic behavior at low temperatures (Chapter 5), which likely comes about as a result of the different manner in which interlayer Cu^{2+} is coordinated and their different packing structures.

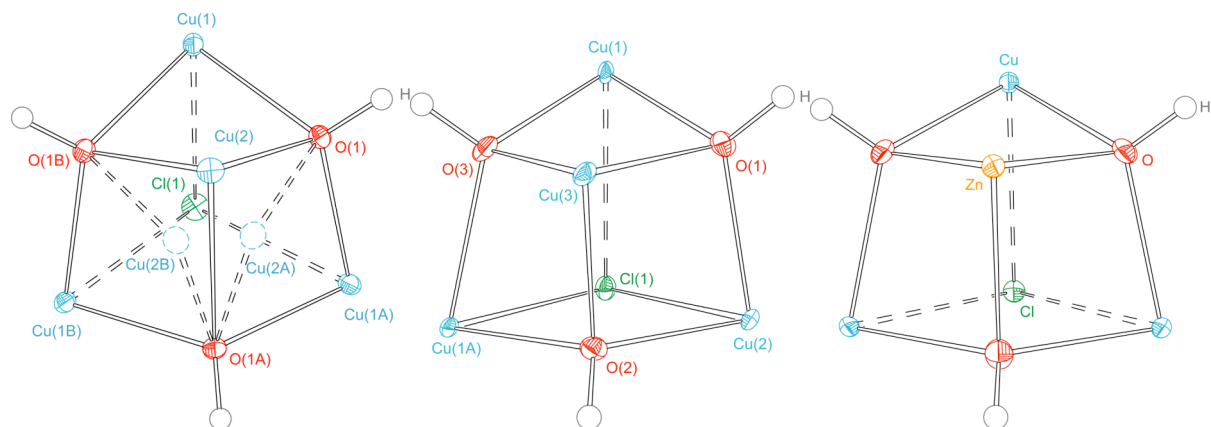


Figure 4.12. Atom labeling scheme for triangles of claringbullite, clinoatacamite, and herbertsmithite.

Table 4.3. Structural Comparison of claringbullite, clinoatacamite, and herbertsmithite.

	claringbullite	clinoatacamite	herbertsmithite
Bond	Bond distances (Å)		
Cu—O	1.9478(19)	1.932(3) Cu(1)—O(1) 2.001(3) Cu(1)—O(3) 1.991(3) Cu(1A)—O(2) 1.998(3) Cu(1A)—O(3) 1.943(3) Cu(2)—O(1) 2.006(3) Cu(2)—O(2)	1.982(2)
Cu—Cl	2.9939(4)	2.822(10) Cu(1)—Cl(1) 2.7514(10) Cu(1A)—Cl(1) 2.7685(11) Cu(2)—Cl(1)	2.7697(17) 2.7698(17)
M—O	1.984(4) Cu(2)—O(1) 1.984(4) Cu(2)—O(1B) 2.454(4) Cu(2)—O(1A)	2.356(3) Cu(3)—O(1) 1.980(3) Cu(3)—O(2) 2.022(3) Cu(3)—O(3)	2.101(5)
Angle	Bond angles (°)		
Cu—O—Cu	117.77(18)	124.15(14) Cu(1)—O(1)—Cu(2) 117.14(13) Cu(2)—O(2)—Cu(1A) 116.96(14) Cu(1)—O(3)—Cu(1A) 119.41(80) (avg)	119.1(2)
Cu—O—M	87.63(11) Cu(1)—O(1)—Cu(2) 87.63(11) Cu(1)—O(1B)—Cu(2) 107.49(17) Cu(1)—O(1)—Cu(2A) 107.49(17) Cu(1)—O(1B)—Cu(2B) 97.56(14) (avg)	92.65(11) Cu(1)—O(1)—Cu(3) 101.48(12) Cu(1)—O(3)—Cu(3) 97.19(11) Cu(1A)—O(2)—Cu(3) 95.62(12) Cu(1A)—O(3)—Cu(3) 90.94(11) Cu(2)—O(1)—Cu(3) 101.11(12) Cu(2)—O(2)—Cu(3) 96.49(95) (avg)	97.04(15)

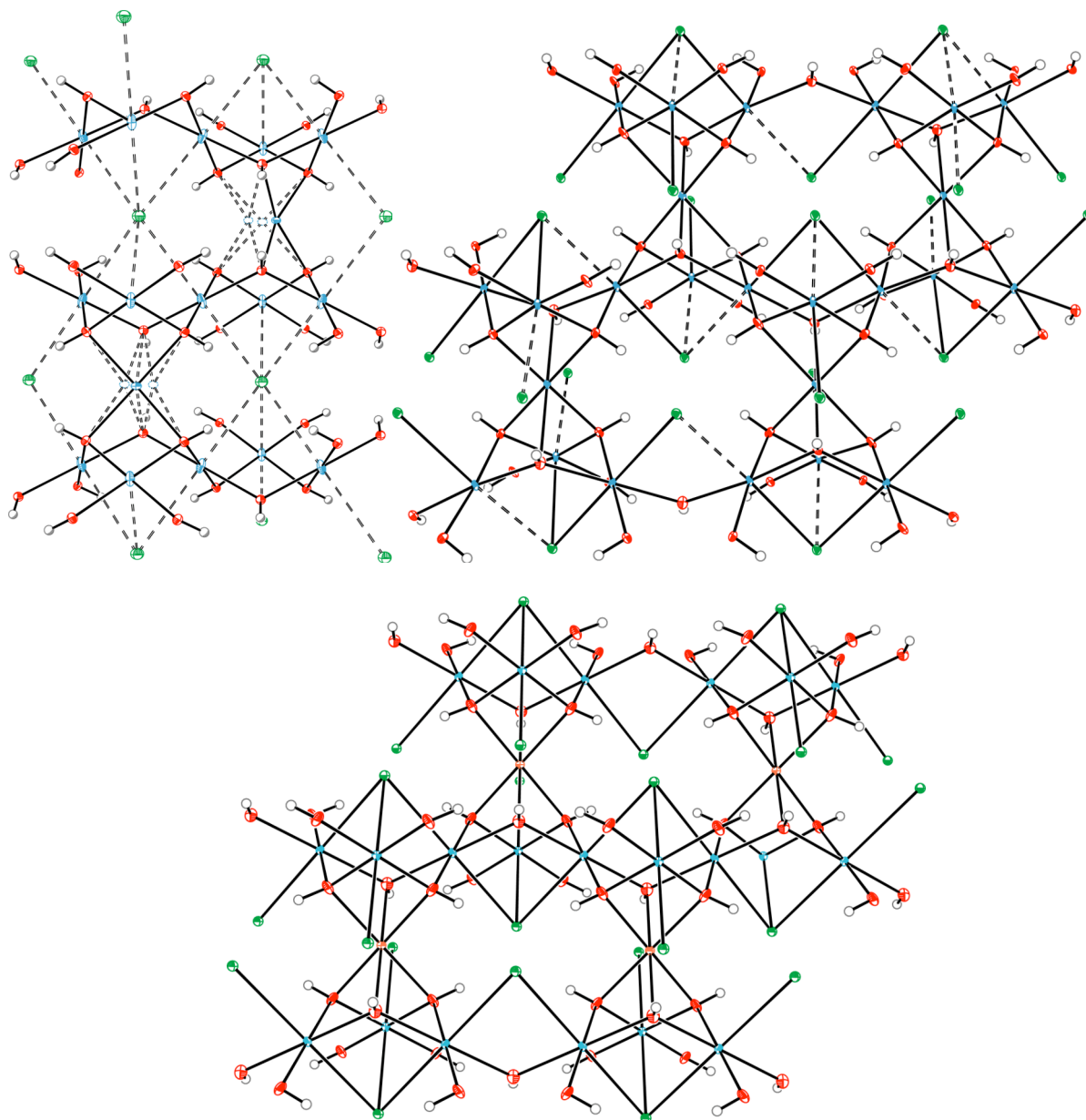


Figure 4.13. (Top left) AA packing of claringbullite, as viewed down the $(1\ 1\ 0)$ axis. Cl^- ions (green) are shared between two layers. $\text{Cu}(2)$ and Cl atoms are coplanar. X^- ions (not shown) are coplanar with $\text{Cu}(2)$ and Cl as well, residing in the center of the hexagonal channel. (Top right) ABC packing of clinoatacamite, as viewed down the $(\bar{1}\ 1\ 2)$ axis, showing that each layer has its own Cl^- ions, above and below. (Bottom) Herbertsmithite, as viewed down its $(1\ 1\ 0)$ axis, shows ABC packing and Cl^- ion positioning similar to that in clinoatacamite. In both herbertsmithite and clinoatacamite, Cl^- ions are not coplanar with the interlayer Zn and/or Cu .

4.3.2.4 Single-Crystal X-ray Diffraction of $\text{Zn}_x\text{Cu}_{4-x}(\text{OH})_6\text{Cl}_2$

Several authors have recently pointed to the possibility of antisite disorder³⁶⁻³⁹ — isolated Cu^{2+} spins on the Zn^{2+} site that are weakly coupled to the kagomé layers and nonmagnetic Zn^{2+} defects in the Cu^{2+} kagomé planes — to explain the rise below 50 K in the low temperature susceptibility of herbertsmithite. (The rise in the data is further discussed in Chapter 5.) These authors have used bulk susceptibility, neutron powder diffraction, and NMR measurements to estimate the site occupancies to be 6–10% Zn substitution onto the kagomé plane, and 18–30% Cu substitution onto the interlayer site.³⁶⁻³⁹ Another possible interpretation of these data is that the rise in susceptibility is intrinsic to the system and related to the presence of the Dzyaloshinsky-Moriya interaction^{40,41} and/or the presence of orientational disorder of the O–H bonds.⁴² We have maintained that there is a strong energetic preference for the Jahn-Teller-distorted Cu^{2+} over the d^{10} symmetric Zn^{2+} to reside in the tetragonally elongated intralayer site of the kagomé plane. To further characterize our systems and to assess the validity of antisite disorder claims, we present here the R-factor statistical results of single-crystal X-ray diffraction studies using $\text{MoK}\alpha$ radiation for the series $\text{Zn}_x\text{Cu}_{4-x}(\text{OH})_6\text{Cl}_2$, with $0 \leq x \leq 1$. While these single-crystal studies cannot rule out antisite disorder within statistical error entirely, the crystals studied are all better modeled with exclusively Cu^{2+} on the intralayer kagomé site.

In the structures of $\text{Zn}_x\text{Cu}_{4-x}(\text{OH})_6\text{Cl}_2$ ($x = 0.33, 0.42, 1.00$), the crystals were selected from the reaction that produced the bulk sample of $\text{Zn}_{0.8}\text{Cu}_{3.2}(\text{OH})_6\text{Cl}_2$. Additional crystals were selected from aqueous zone refinement reactions of CuO with ZnCl_2 , with and without added HCl . One of the crystals studied (c04072b) is a specimen from a naturally occurring sample from the San Francisco Mine in Sierra Gorda, Chile, purchased from Simkev Minerals. None of the crystals showed significant decay during data collection. Data were integrated and corrected for

Lorentz and polarization effects with SAINT+ 6.22 and were corrected for absorption effects with SADABS 2.03.^{31,32}

Space group assignments were based on systematic absences, E^2 statistics, and successful refinement of the structures. Structures were solved by Patterson methods with the aid of successive difference Fourier maps and were refined against all data using SHELXL.³³ Thermal parameters for all non-hydrogen atoms were refined anisotropically. Hydrogen atoms were found in the difference-Fourier map, restrained to maintain an O-H bond distance of 0.82(3) Å, and refined with isotropic thermal parameters. For all structures reported herein, original refinements were carried out in which the Zn (interlayer) site was fully occupied by a Zn atom. Those refinements were compared with an alternative refinement strategy in which the site was occupied by a Cu/Zn mixture (the ratio was allowed to refine as a free variable). The Hamilton R-factor test³⁰ indicated that there was a statistically significant preference for Cu/Zn mixture on the interlayer site for several of the crystals ($x = 0.33$, $x = 0.42$, and $x = 0.76$) but not for the others. For the former structures, the Cu and Zn thermal parameters were constrained to be equal to each other using the eadp command for the same-site atoms.

In our analysis of the data, we note that since Zn^{2+} has a higher electron density within a given volume than Cu^{2+} , if Zn^{2+} is assigned to what is actually a Cu^{2+} site, U_{eq} will be too large. If Cu^{2+} is assigned to a Zn^{2+} site, U_{eq} will be too small. In comparing the models, in each instance we chose the model with the lowest R_1 and wR_2 factors as the best one.³⁰ If two models had equal values for these factors, we gave preference to the simpler one.

Table 4.4. R-factor statistical data on clinoatacamite: c04042a, $\text{Cu}_2(\text{OH})_3\text{Cl}$ in $P2_1/n$. See also Appendix A.3, Figures A.3.3 and Tables A.3.8-A.3.13.

	x	y	z	Occ.	U_{eq}	R_1	wR_2	Ratio
M_i	0.240592	0.235429	0.751546	11.00000				
M_{k1}	0.000000	0.500000	1.000000	10.50000				
M_{k2}	0.000000	0.000000	0.500000	10.50000				
Cu_i	All Cu (position 1 is interlayer)				0.0057	0.0290	0.0745	
Cu_{k1}					0.0060			
Cu_{k2}					0.0056			
Zn_i	All Zn				0.0069	0.0294	0.0772	
Zn_{k1}					0.0072			
Zn_{k2}					0.0068			
Zn_i	Zn on interlayer, all Cu on kagomé				0.0076	0.0300	0.0783	
Cu_{k1}					0.0050			
Cu_{k2}					0.0046			
Cu_i	Cu on interlayer, one Zn on kagomé				0.0054	0.0296	0.0768	
Zn_{k1}					0.0085			
Cu_{k2}					0.0052			
Cu_i	Cu on interlayer, one Zn on kagomé				0.0054	0.0297	0.0763	
Cu_{k1}					0.0057			
Zn_{k2}					0.0081			
Cu_i/Zn_i	All mix				0.0057	0.0290	0.0745	100/0(0.1)
$\text{Cu}_{k1}/\text{Zn}_{k1}$					0.0062			96/4(8)
$\text{Cu}_{k2}/\text{Zn}_{k2}$					0.0057			97/3(8)

The sample was synthesized according to Section 4.2.3 *Method 2* in the absence of Zn^{2+} ions and therefore provides a good control. The best and simplest model is the one where all metals are Cu. The model with all sites mixed does not provide any significant statistical improvement and is within error of the all-Cu model. Note how U_{eq} values get larger as Zn is (incorrectly) substituted onto the Cu sites.

Table 4.5. R-factor statistical data on mps3atest. See also Appendix A.3, Figure A.3.5 and Tables A.3.15-A.3.20.

	x	y	z	Occ.	U_{eq}	R_1	wR_2	Ratio
M_k	0.833333	0.166667	0.166667	10.25000				
M_i	1.000000	0.000000	0.000000	10.08333				
Cu_k	Intuitive (Cu on kagomé, Zn on interlayer)				0.0081	0.0207	0.0554	
Zn_i					0.0090			
Cu_k	All Cu				0.0085	0.0206	0.0531	
Cu_i					0.0062			
Zn_k	All Zn				0.0099	0.0217	0.0575	
Zn_i					0.0077			
Zn_k	Zn on kagomé, Cu on interlayer				0.0103	0.0232	0.0586	
Cu_i					0.0048			
Cu_k	Cu on kagomé, mix on interlayer				0.0082	0.0206	0.0554	100%
Zn_i/Cu_i	(EADP for same-site atoms)				0.0088			92/8(±5)
Cu_k/Zn_k	mix on kagomé, Zn on interlayer				0.0082	0.0207	0.0557	94/6(±5)
Zn_i					0.0089			100%
Cu_k/Zn_k	mix on kagomé, mix on interlayer				0.0083	0.0206	0.0554	95/5(±5)
Zn_i/Cu_i					0.0087			92/8(±5)

The best model is the one in which the kagomé site is 100% Cu and the interlayer site is 100% Zn. Trace Cu substitutions of 8% in the interlayer site cannot be ruled out from this analysis.

Table 4.6. R-factor statistical data on Zn_{0.42}-paratacamite: c04041a. See also Appendix A.3, Figures A.3.6 and Tables A.3.23-A.3.26.

	x	y	z	Occ.	U_{eq}	R_1	wR_2	Ratio
M_i	0.333333	0.666667	0.166667	10.08333				
M_k	0.166667	0.833333	0.333333	10.25000				
Zn_i Cu_k	Intuitive (Zn on interlayer, Cu on kagomé)				0.0095 0.0086	0.0224	0.0544	
Cu_i Cu_k	All Cu				0.0068 0.0090	0.0222	0.0494	
Zn_i Zn_k	All Zn				0.0082 0.0104	0.0231	0.0547	
Cu_i Zn_k	Cu on interlayer, Zn on kagomé				0.0054 0.0106	0.0252	0.0608	
Zn_i/Cu_i Cu_k	mix on interlayer, Cu on kagomé (EADP for same-site atoms)				0.0079 0.0088	0.0218	0.0483	41/59(±5) 100%
Zn_i Cu_k/Zn_k	Zn on interlayer, mix on kagomé				0.0092 0.0091	0.0221	0.0531	100% 77/23(±15)
Cu_i/Zn_i Zn_k/Cu_k	mix on interlayer, mix on kagomé				0.0090 0.0089	0.0220	0.0518	Not conclusive

The best model has 41% Zn and 59% Cu on the interlayer site, and 100% Cu on the kagomé site.

Table 4.7. R-factor statistical data on Zn_{0.76}-paratacamite: 08038_cu_mix. Synthesized from CuO + ZnCl₂ + HCl in zone furnace. See also Appendix A.3, Tables A.3.31-A.3.36.

	x	y	z	Occ.	U_{eq}	R_1	wR_2	Ratio
M_k	0.500000	0.500000	0.000000	10.25000				
M_i	0.333333	0.666667	0.166667	10.08333				
Cu_k Zn_i	Intuitive (Cu on kagomé, Zn on interlayer)				0.0051 0.0053	0.0112	0.0284	
Cu_k Cu_i	All Cu				0.0055 0.0035	0.0134	0.0330	
Zn_k Zn_i	All Zn				0.0061 0.0041	0.0146	0.0365	
Zn_k Cu_i	Zn on kagomé, Cu on interlayer				0.0064 0.0022	0.0189	0.0476	
Cu_k Zn_i/Cu_i	Cu on kagomé, mix on interlayer (EADP for same-site atoms)				0.0053 0.0049	0.0112	0.0282	100% 76/24(±8)
Cu_k/Zn_k Zn_i	mix on kagomé, Zn on interlayer				0.0052 0.0053	0.0112	0.0285	94/6(±8) 100%
Cu_k/Zn_k Zn_i/Cu_i	mix on kagomé, mix on interlayer partially isotropic in this case				0.0052 0.0049	0.0199	0.0548	97/3(±11) 86/14(±9)

The best model gives 100% Cu on the kagomé site, and 76% Zn and 24% Cu on the interlayer site.

Table 4.8. R-factor statistical data on herbertsmithite: c05017a. See also Appendix A.3, Figures A.3.7 and Tables A.3.33-A.3.38.

	<i>x</i>	<i>y</i>	<i>z</i>	Occ.	U_{eq}	R_1	wR_2	Ratio
M_k	0.833333	0.166667	0.166667	10.25000				
M_i	0.000000	0.000000	0.000000	10.08333				
Cu_k Zn_i	Intuitive (Cu on kagomé, Zn on interlayer)				0.0064 0.0068	0.0213	0.0642	
Cu_k Cu_i	All Cu				0.0068 0.0042	0.0222	0.0675	
Zn_k Zn_i	All Zn				0.0082 0.0055	0.0221	0.0656	
Zn_k Cu_i	Zn on kagomé, Cu on interlayer				0.0086 0.0027	0.0249	0.0697	
Cu_k Zn_i/Cu_i	Cu on kagomé, mix on interlayer (EADP for same-site atoms)				0.0066 0.0058	0.0213	0.0651	100% 60/40(±30)
Cu_k/Zn_k Zn_i	mix on kagomé, Zn on interlayer				0.0069 0.0065	0.0211	0.0643	70/30(±30) 100%
Cu_k/Zn_k Zn_i/Cu_i	mix on kagomé, mix on interlayer				0.0066 0.0059	0.0213	0.0651	100/0(±40) 60/40(±40)

The best model gives 100% Cu on the kagomé site, and 100% Zn on the interlayer site.

Table 4.9. R-factor statistical data on herbertsmithite: 07036. See also Appendix A.3, Tables A.3.39-A.3.45.

	<i>x</i>	<i>y</i>	<i>z</i>	Occ.	U_{eq}	R_1	wR_2	Ratio
M_i	0.666667	0.333333	0.333333	10.08333				
M_k	0.333333	0.166667	0.166667	10.25000				
Zn_i Cu_k	Intuitive (Zn on interlayer, Cu on kagomé)				0.0082 0.0081	0.0255	0.0669	
Cu_i Cu_k	All Cu				0.0062 0.0084	0.0278	0.0705	
Zn_i Zn_k	All Zn				0.0070 0.0092	0.0290	0.0744	
Cu_i Zn_k	Cu on interlayer, Zn on kagomé				0.0050 0.0095	0.0324	0.0830	
Zn_i/Cu_i Cu_k	mix on interlayer, Cu on kagomé (EADP for same-site atoms)				0.0082 0.0081	0.0255	0.0668	100/0(±3) 100%
Zn_i Cu_k/Zn_k	Zn on interlayer, mix on kagomé				0.0082 0.0081	0.0255	0.0669	100% 99/1(±7)
Cu_i/Zn_i Zn_k/Cu_k	mix on interlayer, mix on kagomé				0.0081 0.0081	0.0257	0.0673	100/0(±2) 100/0(±2)

The best model is the one in which the interlayer site is 100% Zn, and the kagomé site is 100% Cu.

Table 4.10. R-factor statistical data on herbertsmithite: 08039. Synthesized from CuO + ZnCl₂ in zone furnace. See also Appendix A.3, Tables A.3.46-A.3.52.

	x	y	z	Occ.	U_{eq}	R_1	wR_2	Ratio
M _k	0.500000	0.500000	0.000000	10.25000				
M _i	0.333333	0.666667	0.166667	10.08333				
Cu _k	Intuitive (Cu on kagomé, Zn on interlayer)				0.0074	0.0180	0.0466	
Zn _i					0.0075			
Cu _k	All Cu				0.0077	0.0204	0.0526	
Cu _i					0.0054			
Zn _k	All Zn				0.0086	0.0205	0.0520	
Zn _i					0.0062			
Zn _k	Zn on kagomé, Cu on interlayer				0.0089	0.0250	0.0620	
Cu _i					0.0042			
Cu _k	Cu on kagomé, mix on interlayer				0.0074	0.0180	0.0466	100%
Zn _i /Cu _i	(EADP for same-site atoms)				0.0075			99/1(±11)
Cu _k /Zn _k	mix on kagomé, Zn on interlayer				0.0075	0.0180	0.0466	96/4(±12)
Zn _i					0.0074			100%
Cu _k /Zn _k	mix on kagomé, mix on interlayer				0.0075	0.0180	0.0467	97/3(±11)
Zn _i /Cu _i					0.0074			98/2(±9)

The best and simplest model is the one in which the kagomé site is 100% Cu and interlayer site is 100% Zn. Trace substitutions cannot be ruled out, but the data support the pure model equally well.

Table 4.11. R-factor statistical data on herbertsmithite: c04072b. Naturally occurring specimen from Sierra Gorda, Chile. See also Appendix A.3, Tables A.3.53-A.3.58.

	x	y	z	Occ.	U_{eq}	R_1	wR_2	Ratio
M _k	0.166667	0.833333	0.333333	10.25000				
M _i	0.333333	0.666667	0.166667	10.08333				
Cu _k	Intuitive (Cu on kagomé, Zn on interlayer)				0.0077	0.0206	0.0512	
Zn _i					0.0079			
Cu _k	All Cu				0.0077	0.0218	0.0564	
Cu _i					0.0056			
Zn _k	All Zn				0.0086	0.0224	0.0591	
Zn _i					0.0065			
Zn _k	Zn on kagomé, Cu on interlayer				0.0088	0.0261	0.0693	
Cu _i					0.0043			
Cu _k	Cu on kagomé, mix on interlayer				0.0075	0.0206	0.0511	100%
Zn _i /Cu _i	(EADP for same-site atoms)				0.0078			95/5(±8)
Cu _k /Zn _k	mix on kagomé, Zn on interlayer				0.0075	0.0205	0.0513	98/2(±6)
Zn _i					0.0079			100%
Cu _k /Zn _k	mix on kagomé, mix on interlayer				0.0075	0.0206	0.0513	99/1(±6)
Zn _i /Cu _i					0.0078			95/5(±6)

The best model has the kagomé site as 100% Cu, and the interlayer site as 100% Zn within error.

Interestingly, Braithwaite *et al.* cite the existence of superlattice reflections in their single-crystal X-ray structures to support the contention of that there are locally ordered domains of Zn substitution on the interlayer site in paratacamite. They also note that such superlattice reflections disappear near the phase transition to clinoatacamite at $x = 0.33$ and near the herbertsmithite end-member material.²⁰ We do not note the presence of superlattice reflections in any of our paratacamite structures.

Future experiments on our herbertsmithite crystals might include conventional single-crystal X-ray studies using $\text{CuK}\alpha$ radiation, single-crystal anomalous X-ray scattering at a synchrotron source (a two-wavelength anomalous dispersion (δ synthesis) experiment should be applicable even to a centrosymmetric structure),⁴³ and single-crystal neutron structural determination. In our powder samples, it may also be possible to use other spectroscopic methods to distinguish Cu and Zn local site environments. There have been reports of the analysis of Cu-Zn solid solutions in the sanmartinite – cuproscheelite series ($\text{ZnWO}_4\text{--CuWO}_4$) using Cu-2p XAS and EXAFS, although the Cu EXAFS results were inconclusive.^{44,45}

4.4 Conclusions

This Chapter has discussed the synthesis and structures of the copper(II) hydroxychloride minerals: claringbullite, clinoatacamite, Zn-paratacamite, and herbertsmithite. Herbertsmithite bears a perfect kagomé lattice with layers isolated by the diamagnetic Zn^{2+} ion. Single-crystal X-ray studies show that existing crystals of the Zn-paratacamite/herbertsmithite series are statistically better modeled with exclusively Cu^{2+} on the kagomé plane, though, based on single crystal X-ray data with $\text{MoK}\alpha$, the antisite disorder model is within statistical error and cannot be ruled out entirely.

4.5 References

1. Fejer, E. E.; Clark, A. M.; Couper, A. G.; Elliott, C. J. *Mineral. Mag.* **1977**, *41*, 433-436.
2. Burns, P. C.; Cooper, M. A.; Hawthorne, F. C. *Can. Mineral.* **1995**, *33*, 633-639.
3. Hawthorne, F. C.; Schindler, M. *Can. Mineral.* **2000**, *38*, 751-761.
4. Feitknecht, W.; Maget, K. *Helv. Chim. Acta* **1949**, *32*, 1639-1653.
5. Wells, A. F. *Acta Crystallogr.* **1949**, *2*, 175-180.
6. Parise, J. B.; Hyde, B. G. *Acta Crystallogr. C* **1986**, *C42*, 1277-1280.
7. Hawthorne, F. C. *Mineral. Mag.* **1985**, *49*, 87-89.
8. Eby, R. K.; Hawthorne, F. C. *Acta Crystallogr. B.* **1993**, *B49*, 28-56.
9. Oswald, H. R.; Feitknecht, W. *Helv. Chim. Acta* **1964**, *47*, 272-289.
10. Frondel, C. *Mineral. Mag. J. Mineral. Soc.* **1950**, *29*, 34-45.
11. Fleet, M. E. *Acta Crystallogr. B* **1975**, *B31*, 183-187.
12. Sharkey, J. B.; Lewin, S. Z. *Am. Mineral.* **1971**, *56*, 181-194.
13. Pollard, A. M.; Thomas, R. G.; Williams, P. A. *Mineral. Mag.* **1989**, *53*, 557-563.
14. Feitknecht, W.; Maget, K. *Helv. Chim. Acta* **1949**, *32*, 1653-1667.
15. Feitknecht, W.; Maget, K. *Helv. Chim. Acta* **1949**, *32*, 1667-1674.
16. Nickel, E. H.; Clout, J. F. M.; Gartrell, B. J. *Mineral. Rec.* **1994**, *25*, 283-291, 302.
17. Clissold, M. E.; Leverett, P.; Williams, P. A.; Hibbs, D. E.; Nickel, E. H. *Can. Mineral.* **2007**, *45*, 317-320.
18. Grice, J. D.; Szymanski, J. T.; Jambor, J. L. *Can. Mineral.* **1996**, *34*, 73-78.
19. Jambor, J. L.; Dutrizac, J. E.; Roberts, A. C.; Grice, J. D.; Szymanski, J. T. *Can. Mineral.* **1996**, *34*, 61-72.
20. Braithwaite, R. S. W.; Mereiter, K.; Paar, W. H.; Clark, A. M. *Mineral. Mag.* **2004**, *68*, 527-539.
21. Lafontaine, M. A.; Le Bail, A.; Ferey, G. *J. Solid State Chem.* **1990**, *85*, 220-227.
22. Wills, A. S.; Raymond, S.; Henry, J. Y. *J. Magn. Magn. Mater.* **2004**, *272-276*, 850-851.

Chapter 4

23. Zheng, X. G.; Kawae, T.; Kashitani, Y.; Li, C. S.; Tateiwa, N.; Takeda, K.; Yamada, H.; Xu, C. N.; Ren, Y. *Phys. Rev. B* **2005**, *71*, 052409/052401-052409/052404.
24. Zheng, X. G.; Kubozono, H.; Nishiyama, K.; Higemoto, W.; Kawae, T.; Koda, A.; Xu, C. N. *Phys. Rev. Lett.* **2005**, *95*, 057201/057201-057201/057204.
25. de Wolff, P. M. *Acta Crystallogr.* **1953**, *6*, 359-360.
26. Malcherek, T.; Schlueter, J. *Acta Crystallogr. B.* **2007**, *B63*, 157-160.
27. Schluter, J.; Malcherek, T. *Neues Jahrb. Mineral., Abh.* **2007**, *184*, 39-43.
28. Krause, W.; Bernhardt, H. J.; Braithwaite, R. S. W.; Kolitsch, U.; Pritchard, R. *Mineral. Mag.* **2006**, *70*, 329-340.
29. Hawthorne, F. C.; Sokolova, E. *Can. Mineral.* **2002**, *40*, 939-946.
30. Hamilton, W. C. *Acta Crystallogr.* **1965**, *18*, 502-510.
31. SAINT; Bruker-AXS Inc.: Madison, Wisconsin, U.S.A., 2005.
32. Sheldrick, G. M. University of Goettingen, Germany, 2007.
33. Sheldrick, G. M. *Acta Crystallogr. A* **2008**, *A64*, 112-122.
34. Frost, R. L. *Spectrochim. Acta, Part A* **2003**, *59A*, 1195-1204.
35. Bartlett, B. M. Ph.D. Thesis, Massachusetts Institute of Technology, 2005.
36. de Vries, M. A.; Kamenev, K. V.; Kockelmann, W. A.; Sanchez-Benitez, J.; Harrison, A. *LANL, Preprint Archive, Condens. Matt.* **2007**, 1-4, arXiv:0705 0654v0701 [cond-mat str-el].
37. Lee, S. H.; Kikuchi, H.; Qiu, Y.; Lake, B.; Huang, Q.; Habicht, K.; Kiefer, K. *Nat. Mater.* **2007**, *6*, 853-857.
38. Bert, F.; Nakamae, S.; Ladiou, F.; L'Hote, D.; Bonville, P.; Duc, F.; Trombe, J. C.; Mendels, P. *Phys. Rev. B* **2007**, *76*, 132411/132411-132411/132414.
39. Olariu, A.; Mendels, P.; Bert, F.; Duc, F.; Trombe, J. C.; de Vries, M. A.; Harrison, A. *Phys. Rev. Lett.* **2008**, *100*, 087202/087201-087202/087204.
40. Rigol, M.; Singh, R. R. P. *Phys. Rev. Lett.* **2007**, *98*, 207204/207201-207204/207204.
41. Rigol, M.; Singh, R. R. P. *Phys. Rev. B* **2007**, *76*, 184403/184401-184403/184412.
42. Imai, T.; Nytko, E. A.; Bartlett, B. M.; Shores, M. P.; Nocera, D. G. *Phys. Rev. Lett.* **2008**, *100*, 077203/077201-077203/077204.

Chapter 4

43. Wulf, R. *Acta Crystallogr. A* **1990**, *A46*, 681-688.
44. Schofield, P. F.; Henderson, C. M. B.; Redfern, S. A. T.; van der Laan, G. *Phys. Chem. Miner.* **1993**, *20*, 375-381.
45. Schofield, P. F.; Charnock, J. M.; Cressey, G.; Henderson, C. M. B. *Mineral. Mag.* **1994**, *58*, 185-199.

Chapter 5.
Magnetism of Copper(II) Hydroxylchloride Minerals, Spin Liquid States, and the Search for RVB Superconductivity

Portions of this work have been published as Shores, M. P.; Nytko, E. A.; Bartlett, B. M.; Nocera, D. G. *J. Am. Chem. Soc.* **2005**, *127*, 13462-13463.

5.1 Introduction

We have undertaken detailed investigations of the magnetic properties of the copper(II) hydroxychloride minerals—claringbullite, clinoatacamite, and Zn-paratacamite/herbertsmithite—presented in the previous Chapter. The results of these studies are discussed in the first part of this Chapter. The second part of this Chapter details our motivation for attempting redox chemistry and bulk electrochemistry on herbertsmithite powder samples and presents the outcomes of these experiments. We conclude with an outlook for future work on this project.

5.2 Experimental

5.2.1 Magnetic Measurements

DC magnetic susceptibility data were collected on (ground-up) crystalline samples contained in gelatin capsules using Quantum Design MPMS-5S and MPMS-XL SQUID magnetometers at temperatures ranging from 2 to 350 K and field strengths varying from -50 to 50 kOe.

5.2.2 Electrochemical Measurements

Preliminary electrochemical measurements have been carried out for $\text{ZnCu}_3(\text{OH})_6\text{Cl}_2$ on an ITO (indium tin oxide) surface. Initial experiments were performed on ground $\text{ZnCu}_3(\text{OH})_6\text{Cl}_2$ supported by Nafion, a sulfonated tetrafluorethylene copolymer. A solution of 5% Nafion in a mixture of lower aliphatic alcohols and water was purchased from Fluka. The measurements were carried out in acetonitrile with 1 M tetrabutylammonium hexafluorophosphate as an electrolyte. The three electrodes used were: the Nafion supported sample on ITO as the working electrode, a Pt mesh counterelectrode, and a saturated Ag/AgCl (+0.197 V vs. NHE) reference electrode.

5.3 Results

5.3.1 Magnetic Properties of Claringbullite

The DC susceptibility of claringbullite, $\text{Cu}_4(\text{OH})_x\text{Cl}_y\text{F}_z$ ($x + y + z = 8$), shown in Figure 5.1.a, exhibits a ferromagnetic ordering at 17 K. Magnetization versus field at 5 K (Figure 5.1.b) shows hysteresis with a coercive field of $H_{\text{coercive}} = 300$ Oe and a remanent magnetization of $M_r = 295$ emu Oe / mol Cu. Curie-Weiss analysis of χ^{-1} from 200 – 300 K (Figure 5.2) reveals mean antiferromagnetic nearest neighbor exchange with $\Theta = -177$ K, indicating a frustrated system with $f = 10.4$.

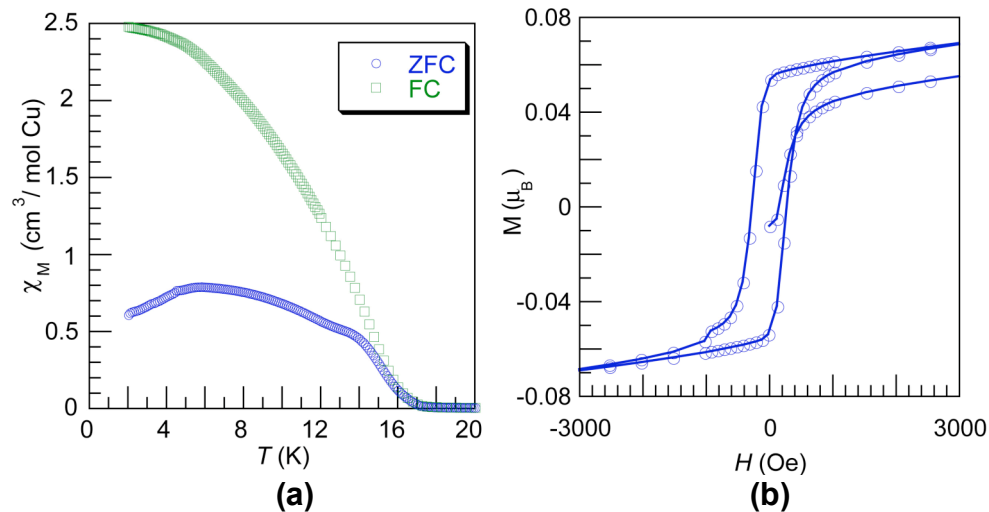


Figure 5.1. (a) ZFC (\circ) and FC (\square) susceptibility of $\text{Cu}_4(\text{OH})_x\text{Cl}_y\text{F}_z$, measured with 100 Oe field. For FC, $H_C = 100$ Oe. (b) Magnetization of $\text{Cu}_4(\text{OH})_x\text{Cl}_y\text{F}_z$ showing hysteresis at 5 K.

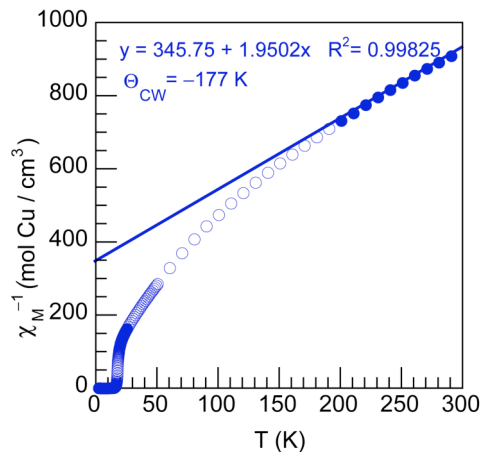


Figure 5.2. Curie-Weiss plot for $\text{Cu}_4(\text{OH})_x\text{Cl}_y\text{F}_z$ ($x + y + z = 8$).

5.3.2 Magnetic Properties of Clinoatacamite

Figure 5.3.a shows the DC susceptibility plot of clinoatacamite, $\text{Cu}_2(\text{OH})_3\text{Cl}$, which exhibits evidence of a ferromagnetic ordering transition at 6.5 K. Magnetization versus field at 2 K (Figure 5.3.b) shows hysteresis with a coercive field of $H_{\text{coercive}} = 1090$ Oe and a remanent magnetization of $M_r = 445$ emu Oe / mol Cu. Curie-Weiss analysis of χ^{-1} from 150 – 350 K (Figure 5.6) reveals mean antiferromagnetic nearest neighbor exchange with $\Theta = -194$ K, indicating a frustrated system with $f = 29.8$. A frequency independent maximum in the AC susceptibility precludes the presence of spin glass behavior in clinoatacamite (Figure 5.4).

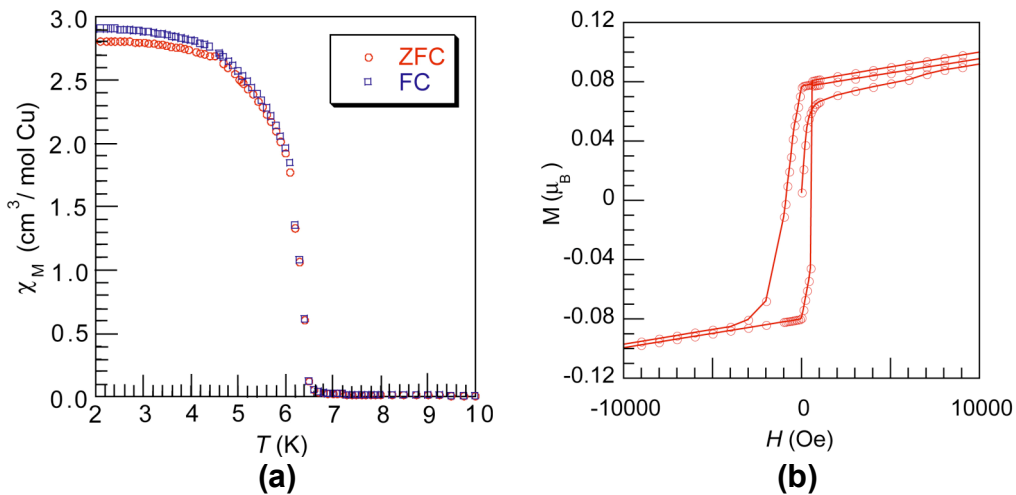


Figure 5.3. (a) ZFC (\circ) and FC (\square) susceptibility of $\text{Cu}_2(\text{OH})_3\text{Cl}$, measured with 100 Oe field. For FC, $H_C = 100$ Oe. (b) Magnetization of $\text{Cu}_2(\text{OH})_3\text{Cl}$ showing hysteresis at 2 K.

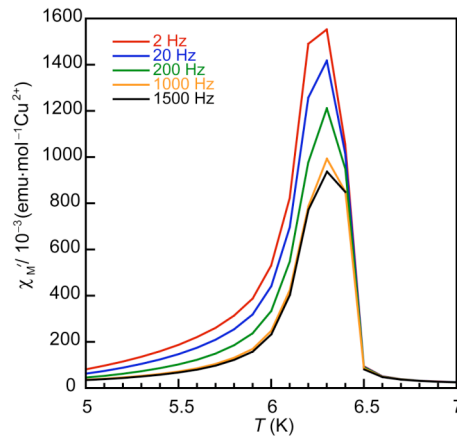


Figure 5.4. Frequency independent maximum in the AC susceptibility of $\text{Cu}_2(\text{OH})_3\text{Cl}$.

5.3.3 Magnetic Properties of Zn-Paratacamites and Herbertsmithite

The DC susceptibility plots of $\text{Zn}_x\text{Cu}_{4-x}(\text{OH})_6\text{Cl}_2$ ($0 \leq x \leq 1$) are shown in Figure 5.5.a. As Zn(II) ions are substituted onto the interlayer site, a ferromagnetic transition is maintained, but T_c decreases. At full Zn(II) occupancy, no magnetic ordering is observed for $\text{ZnCu}_3(\text{OH})_6\text{Cl}_2$: first to the 2 K temperature limit of the SQUID susceptometer and then to 50 mK in an AC susceptibility measurement at the National High Field Magnet Laboratory in Tallahassee, FL (in collaboration with Professor Young Lee's group at MIT).¹ $\text{ZnCu}_3(\text{OH})_6\text{Cl}_2$ also shows no measurable hysteresis at 2 K (Figure 5.7.b), further indicating no ferromagnetic component to its magnetism. Fits of the high temperature inverse susceptibility for the series $\text{Zn}_x\text{Cu}_{4-x}(\text{OH})_6\text{Cl}_2$ ($0 \leq x \leq 1$) to the Curie-Weiss Law yield large negative Θ values (Figure 5.6). Figure 5.5.b shows that $|\Theta|$ increases monotonically as more Zn is incorporated into the interlayer site, reaching a maximum value of 314 K for the $x = 1$ end-member material herbertsmithite, $\text{ZnCu}_3(\text{OH})_6\text{Cl}_2$. T_c ,

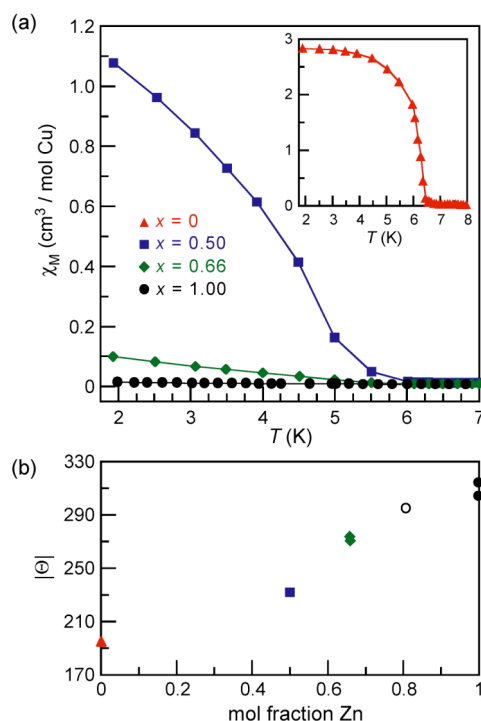


Figure 5.5. (a) Low temperature dependence of χ_M for compounds in the solid solution $\text{Zn}_x\text{Cu}_{4-x}(\text{OH})_6\text{Cl}_2$ for $x = 0$ (red, \blacktriangle), 0.50 (blue, \blacksquare), 0.66 (green, \blacklozenge), and 1.00 (black, \bullet) as measured under ZFC conditions at 100 Oe (inset, $x = 0$). Lines are shown to guide the eye. (b) Dependence of $|\Theta|$ on interlayer site occupancy, the additional point is for $x = 0.80$ (\circ).

Θ , and f values are tabulated in Table 5.1. Evaluation of the frustration parameter,² f , indicates that all compounds studied have a high degree of spin frustration, and f increases monotonically over the series. The value of this parameter for herbertsmithite is greater than 6280 but otherwise unquantifiably large, thus making herbertsmithite the most frustrated structurally perfect pure kagomé compound ever studied.

Table 5.1. T_c , Θ , and f for clinoatacamite/Zn-paratacamite/herbertsmithite series.

x	T_c (K)	Θ (K)	f
0	6.5	-194	29.8
0.50	5.5	-231	42
0.66	5	-272	54.4
1	< 50 mK	-314	> 6280

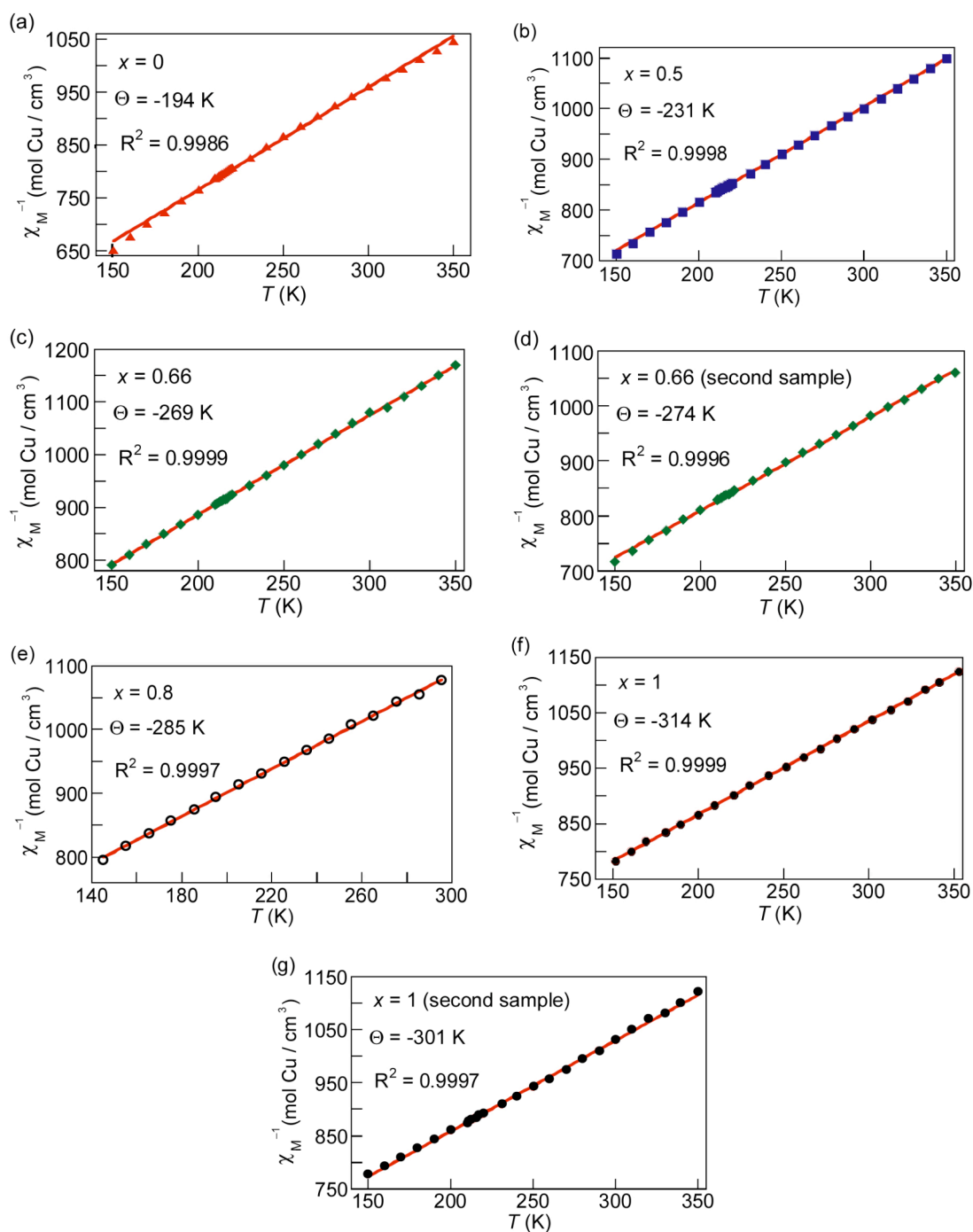


Figure 5.6. Temperature dependence of χ_M^{-1} for Zn_xCu_{4-x}(OH)₆Cl₂. Values for Θ were determined by fitting data in the temperature range $150 \leq T \leq 350$ K, except for $x = 0.8$, which was fit from 200 to 300 K. Red lines indicate best fits obtained.

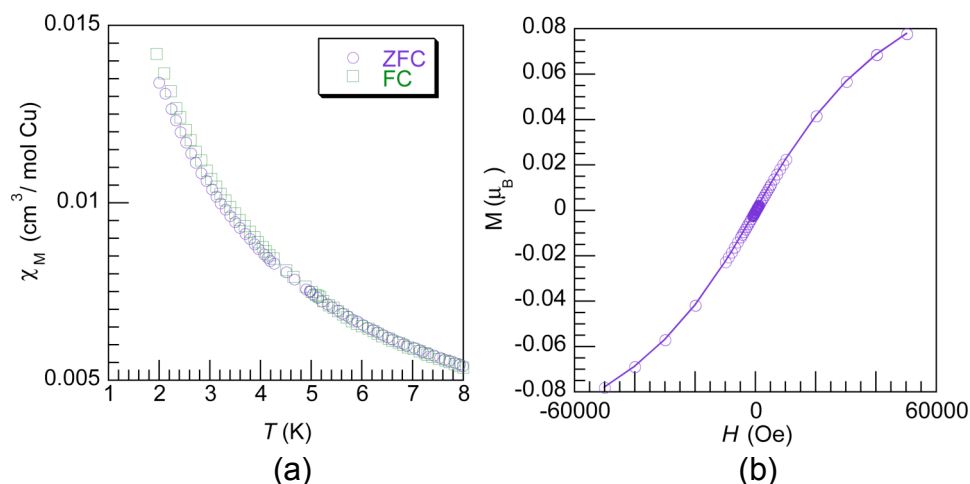


Figure 5.7. (a) ZFC (\circ) and FC (\square) susceptibility of $\text{ZnCu}_3(\text{OH})_6\text{Cl}_2$, measured with 100 Oe field, and showing no transition to LRO. For FC, $H_C = 100$ Oe. (b) Magnetization (\circ) versus field of $\text{ZnCu}_3(\text{OH})_6\text{Cl}_2$ shows no measurable hysteresis at 2 K.

Finally, Figure 5.8 presents the magnetic susceptibility of a single crystal from a naturally occurring sample of herbertsmithite (purchased from Simkev Minerals in Ontario, CA) from the San Francisco Mine in Sierra Gorda, Chile. The susceptibility data were taken by K. Matan. A single crystal from the same specimen was analyzed crystallographically (see Table 4.11) and found to contain 100 % Cu on the kagomé site and 100% Zn on the interlayer site within error. This result highlights the necessity of synthetic inorganic chemistry for producing (and characterizing) materials of adequate purity for magnetic studies, as the natural sample shows transitions below 6.5 K that are absent in the pure powder sample of synthetic herbertsmithite, $\text{ZnCu}_3(\text{OH})_6\text{Cl}_2$ (Figure 5.7). The natural sample, therefore, contains phase impurities that inhibit its use for studies of spin frustration physics.

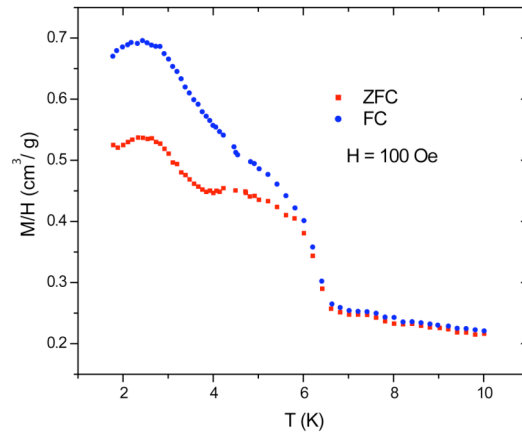


Figure 5.8. ZFC (■, red) and FC (●, blue) mass susceptibility of crystalline $\text{ZnCu}_3(\text{OH})_6\text{Cl}_2$ specimen from the San Francisco Mine in Sierra Gorda, Chile.

5.4 Discussion of Magnetic Properties

The magnetism of the minerals discussed above—claringbullite, clinoatacamite, and the $\text{Zn}_x\text{Cu}_{4-x}(\text{OH})_6\text{Cl}_2$ series, where $0.33 \geq x \geq 1$ —shows the effects of strong geometric frustration, which inhibits the tendency for spins to order and hence suppresses T_c relative to Θ . Claringbullite exhibits a ferromagnetic ordering transition at $T_c = 17$ K despite having $\Theta = -177$ K, indicating a frustrated system with $f = 10.4$. Clinoatacamite orders at 6.5 K with $\Theta = -194$ K for $f = 29.8$. We note a monotonic increase in $|\Theta|$ as more Zn is incorporated into the interlayer site in the $\text{Zn}_x\text{Cu}_{4-x}(\text{OH})_6\text{Cl}_2$ series, reaching a maximum at 314 K for $x = 1$; at the same time, T_c exhibits a monotonic decrease, until we see no ordering behavior at all to 50 mK for the $x = 1$ herbertsmithite material.

A mean-field theory analysis of Θ gives isotropic values for J , the nearest-neighbor exchange coupling constant (Equation 1.3). Evaluating this expression for J yields -82 cm⁻¹ for claringbullite, -90 cm⁻¹ for clinoatacamite, and -218 cm⁻¹ for herbertsmithite. We note that z in this equation, the number of paramagnetic nearest neighbors, is six for the former compounds, but only four for the latter. In all of these compounds, each Cu(II) ion has four nearest-neighbor

ions in the kagomé plane. An additional two Cu(II) ions reside above and below the kagomé planes in both claringbullite and clinoatacamite (as shown in Figure 4.13). In herbertsmithite, these Cu(II) ions are replaced by diamagnetic Zn(II), which serves to isolate the layers magnetically. Because the J values obtained for claringbullite and clinoatacamite are more positive than those obtained for herbertsmithite, they indicate a ferromagnetic component to the magnetism in the former two compounds, consistent with the observation of ferromagnetic ordering and hysteresis below T_c in both.

We can rationalize the magnetic behavior of the Cu(II) hydroxychloride minerals through a Goodenough-Kanamori analysis³⁻⁶ of the Cu–O–Cu superexchange pathways. Superexchange with σ -symmetry in a d^9 system is predicted to be antiferromagnetic for bridge angles between $\sim 90^\circ$ and 180° because of strong orbital overlap between the metal $d_{x^2-y^2}$ and the bridging ligand sp^3 hybrid orbital, and ferromagnetic for bridge angles less than $\sim 90^\circ$ because of orbital orthogonality in this pathway. Hatfield and Hodgson's magnetostructural analysis of μ -hydroxy-bridged Cu(II) dimers is in line with Goodenough-Kanamori predictions and supports this contention, yielding a critical angle of 97.54° for crossover between antiferromagnetic and ferromagnetic exchange in μ -hydroxy-bridged Cu(II) dimers.⁷ A strong σ -symmetry superexchange pathway involving $\text{Cu}(d_{x^2-y^2})\text{—O}(sp^3)\text{—Cu}(d_{x^2-y^2})$ within the kagomé is common to the Cu(II) hydroxychloride minerals, and from Table 4.3 these $\text{Cu}_{\text{intra}}\text{—O—Cu}_{\text{intra}}$ angles are 117.8° in claringbullite, 119.4° (average) in clinoatacamite, and 119.1° in herbertsmithite. Such angles, therefore, are expected to give rise to strong antiferromagnetic exchange within the kagomé planes, consistent with large negative values of Θ and J .

With the introduction of Cu(II) ions into the interlayer site in the $\text{Zn}_x\text{Cu}_{4-x}(\text{OH})_6\text{Cl}_2$ series, as well as in clinoatacamite and claringbullite, a ferromagnetic exchange interaction is

engendered owing to the introduction of an additional $\text{Cu}_{\text{intra}}\text{-O-Cu}_{\text{inter}}$ superexchange pathway. From Table 4.3, this angle averages 97.6° in claringbullite and 96.5° in clinoatacamite, accounting for the observation of a ferromagnetic ordering temperature and hysteresis below that temperature in both compounds. The strongly frustrated interactions in the kagomé plane, however, inhibit observation of an antiferromagnetic ordering transition which, based on values of Θ , would be expected at 177 K and 194 K respectively, were these systems not frustrated.

Clinoatacamite and claringbullite have similar kagomé structures (Table 4.3) and indeed show similar bulk magnetic behavior: both show a transition to 3-D ferromagnetic LRO. The transitions do, however, occur at slightly different temperatures (17 K for claringbullite and 6.5 K for clinoatacamite). Although single-crystal neutron studies are obviously needed to assign spin structures, a number of interesting observations can be made, with the caveat that such observations are only speculative. First, although the SQUID data for clinoatacamite are featureless to 6.5 K, several authors have observed a subtle feature in muon spin rotation (μSR) measurements and heat capacity measurements at 18 K,⁸⁻¹¹ indicating the possibility of some type of LRO developing in clinoatacamite at that temperature. Interestingly, this 18 K temperature is very close to the 17 K temperature at which claringbullite shows ferromagnetic 3-D LRO. In Chapter 4, we noted that despite the similarities of their in-kagomé-plane structures, there is a difference in packing structures between clinoatacamite and claringbullite, with clinoatacamite featuring ABC packing and claringbullite featuring AA packing of layers. The argument can be made, furthermore, that an ABC packing configuration is more frustrating than an AA arrangement of layers.¹² Is clinoatacamite undergoing some weak transition to 2-D order (perhaps due to DM) at 18 K and then showing a further transition to 3-D order at 6.5 K due to out-of-plane superexchange? Do these transitions coincide at 18 K in claringbullite, which

is a less frustrated structure because of the AA manner in which its layers pack?

We have synthesized herbertsmithite and studied its magnetic properties. With no interlayer Cu(II) ion, it is the first example of a structurally perfect $S = \frac{1}{2}$ kagomé with magnetically isolated layers and shows no evidence of LRO to 50 mK. With pure deuterated powder in hand, we undertook various physical measurements with collaborators to see if this material fits the predictions for the ground state of an $S = \frac{1}{2}$ kagomé Heisenberg antiferromagnet. The results of these experiments shed some light on the theoretical discussion of whether or not the $S = \frac{1}{2}$ kagomé will support an RVB spin liquid phase with a finite singlet-triplet gap (short range dimer correlations)¹³⁻¹⁷ and are summarized below.

5.5 Summary of Neutron Scattering Results

Our results showed the absence of magnetic ordering or a spin gap to 50 mK. We saw a near temperature independence of the inelastic scattering for positive energy transfers, the absence of a spin gap to 0.1 meV at 35 mK, diffuse scattering that pointed to the absence of a well-defined length scale to describe the dimer spin correlations, and only 20% of the total scattering expected for a $S = \frac{1}{2}$ spin system from the triple-axis measurement.¹ Taken together, these data indicate that singlets are not restricted to nearest-neighbor dimers in herbertsmithite, raising the intriguing possibility that longer range RVB-like spin liquid states^{18,19} may exist on the $S = \frac{1}{2}$ kagomé.

5.6 Summary of Results of Local Probe Measurements: ^{63}Cu , ^{35}Cl , ^1H NMR and μSR (muon spin rotation)

We note that the susceptibility of herbertsmithite continually increases to 50 mK; such an increase may suggest the presence of a Curie tail due to free $S = \frac{1}{2}$ spins. However, fitting the data to a Brillouin function yields values much lower than expected than for the free spin prediction. Muon spin rotation measurements undertaken in collaboration with Amit Keren show

that the muon Knight shift and transverse relaxation rate have temperature dependences similar to the measured susceptibility,²⁰ indicating that the measured susceptibility may be intrinsic to the kagomé system.

³⁵Cl NMR measurements, undertaken in collaboration with Takashi Imai, indicate that the mysterious increase in χ_{bulk} and the upturn in the ³⁵K (the ³⁵Cl NMR Knight Shift) is indicative of local ordering behavior. The peak in ³⁵(1/T₁) near 50 K arises from lattice freezing. The quadrupole split satellite transitions of ³⁵Cl NMR show no noticeable change, indicating no Zn/Cu antisite disorder on the lattice. Taken together, these results indicate that OH bonds may be freezing with random orientations below 50 K.²¹ To the extent that local symmetry may break down from this freezing, DM interactions in herbertsmithite^{22,23} may be enhanced.

5.7 Doping an $S = \frac{1}{2}$ Kagomé: RVB-Like Spin Liquid Phases and Superconductivity?

Will a doped $S = \frac{1}{2}$ kagomé lattice support an RVB spin-liquid type phase or RVB superconductivity? This question has intrigued theorists.²⁴ We sought to answer this question experimentally by exploring the redox and electrochemistry of ZnCu₃(OH)₆Cl₂. First, however, we should recall how the RVB picture works in theory for doped La₂CuO₄.

Section 1.2 discussed how undoped La₂CuO₄ orders antiferromagnetically, behaving as a Mott insulator.^{25,26} The material only becomes superconducting at high enough hole concentrations and low enough temperatures.²⁵⁻²⁷ In the RVB picture, $S = \frac{1}{2}$ lattices are important because strong quantum fluctuations favor singlet formation rather than classical Néel ordering behavior, which is believed to destroy the RVB spin liquid phase.²⁸

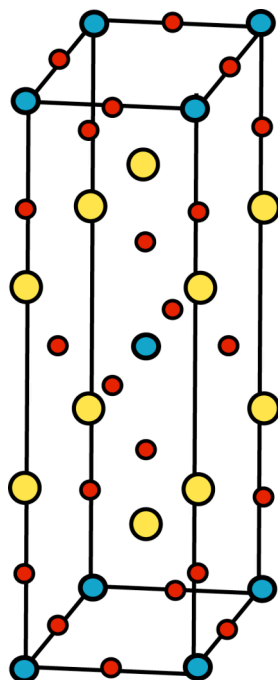


Figure 5.9. Tetragonal unit cell of La_2CuO_4 , showing square-planar CuO_2 layers. Cu atoms are in teal, O in red, and La in yellow.

The parent La_2CuO_4 (La214) compound crystallizes with the tetragonal K_2NiF_4 structure,²⁹ shown in Figure 5.9, but undergoes a phase transition at approximately 533 K^{30,31} to a lower symmetry orthorhombic structure in which the CuO_6 octahedra are further tilted. Hole doping in La_2CuO_4 has typically been achieved synthetically through annealing with divalent metal ions as for $\text{La}_{(2-x)}(\text{Ba,Sr})_x\text{CuO}_{4-y}$ ³² or annealing under excess oxygen, as with $\text{LaCu}_2\text{O}_{4+y}$.³³⁻³⁵ Bulk electrochemical methods are also known in the processing of LaCu_2O_4 to $\text{LaCu}_2\text{O}_{4+y}$,³⁶⁻⁴⁰ as are chemical oxidations with NaClO ⁴¹⁻⁴⁶ and KMnO_4 .⁴⁷⁻⁵⁰ The kinetics of both chemical and electrochemical methods for doping La_2CuO_4 , however,

depend heavily on the porosity of the material, and so the annealing processes have acquired more standard laboratory usage.

Will an oxidation of $\text{ZnCu}_3(\text{OH})_6\text{Cl}_2$ be reversible, or will the compound decompose?

The hydroxy ligand environment of copper(II) in $\text{ZnCu}_3(\text{OH})_6\text{Cl}_2$ presents a readily apparent challenge: Cu^{3+} is known to be unstable in such ligand environments. Cyclic voltammetry studies

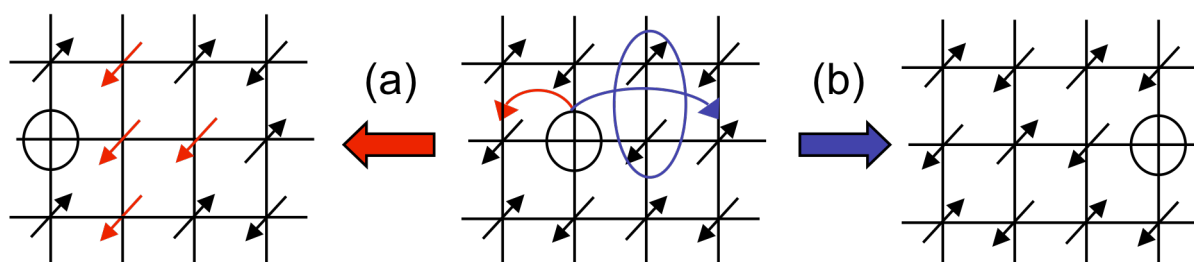


Figure 5.10. Transport in hole-doped lanthanum cuprates. In (a), nearest-neighbor hole hopping mechanism would result in frustration, but in (b), transport through a singlet pair in an RVB spin liquid does not create frustration.

of copper pertellurates and periodates in basic aqueous media show a $\text{Cu}^{2+}/\text{Cu}^{3+}$ couple at 614 mV vs. NHE.⁵¹⁻⁵³ The reaction is irreversible at low pH and only quasi-reversible at high pH, where the Cu(II) to Cu(III) oxidation occurs more facilely but where $\text{Cu}(\text{OH})_2$ precipitates from solution if inadequate concentrations of counterion are present. Adding aqueous hydroxide or amine bases to the materials prepared in Chapter 4 will result in precipitation of CuO, thus inhibiting our use of oxidants that require added base.

Doping *electrons* to form superconducting lanthanide cuprate phases is also known, though these materials generally contain Nd^{3+} instead of La^{3+} . The parent compound Nd_2CuO_4 still consists of CuO_2 square planes but differs slightly from La_2CuO_4 in the oxygen coordination environment of the lanthanide atoms.⁵⁴ Typically such materials are annealed in the presence of tetravalent metals under various partial pressures of oxygen, as is the case with $\text{Nd}_{2-x}\text{Ce}_x\text{CuO}_{4-y}$.^{55,56} We also tried some reduction chemistry of $\text{ZnCu}_3(\text{OH})_6\text{Cl}_2$, noting that the $\text{Cu}^{2+}/\text{Cu}^+$ standard reduction potential is 0.16 V.

5.7.1 Redox Chemistry of $\text{ZnCu}_3(\text{OH})_6\text{Cl}_2$

Powder samples of $\text{ZnCu}_3(\text{OH})_6\text{Cl}_2$ were treated under various conditions with various oxidants and reductants. The desired goal of these experiments was to observe oxidation or reduction chemistry with no change in lattice structure of $\text{ZnCu}_3(\text{OH})_6\text{Cl}_2$. A successful experiment, then, would show no change by pXRD but would show a large diamagnetic susceptibility at a certain critical temperature as measured by SQUID, indicative of the Meissner effect and the onset of superconductivity. The conditions for these reactions are summarized in Table 5.2.

Table 5.2. Summary of Redox Chemistry of $\text{ZnCu}_3(\text{OH})_6\text{Cl}_2$.

Oxidant	Conditions	Results
O_3 / air	10:1 CH_2Cl_2 , 0 °C, 20 mins.	NR, no difference in χ
xs NaOCl, stoich. NaOH	H_2O , RT, stir in air, 30 mins.	CuO
xs NaOCl, no added base	H_2O , RT, stir in air, 96 h.	NR, no difference in χ
stoich. $\text{Na}_2\text{S}_2\text{O}_8$	H_2O , RT, stir in air, 93 h.	NR, no difference in χ
stoich. $\text{Na}_2\text{S}_2\text{O}_8$, stoich. NaOH	H_2O , RT, stir in air, 93 h.	Gray-green powder, NR by pXRD, no difference in χ
stoich. $\text{Na}_2\text{S}_2\text{O}_8$	H_2O , reflux 100 °C in air, 48 h.	Messy, $\text{Na}_2\text{Cu}_2(\text{SO}_4)_2 \cdot 2\text{H}_2\text{O}$, among other phases
stoich. KMnO_4	H_2O , RT, stir in air, 50 h	Paratacamite substructure + $\text{CuCl}_2(\text{H}_2\text{O})_2$
stoich. KMnO_4	H_2O , reflux 100 °C in air, 50 h.	Green-brown powder, NR by pXRD, no difference in χ
stoich. H_2O_2	H_2O , reflux 100 °C in air, 50 h.	Green-brown powder, NR by pXRD, no difference in χ
Reductant	Conditions	Results
KO_2	Reflux CH_3CN , Ar, 18 h.	Gray-black powder, NR by pXRD, no difference in χ
Na	Reflux <i>o</i> -xylene, Ar, 18 h.	Paratacamite substructure + CuO
Na-naphthalide	Reflux THF, Ar, 18 h.	Paratacamite substructure

When chemistry is observed in the reactions in Table 5.1, it is either acid-base chemistry or other lattice decomposition chemistry. The darkening in color of some of the products likely indicates some surface decomposition that may go undetected by pXRD and SQUID. We note that impurities of up to 5% by mass can go undetected in pXRD, and that although CuO orders antiferromagnetically at 230 K, it shows a broad maximum in its susceptibility centered at 550 K, making it difficult to detect by SQUID measurement.^{58,59} A control experiment for characterization involved physical mixing of CuO and pure herbertsmithite phases in an attempt to detect CuO on the SQUID. The parent sample of herbertsmithite had $\Theta = -314$ K, while 1% and 3% by mass doped samples had -331 and -342 K respectively. In the attempted redox reactions analyzed by SQUID measurements, no such change in the value of Θ was noted.

Oxidation chemistry might be problematic in $\text{ZnCu}_3(\text{OH})_6\text{Cl}_2$ because in order to balance the positive charge that accumulates after loss of an electron, either cations must be lost or

bridging hydroxy groups must be deprotonated. Zn^{2+} is necessary to hold the layers together electrostatically, and addition of hydroxide or amine bases yields CuO and/or soluble blue aminocopper species, presumably through the deprotonation of the hydroxy layers.

5.7.2 Electrochemistry of $\text{ZnCu}_3(\text{OH})_6\text{Cl}_2$

Figure 5.11 shows the cyclic voltammogram of a ground powder sample of $\text{ZnCu}_3(\text{OH})_6\text{Cl}_2$, starting at an open circuit potential of 1 V and scanning cathodically under the conditions described in Section 5.2.2. We see an irreversible reduction wave occurring around 300 mV vs. Ag/AgCl (~ 500 mV vs. NHE). There is no corresponding oxidation wave. The peak current decays with successive cycles and a soluble, yellow product appears, indicating sample decomposition. No other oxidation is observed within the solvent window of CH_3CN .

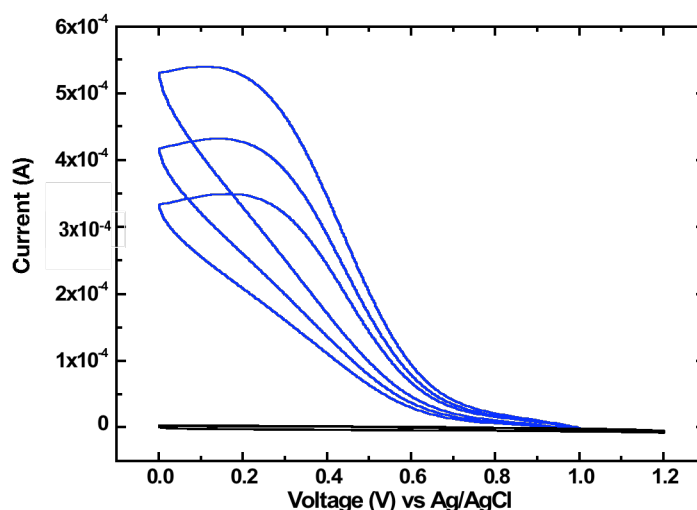


Figure 5.11. Cyclic voltammogram of ground powder sample of $\text{ZnCu}_3(\text{OH})_6\text{Cl}_2$, starting at an open circuit potential of 1 V and scanning cathodically. The peak current decays with successive cycles. The lowest line, shown here in black, corresponds to the measured background current.

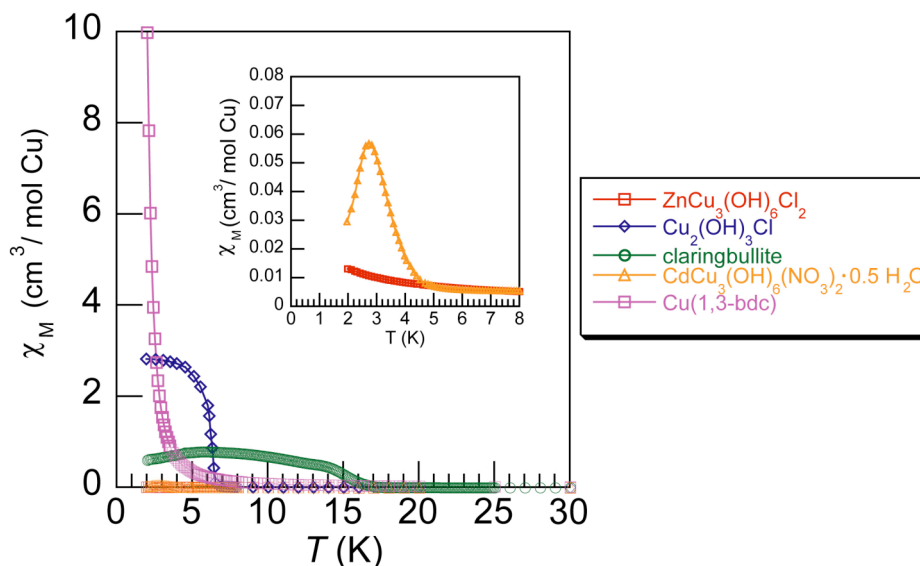


Figure 5.12. ZFC magnetic susceptibility versus temperature for the compounds prepared in this Thesis. $H_{meas} = 100$ Oe. Inset: Enlargement of scale showing susceptibility behavior of $\text{CdCu}_3(\text{OH})_6(\text{NO}_3)_2 \cdot 0.5 \text{H}_2\text{O}$ and $\text{ZnCu}_3(\text{OH})_6\text{Cl}_2$.

Table 5.3. T_c , Θ , and f for frustrated $S = \frac{1}{2}$ kagomé systems presented in this Thesis.

	T_c (K)	Θ (K)	f
$\text{Cu}(1,3\text{-bdc})$	2	-33	16.5
$\text{CdCu}_3(\text{OH})_6(\text{NO}_3)_2 \cdot 0.5\text{H}_2\text{O}$	5	-114	22.8
$\text{Cu}_4(\text{OH})_x\text{Cl}_y\text{F}_z$ ($x + y + z = 8$)	17	-177	10.4
$\text{Cu}_2(\text{OH})_3\text{Cl}$	6.5	-194	29.8
$\text{Zn}_{0.50}\text{Cu}_{3.50}(\text{OH})_6\text{Cl}_2$	5.5	-231	42
$\text{Zn}_{0.66}\text{Cu}_{3.34}(\text{OH})_6\text{Cl}_2$	5	-272	54.4
$\text{ZnCu}_3(\text{OH})_6\text{Cl}_2$	< 50 mK	-314	> 6280

5.8 Conclusions and Future Outlook

Prior to the inception of this Thesis work, no structurally perfect $S = \frac{1}{2}$ kagomé compound existed for testing of theoretical predictions on this important lattice.⁶⁰ This Thesis work has presented the optimization of kagomé systems to maximize geometric frustration and minimize interlayer exchange—we moved from covalently linked layers in a MOF kagomé, to hydrogen-bonded layers in $\text{CdCu}_3(\text{OH})_6(\text{NO}_3)_2 \cdot 0.5\text{H}_2\text{O}$, to electrostatically linked layers in the Cu(II) hydroxychloride minerals—culminating in the synthesis of a 2-D system with

magnetically isolated kagomé layers, herbertsmithite, $\text{ZnCu}_3(\text{OH})_6\text{Cl}_2$. The low temperature magnetic susceptibility data for these compounds is compared in Figure 5.12. Table 5.3 summarizes the values of Θ , T_c , and the frustration parameter f for all compounds presented herein. $\text{ZnCu}_3(\text{OH})_6\text{Cl}_2$ shows no LRO to 50 mK despite $\Theta = -314$ K, indicative of strong frustration and spin liquid behavior. Furthermore, gapless excitations in the neutron scattering data indicate that singlet pairs are not restricted to nearest neighbors and that a longer range RVB-like spin liquid state might exist on this $S = \frac{1}{2}$ kagomé.

What is the precise nature of herbertsmithite's spin liquid state? Does the spin liquid state observed reflect the intrinsic properties of the $S = \frac{1}{2}$ kagomé? To answer these questions conclusively, we must perform neutron scattering measurements on sufficiently large single crystals. Our X-ray results indicate that the crux of this problem and the future of this project lie not only in our ability to synthesize crystals but also in our ability to characterize these materials. To direct our efforts at synthesis of larger crystals, we must develop a means of rapid characterization to assess adequately the success of our crystal-growing reactions, in which a large number of small crystals of varying interlayer Zn^{2+} content are routinely formed. Future efforts should be directed towards crystal growth and characterization, as well as further exploration of redox chemistry and electrochemistry of the herbertsmithite system.

5.9 References

1. Helton, J. S.; Matan, K.; Shores, M. P.; Nytko, E. A.; Bartlett, B. M.; Yoshida, Y.; Takano, Y.; Suslov, A.; Qiu, Y.; Chung, J. H.; Nocera, D. G.; Lee, Y. S. *Phys. Rev. Lett.* **2007**, *98*, 107204.
2. Ramirez, A. P. *Annu. Rev. Mater. Sci.* **1994**, *24*, 453-480.
3. Goodenough, J. B. *Phys. Chem. Sol.* **1958**, *6*, 287-297.
4. Kanamori, J. *Phys. Chem. Sol.* **1959**, *10*, 87-98.
5. Ginsberg, A. P. *Inorg. Chim. Acta, Rev.* **1971**, *5*, 45-68.
6. Kahn, O. *Molecular Magnetism*; VCH: New York, 1993.
7. Crawford, V. H.; Richardson, H. W.; Wasson, J. R.; Hodgson, D. J.; Hatfield, W. E. *Inorg. Chem.* **1976**, *15*, 2107-2110.
8. Helton, J. S.; Matan, K.; Chung, J.-H.; Shores, M. P.; Nytko, E. A.; Bartlett, B. M.; Chen, Y.; Huang, Q.; Lynn, J. W.; Nocera, D. G.; Lee, Y. S. **2008**, Manuscript in preparation.
9. Zheng, X. G.; Kawae, T.; Kashitani, Y.; Li, C. S.; Tateiwa, N.; Takeda, K.; Yamada, H.; Xu, C. N.; Ren, Y. *Phys. Rev. B* **2005**, *71*, 052409/052401-052409/052404.
10. Zheng, X. G.; Kubozono, H.; Nishiyama, K.; Higemoto, W.; Kawae, T.; Koda, A.; Xu, C. N. *Phys. Rev. Lett.* **2005**, *95*, 057201/057201-057201/057204.
11. Mendels, P.; Bert, F.; de Vries, M. A.; Olariu, A.; Harrison, A.; Duc, F.; Trombe, J. C.; Lord, J. S.; Amato, A.; Baines, C. *Phys. Rev. Lett.* **2007**, *98*, 077204/077201-077204/077204.
12. Greedan, J. E. *J. Mater. Chem.* **2001**, *11*, 37-53.
13. Waldtmann, C.; Everts, H. U.; Bernu, B.; Lhuillier, C.; Sindzingre, P.; Lecheminant, P.; Pierre, L. *Eur. Phys. J. B* **1998**, *2*, 501-507.
14. Mambrini, M.; Mila, F. *Eur. Phys. J. B* **2000**, *17*, 651-659.
15. Hastings, M. B. *Phys. Rev. B* **2001**, *63*, 014413/014411-014413/014416.
16. Lhuillier, C. *LANL, Preprint Archive, Condens. Matt.* **2005**, 1-101, arXiv:cond-mat/0502464.
17. Misguich, G.; Lhuillier, C. In *Frustrated Spin Systems*; Diep, H. T., Ed.; World Scientific Publishing Co. Pte. Ltd.: Singapore, 2004, p 229-306.
18. Lee, S.-S.; Lee, P. A. *Phys. Rev. Lett.* **2005**, *95*, 036403/036401-036403/036404.

19. Motrunich, O. I. *Phys. Rev. B* **2005**, 72, 045105/045101-045105/045107.
20. Ofer, O.; Keren, A.; Nytko, E. A.; Shores, M. P.; Bartlett, B. M.; Nocera, D. G.; Baines, C.; Amato, A. *LANL, Preprint Archive, Condens. Matt.* **2006**, 1-5, arXiv:cond-mat/0610540.
21. Imai, T.; Nytko, E. A.; Bartlett, B. M.; Shores, M. P.; Nocera, D. G. *Phys. Rev. Lett.* **2008**, 100, 077203/077201-077203/077204.
22. Rigol, M.; Singh, R. R. P. *Phys. Rev. B* **2007**, 76, 184403/184401-184403/184412.
23. Rigol, M.; Singh, R. R. P. *Phys. Rev. Lett.* **2007**, 98, 207204/207201-207204/207204.
24. Lauchli, A.; Poilblanc, D. *Phys. Rev. Lett.* **2004**, 92, 236404/236401-236404/236404.
25. Lee, P. A.; Nagaosa, N.; Wen, X.-G. *Rev. Mod. Phys.* **2006**, 78, 17-85.
26. Birgeneau, R. J.; Aharony, A.; Belk, N. R.; Chou, F. C.; Endoh, Y.; Greven, M.; Hosoya, S.; Kastner, M. A.; Lee, C. H.; et al. *J. Phys. Chem. Solids* **1995**, 56, 1913-1919.
27. Aharony, A.; Birgeneau, R. J.; Coniglio, A.; Kastner, M. A.; Stanley, H. E. *Phys. Rev. Lett.* **1988**, 60, 1330-1333.
28. Anderson, P. W.; Lee, P. A.; Randeria, M.; Rice, T. M.; Trivedi, N.; Zhang, F. C. *J. Phys.: Condens. Matter* **2004**, 16, R755-R769.
29. Grande, B.; Mueller-Buschbaum, H.; Schweizer, M. Z. *Anorg. Allg. Chem.* **1977**, 428, 120-124.
30. Fleming, R. M.; Batlogg, B.; Cava, R. J.; Rietman, E. A. *Phys. Rev. B* **1987**, 35, 7191-7194.
31. Johnston, D. C.; Stokes, J. P.; Goshorn, D. P.; Lewandowski, J. T. *Phys. Rev. B* **1987**, 36, 4007-4010.
32. Tranquada, J. M.; Heald, S. M.; Moodenbaugh, A. R. *Phys. Rev. B* **1987**, 36, 5263-5274.
33. Schirber, J. E.; Morosin, B.; Merrill, R. M.; Hlava, P. F.; Venturini, E. L.; Kwak, J. F.; Nigrey, P. J.; Baughman, R. J.; Ginley, D. S. *Physica C* **1988**, 152, 121-123.
34. Demazeau, G.; Tresse, F.; Plante, T.; Chevalier, B.; Etourneau, J.; Michel, C.; Hervieu, M.; Raveau, B.; Lejay, P. *Physica C* **1988**, 153-155, 824-825.
35. Dabrowski, B.; Zhang-MacCoy, V.; Wang, Z.; Hannon, R.; Jorgensen, J. D.; Hunter, B. A.; Hinks, D. G.; Wagner, J. L.; Hitterman, R. L. *J. Supercond.* **1994**, 7, 45-48.
36. Lee, Y. S.; Birgeneau, R. J.; Kastner, M. A.; Endoh, Y.; Wakimoto, S.; Yamada, K.; Erwin, R. W.; Lee, S. H.; Shirane, G. *Phys. Rev. B* **1999**, 60, 3643-3654.

Chapter 5

37. Li, Z. G.; Feng, H. H.; Yang, Z. Y.; Hamed, A.; Ting, S. T.; Hor, P. H.; Bhavaraju, S.; DiCarlo, J. F.; Jacobson, A. J. *Phys. Rev. Lett.* **1996**, *77*, 5413-5416.
38. Grenier, J. C.; Wattiaux, A.; Monroux, C.; Pouchard, M.; Locquet, J. P. *Physica C* **1994**, *235-240*, 79-82.
39. Chou, F. C.; Johnston, D. C.; Cheong, S. W.; Canfield, P. C. *Physica C* **1993**, *216*, 66-76.
40. Blakeslee, P.; Birgeneau, R. J.; Chou, F. C.; Christianson, R.; Kastner, M. A.; Lee, Y. S.; Wells, B. O. *Phys. Rev. B* **1998**, *57*, 13915-13921.
41. Liu, Y.; Wan, S. L.; Li, X. G. *Supercond. Sci. Technol.* **2007**, *20*, 870-874.
42. Liu, L. H.; Che, G. C.; Zhao, J.; Zhao, Z. X. *Physica C* **2005**, *425*, 37-43.
43. Tu, Q. Y.; Chen, X. L.; Ma, B. K.; Zhao, Z. X.; Li, J. Q.; Liang, J. K. *Physica C* **2002**, *370*, 94-100.
44. Michel, C. R.; Casan-Pastor, N. *Physica C* **1997**, *278*, 149-159.
45. Jacob, A.; Barbut, D.; Wattiaux, A.; Delville, M.-H.; Grenier, J.-C.; Pouchard, M.; Etourneau, J. *J. Mater. Chem.* **2000**, *10*, 829-831.
46. Wang, C. C.; Cui, M. L.; Zheng, X.; Zhu, J. *Appl. Phys. A* **2004**, *78*, 1193-1196.
47. Tu, Q. Y.; Ma, B. K.; Chen, X. L.; Lan, Y. C.; Xu, Y. X.; Liang, J. K.; Zhao, Z. X.; Li, J. Q. *Mod. Phys. Lett. B* **2001**, *15*, 1171-1179.
48. Lan, Y. C.; Chen, X. L.; Cao, Y. G.; Huang, J. K.; Che, G. C.; Liu, G. D.; Xu, Y. P.; Xu, T.; Li, J. Y. *Physica C* **2000**, *336*, 151-156.
49. Rapp, R. P.; Mehta, A.; DiCarlo, J.; Navrotsky, A. *J. Mater. Res.* **1994**, *9*, 8-12.
50. Takayama-Muromachi, E.; Sasaki, T.; Matsui, Y. *Physica C* **1993**, *207*, 97-101.
51. Raspi, G.; Zanello, P.; Cinquantini, A.; Corti, P. *Anal. Chim. Acta* **1973**, *66*, 435-442.
52. Wu, Z.; Zhang, Z.; Liu, L. *Electrochim. Acta* **1997**, *42*, 2719-2723.
53. Ogorevc, B.; Tavcar, G.; Hudnik, V.; Pejovnik, S. *J. Electroanal. Chem.* **1993**, *351*, 81-90.
54. Makarova, I. P.; Simonov, V. I.; Blomberg, M. K.; Merisalo, M. J. *Acta Crystallogr. B.* **1996**, *B52*, 93-99.
55. Plebanczyk, M.; Klimeczuk, T.; Gortenmulder, T.; Fiertek, P.; Sadowski, W. *Materials Science* **2006**, *24*, 991-1002.

Chapter 5

56. Prasad Beesabathina, D.; Salamanca-Riba, L.; Peng, J. L.; Li, Z. Y.; Greene, R. L. *Physica C* **1993**, *208*, 79-85.
57. Bartlett, B. M. Ph.D. Thesis, Massachusetts Institute of Technology, 2005.
58. Forsyth, J. B.; Brown, P. J.; Wanklyn, B. M. *Journal of Physics C: Solid State Physics* **1988**, *21*, 2917-2929.
59. Koo, H. J.; Whangbo, M.-H. *Inorg. Chem.* **2003**, *42*, 1187-1192.
60. Lhuillier, C.; Misguich, G. *Lect. Notes Phys.* **2002**, *595*, 161-190.

Appendix A.
Structural Characterization of Compounds

Appendix A.1**Notes on the Structures of bdc derivatives**

The structures of Cu(1,3-bdc) and Cu(1,3-bdc)•0.11H₂O are identical with the exception of the partially occupied water molecule on a special position in the latter case. The two structures, however, are not strictly isostructural and it is not possible to use one model in a refinement against the other dataset. Although the *x* and *z* positions of all atoms in both structures are identical within error, the *y* coordinate of Cu(1) differs by 0.5, and the *y* coordinates of all other atoms are different. The additional water molecule is located on the crystallographic $\bar{3}$ axis (coordinates 0,0,0; Wykoff *b*); its occupancy was refined freely and eventually set at the convergence value of 0.322×0.16667 .

The structure of the C₃₂H₂₄Cu₆O₂₆ byproduct contains a 16-membered ring. The structure provides evidence that some 1,3-benzenedicarboxylate is oxidized in the 2-position under the given conditions. Excluding their bond to one another, Cu(1) and Cu(2) are each in pseudo-square planar coordination environments, each with two bonds to monodentate carboxylate oxygens and two bonds to the newly formed oxide. The Cu(1)–Cu(2) distance is 2.9714(5) Å, which is within bonding distance for two Cu(II) ions. Cu(3) is pseudo-square pyramidal; the base of the pyramid contains two bonds to monodentate carboxylate oxygens and two bonds to water molecules, and the apex of the pyramid is a bonded water molecule. Remarkably, in this incomplete octahedral coordination sphere, no residual electron density can be found near the site of the missing ligand. The two Cu(3) atoms bridge the two Cu(1)–Cu(2) dimers in a ring-like structure in the formula unit. The restraints used in the solution of this structure involve the O–H and H•••H distances in the water molecules. The compound crystallizes in the centrosymmetric space group $P\bar{1}$. The packing diagram viewed along the *c* axis of the unit cell shows that the 16-membered ring is not planar and the planes of the dimers are staggered with respect to one another.

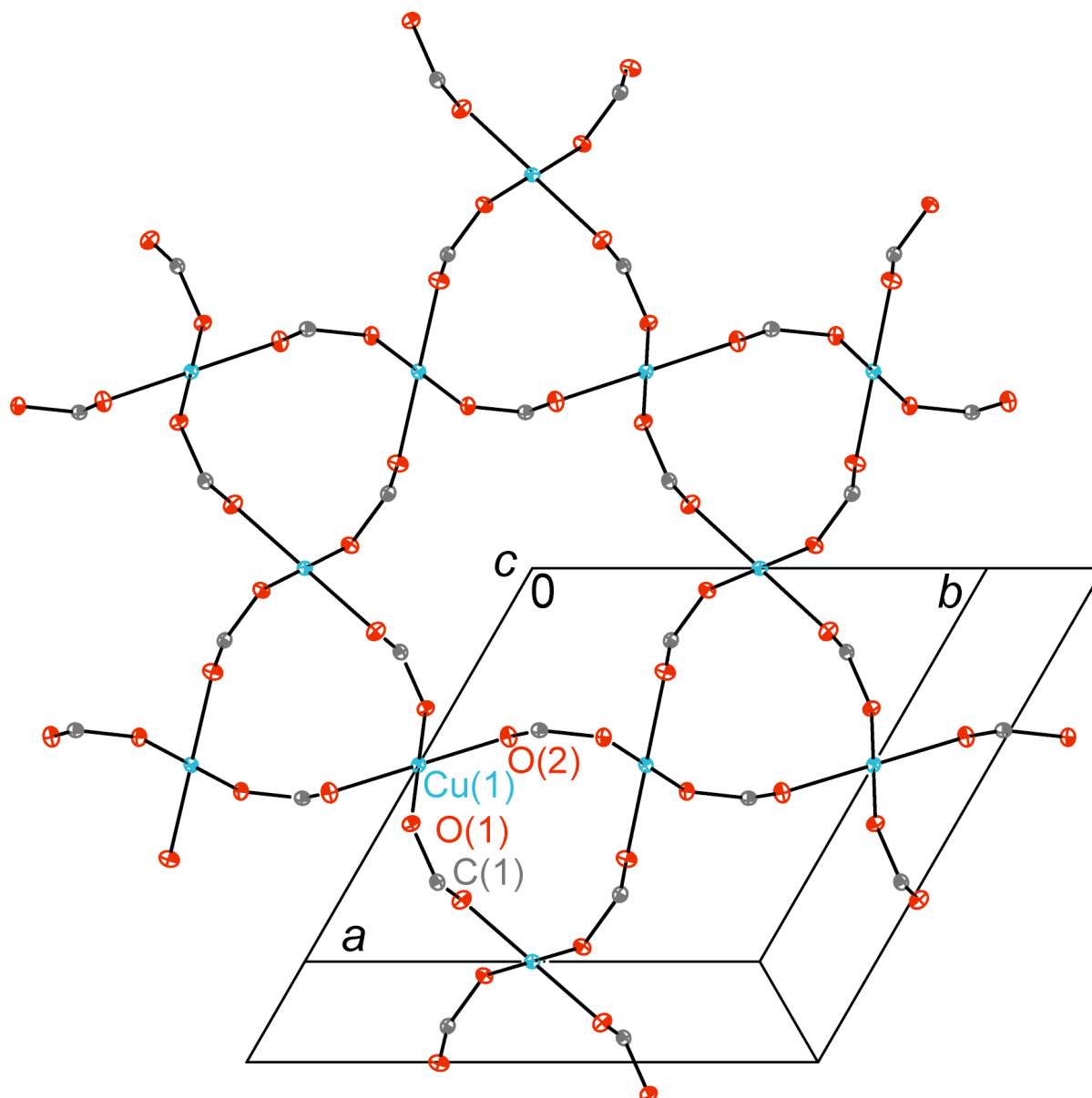


Figure A.1.1. A portion of the crystal structure of Cu(1,3-bdc), with unit cell. 50% ellipsoids are shown. Symmetry equivalent atoms (shown but not labeled here) are given in Tables A.1.3 and A.1.4. Phenyl-ring carbon and hydrogen atoms are omitted for clarity.

Table A.1.1. Crystal data and structure refinement for Cu(1,3-bdc).

Identification code	07060	
Empirical formula	C ₈ H ₄ CuO ₄	
Formula weight	227.65	
Temperature	100(2) K	
Wavelength	0.71073 Å	
Crystal system	Hexagonal	
Space group	<i>P6₃/m</i>	
Unit cell dimensions	$a = 9.1081(2) \text{ \AA}$	$\alpha = 90^\circ$
	$b = 9.1081(2) \text{ \AA}$	$\beta = 90^\circ$
	$c = 15.9432(5) \text{ \AA}$	$\gamma = 120^\circ$
Volume, <i>Z</i>	1145.41(5) Å ³	6
Density (calculated)	1.980 g/cm ³	
Absorption coefficient	2.831 mm ⁻¹	
F(000)	678	
Crystal size	0.48 × 0.35 × 0.15 mm	
θ range for data collection	2.56 to 29.57°	
Limiting indices	$-12 \leq h \leq 12$	
	$-12 \leq k \leq 12$	
	$-22 \leq l \leq 22$	
Reflections collected	25614	
Independent reflections	1119 ($R_{\text{int}} = 0.0247$)	
Completeness to $\theta = 29.57^\circ$	100.0 %	
Refinement method	Full-matrix least-squares on F^2	
Data / restraints / parameters	1119 / 0 / 64	
Goodness-of-fit on F^2	1.098	
Final R indices [$I > 2\sigma(I)$]	$R_1 = 0.0212$	$wR_2 = 0.0667$
R indices (all data)	$R_1 = 0.0217$	$wR_2 = 0.0674$
Largest diff. peak and hole	0.528 eÅ ⁻³	-0.633 eÅ ⁻³

Appendix A

Table A.1.2. Atomic coordinates [$\times 10^4$] and equivalent isotropic displacement parameters [$\text{\AA}^2 \times 10^3$] for Cu(1,3-bdc). U_{eq} is defined as one third of the trace of the orthogonalized U_{ij} tensor.

	x	y	z	U_{eq}
Cu(1)	5000	0	0	7(1)
O(1)	6360(1)	570(1)	1002(1)	9(1)
O(2)	4262(1)	1614(1)	261(1)	11(1)
C(1)	7828(2)	1867(2)	950(1)	8(1)
C(2)	8839(2)	2404(2)	1741(1)	8(1)
C(3)	10610(2)	3362(2)	1740(1)	10(1)
C(4)	11485(2)	3829(2)	2500	11(1)
C(5)	7962(2)	1915(2)	2500	8(1)

Table A.1.3. Bond lengths [\AA] for Cu(1,3-bdc).

Cu(1)-O(1) ^a	1.9265(9)	C(1)-C(2)	1.4929(16)
Cu(1)-O(1)	1.9265(9)	C(2)-C(5)	1.3948(14)
Cu(1)-O(2) ^a	1.9428(9)	C(2)-C(3)	1.3985(16)
Cu(1)-O(2)	1.9428(9)	C(3)-C(4)	1.3949(14)
O(1)-C(1)	1.2685(15)	C(4)-C(3) ^d	1.3949(14)
O(2)-C(1) ^b	1.2680(14)	C(5)-C(2) ^d	1.3948(14)
C(1)-O(2) ^c	1.2680(14)		

Symmetry transformations used to generate equivalent atoms:

^a $-x + 1, -y, -z$

^b $-x + y + 1, -x + 1, z$

^c $-y + 1, x - y, z$

^d $x, y, -z + 1/2$

Appendix A

Table A.1.4. Bond angles [°] for Cu(1,3-bdc).

O(1) ^a -Cu(1)-O(1)	180.00(7)	O(2) ^c -C(1)-C(2)	122.61(11)
O(1) ^a -Cu(1)-O(2) ^a	92.14(4)	O(1)-C(1)-C(2)	116.13(10)
O(1)-Cu(1)-O(2) ^a	87.86(4)	C(5)-C(2)-C(3)	119.90(12)
O(1) ^a -Cu(1)-O(2)	87.86(4)	C(5)-C(2)-C(1)	117.85(11)
O(1)-Cu(1)-O(2)	92.14(4)	C(3)-C(2)-C(1)	122.25(11)
O(2) ^a -Cu(1)-O(2)	180.00(7)	C(4)-C(3)-C(2)	119.60(12)
C(1)-O(1)-Cu(1)	115.67(8)	C(3)-C(4)-C(3) ^d	120.64(16)
C(1) ^b -O(2)-Cu(1)	132.42(8)	C(2) ^d -C(5)-C(2)	120.34(15)
O(2) ^c -C(1)-O(1)	121.26(11)		

Symmetry transformations used to generate equivalent atoms:

^a $-x + 1, -y, -z$ ^b $-x + y + 1, -x + 1, z$ ^c $-y + 1, x - y, z$ ^d $x, y, -z + 1/2$

Appendix A

Table A.1.5. Anisotropic displacement parameters [$\text{\AA}^2 \times 10^3$] for Cu(1,3-bdc). The anisotropic displacement factor exponent takes the form: $-2\pi^2[(ha^*)^2U_{11} + \dots + 2hka^*b^*U_{12}]$.

	U_{11}	U_{22}	U_{33}	U_{23}	U_{13}	U_{12}
Cu(1)	8(1)	7(1)	4(1)	-1(1)	-1(1)	4(1)
O(1)	9(1)	10(1)	7(1)	-1(1)	-1(1)	3(1)
O(2)	16(1)	13(1)	6(1)	-1(1)	0(1)	9(1)
C(1)	10(1)	9(1)	6(1)	-1(1)	0(1)	5(1)
C(2)	9(1)	9(1)	6(1)	-1(1)	-1(1)	4(1)
C(3)	9(1)	12(1)	8(1)	1(1)	1(1)	5(1)
C(4)	8(1)	13(1)	11(1)	0	0	5(1)
C(5)	8(1)	8(1)	7(1)	0	0	3(1)

Table A.1.6. Hydrogen coordinates [$\times 10^4$] and isotropic displacement parameters [$\text{\AA}^2 \times 10^3$] for Cu(1,3-bdc).

	x	y	z	U_{eq}
H(3)	11214	3693	1224	12
H(4)	12689	4472	2500	13
H(5)	6760	1246	2500	10

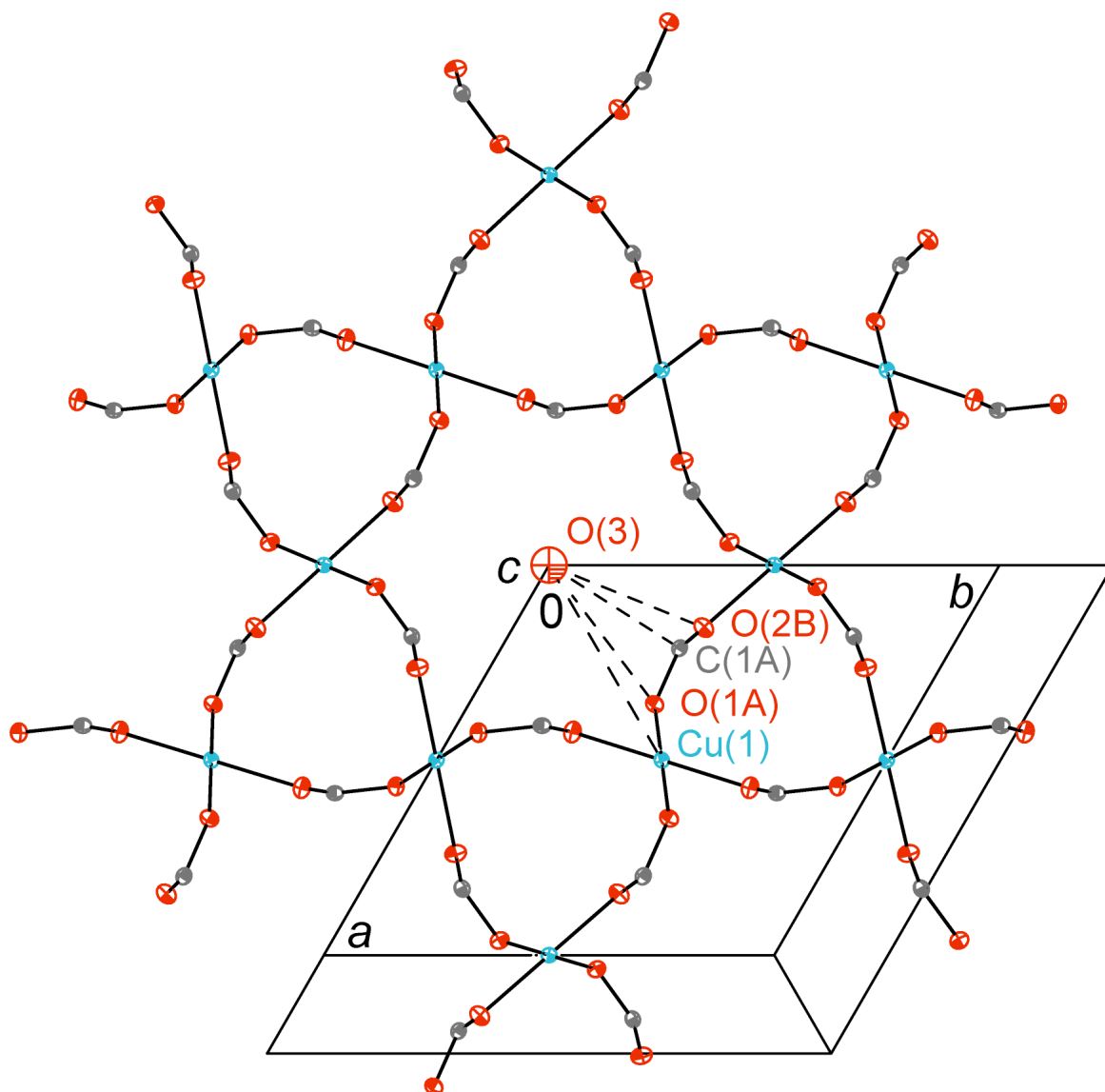


Figure A.1.2. A portion of the crystal structure of $\text{Cu}(1,3\text{-bdc})\cdot 0.11\text{H}_2\text{O}$, with unit cell. 50% ellipsoids are shown. O(3) is the oxygen atom of a solvated water molecule statistically distributed over 1/9 of sites. Symmetry equivalent atoms (shown but not labeled here) are given in Tables A.1.9 and A.1.10. Phenyl-ring carbon atoms and all hydrogen atoms are omitted for clarity. The distances between O(3) and other atoms in the structure are as follows: O(3)–Cu(1), 4.5528(2) Å. O(3)–O(1A), 3.9405(8) Å. O(3)–C(1A), 3.5303(11) Å. O(3)–O(2B), 3.4166(8) Å.

Table A.1.7. Crystal data and structure refinement for Cu(1,3-bdc)•0.11H₂O.

Identification code	05251	
Empirical formula	C ₈ H ₄ CuO _{4.11}	
Formula weight	229.44	
Temperature	100(2) K	
Wavelength	0.71073 Å	
Crystal system	Hexagonal	
Space group	<i>P6₃/m</i>	
Unit cell dimensions	$a = 9.1056(3)$ Å	$\alpha = 90^\circ$
	$b = 9.1056(3)$ Å	$\beta = 90^\circ$
	$c = 15.9550(12)$ Å	$\gamma = 120^\circ$
Volume, <i>Z</i>	1145.63(10) Å ³	6
Density (calculated)	1.995 g/cm ³	
Absorption coefficient	2.832 mm ⁻¹	
F(000)	683	
Crystal size	0.15 × 0.10 × 0.10 mm	
θ range for data collection	2.55 to 29.55°	
Limiting indices	$-12 \leq h \leq 12$	
	$-12 \leq k \leq 12$	
	$-22 \leq l \leq 22$	
Reflections collected	22913	
Independent reflections	1118 ($R_{\text{int}} = 0.0311$)	
Completeness to $\theta = 29.55^\circ$	100.0 %	
Refinement method	Full-matrix least-squares on F^2	
Data / restraints / parameters	1118 / 0 / 66	
Goodness-of-fit on F^2	1.101	
Final R indices [$I > 2\sigma(I)$]	$R_1 = 0.0217$	$wR_2 = 0.0621$
R indices (all data)	$R_1 = 0.0235$	$wR_2 = 0.0637$
Largest diff. peak and hole	0.578 eÅ ⁻³	-1.128 eÅ ⁻³

Appendix A

Table A.1.8. Atomic coordinates [$\times 10^4$] and equivalent isotropic displacement parameters [$\text{\AA}^2 \times 10^3$] for Cu(1,3-bdc) \cdot 0.11H₂O. U_{eq} is defined as one third of the trace of the orthogonalized U_{ij} tensor.

	x	y	z	U_{eq}
Cu(1)	5000	5000	0	8(1)
O(1)	6361(1)	5790(1)	1002(1)	11(1)
O(2)	4259(1)	2646(1)	261(1)	13(1)
C(1)	7826(1)	5961(1)	950(1)	10(1)
C(2)	8838(1)	6435(1)	1741(1)	10(1)
C(3)	10612(1)	7250(1)	1741(1)	12(1)
C(4)	11484(2)	7656(2)	2500	12(1)
C(5)	7963(2)	6049(2)	2500	10(1)
O(3)	0	0	0	61(4)

Table A.1.9. Bond lengths [\AA] for Cu(1,3-bdc) \cdot 0.11H₂O.

Cu(1)-O(1) ^a	1.9275(8)	C(1)-C(2)	1.4932(15)
Cu(1)-O(1)	1.9275(8)	C(2)-C(5)	1.3940(13)
Cu(1)-O(2)	1.9437(8)	C(2)-C(3)	1.4006(16)
Cu(1)-O(2) ^a	1.9437(8)	C(3)-C(4)	1.3934(14)
O(1)-C(1)	1.2665(14)	C(4)-C(3) ^d	1.3934(14)
O(2)-C(1) ^b	1.2692(14)	C(5)-C(2) ^d	1.3940(13)
C(1)-O(2) ^c	1.2692(14)		

Symmetry transformations used to generate equivalent atoms:

^a $-x + 1, -y + 1, -z$ ^b $-y + 1, x - y, z$ ^c $-x + y + 1, -x + 1, z$ ^d $x, y, -z + \frac{1}{2}$

Appendix A

Table A.1.10. Bond angles [°] for Cu(1,3-bdc)•0.11H₂O.

O(1) ^a -Cu(1)-O(1)	180.00(3)	O(1)-C(1)-C(2)	116.12(10)
O(1) ^a -Cu(1)-O(2)	87.84(3)	O(2) ^c -C(1)-C(2)	122.63(10)
O(1)-Cu(1)-O(2)	92.16(3)	C(5)-C(2)-C(3)	119.78(11)
O(1) ^a -Cu(1)-O(2) ^a	92.16(3)	C(5)-C(2)-C(1)	117.97(10)
O(1)-Cu(1)-O(2) ^a	87.84(3)	C(3)-C(2)-C(1)	122.25(10)
O(2)-Cu(1)-O(2) ^a	180.00(5)	C(4)-C(3)-C(2)	119.55(11)
C(1)-O(1)-Cu(1)	115.69(7)	C(3)-C(4)-C(3) ^d	120.81(15)
C(1) ^b -O(2)-Cu(1)	132.36(8)	C(2) ^d -C(5)-C(2)	120.53(14)
O(1)-C(1)-O(2) ^c	121.25(10)		

Symmetry transformations used to generate equivalent atoms:

^a $-x + 1, -y + 1, -z$ ^b $-y + 1, x - y, z$ ^c $-x + y + 1, -x + 1, z$ ^d $x, y, -z + \frac{1}{2}$

Appendix A

Table A.1.11. Anisotropic displacement parameters [$\text{\AA}^2 \times 10^3$] for Cu(1,3-bdc) \cdot 0.11H₂O. The anisotropic displacement factor exponent takes the form: $-2\pi^2[(ha^*)^2U_{11} + \dots + 2hka^*b^*U_{12}]$.

	U_{11}	U_{22}	U_{33}	U_{23}	U_{13}	U_{12}
Cu(1)	10(1)	10(1)	6(1)	0(1)	-1(1)	5(1)
O(1)	12(1)	14(1)	9(1)	0(1)	-1(1)	7(1)
O(2)	19(1)	12(1)	8(1)	0(1)	-1(1)	8(1)
C(1)	11(1)	9(1)	9(1)	1(1)	0(1)	5(1)
C(2)	12(1)	11(1)	8(1)	0(1)	-1(1)	6(1)
C(3)	11(1)	12(1)	11(1)	0(1)	2(1)	5(1)
C(4)	9(1)	13(1)	13(1)	0	0	3(1)
C(5)	10(1)	10(1)	10(1)	0	0	5(1)
O(3)	54(6)	54(6)	75(12)	0	0	27(3)

Table A.1.12. Hydrogen coordinates [$\times 10^4$] and isotropic displacement parameters [$\text{\AA}^2 \times 10^3$] for Cu(1,3-bdc) \cdot 0.11H₂O.

	x	y	z	U_{eq}
H(3)	11216	7523	1226	14
H(4)	12687	8216	2500	15
H(5)	6761	5519	2500	12

Appendix A

Table A.1.13. Bragg reflections and Miller indices of pXRD pattern for Cu(1,3-bdc) matched to 07060 structure.

$2\theta_{\text{obs}}$	d_{obs}	% I_{obs}	$2\theta_{\text{calcd}}$	d_{calcd}	% I_{calcd}	Δd	hkl
11.190	7.9006	91.7	11.208	7.8879	3.2	0.0127	1 0 0
12.487	7.0831	22.7	12.510	7.0699	4.9	0.0132	1 0 1
15.840	5.5903	10.5	15.793	5.6069	2.9	-0.0166	1 0 2
19.451	4.5600	100.0	19.476	4.5541	7.7	0.0059	1 1 0
20.237	4.3845	7.7	20.263	4.3789	10.4	0.0056	1 1 1
22.472	3.9533	11.0	22.466	3.9543	2.6	-0.0010	1 1 2
23.204	3.8301	4.2	23.214	3.8285	7.3	0.0016	2 0 1
25.159	3.5368	43.4	25.172	3.5350	12.8	0.0018	2 0 2
28.201	3.1618	11.2	28.153	3.1671	7.5	-0.0053	2 0 3
29.889	2.9869	5.6	29.947	2.9813	1.9	0.0056	1 2 0
31.965	2.7976	4.7	32.025	2.7924	4.0	0.0052	1 2 2
39.432	2.2833	10.2	39.535	2.2776	0.7	0.0057	0 0 7
39.864	2.2596	1.8	39.964	2.2542	4.2	0.0054	2 2 1
41.096	2.1946	10.3	41.093	2.1948	2.0	-0.0002	3 0 4
42.726	2.1146	1.8	42.830	2.1097	1.4	0.0049	1 3 2
44.664	2.0273	1.1	44.633	2.0286	0.9	-0.0013	3 0 5
45.804	1.9794	3.6	45.859	1.9771	3.7	0.0023	2 2 4
47.317	1.9196	5.2	47.363	1.9178	0.9	0.0018	3 1 4
50.214	1.8154	3.1	50.378	1.8099	1.7	0.0055	1 2 7
51.551	1.7714	3.4	51.549	1.7715	0.4	-0.0001	0 0 9
52.999	1.7264	2.3	52.932	1.7284	0.4	-0.0020	1 0 9
58.200	1.5839	1.6	58.214	1.5835	2.0	0.0004	4 0 6

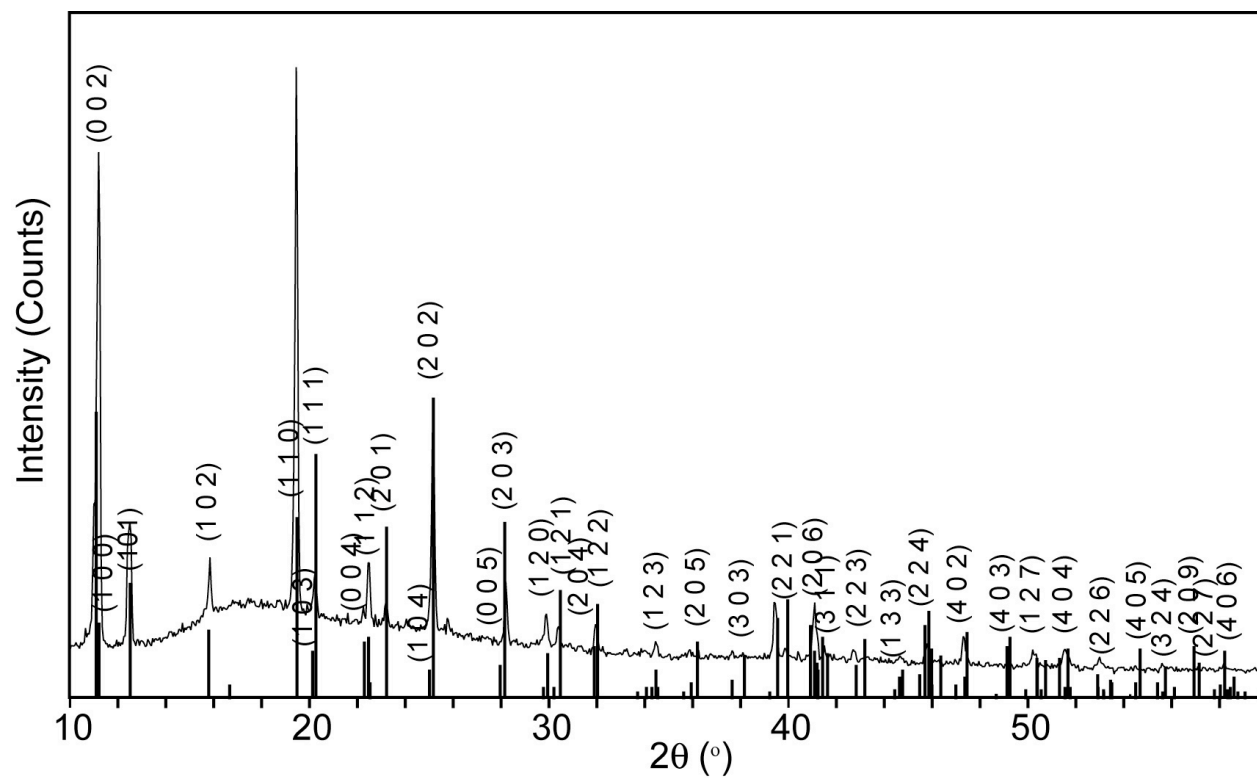


Figure A.1.3. pXRD pattern for Cu(1,3-bdc) matched to 07060 structure.

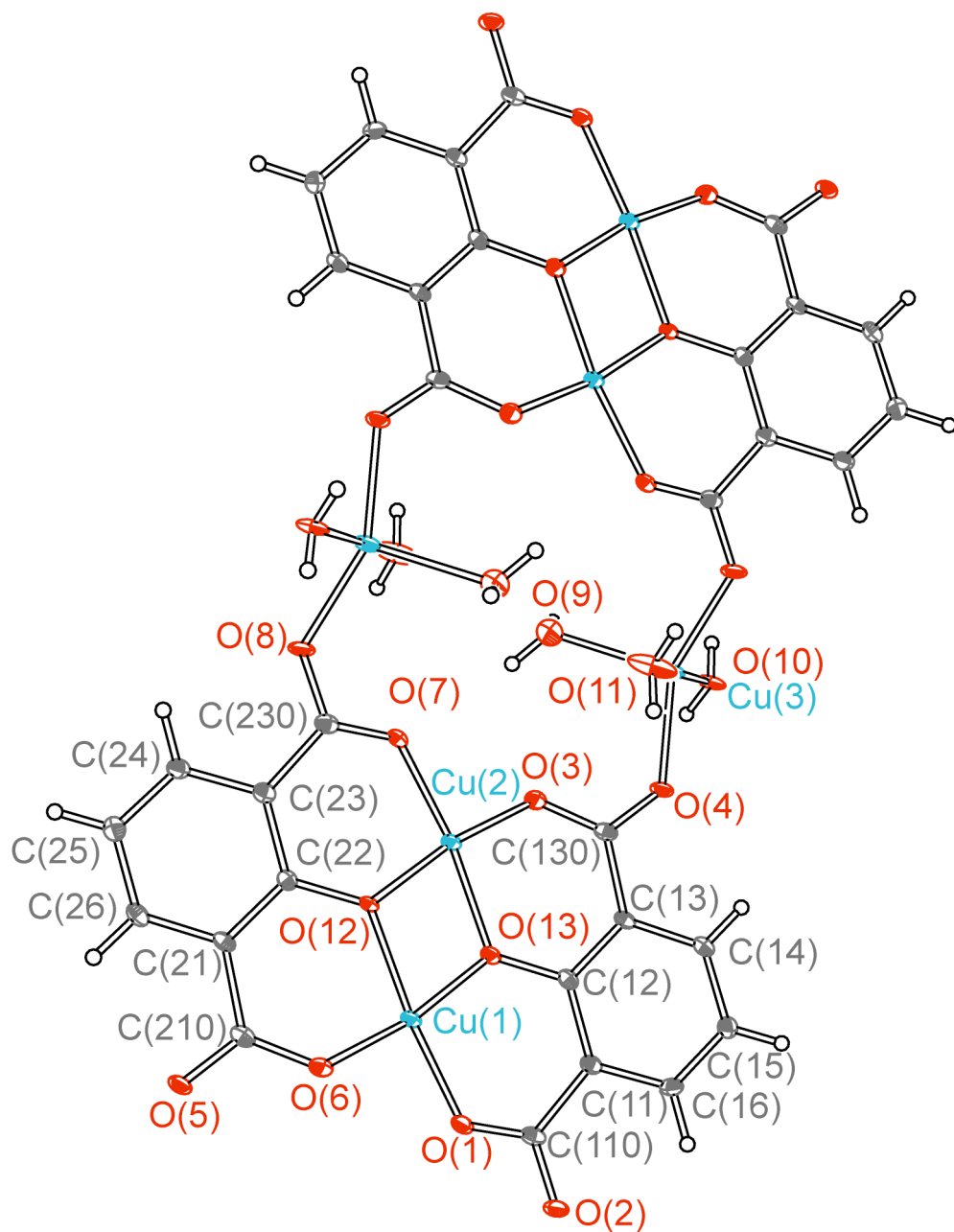


Figure A.1.4. A portion of the crystal structure of $C_{32}H_{24}Cu_6O_{26}$. 50% ellipsoids are shown. Symmetry equivalent atoms (shown but not labeled here) are given in Tables A.1.15 and A.1.16.

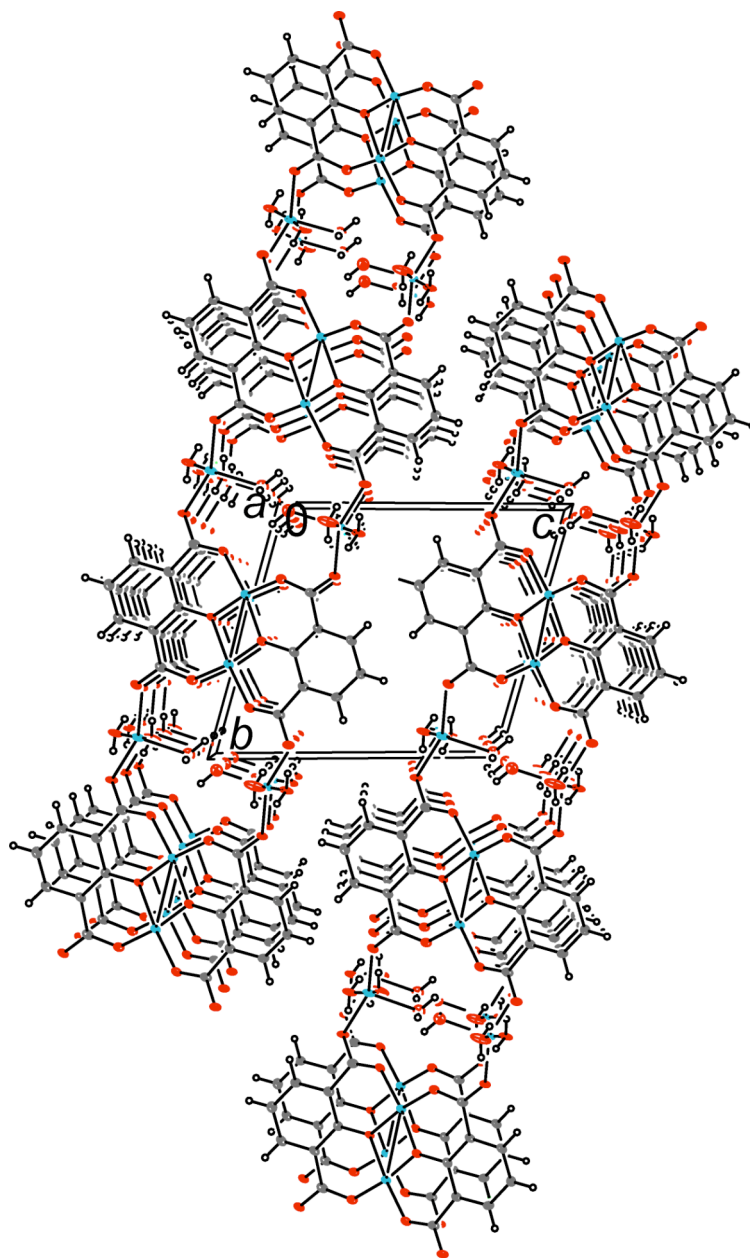


Figure A.1.5. Packing diagram for $C_{32}H_{24}Cu_6O_{26}$, as viewed down the crystallographic *a* axis. 50% thermal ellipsoids are shown. Cu atoms are shown in teal, O atoms in red, C atoms in gray, and H atoms in white.

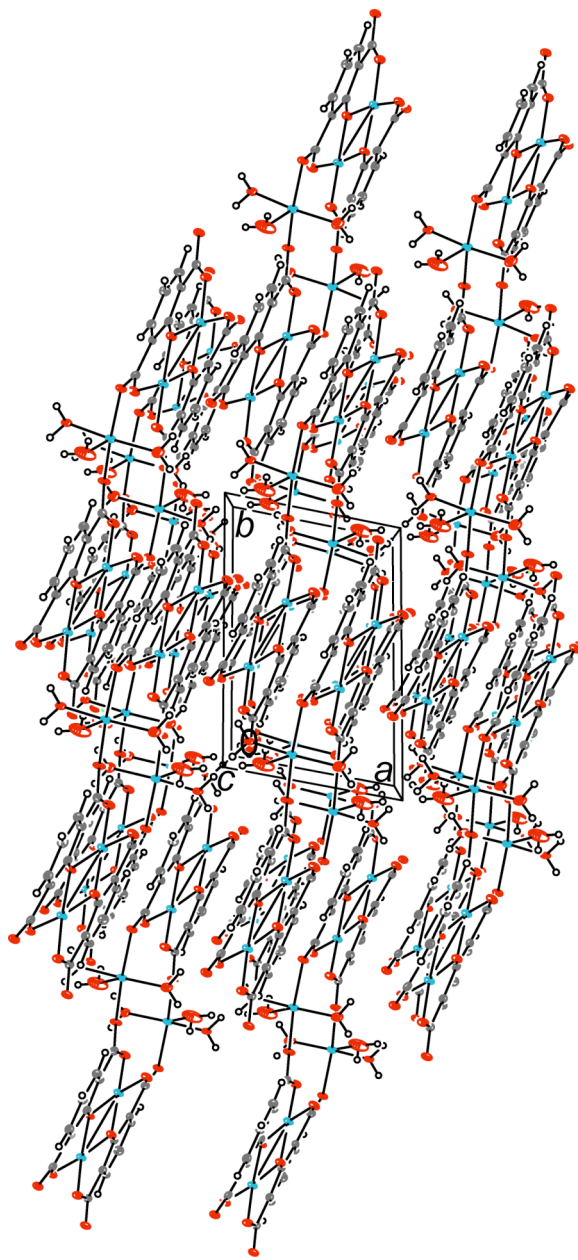


Figure A.1.6. Packing diagram for $C_{32}H_{24}Cu_6O_{26}$, as viewed down the crystallographic c axis. 50% thermal ellipsoids are shown. Cu atoms are shown in teal, O atoms in red, C atoms in gray, and H atoms in white.

Table A.1.14. Crystal data and structure refinement for $C_{32}H_{24}Cu_6O_{26}$.

Identification code	06218	
Empirical formula	$C_{32}H_{24}Cu_6O_{26}$	
Formula weight	1205.75	
Temperature	100(2) K	
Wavelength	0.71073 Å	
Crystal system	Triclinic	
Space group	$P\bar{1}$	
Unit cell dimensions	$a = 7.0738(6)$ Å	$\alpha = 104.0140(10)^\circ$
	$b = 10.8611(8)$ Å	$\beta = 99.4120(10)^\circ$
	$c = 12.0790(9)$ Å	$\gamma = 98.2080(10)^\circ$
Volume, Z	$872.01(12)$ Å ³	1
Density (calculated)	2.296 g/cm ³	
Absorption coefficient	3.705 mm ⁻¹	
F(000)	598	
Crystal size	$0.20 \times 0.10 \times 0.02$ mm	
θ range for data collection	1.97 to 29.13°	
Limiting indices	$-9 \leq h \leq 9$	
	$-14 \leq k \leq 14$	
	$-16 \leq l \leq 16$	
Reflections collected	18271	
Independent reflections	4692 ($R_{\text{int}} = 0.0450$)	
Completeness to $\theta = 29.13^\circ$	99.7 %	
Refinement method	Full-matrix least-squares on F^2	
Data / restraints / parameters	4692 / 9 / 307	
Goodness-of-fit on F^2	1.021	
Final R indices [$I > 2\sigma(I)$]	$R_1 = 0.0333$	$wR_2 = 0.0699$
R indices (all data)	$R_1 = 0.0512$	$wR_2 = 0.0768$
Largest diff. peak and hole	0.689 eÅ ⁻³	-0.540 eÅ ⁻³

Appendix A

Table A.1.15. Atomic coordinates [$\times 10^4$] and equivalent isotropic displacement parameters [$\text{\AA}^2 \times 10^3$] for $\text{C}_{32}\text{H}_{24}\text{Cu}_6\text{O}_{26}$. U_{eq} is defined as one third of the trace of the orthogonalized U_{ij} tensor.

	x	y	z	U_{eq}
Cu(1)	6472(1)	3610(1)	-80(1)	10(1)
Cu(2)	8589(1)	6226(1)	50(1)	10(1)
Cu(3)	3842(1)	996(1)	2305(1)	13(1)
O(1)	8901(3)	7858(2)	1121(2)	12(1)
O(2)	8597(3)	9266(2)	2712(2)	13(1)
O(3)	4939(3)	3019(2)	907(2)	14(1)
O(4)	4416(3)	2887(2)	2629(2)	12(1)
O(5)	10652(3)	6967(2)	-2650(2)	12(1)
O(6)	10140(3)	6797(2)	-936(2)	13(1)
O(7)	6048(3)	1993(2)	-1191(2)	13(1)
O(8)	6403(3)	605(2)	-2776(2)	15(1)
O(9)	2253(4)	379(2)	463(2)	37(1)
O(10)	1550(3)	1210(2)	2982(2)	15(1)
O(11)	6415(3)	882(2)	1946(3)	32(1)
O(12)	8049(3)	4469(2)	-930(2)	10(1)
O(13)	6970(3)	5370(2)	880(2)	11(1)
C(11)	7636(4)	7083(3)	2651(2)	10(1)
C(12)	6904(4)	5777(3)	2024(2)	10(1)
C(13)	6079(4)	4898(2)	2589(2)	9(1)
C(14)	6121(4)	5343(3)	3788(2)	11(1)
C(15)	6894(4)	6599(3)	4412(2)	13(1)
C(16)	7610(4)	7471(3)	3842(2)	12(1)
C(21)	8860(4)	4960(3)	-2649(2)	10(1)
C(22)	8048(4)	4083(3)	-2084(2)	9(1)
C(23)	7295(4)	2780(3)	-2715(2)	11(1)
C(24)	7297(4)	2400(3)	-3909(2)	12(1)
C(25)	7996(4)	3275(3)	-4483(2)	13(1)
C(26)	8790(4)	4537(3)	-3849(2)	12(1)
C(110)	8423(4)	8119(3)	2124(2)	11(1)
C(130)	5117(4)	3530(3)	2000(2)	11(1)
C(210)	9923(4)	6319(3)	-2047(2)	11(1)

Appendix A

C(230)	6541(4)	1750(3)	-2171(2)	11(1)
--------	---------	---------	----------	-------

Appendix A

Table A.1.16. Bond lengths [Å] for C₃₂H₂₄Cu₆O₂₆.

Cu(1)-O(7)	1.8846(19)	O(8)-C(230)	1.262(3)
Cu(1)-O(3)	1.8980(19)	O(8)-Cu(3) ^a	1.9500(19)
Cu(1)-O(12)	1.9267(18)	O(13)-C(12)	1.355(3)
Cu(1)-O(13)	1.9295(18)	O(12)-C(22)	1.354(3)
Cu(1)-Cu(2)	2.9714(5)	C(11)-C(16)	1.401(4)
Cu(2)-O(1)	1.8840(19)	C(11)-C(12)	1.412(4)
Cu(2)-O(6)	1.8969(19)	C(11)-C(110)	1.505(4)
Cu(2)-O(13)	1.9244(18)	C(12)-C(13)	1.416(3)
Cu(2)-O(12)	1.9334(18)	C(13)-C(14)	1.405(4)
Cu(3)-O(8) ^a	1.9500(19)	C(13)-C(130)	1.490(4)
Cu(3)-O(10)	1.950(2)	C(14)-C(15)	1.371(4)
Cu(3)-O(11)	1.952(2)	C(15)-C(16)	1.386(4)
Cu(3)-O(4)	1.9647(18)	C(21)-C(26)	1.400(4)
Cu(3)-O(9)	2.216(3)	C(21)-C(22)	1.411(4)
O(1)-C(110)	1.288(3)	C(21)-C(210)	1.503(4)
O(2)-C(110)	1.252(3)	C(22)-C(23)	1.413(4)
O(3)-C(130)	1.280(3)	C(23)-C(24)	1.401(4)
O(4)-C(130)	1.262(3)	C(23)-C(230)	1.505(4)
O(5)-C(210)	1.248(3)	C(24)-C(25)	1.388(4)
O(6)-C(210)	1.291(3)	C(25)-C(26)	1.383(4)
O(7)-C(230)	1.266(3)		

Symmetry transformations used to generate equivalent atoms:

^a $-x + 1, -y, -z$

Appendix A

Table A.1.17. Bond angles [°] for C₃₂H₂₄Cu₆O₂₆.

O(7)-Cu(1)-O(3)	95.27(8)	C(130)-O(3)-Cu(1)	126.16(17)
O(7)-Cu(1)-O(12)	93.37(8)	C(130)-O(4)-Cu(3)	126.70(17)
O(3)-Cu(1)-O(12)	171.28(8)	C(210)-O(6)-Cu(2)	126.77(17)
O(7)-Cu(1)-O(13)	171.89(8)	C(230)-O(7)-Cu(1)	127.52(17)
O(3)-Cu(1)-O(13)	92.07(8)	C(230)-O(8)-Cu(3) ^a	129.34(18)
O(12)-Cu(1)-O(13)	79.23(8)	C(12)-O(13)-Cu(2)	126.82(16)
O(7)-Cu(1)-Cu(2)	133.08(6)	C(12)-O(13)-Cu(1)	127.37(16)
O(3)-Cu(1)-Cu(2)	131.56(6)	Cu(2)-O(13)-Cu(1)	100.89(8)
O(12)-Cu(1)-Cu(2)	39.75(5)	C(22)-O(12)-Cu(1)	127.00(16)
O(13)-Cu(1)-Cu(2)	39.49(5)	C(22)-O(12)-Cu(2)	127.04(16)
O(1)-Cu(2)-O(6)	95.90(8)	Cu(1)-O(12)-Cu(2)	100.67(8)
O(1)-Cu(2)-O(13)	93.45(8)	C(16)-C(11)-C(12)	119.0(2)
O(6)-Cu(2)-O(13)	170.65(8)	C(16)-C(11)-C(110)	116.5(2)
O(1)-Cu(2)-O(12)	172.63(8)	C(12)-C(11)-C(110)	124.5(2)
O(6)-Cu(2)-O(12)	91.46(8)	O(13)-C(12)-C(11)	120.1(2)
O(13)-Cu(2)-O(12)	79.19(8)	O(13)-C(12)-C(13)	120.1(2)
O(1)-Cu(2)-Cu(1)	133.06(6)	C(11)-C(12)-C(13)	119.8(2)
O(6)-Cu(2)-Cu(1)	131.03(6)	C(14)-C(13)-C(12)	118.3(2)
O(13)-Cu(2)-Cu(1)	39.62(5)	C(14)-C(13)-C(130)	116.9(2)
O(12)-Cu(2)-Cu(1)	39.58(5)	C(12)-C(13)-C(130)	124.8(2)
O(8) ^a -Cu(3)-O(10)	83.46(8)	C(15)-C(14)-C(13)	122.1(2)
O(8) ^a -Cu(3)-O(11)	93.71(9)	C(14)-C(15)-C(16)	119.3(3)
O(10)-Cu(3)-O(11)	168.69(11)	C(15)-C(16)-C(11)	121.3(2)
O(8) ^a -Cu(3)-O(4)	152.98(8)	C(26)-C(21)-C(22)	119.0(2)
O(10)-Cu(3)-O(4)	86.66(8)	C(26)-C(21)-C(210)	116.2(2)
O(11)-Cu(3)-O(4)	91.08(9)	C(22)-C(21)-C(210)	124.8(2)
O(8) ^a -Cu(3)-O(9)	103.46(9)	O(12)-C(22)-C(21)	120.5(2)
O(10)-Cu(3)-O(9)	96.01(10)	O(12)-C(22)-C(23)	119.7(2)
O(11)-Cu(3)-O(9)	95.29(12)	C(21)-C(22)-C(23)	119.8(2)
O(4)-Cu(3)-O(9)	102.55(9)	C(24)-C(23)-C(22)	118.9(2)
C(110)-O(1)-Cu(2)	127.92(17)	C(24)-C(23)-C(230)	117.4(2)

Table A.1.17. Bond angles [°] for C₃₂H₂₄Cu₆O₂₆ (continued).

C(22)-C(23)-C(230)	123.7(2)	O(4)-C(130)-C(13)	116.6(2)
C(25)-C(24)-C(23)	121.5(3)	O(3)-C(130)-C(13)	122.9(2)
C(26)-C(25)-C(24)	119.0(3)	O(5)-C(210)-O(6)	120.6(2)
C(25)-C(26)-C(21)	121.7(2)	O(5)-C(210)-C(21)	117.8(2)
O(2)-C(110)-O(1)	120.9(2)	O(6)-C(210)-C(21)	121.6(2)
O(2)-C(110)-C(11)	116.7(2)	O(8)-C(230)-O(7)	121.6(2)
O(1)-C(110)-C(11)	122.5(2)	O(8)-C(230)-C(23)	114.9(2)
O(4)-C(130)-O(3)	120.5(2)	O(7)-C(230)-C(23)	123.5(2)

Symmetry transformations used to generate equivalent atoms:

$$^a -x + 1, -y, -z$$

Table A.1.18. Anisotropic displacement parameters [$\text{\AA}^2 \times 10^3$] for $\text{C}_{32}\text{H}_{24}\text{Cu}_6\text{O}_{26}$. The anisotropic displacement factor exponent takes the form: $-2\pi^2[(ha^*)^2U_{11} + \dots + 2hka^*b^*U_{12}]$.

	U_{11}	U_{22}	U_{33}	U_{23}	U_{13}	U_{12}
Cu(1)	14(1)	7(1)	11(1)	3(1)	4(1)	-1(1)
Cu(2)	13(1)	7(1)	12(1)	4(1)	4(1)	-1(1)
Cu(3)	15(1)	6(1)	20(1)	5(1)	7(1)	1(1)
O(1)	17(1)	9(1)	14(1)	5(1)	6(1)	2(1)
O(2)	16(1)	7(1)	17(1)	3(1)	6(1)	0(1)
O(3)	17(1)	10(1)	13(1)	3(1)	4(1)	-2(1)
O(4)	16(1)	6(1)	15(1)	4(1)	6(1)	0(1)
O(5)	15(1)	9(1)	15(1)	6(1)	6(1)	0(1)
O(6)	16(1)	9(1)	14(1)	4(1)	4(1)	-2(1)
O(7)	19(1)	8(1)	12(1)	5(1)	5(1)	0(1)
O(8)	20(1)	5(1)	19(1)	3(1)	6(1)	0(1)
O(9)	66(2)	20(1)	21(1)	7(1)	3(1)	-4(1)
O(10)	15(1)	6(1)	28(1)	7(1)	8(1)	2(1)
O(11)	22(1)	14(1)	68(2)	19(1)	19(1)	6(1)
O(12)	15(1)	6(1)	10(1)	4(1)	4(1)	-2(1)
O(13)	14(1)	8(1)	12(1)	4(1)	5(1)	0(1)
C(11)	9(1)	9(1)	13(1)	5(1)	2(1)	2(1)
C(12)	9(1)	10(1)	12(1)	6(1)	3(1)	4(1)
C(13)	7(1)	8(1)	13(1)	5(1)	3(1)	2(1)
C(14)	11(1)	10(1)	14(1)	6(1)	5(1)	3(1)
C(15)	16(1)	13(1)	11(1)	4(1)	4(1)	3(1)
C(16)	14(1)	8(1)	14(1)	1(1)	4(1)	2(1)
C(21)	10(1)	9(1)	14(1)	6(1)	3(1)	4(1)
C(22)	8(1)	10(1)	11(1)	4(1)	2(1)	4(1)
C(23)	11(1)	10(1)	13(1)	4(1)	2(1)	2(1)
C(24)	12(1)	10(1)	13(1)	4(1)	1(1)	2(1)
C(25)	14(1)	15(1)	13(1)	5(1)	3(1)	4(1)
C(26)	11(1)	13(1)	14(1)	8(1)	3(1)	4(1)
C(110)	9(1)	9(1)	17(1)	5(1)	2(1)	2(1)
C(130)	11(1)	8(1)	15(1)	4(1)	5(1)	3(1)

Appendix A

Cu(210)	9(1)	11(1)	16(1)	7(1)	4(1)	5(1)
Cu(230)	9(1)	9(1)	15(1)	4(1)	-1(1)	2(1)

Table A.1.19. Hydrogen coordinates [$\times 10^4$] and isotropic displacement parameters [$\text{\AA}^2 \times 10^3$] for $\text{C}_{32}\text{H}_{24}\text{Cu}_6\text{O}_{26}$.

	x	y	z	U_{eq}
H(9A)	1100(30)	200(40)	470(40)	56
H(9B)	2350(60)	880(30)	60(30)	56
H(10A)	970(40)	1750(20)	2780(30)	23
H(10B)	660(40)	570(20)	2860(30)	23
H(11A)	7210(50)	1560(20)	2120(40)	47
H(11B)	7070(50)	340(30)	2100(40)	47
H(14)	5596	4756	4178	13
H(15)	6939	6868	5226	15
H(16)	8092	8349	4266	14
H(24)	6809	1523	-4336	14
H(25)	7930	3012	-5301	16
H(26)	9300	5132	-4236	14

Appendix A

Table A.1.20. Hydrogen bond lengths [\AA] and angles [$^\circ$] for $\text{C}_{32}\text{H}_{24}\text{Cu}_6\text{O}_{26}$.

D-H \cdots A	$d(\text{D-H})$	$d(\text{H}\cdots\text{A})$	$d(\text{D}\cdots\text{A})$	$\angle(\text{DHA})$
O(9)-H(9A) \cdots O(9) ^b	0.809(18)	2.38(3)	3.119(6)	153(4)
O(9)-H(9B) \cdots O(1) ^c	0.820(18)	2.36(3)	3.115(3)	154(4)
O(9)-H(9B) \cdots O(3)	0.820(18)	2.61(4)	3.080(3)	118(3)
O(10)-H(10A) \cdots O(5) ^c	0.821(17)	1.946(19)	2.752(3)	166(3)
O(10)-H(10B) \cdots O(2) ^d	0.837(17)	1.833(18)	2.667(3)	174(3)
O(11)-H(11A) \cdots O(5) ^e	0.823(18)	1.93(2)	2.751(3)	171(4)
O(11)-H(11B) \cdots O(2) ^f	0.836(18)	1.89(2)	2.723(3)	171(4)

Symmetry transformations used to generate equivalent atoms:

$$^a -x + 1, -y, -z$$

$$^b -x, -y, -z$$

$$^c -x + 1, -y + 1, -z$$

$$^d x - 1, y - 1, z$$

$$^e -x + 2, -y + 1, -z$$

$$^f x, y - 1, z$$

Appendix A.2

Selected bond distances and angles for $\text{CdCu}_3(\text{OH})_6(\text{NO}_3)_2 \cdot x\text{H}_2\text{O}$: O(1)–Cu(1)–O(1A), 86.7; O(1)–Cu(1)–O(1F), 93.3; O(1A)–Cu(1)–O(2), 84.4; O(1F)–Cu(1)–O(2), 95.6. OW \cdots O(1) 3.283 Å. Others were mentioned in the text.

Table A.2.1. Selected interatomic distances [Å] and angles [°] for $\text{Cu}_2(\text{OH})_3\text{NO}_3$, rouaite, from Chapter 3, Ref. [11].

Cu(1)-O(1W)	1.919	Cu(2A)-O(2W)	2.047
Cu(1)-O(2W)	1.994	Cu(2A)-O(1AW)	2.308
O(1W)-Cu(1)-O(2W)	94.6	O(2W)-Cu(2A)-O(1AW)	75.8
Cu(1)-O(3W)	2.007	Cu(2A)-O(3AW)	1.953
O(1W)-Cu(1)-O(3W)	84.3	O(2W)-Cu(2A)-O(3AW)	102.1
O(2W)-Cu(1)-O(2W)	176.8	O(1AW)-Cu(2A)-O(3AW)	75.9
Cu(1)-O(4W)	2.434	Cu(2A)-O(3Z)	2.027
O(1W)-Cu(1)-O(4W)	87.9	O(2W)-Cu(2A)-O(3Z)	78.3
O(2W)-Cu(1)-O(4W)	80.8	O(1AW)-Cu(2A)-O(3Z)	106.8
O(3W)-Cu(1)-O(4W)	96.1	O(3AW)-Cu(2A)-O(3Z)	177.3
Cu(1)-O(1AW)	1.940	Cu(2A)-O(2AZ)	1.946
O(1W)-Cu(1)-O(1AW)	177.7	O(2W)-Cu(2A)-O(2AZ)	174.6
O(2W)-Cu(1)-O(1AW)	86.0	O(1AW)-Cu(2A)-O(2AZ)	108.2
O(3W)-Cu(1)-O(1AW)	95.0	O(3AW)-Cu(2A)-O(2AZ)	82.5
O(4W)-Cu(1)-O(1AW)	90.0	O(3Z)-Cu(2A)-O(2AZ)	97.0
Cu(1)-O(4AW)	2.371	Cu(2A)-O(4AZ)	2.392
O(1W)-Cu(1)-O(4AW)	92.8	O(2W)-Cu(2A)-O(4AZ)	93.9
O(2W)-Cu(1)-O(4AW)	99.9	O(1AW)-Cu(2A)-O(4AZ)	164.2
O(3W)-Cu(1)-O(4AW)	83.2	O(3AW)-Cu(2A)-O(4AZ)	95.0
O(4W)-Cu(1)-O(4AW)	178.9	O(3Z)-Cu(2A)-O(4AZ)	82.3
O(1AW)-Cu(1)-O(4AW)	89.3	O(2AZ)-Cu(2A)-O(4AZ)	82.9
O(5) \cdots H(2)	2.190	O(6) \cdots H(3)	2.261
Cu(1B)-O(4AZ)-Cu(1C)	78.6	Cu(1C)-O(4AZ)-Cu(2A)	85.6
Cu(1C)-O(4Z)-Cu(1D)	78.6	Cu(1C)-O(1Z)-Cu(2B)	95.2
Cu(1B)-O(4AZ)-Cu(2A)	84.2	Cu(2B)-O(1Z)-Cu(1D)	95.5
Cu(2B)-O(4W)-Cu(1A)	84.2	Cu(2A)-O(1AW)-Cu(1D)	95.5

Appendix A

Table A.2.2. Bragg reflections and Miller indices of pXRD pattern for $\text{CdCu}_3(\text{OH})_6(\text{NO}_3)_2 \cdot x\text{H}_2\text{O}$, matched to PDF # 01-072-1433, $P\bar{3}m1$.

$2\theta_{\text{obs}}$	d_{obs}	% I_{obs}	$2\theta_{\text{calcd}}$	d_{calcd}	% I_{calcd}	Δd	hkl
12.639	6.9978	100.0	12.674	6.9789	100.0	0.0189	0 0 1
20.197	4.3931	12.2	20.231	4.3858	11.5	0.0073	1 0 1
25.421	3.5010	25.8	25.444	3.4979	26.9	0.0031	0 0 2
27.321	3.2617	6.3	27.386	3.2540	6.0	0.0077	1 1 0
29.995	2.9766	4.3	30.033	2.9730	5.7	0.0033	0 1 2
31.676	2.8225	18.8	31.717	2.8189	17.5	0.0036	2 0 0
34.220	2.6182	29.6	34.261	2.6152	46.9	0.0030	0 2 1
41.038	2.1976	13.0	41.064	2.1963	32.0	0.0013	0 2 2
56.354	1.6313	5.7	56.444	1.6289	7.8	0.0024	2 2 0
58.038	1.5879	4.1	58.089	1.5866	9.7	0.0013	2 2 1

Table A.2.3. Bragg reflections and Miller indices of pXRD pattern for $\text{CdCu}_3(\text{OH})_6(\text{NO}_3)_2 \cdot x\text{H}_2\text{O}$, matched to PDF # 01-070-1904, $P\bar{1}$.

$2\theta_{\text{obs}}$	d_{obs}	% I_{obs}	$2\theta_{\text{calcd}}$	d_{calcd}	% I_{calcd}	Δd	hkl
12.639	6.9978	100.0	12.674	6.9789	100.0	0.0189	0 1 0
20.197	4.3931	12.2	20.231	4.3858	11.5	0.0073	$\bar{1}$ 1 1
25.421	3.5010	25.8	25.444	3.4979	26.9	0.0031	0 2 0
27.321	3.2617	6.3	27.386	3.2540	6.0	0.0077	$\bar{1}$ 0 2
29.995	2.9766	4.3	30.033	2.9730	5.7	0.0033	$\bar{1}$ 2 0
31.676	2.8225	18.8	31.717	2.8189	17.5	0.0036	2 0 0
34.220	2.6182	29.6	34.261	2.6152	46.9	0.0030	$\bar{2}$ 1 0
41.038	2.1976	13.0	41.064	2.1963	32.0	0.0013	$\bar{2}$ $\bar{2}$ 2
56.354	1.6313	5.7	56.444	1.6289	7.8	0.0024	$\bar{4}$ 0 2
58.038	1.5879	4.1	58.089	1.5866	9.7	0.0013	2 $\bar{1}$ 2

Appendix A

Table A.2.4. Bragg reflections and Miller indices of pXRD pattern for $\text{Cu}_2(\text{OH})_3\text{NO}_3$, rouaite, in $P2_1$, matched to PDF # 04-010-3058.

$2\theta_{\text{obs}}$	d_{obs}	% I_{obs}	$2\theta_{\text{calcd}}$	d_{calcd}	% I_{calcd}	Δd	hkl
12.788	6.9167	100.0	12.805	6.9078	100.0	0.0089	0 0 1
25.750	3.4570	25.9	25.773	3.4539	25.6	0.0031	0 0 2
32.083	2.7875	2.3	32.111	2.7852	2.9	0.0023	0 2 1
33.588	2.6660	4.1	33.621	2.6635	15.5	0.0025	$\bar{2}$ 0 1
36.446	2.4633	2.4	36.467	2.4619	20.4	0.0014	1 2 1

Appendix A.3

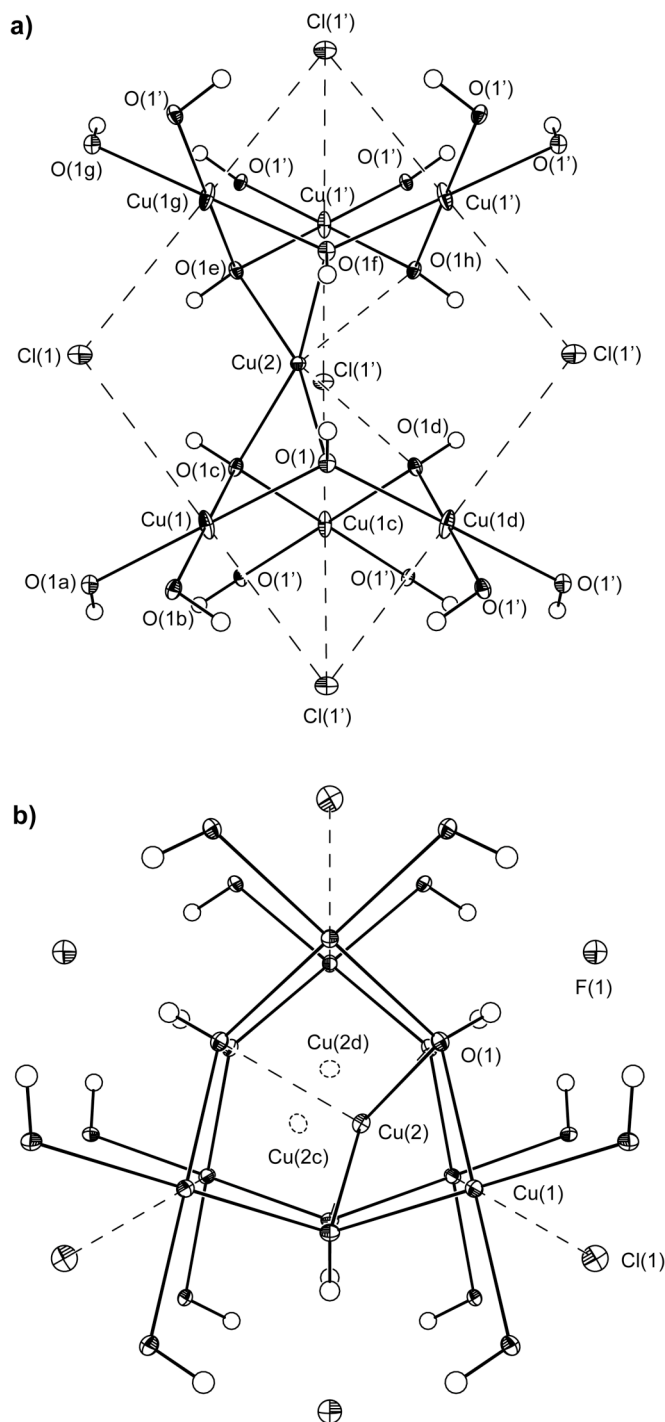


Figure A.3.1. (a) A portion of the crystal structure of $\text{Cu}\{\text{Cu}_3(\text{OH})_6\}\text{ClF}$, claringbullite, syn. with 40% ellipsoids shown. Atoms labeled with letters correspond to symmetry equivalent atoms as found in Tables A.3.3 and A.3.4. Hydrogen atoms are not labeled. (b) A view of the structure down the c axis, highlighting the crystallographically disordered Cu(2) atom.

Table A.3.1. Crystal data and structure refinement for Cu{Cu₃(OH)₆}ClF, claringbullite, syn.

Identification code	08115	
Empirical formula	H ₆ ClCu ₄ FO ₆	
Formula weight	410.66	
Temperature	100(2) K	
Wavelength	0.71073 Å	
Crystal system	Hexagonal	
Space group	<i>P</i> 6 ₃ / <i>mmc</i>	
Unit cell dimensions	<i>a</i> = 6.6703(12) Å	$\alpha = 90^\circ$
	<i>b</i> = 6.6703(12) Å	$\beta = 90^\circ$
	<i>c</i> = 9.1701(16) Å	$\gamma = 120^\circ$
Volume, Z	353.34(11) Å ³	2
Density (calculated)	3.860 g/cm ³	
Absorption coefficient	12.253 mm ⁻¹	
F(000)	392	
Crystal size	0.06 × 0.06 × 0.01 mm	
θ range for data collection	3.53 to 29.52°	
Limiting indices	$-9 \leq h \leq 8$	
	$-6 \leq k \leq 9$	
	$-12 \leq l \leq 12$	
Reflections collected	4943	
Independent reflections	218 ($R_{\text{int}} = 0.0460$)	
Completeness to $\theta = 29.52^\circ$	99.1 %	
Absorption correction	Semi-empirical from equivalents	
Max. and min. transmission	0.8873	0.5268
Refinement method	Full-matrix least-squares on F ²	
Data / restraints / parameters	218 / 7 / 22	
Goodness-of-fit on F ²	1.225	
Final R indices [$I > 2\sigma(I)$]	$R_1 = 0.0307$	$wR_2 = 0.0720$
R indices (all data)	$R_1 = 0.0332$	$wR_2 = 0.0731$
Largest diff. peak and hole	0.822 eÅ ⁻³	-2.130 eÅ ⁻³

Appendix A

Table A.3.2. Atomic coordinates [$\times 10^4$] and equivalent isotropic displacement parameters [$\text{\AA}^2 \times 10^3$] for 08115, $\text{Cu}\{\text{Cu}_3(\text{OH})_6\}\text{ClF}$, claringbullite, syn. U_{eq} is defined as one third of the trace of the orthogonalized U_{ij} tensor.

	x	y	z	U_{eq}
Cu(1)	5000	0	0	11(1)
Cu(2)	3729(2)	-2541(5)	2500	6(1)
Cl(1)	6667(4)	3333	2500	12(1)
F(1)	0	0	2500	12(2)
O(1)	2018(3)	-2018(3)	915(4)	7(1)

Table A.3.3. Bond lengths [\AA] for 08115, $\text{Cu}\{\text{Cu}_3(\text{OH})_6\}\text{ClF}$, claringbullite, syn.

Cu(1)-O(1) ^a	1.9478(19)	Cu(2)-O(1)	1.984(4)
Cu(1)-O(1) ^b	1.9478(19)	Cu(2)-O(1) ^e	1.984(4)
Cu(1)-O(1) ^c	1.9478(19)	Cu(2)-O(1) ^f	1.984(4)
Cu(1)-O(1)	1.9478(19)	Cu(2)-O(1) ^c	1.984(4)
Cu(1)-Cu(2)	2.7223(15)	Cu(2)-O(1) ^d	2.4540(43)
Cu(1)-Cu(2) ^a	2.7223(15)	Cu(2)-O(1) ^h	2.4540(43)
Cu(1)-Cl(1)	2.9939(4)	O(1)-Cu(1) ^d	1.9478(19)
Cu(2)-Cu(2) ^d	0.792(5)	O(1)-Cu(2) ^d	1.984(4)
Cu(2)-Cu(2) ^c	0.792(5)	F(1)···H(1)	1.92(2)
Cu(2)-Cu(1) ^g	2.7223(15)		

Symmetry transformations used to generate equivalent atoms:

$$^a -x + 1, -y, -z \quad ^b x - y, x, -z$$

$$^e -x + y + 1, -x, -z + \frac{1}{2}$$

$$^h -y, x - y - 1, -z + \frac{1}{2}$$

$$^c -x + y + 1, -x, z$$

$$^f x, y, -z + \frac{1}{2}$$

$$^d -y, x - y - 1, z$$

$$^g -x + 1, -y, z + \frac{1}{2}$$

Table A.3.4. Bond angles [°] for 08115, Cu{Cu₃(OH)₆}ClF, claringbullite, syn.

O(1) ^a -Cu(1)-O(1) ^b	85.0(2)	O(1)-Cu(2)-O(1) ^c	83.09(18)
O(1) ^a -Cu(1)-O(1) ^c	95.0(2)	O(1) ^e -Cu(2)-O(1) ^c	94.2(2)
O(1) ^b -Cu(1)-O(1) ^c	180.0(2)	O(1) ^f -Cu(2)-O(1) ^c	162.47(18)
O(1) ^a -Cu(1)-O(1)	180.0	Cu(2) ^d -Cu(2)-Cu(1) ^g	117.84(4)
O(1) ^b -Cu(1)-O(1)	95.0(2)	Cu(2) ^c -Cu(2)-Cu(1) ^g	117.84(4)
O(1) ^c -Cu(1)-O(1)	85.0(2)	O(1)-Cu(2)-Cu(1) ^g	122.34(13)
O(1) ^a -Cu(1)-Cu(2)	133.26(11)	O(1) ^e -Cu(2)-Cu(1) ^g	45.63(6)
O(1) ^b -Cu(1)-Cu(2)	133.26(11)	O(1) ^f -Cu(2)-Cu(1) ^g	45.63(6)
O(1) ^c -Cu(1)-Cu(2)	46.74(11)	O(1) ^c -Cu(2)-Cu(1) ^g	122.34(13)
O(1)-Cu(1)-Cu(2)	46.74(11)	Cu(2) ^d -Cu(2)-Cu(1)	117.84(4)
O(1) ^a -Cu(1)-Cu(2) ^a	46.74(11)	Cu(2) ^c -Cu(2)-Cu(1)	117.84(4)
O(1) ^b -Cu(1)-Cu(2) ^a	46.74(11)	O(1)-Cu(2)-Cu(1)	45.63(6)
O(1) ^c -Cu(1)-Cu(2) ^a	133.26(11)	O(1) ^e -Cu(2)-Cu(1)	122.34(13)
O(1)-Cu(1)-Cu(2) ^a	133.26(11)	O(1) ^f -Cu(2)-Cu(1)	122.34(13)
Cu(2)-Cu(1)-Cu(2) ^a	180.0	O(1) ^c -Cu(2)-Cu(1)	45.63(6)
Cu(2) ^d -Cu(2)-Cu(2) ^c	60.0	Cu(1) ^g -Cu(2)-Cu(1)	114.73(10)
Cu(2) ^d -Cu(2)-O(1)	78.48(7)	Cu(1) ^d -O(1)-Cu(1)	117.77(18)
Cu(2) ^c -Cu(2)-O(1)	117.62(11)	Cu(1) ^d -O(1)-Cu(2)	107.49(17)
Cu(2) ^d -Cu(2)-O(1) ^e	117.62(11)	Cu(1)-O(1)-Cu(2)	87.63(11)
Cu(2) ^c -Cu(2)-O(1) ^e	78.48(7)	Cu(1) ^d -O(1)-Cu(2) ^d	87.63(11)
O(1)-Cu(2)-O(1) ^e	162.47(18)	Cu(1)-O(1)-Cu(2) ^d	107.49(17)
Cu(2) ^d -Cu(2)-O(1) ^f	78.48(7)	Cu(2)-O(1)-Cu(2) ^d	23.04(15)
Cu(2) ^c -Cu(2)-O(1) ^f	117.62(11)	O(1)-Cu(1)-Cl(1)	93.17(9)
O(1)-Cu(2)-O(1) ^f	94.2(2)	O(1) ^a -Cu(1)-Cl(1)	86.83(9)
O(1) ^e -Cu(2)-O(1) ^f	83.09(18)	O(1) ^c -Cu(1)-Cl(1)	93.17(9)
Cu(2) ^d -Cu(2)-O(1) ^c	117.62(11)	O(1) ^b -Cu(1)-Cl(1)	86.83(9)
Cu(2) ^c -Cu(2)-O(1) ^c	78.48(7)		

Symmetry transformations used to generate equivalent atoms:

^a $-x + 1, -y, -z$

^b $x - y, x, -z$

^c $-x + y + 1, -x, z$

^d $-y, x - y - 1, z$

^e $-x + y + 1, -x, -z + \frac{1}{2}$

^f $x, y, -z + \frac{1}{2}$

^g $-x + 1, -y, z + \frac{1}{2}$

^h $-y, x - y - 1, -z + \frac{1}{2}$

Appendix A

Table A.3.5. Anisotropic displacement parameters [$\text{\AA}^2 \times 10^3$] for 08115, $\text{Cu}\{\text{Cu}_3(\text{OH})_6\}\text{ClF}$, claringbullite, syn. The anisotropic displacement factor exponent takes the form: $-2\pi^2[(ha^*)^2U_{11} + \dots + 2hka^*b^*U_{12}]$.

	U_{11}	U_{22}	U_{33}	U_{23}	U_{13}	U_{12}
Cu(1)	5(1)	6(1)	21(1)	5(1)	3(1)	3(1)
Cu(2)	7(1)	6(1)	5(1)	0	0	3(1)
Cl(1)	14(1)	14(1)	8(2)	0	0	7(1)
F(1)	11(2)	11(2)	13(4)	0	0	6(1)
O(1)	7(1)	7(1)	9(2)	-1(1)	1(1)	4(1)

Table A.3.6. Hydrogen coordinates [$\times 10^4$] and isotropic displacement parameters [$\text{\AA}^2 \times 10^3$] for 08115, $\text{Cu}\{\text{Cu}_3(\text{OH})_6\}\text{ClF}$, claringbullite, syn.

	x	y	z	U_{eq}
H(1)	1390(30)	-1390(30)	1360(60)	9

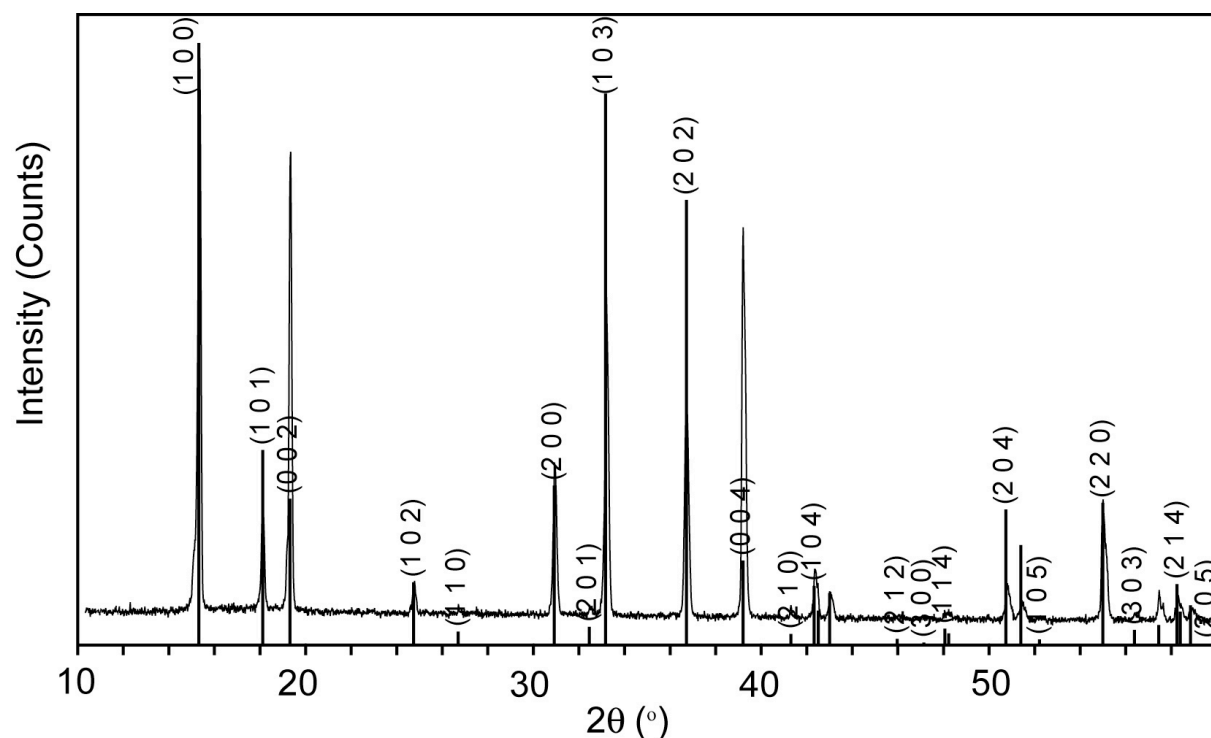


Figure A.3.2. pXRD of claringbullite, matched and indexed to PDF # 01-086-0899.

Table A.3.7. Bragg reflections and Miller indices of pXRD pattern for claringbullite, syn matched to PDF # 01-086-0899.

$2\theta_{\text{obs}}$	d_{obs}	% I_{obs}	$2\theta_{\text{calcd}}$	d_{calcd}	% I_{calcd}	Δd	hkl
15.351	5.7674	100.0	15.319	5.7793	100.0	-0.0119	1 0 0
18.130	4.8890	18.8	18.121	4.8915	32.2	-0.0025	1 0 1
19.347	4.5841	80.9	19.312	4.5925	24.1	-0.0084	0 0 2
24.787	3.5891	5.7	24.742	3.5955	10.2	-0.0026	1 0 2
30.933	2.8885	26.9	30.921	2.8896	26.3	-0.0011	2 0 0
33.211	2.6954	56.0	33.160	2.6994	91.6	-0.0040	1 0 3
36.712	2.4460	39.1	36.716	2.4458	73.9	-0.0002	2 0 2
39.210	2.2957	68.9	39.201	2.2963	13.8	-0.0006	0 0 4
41.309	2.1838	2.2	41.298	2.1844	1.6	-0.0006	2 1 0
42.354	2.1323	8.5	42.319	2.1340	9.6	-0.0017	1 0 4
43.016	2.1010	4.6	43.006	2.1015	8.4	-0.0005	2 0 3
48.229	1.8854	1.8	48.229	1.8854	1.7	0	3 0 1
50.809	1.7955	6.3	50.742	1.7978	22.3	-0.0023	2 0 4
51.431	1.7753	3.5	51.394	1.7765	16.4	-0.0012	2 1 3
55.010	1.6679	21.2	54.996	1.6683	23.4	-0.0004	2 2 0
57.472	1.6022	5.1	57.446	1.6029	3.1	-0.0007	3 1 0
58.309	1.5812	4.3	58.249	1.5827	9.9	-0.0015	2 1 4
58.832	1.5684	2.6	58.844	1.5681	6.4	0.0003	2 2 2

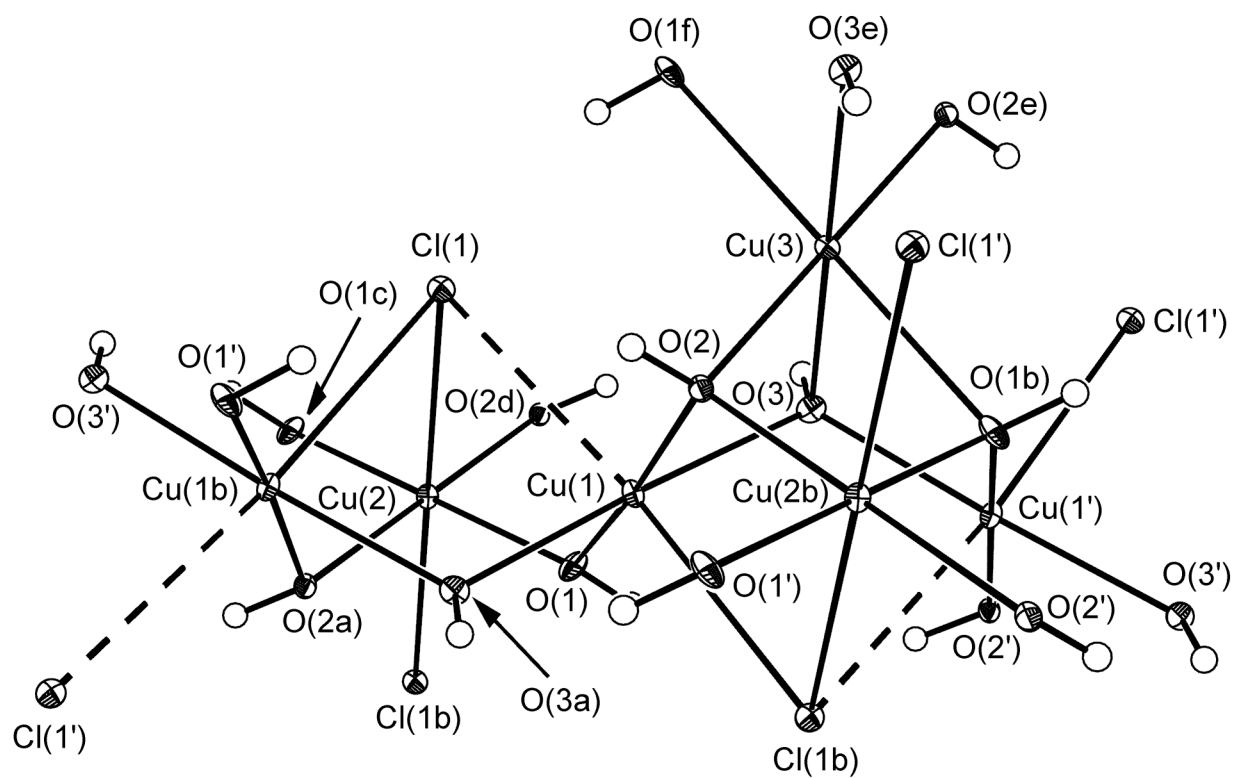


Figure A.3.3. A portion of the crystal structure of $\text{Cu}\{\text{Cu}_3(\text{OH})_6\}\text{Cl}_2$, clinoatacamite, syn. With 40% ellipsoids shown. Atoms labeled with letters correspond to symmetry equivalent atoms as found in Tables A.3.10 and A.3.11. Hydrogen atoms are not labeled.

Table A.3.8. Crystal data and structure refinement for $\text{Cu}\{\text{Cu}_3(\text{OH})_6\}\text{Cl}_2$, clinoatacamite, syn.

Identification code	c04042a	
Empirical formula	$\text{H}_3\text{ClCu}_2\text{O}_3$	
Formula weight	213.55	
Temperature	150(2) K	
Wavelength	0.71073 Å	
Crystal system	monoclinic	
Space group	$P2_1/n$	
Unit cell dimensions	$a = 6.1565(9)$ Å	$\alpha = 90^\circ$
	$b = 6.8138(11)$ Å	$\beta = 99.800(4)^\circ$
	$c = 9.1188(14)$ Å	$\gamma = 90^\circ$
Volume, Z	$376.94(10)$ Å ³	4
Density (calculated)	3.763 g/cm ³	
Absorption coefficient	11.819 mm ⁻¹	
F(000)	408	
Crystal size	0.15 × 0.10 × 0.10 mm	
θ range for data collection	3.72 to 26.43°	
Limiting indices	$-7 \leq h \leq 7$ $-8 \leq k \leq 7$ $-11 \leq l \leq 10$	
Reflections collected	3798	
Independent reflections	784 ($R_{\text{int}} = 0.0493$)	
Completeness to $\theta = 26.43^\circ$	99.5 %	
Absorption correction	Semi-empirical from equivalents	
Max. and min. transmission	1.0	0.626876
Refinement method	Full-matrix least-squares on F^2	
Data / restraints / parameters	784 / 0 / 70	
Goodness-of-fit on F^2	1.123	
Final R indices [$I > 2\sigma(I)$]	$R_1 = 0.0290$	$wR_2 = 0.0731$
R indices (all data)	$R_1 = 0.0312$	$wR_2 = 0.0745$
Largest diff. peak and hole	1.068 eÅ^{-3}	-0.948 eÅ^{-3}

Appendix A

Table A.3.9. Atomic coordinates [$\times 10^4$] and equivalent isotropic displacement parameters [$\text{\AA}^2 \times 10^3$] for c04042a, $\text{Cu}\{\text{Cu}_3(\text{OH})_6\}\text{Cl}_2$, clinoatacamite, syn. U_{eq} is defined as one third of the trace of the orthogonalized U_{ij} tensor.

	x	y	z	U_{eq}
Cu(1)	2406(1)	2354(1)	7516(1)	6(1)
Cu(2)	0	5000	10000	6(1)
Cu(3)	0	0	5000	6(1)
O(1)	1908(4)	2917(4)	9508(3)	10(1)
O(2)	2573(4)	1784(4)	5396(3)	7(1)
O(3)	780(5)	-194(4)	7240(3)	8(1)
Cl(1)	-1121(2)	5045(1)	6928(1)	8(1)

Table A.3.10. Bond lengths [\AA] for c04042a, $\text{Cu}\{\text{Cu}_3(\text{OH})_6\}\text{Cl}_2$, clinoatacamite, syn.

Cu(1)-O(1)	1.932(3)	Cu(2)-O(2) ^d	2.006(3)
Cu(1)-O(2)	1.991(3)	Cu(2)-Cl(1) ^c	2.7685(11)
Cu(1)-O(3)	1.998(3)	Cu(2)-Cl(1)	2.7685(11)
Cu(1)-O(3) ^a	2.001(3)	Cu(3)-O(2)	1.980(3)
Cu(1)-Cl(1) ^b	2.7514(10)	Cu(3)-O(2) ^e	1.980(3)
Cu(1)-Cu(3)	2.9786(5)	Cu(3)-O(3) ^e	2.022(3)
Cu(2)-O(1) ^c	1.943(3)	Cu(3)-O(3)	2.022(3)
Cu(2)-O(1)	1.943(3)	Cu(3)-O(1) ^f	2.356(3)
Cu(2)-O(2) ^a	2.006(3)	Cu(3)-O(1) ^b	2.356(3)

Symmetry transformations used to generate equivalent atoms:

$$^a -x + 1/2, y + 1/2, -z + 3/2$$

$$^d x - 1/2, -y + 1/2, z + 1/2$$

$$^b -x + 1/2, y - 1/2, -z + 3/2$$

$$^e -x, -y, -z + 1$$

$$^c -x, -y + 1, -z + 2$$

$$^f x - 1/2, -y + 1/2, z - 1/2$$

Appendix A

Table A.3.11. Bond angles [°] for c04042a, Cu{Cu₃(OH)₆}Cl₂, clinoatacamite, syn.

O(1)-Cu(1)-O(2)	173.90(11)	O(2) ^e -Cu(3)-O(3)	100.92(11)
O(1)-Cu(1)-O(3)	97.71(13)	O(3) ^e -Cu(3)-O(3)	180.0
O(2)-Cu(1)-O(3)	79.39(12)	O(2)-Cu(3)-O(1) ^f	105.09(11)
O(1)-Cu(1)-O(3) ^a	84.53(12)	O(2) ^e -Cu(3)-O(1) ^f	74.91(11)
O(2)-Cu(1)-O(3) ^a	98.69(12)	O(3) ^e -Cu(3)-O(1) ^f	73.91(10)
O(3)-Cu(1)-O(3) ^a	175.99(7)	O(3)-Cu(3)-O(1) ^f	106.09(10)
O(1)-Cu(1)-Cl(1) ^b	101.55(8)	O(2)-Cu(3)-O(1) ^b	74.91(11)
O(2)-Cu(1)-Cl(1) ^b	83.61(8)	O(2) ^e -Cu(3)-O(1) ^b	105.09(11)
O(3)-Cu(1)-Cl(1) ^b	84.78(8)	O(3) ^e -Cu(3)-O(1) ^b	106.09(10)
O(3) ^a -Cu(1)-Cl(1) ^b	91.52(8)	O(3)-Cu(3)-O(1) ^b	73.91(10)
O(1)-Cu(1)-Cu(3)	133.90(9)	O(1) ^f -Cu(3)-O(1) ^b	180.0
O(2)-Cu(1)-Cu(3)	41.27(7)	O(2)-Cu(3)-Cu(1)	41.54(8)
O(3)-Cu(1)-Cu(3)	42.49(8)	O(2) ^e -Cu(3)-Cu(1)	138.46(8)
O(3) ^a -Cu(1)-Cu(3)	136.92(9)	O(3) ^e -Cu(3)-Cu(1)	138.11(7)
Cl(1) ^b -Cu(1)-Cu(3)	97.05(2)	O(3)-Cu(3)-Cu(1)	41.89(7)
O(1) ^c -Cu(2)-O(1)	180.000(1)	O(1) ^f -Cu(3)-Cu(1)	95.86(7)
O(1) ^c -Cu(2)-O(2) ^a	95.57(12)	O(1) ^b -Cu(3)-Cu(1)	84.14(7)
O(1)-Cu(2)-O(2) ^a	84.43(12)	O(2)-Cu(3)-Cu(1) ^e	138.46(8)
O(1) ^c -Cu(2)-O(2) ^d	84.43(12)	O(2) ^e -Cu(3)-Cu(1) ^e	41.54(8)
O(1)-Cu(2)-O(2) ^d	95.57(12)	O(3) ^e -Cu(3)-Cu(1) ^e	41.89(7)
O(2) ^a -Cu(2)-O(2) ^d	180.00(12)	O(3)-Cu(3)-Cu(1) ^e	138.11(7)
O(1) ^c -Cu(2)-Cl(1) ^c	80.25(8)	O(1) ^f -Cu(3)-Cu(1) ^e	84.14(7)
O(1)-Cu(2)-Cl(1) ^c	99.75(8)	O(1) ^b -Cu(3)-Cu(1) ^e	95.86(7)
O(2) ^a -Cu(2)-Cl(1) ^c	97.11(8)	Cu(1)-Cu(3)-Cu(1) ^e	180.0
O(2) ^d -Cu(2)-Cl(1) ^c	82.89(8)	Cu(1)-O(1)-Cu(2)	124.15(14)
O(1) ^c -Cu(2)-Cl(1)	99.75(8)	Cu(1)-O(1)-Cu(3) ^a	92.65(11)
O(1)-Cu(2)-Cl(1)	80.25(8)	Cu(2)-O(1)-Cu(3) ^a	90.94(11)
O(2) ^a -Cu(2)-Cl(1)	82.89(8)	Cu(3)-O(2)-Cu(1)	97.19(11)
O(2) ^d -Cu(2)-Cl(1)	97.11(8)	Cu(3)-O(2)-Cu(2) ^b	101.10(12)
Cl(1) ^c -Cu(2)-Cl(1)	180.0	Cu(1)-O(2)-Cu(2) ^b	117.14(13)
O(2)-Cu(3)-O(2) ^e	180.00(12)	Cu(1)-O(3)-Cu(1) ^b	116.96(14)
O(2)-Cu(3)-O(3) ^e	100.92(11)	Cu(1)-O(3)-Cu(3)	95.62(12)
O(2) ^e -Cu(3)-O(3) ^e	79.08(11)	Cu(1) ^b -O(3)-Cu(3)	101.48(12)
O(2)-Cu(3)-O(3)	79.08(11)	Cu(1) ^a -Cl(1)-Cu(2)	76.32(3)

Symmetry transformations used to generate equivalent atoms:

^a $-x + 1/2, y + 1/2, -z + 3/2$

^d $x - 1/2, -y + 1/2, z + 1/2$

^b $-x + 1/2, y - 1/2, -z + 3/2$

^e $-x, -y, -z + 1$

^c $-x, -y + 1, -z + 2$

^f $x - 1/2, -y + 1/2, z - 1/2$

Table A.3.12. Anisotropic displacement parameters [$\text{\AA}^2 \times 10^3$] for c04042a, $\text{Cu}\{\text{Cu}_3(\text{OH})_6\}\text{Cl}_2$, clinoatacamite, syn. The anisotropic displacement factor exponent takes the form: $-2\pi^2[(ha^*)^2U_{11} + \dots + 2hka^*b^*U_{12}]$.

	U_{11}	U_{22}	U_{33}	U_{23}	U_{13}	U_{12}
Cu(1)	8(1)	6(1)	4(1)	-1(1)	3(1)	-1(1)
Cu(2)	7(1)	6(1)	6(1)	0(1)	3(1)	0(1)
Cu(3)	7(1)	7(1)	4(1)	0(1)	2(1)	-1(1)
O(1)	13(1)	10(1)	6(1)	4(1)	2(1)	4(1)
O(2)	10(1)	6(1)	6(1)	0(1)	1(1)	-1(1)
O(3)	6(1)	10(1)	9(1)	2(1)	4(1)	0(1)
Cl(1)	9(1)	9(1)	6(1)	0(1)	2(1)	-1(1)

Table A.3.13. Hydrogen coordinates [$\times 10^4$] and isotropic displacement parameters [$\text{\AA}^2 \times 10^3$] for c04042a, $\text{Cu}\{\text{Cu}_3(\text{OH})_6\}\text{Cl}_2$, clinoatacamite, syn.

	x	y	z	U_{eq}
H(1)	2090(90)	1990(90)	10090(60)	31(16)
H(2)	2420(80)	2770(80)	4870(60)	15(13)
H(3)	-410(110)	-230(70)	7610(70)	27(16)

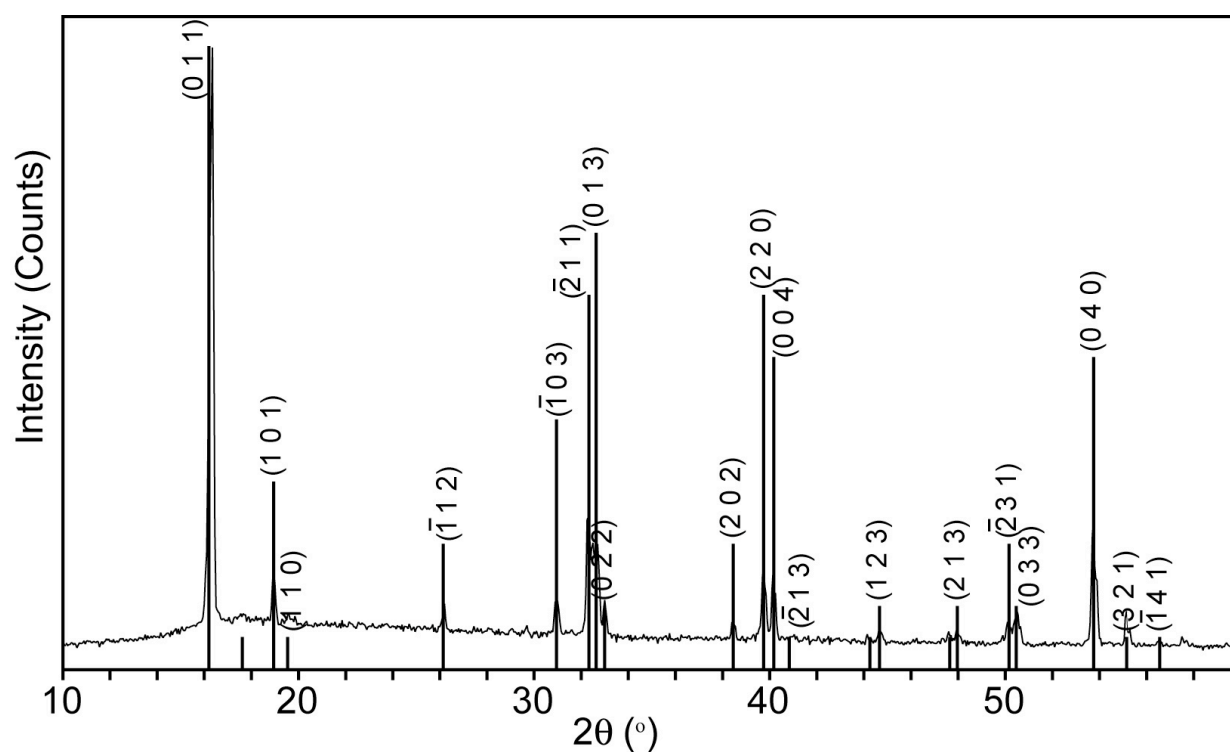


Figure A.3.4. pXRD of clinoatacamite, matched and indexed to PDF # 00-050-1599.

Table A.3.14. Bragg reflections and Miller indices of pXRD pattern for clinoatacamite, syn. matched to PDF # 00-50-1559.

$2\theta_{\text{obs}}$	d_{obs}	% I_{obs}	$2\theta_{\text{calcd}}$	d_{calcd}	% I_{calcd}	Δd	hkl
16.329	5.4239	100.0	16.191	5.4700	100.0	-0.0461	$\bar{1} 0 1$
18.952	4.6787	9.1	18.947	4.6800	30.0	-0.0013	1 0 1
26.181	3.4011	4.5	26.142	3.4060	20.0	-0.0049	0 2 0
30.956	2.8864	6.1	30.950	2.8870	40.0	-0.0006	$\bar{1} 0 3$
32.307	2.7688	20.2	32.328	2.7670	60.0	0.0018	$\bar{2} 1 1$
32.688	2.7373	15.8	32.631	2.7420	70.0	-0.0047	$\bar{2} 0 2$
33.005	2.7118	6.1	32.989	2.7130	10.0	-0.0012	0 2 2
38.459	2.3388	3.0	38.456	2.3390	20.0	-0.0002	2 0 2
39.754	2.2655	11.7	39.746	2.2660	60.0	-0.0005	2 2 0
40.164	2.2434	11.3	40.171	2.2430	50.0	0.0004	0 0 4
44.671	2.0269	2.3	44.670	2.0270	10.0	0.0001	1 2 3
47.619	1.9081	1.7	47.648	1.9070	5.0	0.0011	3 0 1
47.964	1.8952	2.5	47.969	1.8950	10.0	0.0002	2 1 3
50.110	1.8189	3.9	50.167	1.8170	20.0	0.0019	$\bar{2} 3 1$
50.495	1.8060	5.8	50.464	1.8070	10.0	-0.0010	$\bar{1} 0 5$
53.749	1.7041	21.8	53.751	1.7040	50.0	0.0001	0 4 0
55.151	1.6640	5.7	55.151	1.6640	5.0	0	3 2 1

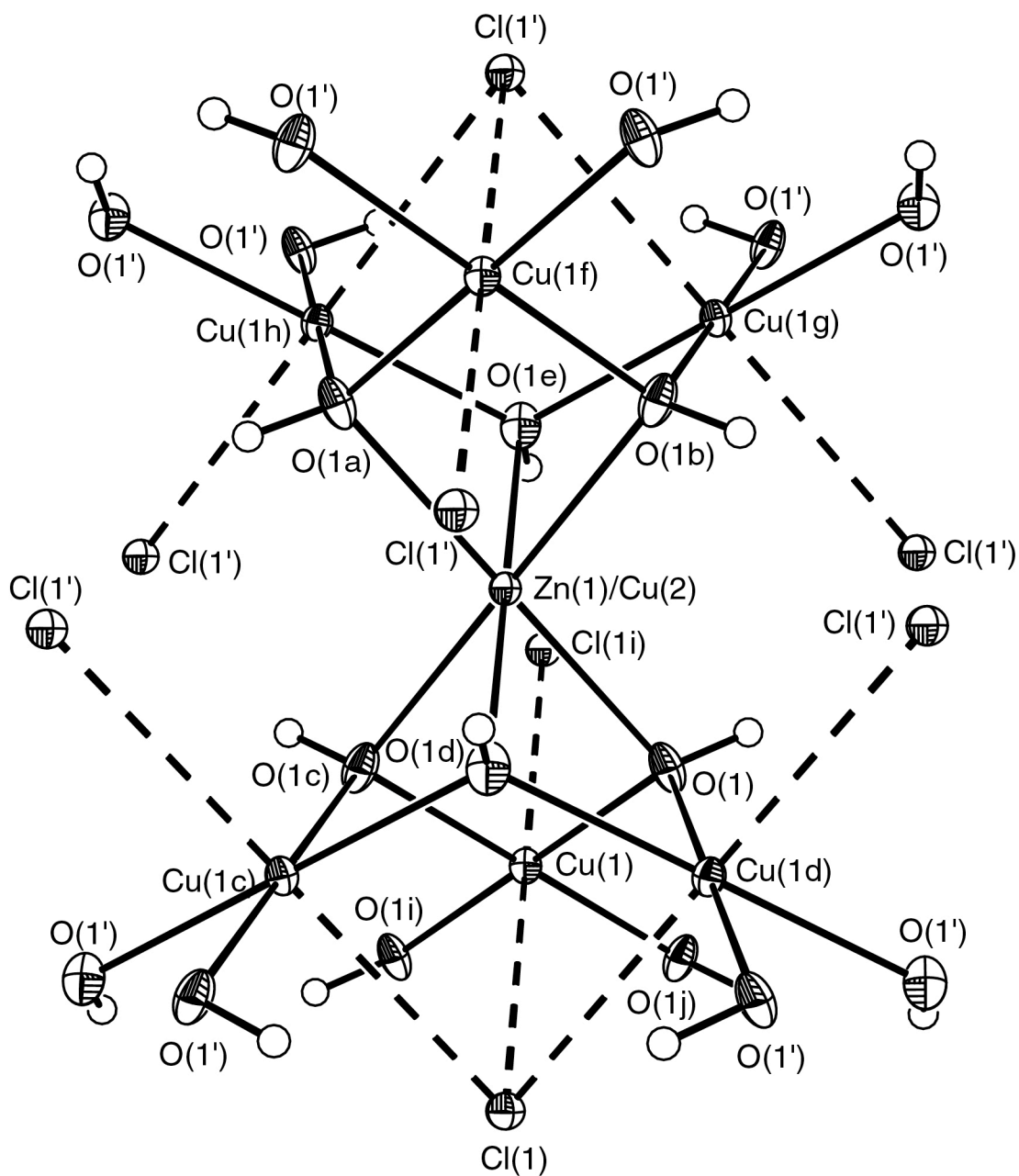


Figure A.3.5. A portion of the crystal structure of $\text{Zn}_{0.33}\text{Cu}_{3.67}(\text{OH})_6\text{Cl}_2$. 50% ellipsoids are shown. Atoms labeled with letters correspond to symmetry equivalent atoms as found in tables A.3.17 and A.3.18. Hydrogen atoms are not labeled.

Table A.3.15. Crystal data and structure refinement for $\text{Zn}_{0.33}\text{Cu}_{3.67}(\text{OH})_6\text{Cl}_2$.

Identification code	mps3atest	
Empirical formula	$\text{H}_6\text{Cl}_2\text{Cu}_{3.67}\text{O}_6\text{Zn}_{0.33}$	
Formula weight	427.72	
Temperature	150(2) K	
Wavelength	0.71073 Å	
Crystal system	Rhombohedral (obverse)	
Space group	$R\bar{3}m$	
Unit cell dimensions	$a = 6.8293(6)$ Å	$\alpha = 90^\circ$
	$b = 6.8293(6)$ Å	$\beta = 90^\circ$
	$c = 14.024(2)$ Å	$\gamma = 120^\circ$
Volume, Z	$566.46(12)$ Å ³	3
Density (calculated)	3.761 g/cm ³	
Absorption coefficient	11.917 mm ⁻¹	
F(000)	613	
Crystal size	0.07 × 0.05 × 0.02 mm	
θ range for data collection	3.74 to 24.70°	
Limiting indices	$-7 \leq h \leq 8$ $-7 \leq k \leq 7$ $-16 \leq l \leq 16$	
Reflections collected	1161	
Independent reflections	138 ($R_{\text{int}} = 0.0404$)	
Completeness to $\theta = 24.70^\circ$	100.0 %	
Refinement method	Full-matrix least-squares on F^2	
Data / restraints / parameters	138 / 1 / 20	
Goodness-of-fit on F^2	1.213	
Final R indices [$I > 2\sigma(I)$]	$R_1 = 0.0202$	$wR_2 = 0.0531$
R indices (all data)	$R_1 = 0.0202$	$wR_2 = 0.0531$
Largest diff. peak and hole	0.394 eÅ ⁻³	-0.776 eÅ ⁻³

Appendix A

Table A.3.18. Bond angles [°] for mps3atest, $\text{Zn}_{0.33}\text{Cu}_{3.67}(\text{OH})_6\text{Cl}_2$.

O(1) ^a -Zn(1)-O(1)	180.00(14)	O(1) ^b -Cu(2)-Cu(1)	140.01(4)
O(1) ^a -Zn(1)-O(1) ^b	76.17(13)	O(1) ^c -Cu(2)-Cu(1)	39.99(4)
O(1)-Zn(1)-O(1) ^b	103.83(13)	O(1) ^e -Cu(2)-Cu(1)	94.44(9)
O(1) ^a -Zn(1)-O(1) ^c	103.83(13)	O(1) ^d -Cu(2)-Cu(1)	85.56(9)
O(1)-Zn(1)-O(1) ^c	76.17(13)	O(1) ^a -Cu(2)-Cu(1) ^d	140.01(4)
O(1) ^b -Zn(1)-O(1) ^c	180.0(2)	O(1)-Cu(2)-Cu(1) ^d	39.99(4)
O(1) ^a -Zn(1)-O(1) ^e	76.17(13)	O(1) ^b -Cu(2)-Cu(1) ^d	94.44(9)
O(1)-Zn(1)-O(1) ^e	103.83(13)	O(1) ^c -Cu(2)-Cu(1) ^d	85.56(9)
O(1) ^b -Zn(1)-O(1) ^e	76.17(13)	O(1) ^e -Cu(2)-Cu(1) ^d	140.01(4)
O(1) ^c -Zn(1)-O(1) ^e	103.83(13)	O(1) ^d -Cu(2)-Cu(1) ^d	39.99(4)
O(1) ^a -Zn(1)-O(1) ^d	103.83(13)	Cu(1)-Cu(2)-Cu(1) ^d	67.884(9)
O(1)-Zn(1)-O(1) ^d	76.17(13)	O(1) ^a -Cu(2)-Cu(1) ^c	94.44(9)
O(1) ^b -Zn(1)-O(1) ^d	103.83(13)	O(1)-Cu(2)-Cu(1) ^c	85.56(9)
O(1) ^c -Zn(1)-O(1) ^d	76.17(13)	O(1) ^b -Cu(2)-Cu(1) ^c	140.01(4)
O(1) ^d -Zn(1)-O(1) ^d	180.0(3)	O(1) ^c -Cu(2)-Cu(1) ^c	39.99(4)
O(1) ^a -Zn(1)-Cu(1)	140.01(4)	O(1) ^e -Cu(2)-Cu(1) ^c	140.01(4)
O(1)-Zn(1)-Cu(1)	39.99(4)	O(1) ^d -Cu(2)-Cu(1) ^c	39.99(4)
O(1) ^b -Zn(1)-Cu(1)	140.01(4)	Cu(1)-Cu(2)-Cu(1) ^c	67.884(9)
O(1) ^c -Zn(1)-Cu(1)	39.99(4)	Cu(1) ^d -Cu(2)-Cu(1) ^c	67.884(9)
O(1) ^e -Zn(1)-Cu(1)	94.44(9)	O(1) ^a -Cu(2)-Cu(1) ^f	39.99(4)
O(1) ^d -Zn(1)-Cu(1)	85.56(9)	O(1)-Cu(2)-Cu(1) ^f	140.01(4)
O(1) ^a -Zn(1)-Cu(1) ^d	140.01(4)	O(1) ^b -Cu(2)-Cu(1) ^f	39.99(4)
O(1)-Zn(1)-Cu(1) ^d	39.99(4)	O(1) ^c -Cu(2)-Cu(1) ^f	140.01(4)
O(1) ^b -Zn(1)-Cu(1) ^d	94.44(9)	O(1) ^e -Cu(2)-Cu(1) ^f	85.56(9)
O(1) ^c -Zn(1)-Cu(1) ^d	85.56(9)	O(1) ^d -Cu(2)-Cu(1) ^f	94.44(9)
O(1) ^e -Zn(1)-Cu(1) ^d	140.01(4)	Cu(1)-Cu(2)-Cu(1) ^f	180.0
O(1) ^d -Zn(1)-Cu(1) ^d	39.99(4)	Cu(1) ^d -Cu(2)-Cu(1) ^f	112.117(9)
Cu(1)-Zn(1)-Cu(1) ^d	67.884(9)	Cu(1) ^c -Cu(2)-Cu(1) ^f	112.117(9)
O(1) ^a -Zn(1)-Cu(1) ^c	94.44(9)	O(1) ^a -Cu(2)-Cu(1) ^g	85.56(9)
O(1)-Zn(1)-Cu(1) ^c	85.56(9)	O(1)-Cu(2)-Cu(1) ^g	94.44(9)
O(1) ^b -Zn(1)-Cu(1) ^c	140.01(4)	O(1) ^b -Cu(2)-Cu(1) ^g	39.99(4)
O(1) ^c -Zn(1)-Cu(1) ^c	39.99(4)	O(1) ^c -Cu(2)-Cu(1) ^g	140.01(4)
O(1) ^e -Zn(1)-Cu(1) ^c	140.01(4)	O(1) ^e -Cu(2)-Cu(1) ^g	39.99(4)
O(1) ^d -Zn(1)-Cu(1) ^c	39.99(4)	O(1) ^e -Cu(2)-Cu(1) ^g	140.01(4)

Table A.3.18. Bond angles [°] for mps3atest, Zn_{0.33}Cu_{3.67}(OH)₆Cl₂ (continued).

Cu(1)-Zn(1)-Cu(1) ^c	67.884(9)	Cu(1)-Cu(2)-Cu(1) ^g	112.117(9)
Cu(1) ^d -Zn(1)-Cu(1) ^c	67.884(9)	Cu(1) ^d -Cu(2)-Cu(1) ^g	112.117(9)
O(1) ^a -Zn(1)-Cu(1) ^f	39.99(4)	Cu(1) ^e -Cu(2)-Cu(1) ^g	180.0
O(1)-Zn(1)-Cu(1) ^f	140.01(4)	Cu(1) ^f -Cu(2)-Cu(1) ^g	67.883(9)
O(1) ^b -Zn(1)-Cu(1) ^f	39.99(4)	O(1) ^a -Cu(2)-Cu(1) ^h	39.99(4)
O(1) ^c -Zn(1)-Cu(1) ^f	140.01(4)	O(1)-Cu(2)-Cu(1) ^h	140.01(4)
O(1) ^e -Zn(1)-Cu(1) ^f	85.56(9)	O(1) ^b -Cu(2)-Cu(1) ^h	85.56(9)
O(1) ^d -Zn(1)-Cu(1) ^f	94.44(9)	O(1) ^c -Cu(2)-Cu(1) ^h	94.44(9)
Cu(1)-Zn(1)-Cu(1) ^f	180.0	O(1) ^e -Cu(2)-Cu(1) ^h	39.99(4)
Cu(1) ^d -Zn(1)-Cu(1) ^f	112.117(9)	O(1) ^d -Cu(2)-Cu(1) ^h	140.01(4)
Cu(1) ^e -Zn(1)-Cu(1) ^f	112.117(9)	Cu(1)-Cu(2)-Cu(1) ^h	112.116(9)
O(1) ^a -Zn(1)-Cu(1) ^g	85.56(9)	Cu(1) ^d -Cu(2)-Cu(1) ^h	180.0
O(1)-Zn(1)-Cu(1) ^g	94.44(9)	Cu(1) ^e -Cu(2)-Cu(1) ^h	112.116(9)
O(1) ^b -Zn(1)-Cu(1) ^g	39.99(4)	Cu(1) ^f -Cu(2)-Cu(1) ^h	67.883(9)
O(1) ^c -Zn(1)-Cu(1) ^g	140.01(4)	Cu(1) ^g -Cu(2)-Cu(1) ^h	67.883(9)
O(1) ^e -Zn(1)-Cu(1) ^g	39.99(4)	O(1) ⁱ -Cu(1)-O(1) ^c	98.0(2)
O(1) ^d -Zn(1)-Cu(1) ^g	140.01(4)	O(1) ⁱ -Cu(1)-O(1)	180.0
Cu(1)-Zn(1)-Cu(1) ^g	112.117(9)	O(1) ^c -Cu(1)-O(1)	82.0(2)
Cu(1) ^d -Zn(1)-Cu(1) ^g	112.117(9)	O(1) ⁱ -Cu(1)-O(1) ^j	82.0(2)
Cu(1) ^e -Zn(1)-Cu(1) ^g	180.0	O(1) ^c -Cu(1)-O(1) ^j	180.0
Cu(1) ^f -Zn(1)-Cu(1) ^g	67.883(9)	O(1)-Cu(1)-O(1) ^j	98.0(2)
O(1) ^a -Zn(1)-Cu(1) ^h	39.99(4)	O(1) ⁱ -Cu(1)-Cu(2)	136.89(10)
O(1)-Zn(1)-Cu(1) ^h	140.01(4)	O(1) ^c -Cu(1)-Cu(2)	43.11(10)
O(1) ^b -Zn(1)-Cu(1) ^h	85.56(9)	O(1)-Cu(1)-Cu(2)	43.11(10)
O(1) ^c -Zn(1)-Cu(1) ^h	94.44(9)	O(1) ^j -Cu(1)-Cu(2)	136.89(10)
O(1) ^e -Zn(1)-Cu(1) ^h	39.99(4)	O(1) ⁱ -Cu(1)-Zn(1)	136.89(10)
O(1) ^d -Zn(1)-Cu(1) ^h	140.01(4)	O(1) ^c -Cu(1)-Zn(1)	43.11(10)
Cu(1)-Zn(1)-Cu(1) ^h	112.116(9)	O(1)-Cu(1)-Zn(1)	43.11(10)
Cu(1) ^d -Zn(1)-Cu(1) ^h	180.0	O(1) ^j -Cu(1)-Zn(1)	136.89(10)
Cu(1) ^e -Zn(1)-Cu(1) ^h	112.116(9)	Cu(2)-Cu(1)-Zn(1)	0.0
Cu(1) ^f -Zn(1)-Cu(1) ^h	67.883(9)	O(1) ⁱ -Cu(1)-Zn(1) ^k	43.11(10)
Cu(1) ^g -Zn(1)-Cu(1) ^h	67.883(9)	O(1) ^c -Cu(1)-Zn(1) ^k	136.89(10)
O(1) ^a -Cu(2)-O(1)	180.00(14)	O(1)-Cu(1)-Zn(1) ^k	136.89(10)
O(1) ^a -Cu(2)-O(1) ^b	76.17(13)	O(1) ^j -Cu(1)-Zn(1) ^k	43.11(10)

Appendix A

Table A.3.18. Bond angles [°] for mps3atest, Zn_{0.33}Cu_{3.67}(OH)₆Cl₂ (continued).

O(1)-Cu(2)-O(1) ^b	103.83(13)	Cu(2)-Cu(1)-Zn(1) ^k	180.0
O(1) ^a -Cu(2)-O(1) ^c	103.83(13)	Zn(1)-Cu(1)-Zn(1) ^k	180.0
O(1)-Cu(2)-O(1) ^c	76.17(13)	O(1) ⁱ -Cu(1)-Cu(2) ^k	43.11(10)
O(1) ^b -Cu(2)-O(1) ^c	180.0(2)	O(1) ^c -Cu(1)-Cu(2) ^k	136.89(10)
O(1) ^a -Cu(2)-O(1) ^e	76.17(13)	O(1)-Cu(1)-Cu(2) ^k	136.89(10)
O(1)-Cu(2)-O(1) ^e	103.83(13)	O(1) ^j -Cu(1)-Cu(2) ^k	43.11(10)
O(1) ^b -Cu(2)-O(1) ^e	76.17(13)	Cu(2)-Cu(1)-Cu(2) ^k	180.0
O(1) ^c -Cu(2)-O(1) ^e	103.83(13)	Zn(1)-Cu(1)-Cu(2) ^k	180.0
O(1) ^a -Cu(2)-O(1) ^d	103.83(13)	Zn(1) ^k -Cu(1)-Cu(2) ^k	0.0
O(1)-Cu(2)-O(1) ^d	76.17(13)	Cu(1) ^d -O(1)-Cu(1)	119.20(15)
O(1) ^b -Cu(2)-O(1) ^d	103.83(13)	Cu(1) ^d -O(1)-Zn(1)	96.90(11)
O(1) ^c -Cu(2)-O(1) ^d	76.17(13)	Cu(1)-O(1)-Zn(1)	96.90(11)
O(1) ^e -Cu(2)-O(1) ^d	180.0(3)	Cu(1) ^d -O(1)-Cu(2)	96.90(11)
O(1) ^a -Cu(2)-Cu(1)	140.01(4)	Cu(1)-O(1)-Cu(2)	96.90(11)
O(1)-Cu(2)-Cu(1)	39.99(4)	Zn(1)-O(1)-Cu(2)	0.0

Symmetry transformations used to generate equivalent atoms:

$$\begin{array}{llll}
 a & -x, -y, -z & b & x-y, x, -z \\
 f & x-2/3, y-1/3, z-1/3 & g & -x+y+1/3, -x+2/3, z-1/3 \\
 i & -x+2/3, -y+1/3, -z+1/3 & j & x-y+2/3, x+1/3, -z+1/3 \\
 d & -y, x-y, z & e & y, -x+y, -z \\
 h & -y+1/3, x-y-1/3, z-1/3 & k & x+2/3, y+1/3, z+1/3
 \end{array}$$

Appendix A

Table A.3.19. Anisotropic displacement parameters [$\text{\AA}^2 \times 10^3$] for mps3atest, $\text{Zn}_{0.33}\text{Cu}_{3.67}(\text{OH})_6\text{Cl}_2$. The anisotropic displacement factor exponent takes the form: $-2\pi^2[(ha^*)^2U_{11} + \dots + 2hka^*b^*U_{12}]$.

	U_{11}	U_{22}	U_{33}	U_{23}	U_{13}	U_{12}
Zn(1)	7(1)	7(1)	8(1)	0	0	4(1)
Cu(2)	7(1)	7(1)	8(1)	0	0	4(1)
Cu(1)	7(1)	8(1)	10(1)	0(1)	-1(1)	4(1)
O(1)	11(1)	9(2)	19(2)	6(1)	3(1)	5(1)
Cl(1)	11(1)	11(1)	10(1)	0	0	5(1)

Table A.3.20. Hydrogen coordinates [$\times 10^4$] and isotropic displacement parameters [$\text{\AA}^2 \times 10^3$] for mps3atest, $\text{Zn}_{0.33}\text{Cu}_{3.67}(\text{OH})_6\text{Cl}_2$.

	x	y	z	U_{eq}
H(1)	1920(20)	3840(40)	840(40)	40(20)

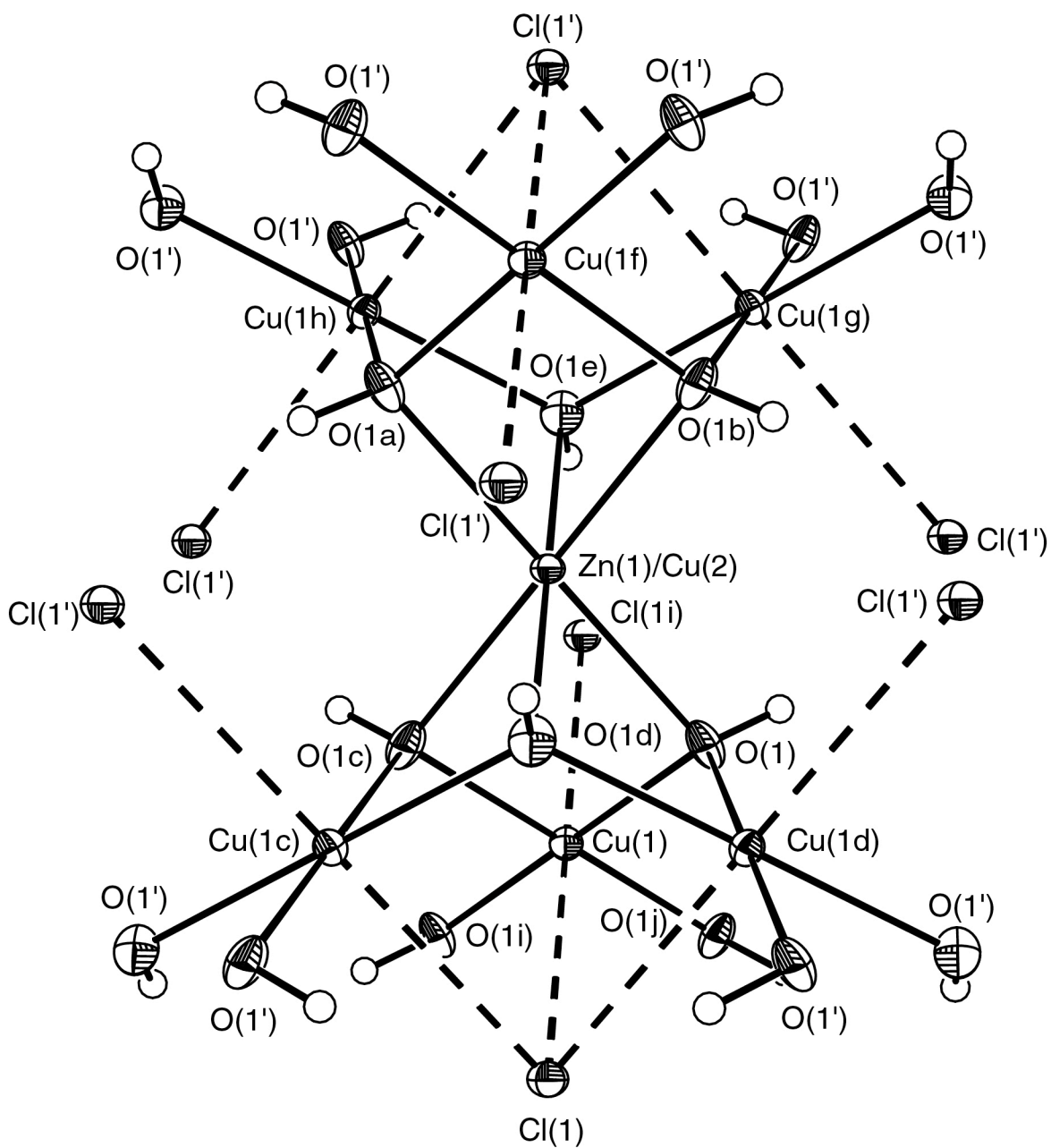


Figure A.3.6. A portion of the crystal structure of $\text{Zn}_{0.42}\text{Cu}_{3.58}(\text{OH})_6\text{Cl}_2$. 50% ellipsoids are shown. Atoms labeled with letters correspond to symmetry equivalent atoms as found in tables A.3.25 and A.3.26. Hydrogen atoms are not labeled.

Table A.3.21. Crystal data and structure refinement for $\text{Zn}_{0.42}\text{Cu}_{3.58}(\text{OH})_6\text{Cl}_2$.

Identification code	c04041a	
Empirical formula	$\text{H}_6\text{Cl}_2\text{Cu}_{3.58}\text{O}_6\text{Zn}_{0.42}$	
Formula weight	427.87	
Temperature	150(2) K	
Wavelength	0.71073 Å	
Crystal system	Rhombohedral (obverse)	
Space group	$R\bar{3}m$	
Unit cell dimensions	$a = 6.8233(9)$ Å	$\alpha = 90^\circ$
	$b = 6.8233(9)$ Å	$\beta = 90^\circ$
	$c = 14.030(3)$ Å	$\gamma = 120^\circ$
Volume, Z	$565.67(17)$ Å ³ ,	3
Density (calculated)	3.768 g/cm ³	
Absorption coefficient	11.964 mm ⁻¹	
F(000)	613	
Crystal size	0.07 × 0.06 × 0.01 mm	
θ range for data collection	3.74 to 24.72°	
Limiting indices	$-8 \leq h \leq 8$ $-8 \leq k \leq 7$ $-15 \leq l \leq 16$	
Reflections collected	1087	
Independent reflections	138 ($R_{\text{int}} = 0.0350$)	
Completeness to $\theta = 24.72^\circ$	100.0 %	
Refinement method	Full-matrix least-squares on F^2	
Data / restraints / parameters	138 / 1 / 20	
Goodness-of-fit on F^2	1.319	
Final R indices [$I > 2\sigma(I)$]	$R_1 = 0.0218$	$wR_2 = 0.0476$
R indices (all data)	$R_1 = 0.0218$	$wR_2 = 0.0476$
Largest diff. peak and hole	0.513 eÅ ⁻³	-0.832 eÅ ⁻³

Appendix A

Table A.3.22. Atomic coordinates [$\times 10^4$] and equivalent isotropic displacement parameters [$\text{\AA}^2 \times 10^3$] for c04041a, $\text{Zn}_{0.42}\text{Cu}_{3.58}(\text{OH})_6\text{Cl}_2$. U_{eq} is defined as one third of the trace of the orthogonalized U_{ij} tensor.

	<i>x</i>	<i>y</i>	<i>z</i>	U_{eq}
Zn(1)	0	0	0	8(1)
Cu(2)	0	0	0	8(1)
Cu(1)	3333	1667	1667	9(1)
O(1)	1269(2)	2538(5)	1053(2)	14(1)
Cl(1)	0	0	3054(1)	11(1)

Table A.3.23. Bond lengths [\AA] for c04041a, $\text{Zn}_{0.42}\text{Cu}_{3.58}(\text{OH})_6\text{Cl}_2$.

Zn(1)-O(1) ^a	2.105(3)	Cu(2)-Cu(1)	3.0573(5)
Zn(1)-O(1)	2.105(3)	Cu(2)-Cu(1) ^d	3.0573(5)
Zn(1)-O(1) ^b	2.105(3)	Cu(2)-Cu(1) ^c	3.0573(5)
Zn(1)-O(1) ^c	2.105(3)	Cu(2)-Cu(1) ^f	3.0574(5)
Zn(1)-O(1) ^d	2.105(3)	Cu(2)-Cu(1) ^g	3.0573(5)
Zn(1)-O(1) ^e	2.105(3)	Cu(2)-Cu(1) ^h	3.0574(5)
Zn(1)-Cu(1)	3.0573(5)	Cu(1)-O(1)	1.9793(13)
Zn(1)-Cu(1) ^d	3.0573(5)	Cu(1)-O(1) ⁱ	1.9792(13)
Zn(1)-Cu(1) ^c	3.0573(5)	Cu(1)-O(1) ^c	1.9793(13)
Zn(1)-Cu(1) ^f	3.0574(5)	Cu(1)-O(1) ^j	1.9793(13)
Zn(1)-Cu(1) ^g	3.0573(5)	Cu(1)-Cl(1) ⁱ	2.7692(10)
Zn(1)-Cu(1) ^h	3.0574(5)	Cu(1)-Cl(1)	2.7692(10)
Cu(2)-O(1) ^a	2.105(3)	Cu(1)-Zn(1) ^k	3.0573(5)
Cu(2)-O(1)	2.105(3)	Cu(1)-Cu(2) ^k	3.0573(5)
Cu(2)-O(1) ^b	2.105(3)	O(1)-Cu(1) ^d	1.9793(13)
Cu(2)-O(1) ^c	2.105(3)	Cl(1)-Cu(1) ^c	2.7692(10)
Cu(2)-O(1) ^d	2.105(3)	Cl(1)-Cu(1) ^d	2.7692(10)
Cu(2)-O(1) ^e	2.105(3)		

Symmetry transformations used to generate equivalent atoms:

$$\begin{array}{lllll}
 {}^a -x, -y, -z & {}^b x-x, x, -z & {}^c -x+y, -x, z & {}^d -y, x-y, z & {}^e y, -x+y, -z \\
 {}^f x-2/3, y-1/3, z-1/3 & {}^g -x+y+1/3, -x+2/3, z-1/3 & {}^h -y+1/3, x-y-1/3, z-1/3 & & \\
 {}^i -x+2/3, -y+1/3, -z+1/3 & {}^j x-y+2/3, x+1/3, -z+1/3 & {}^k x+2/3, y+1/3, z+1/3 & &
 \end{array}$$

Table A.3.24. Bond angles [°] for c04041a, Zn_{0.42}Cu_{3.58}(OH)₆Cl₂.

O(1) ^a -Zn(1)-O(1)	180.00(11)	Cu(1)-Cu(2)-Cu(1) ^d	67.828(12)
O(1) ^a -Zn(1)-O(1) ^b	76.21(11)	O(1) ^a -Cu(2)-Cu(1) ^c	94.44(7)
O(1)-Zn(1)-O(1) ^b	103.79(11)	O(1)-Cu(2)-Cu(1) ^c	85.56(7)
O(1) ^a -Zn(1)-O(1) ^c	103.79(11)	O(1) ^b -Cu(2)-Cu(1) ^c	140.01(3)
O(1)-Zn(1)-O(1) ^c	76.21(11)	O(1) ^c -Cu(2)-Cu(1) ^c	39.99(3)
O(1) ^b -Zn(1)-O(1) ^c	180.00(12)	O(1) ^d -Cu(2)-Cu(1) ^c	39.99(3)
O(1) ^a -Zn(1)-O(1) ^d	103.79(11)	O(1) ^e -Cu(2)-Cu(1) ^c	140.01(3)
O(1)-Zn(1)-O(1) ^d	76.21(11)	Cu(1)-Cu(2)-Cu(1) ^c	67.828(12)
O(1) ^b -Zn(1)-O(1) ^d	103.79(11)	Cu(1) ^d -Cu(2)-Cu(1) ^c	67.828(12)
O(1) ^c -Zn(1)-O(1) ^d	76.21(11)	O(1) ^a -Cu(2)-Cu(1) ^f	39.99(3)
O(1) ^a -Zn(1)-O(1) ^e	76.21(11)	O(1)-Cu(2)-Cu(1) ^f	140.01(3)
O(1)-Zn(1)-O(1) ^e	103.79(11)	O(1) ^b -Cu(2)-Cu(1) ^f	39.99(3)
O(1) ^b -Zn(1)-O(1) ^e	76.21(11)	O(1) ^c -Cu(2)-Cu(1) ^f	140.01(3)
O(1) ^c -Zn(1)-O(1) ^e	103.79(11)	O(1) ^d -Cu(2)-Cu(1) ^f	94.44(7)
O(1) ^d -Zn(1)-O(1) ^e	180.00(13)	O(1) ^e -Cu(2)-Cu(1) ^f	85.56(7)
O(1) ^a -Zn(1)-Cu(1)	140.01(3)	Cu(1)-Cu(2)-Cu(1) ^f	180.0
O(1)-Zn(1)-Cu(1)	39.99(3)	Cu(1) ^d -Cu(2)-Cu(1) ^f	112.173(12)
O(1) ^b -Zn(1)-Cu(1)	140.01(3)	Cu(1) ^c -Cu(2)-Cu(1) ^f	112.173(12)
O(1) ^c -Zn(1)-Cu(1)	39.99(3)	O(1) ^a -Cu(2)-Cu(1) ^g	85.56(7)
O(1) ^d -Zn(1)-Cu(1)	85.56(7)	O(1)-Cu(2)-Cu(1) ^g	94.44(7)
O(1) ^e -Zn(1)-Cu(1)	94.44(7)	O(1) ^b -Cu(2)-Cu(1) ^g	39.99(3)
O(1) ^a -Zn(1)-Cu(1) ^d	140.01(3)	O(1) ^c -Cu(2)-Cu(1) ^g	140.01(3)
O(1)-Zn(1)-Cu(1) ^d	39.99(3)	O(1) ^d -Cu(2)-Cu(1) ^g	140.01(3)
O(1) ^b -Zn(1)-Cu(1) ^d	94.44(7)	O(1) ^e -Cu(2)-Cu(1) ^g	39.99(3)
O(1) ^c -Zn(1)-Cu(1) ^d	85.56(7)	Cu(1)-Cu(2)-Cu(1) ^g	112.173(13)
O(1) ^d -Zn(1)-Cu(1) ^d	39.99(3)	Cu(1) ^d -Cu(2)-Cu(1) ^g	112.173(13)
O(1) ^e -Zn(1)-Cu(1) ^d	140.01(3)	Cu(1) ^c -Cu(2)-Cu(1) ^g	180.0
Cu(1)-Zn(1)-Cu(1) ^d	67.828(12)	Cu(1) ^f -Cu(2)-Cu(1) ^g	67.827(13)
O(1) ^a -Zn(1)-Cu(1) ^c	94.44(7)	O(1) ^a -Cu(2)-Cu(1) ^h	39.99(3)
O(1)-Zn(1)-Cu(1) ^c	85.56(7)	O(1)-Cu(2)-Cu(1) ^h	140.01(3)
O(1) ^b -Zn(1)-Cu(1) ^c	140.01(3)	O(1) ^b -Cu(2)-Cu(1) ^h	85.56(7)
O(1) ^c -Zn(1)-Cu(1) ^c	39.99(3)	O(1) ^c -Cu(2)-Cu(1) ^h	94.44(7)
O(1) ^d -Zn(1)-Cu(1) ^c	39.99(3)	O(1) ^d -Cu(2)-Cu(1) ^h	140.01(3)
O(1) ^e -Zn(1)-Cu(1) ^c	140.01(3)	O(1) ^e -Cu(2)-Cu(1) ^h	39.99(3)

Table A.3.24. Bond angles [°] for c04041a, Zn_{0.42}Cu_{3.58}(OH)₆Cl₂ (continued).

Cu(1)-Zn(1)-Cu(1) ^c	67.828(12)	Cu(1)-Cu(2)-Cu(1) ^h	112.172(12)
Cu(1) ^d -Zn(1)-Cu(1) ^c	67.828(12)	Cu(1) ^d -Cu(2)-Cu(1) ^h	180.0
O(1) ^a -Zn(1)-Cu(1) ^f	39.99(3)	Cu(1) ^c -Cu(2)-Cu(1) ^h	112.172(12)
O(1)-Zn(1)-Cu(1) ^f	140.01(3)	Cu(1) ^f -Cu(2)-Cu(1) ^h	67.827(12)
O(1) ^b -Zn(1)-Cu(1) ^f	39.99(3)	Cu(1) ^g -Cu(2)-Cu(1) ^h	67.827(12)
O(1) ^c -Zn(1)-Cu(1) ^f	140.01(3)	O(1)-Cu(1)-O(1) ⁱ	180.0
O(1) ^d -Zn(1)-Cu(1) ^f	94.44(7)	O(1)-Cu(1)-O(1) ^c	82.02(16)
O(1) ^e -Zn(1)-Cu(1) ^f	85.56(7)	O(1) ⁱ -Cu(1)-O(1) ^c	97.98(16)
Cu(1)-Zn(1)-Cu(1) ^f	180.0	O(1)-Cu(1)-O(1) ^j	97.98(16)
Cu(1) ^d -Zn(1)-Cu(1) ^f	112.173(12)	O(1) ⁱ -Cu(1)-O(1) ^j	82.02(16)
Cu(1) ^c -Zn(1)-Cu(1) ^f	112.173(12)	O(1) ^c -Cu(1)-O(1) ^j	180.0
O(1) ^a -Zn(1)-Cu(1) ^g	85.56(7)	O(1)-Cu(1)-Cl(1) ⁱ	97.61(7)
O(1)-Zn(1)-Cu(1) ^g	94.44(7)	O(1) ⁱ -Cu(1)-Cl(1) ⁱ	82.39(7)
O(1) ^b -Zn(1)-Cu(1) ^g	39.99(3)	O(1) ^c -Cu(1)-Cl(1) ⁱ	97.61(7)
O(1) ^c -Zn(1)-Cu(1) ^g	140.01(3)	O(1) ^j -Cu(1)-Cl(1) ⁱ	82.39(7)
O(1) ^d -Zn(1)-Cu(1) ^g	140.01(3)	O(1)-Cu(1)-Cl(1)	82.39(7)
O(1) ^e -Zn(1)-Cu(1) ^g	39.99(3)	O(1) ⁱ -Cu(1)-Cl(1)	97.61(7)
Cu(1)-Zn(1)-Cu(1) ^g	112.173(13)	O(1) ^c -Cu(1)-Cl(1)	82.39(7)
Cu(1) ^d -Zn(1)-Cu(1) ^g	112.173(13)	O(1) ^j -Cu(1)-Cl(1)	97.61(7)
Cu(1) ^c -Zn(1)-Cu(1) ^g	180.0	Cl(1) ⁱ -Cu(1)-Cl(1)	180.0
Cu(1) ^f -Zn(1)-Cu(1) ^g	67.827(13)	O(1)-Cu(1)-Zn(1)	43.11(8)
O(1) ^a -Zn(1)-Cu(1) ^h	39.99(3)	O(1) ⁱ -Cu(1)-Zn(1)	136.89(8)
O(1)-Zn(1)-Cu(1) ^h	140.01(3)	O(1) ^c -Cu(1)-Zn(1)	43.11(8)
O(1) ^b -Zn(1)-Cu(1) ^h	85.56(7)	O(1) ^j -Cu(1)-Zn(1)	136.89(8)
O(1) ^c -Zn(1)-Cu(1) ^h	94.44(7)	Cl(1) ⁱ -Cu(1)-Zn(1)	85.45(2)
O(1) ^d -Zn(1)-Cu(1) ^h	140.01(3)	Cl(1)-Cu(1)-Zn(1)	94.55(2)
O(1) ^e -Zn(1)-Cu(1) ^h	39.99(3)	O(1)-Cu(1)-Cu(2)	43.11(8)
Cu(1)-Zn(1)-Cu(1) ^h	112.172(12)	O(1) ⁱ -Cu(1)-Cu(2)	136.89(8)
Cu(1) ^d -Zn(1)-Cu(1) ^h	180.0	O(1) ^c -Cu(1)-Cu(2)	43.11(8)
Cu(1) ^c -Zn(1)-Cu(1) ^h	112.172(12)	O(1) ^j -Cu(1)-Cu(2)	136.89(8)
Cu(1) ^f -Zn(1)-Cu(1) ^h	67.827(12)	Cl(1) ⁱ -Cu(1)-Cu(2)	85.45(2)
Cu(1) ^g -Zn(1)-Cu(1) ^h	67.827(12)	Cl(1)-Cu(1)-Cu(2)	94.55(2)
O(1) ^a -Cu(2)-O(1)	180.00(11)	Zn(1)-Cu(1)-Cu(2)	0.0
O(1) ^a -Cu(2)-O(1) ^b	76.21(11)	O(1)-Cu(1)-Zn(1) ^k	136.89(8)

Appendix A

Table A.3.24. Bond angles [°] for c04041a, Zn_{0.42}Cu_{3.58}(OH)₆Cl₂ (continued).

O(1)-Cu(2)-O(1) ^b	103.79(11)	O(1) ⁱ -Cu(1)-Zn(1) ^k	43.11(8)
O(1) ^a -Cu(2)-O(1) ^c	103.79(11)	O(1) ^c -Cu(1)-Zn(1) ^k	136.89(8)
O(1)-Cu(2)-O(1) ^c	76.21(11)	O(1) ^j -Cu(1)-Zn(1) ^k	43.11(8)
O(1) ^b -Cu(2)-O(1) ^c	180.00(12)	Cl(1) ⁱ -Cu(1)-Zn(1) ^k	94.55(2)
O(1) ^a -Cu(2)-O(1) ^d	103.79(11)	Cl(1)-Cu(1)-Zn(1) ^k	85.45(2)
O(1)-Cu(2)-O(1) ^d	76.21(11)	Zn(1)-Cu(1)-Zn(1) ^k	180.0
O(1) ^b -Cu(2)-O(1) ^d	103.79(11)	Cu(2)-Cu(1)-Zn(1) ^k	180.0
O(1) ^c -Cu(2)-O(1) ^d	76.21(11)	O(1)-Cu(1)-Cu(2) ^k	136.89(8)
O(1) ^a -Cu(2)-O(1) ^e	76.21(11)	O(1) ⁱ -Cu(1)-Cu(2) ^k	43.11(8)
O(1)-Cu(2)-O(1) ^e	103.79(11)	O(1) ^c -Cu(1)-Cu(2) ^k	136.89(8)
O(1) ^b -Cu(2)-O(1) ^e	76.21(11)	O(1) ^j -Cu(1)-Cu(2) ^k	43.11(8)
O(1) ^c -Cu(2)-O(1) ^e	103.79(11)	Cl(1) ⁱ -Cu(1)-Cu(2) ^k	94.55(2)
O(1) ^d -Cu(2)-O(1) ^e	180.00(13)	Cl(1)-Cu(1)-Cu(2) ^k	85.45(2)
O(1) ^a -Cu(2)-Cu(1)	140.01(3)	Zn(1)-Cu(1)-Cu(2) ^k	180.0
O(1)-Cu(2)-Cu(1)	39.99(3)	Cu(2)-Cu(1)-Cu(2) ^k	180.0
O(1) ^b -Cu(2)-Cu(1)	140.01(3)	Zn(1) ^k -Cu(1)-Cu(2) ^k	0.0
O(1) ^c -Cu(2)-Cu(1)	39.99(3)	Cu(1)-O(1)-Cu(1) ^d	119.05(13)
O(1) ^d -Cu(2)-Cu(1)	85.56(7)	Cu(1)-O(1)-Cu(2)	96.90(9)
O(1) ^e -Cu(2)-Cu(1)	94.44(7)	Cu(1) ^d -O(1)-Cu(2)	96.90(9)
O(1) ^a -Cu(2)-Cu(1) ^d	140.01(3)	Cu(1)-O(1)-Zn(1)	96.90(9)
O(1)-Cu(2)-Cu(1) ^d	39.99(3)	Cu(1) ^d -O(1)-Zn(1)	96.90(9)
O(1) ^b -Cu(2)-Cu(1) ^d	94.44(7)	Cu(2)-O(1)-Zn(1)	0.0
O(1) ^c -Cu(2)-Cu(1) ^d	85.56(7)	Cu(1) ^c -Cl(1)-Cu(1) ^d	76.05(3)
O(1) ^d -Cu(2)-Cu(1) ^d	39.99(3)	Cu(1) ^c -Cl(1)-Cu(1)	76.05(3)
O(1) ^e -Cu(2)-Cu(1) ^d	140.01(3)	Cu(1) ^d -Cl(1)-Cu(1)	76.05(3)

Symmetry transformations used to generate equivalent atoms:

$$\begin{array}{lllll}
 a & -x, -y, -z & b & x - y, x, -z & c & -x + y, -x, z & d & -y, x - y, z & e & y, -x + y, -z \\
 f & x - 2/3, y - 1/3, z - 1/3 & g & -x + y + 1/3, -x + 2/3, z - 1/3 & h & -y + 1/3, x - y - 1/3, z - 1/3 \\
 i & -x + 2/3, -y + 1/3, -z + 1/3 & j & x - y + 2/3, x + 1/3, -z + 1/3 & k & x + 2/3, y + 1/3, z + 1/3
 \end{array}$$

Appendix A

Table A.3.25. Anisotropic displacement parameters [$\text{\AA}^2 \times 10^3$] for c04041a, $\text{Zn}_{0.42}\text{Cu}_{3.58}(\text{OH})_6\text{Cl}_2$. The anisotropic displacement factor exponent takes the form: $-2\pi^2 [(ha^*)^2 U_{11} + \dots + 2hka^*b^* U_{12}]$.

	U_{11}	U_{22}	U_{33}	U_{23}	U_{13}	U_{12}
Zn(1)	9(1)	9(1)	6(1)	0	0	4(1)
Cu(2)	9(1)	9(1)	6(1)	0	0	4(1)
Cu(1)	8(1)	9(1)	9(1)	0(1)	-1(1)	4(1)
O(1)	14(1)	11(1)	18(1)	7(1)	3(1)	5(1)
Cl(1)	13(1)	13(1)	9(1)	0	0	6(1)

Table A.3.26. Hydrogen coordinates [$\times 10^4$] and isotropic displacement parameters [$\text{\AA}^2 \times 10^3$] for c04041a, $\text{Zn}_{0.42}\text{Cu}_{3.58}(\text{OH})_6\text{Cl}_2$.

	x	y	z	U_{eq}
H(1)	1890(20)	3770(40)	830(30)	17(12)

Table A.3.27. Crystal data and structure refinement for $\text{Zn}_{0.76}\text{Cu}_{3.24}(\text{OH})_6\text{Cl}_2$.

Identification code	08038_cu_mix	
Empirical formula	$\text{H}_6\text{Cl}_2\text{Cu}_{3.24}\text{O}_6\text{Zn}_{0.76}$	
Formula weight	428.50	
Temperature	100(2) K	
Wavelength	0.71073 Å	
Crystal system	Rhombohedral	
Space group	$R\bar{3}m$	
Unit cell dimensions	$a = 6.8447(6)$ Å	$\alpha = 90^\circ$
	$b = 6.8447(6)$ Å	$\beta = 90^\circ$
	$c = 14.116(3)$ Å	$\gamma = 120^\circ$
Volume, Z	$572.75(13)$ Å ³	3
Density (calculated)	3.727 g/cm ³	
Absorption coefficient	11.938 mm ⁻¹	
F(000)	614	
Crystal size	0.08 × 0.04 × 0.03 mm	
θ range for data collection	3.73 to 30.26°	
Limiting indices	$-9 \leq h \leq 9$	
	$-9 \leq k \leq 9$	
	$-19 \leq l \leq 19$	
Reflections collected	5225	
Independent reflections	240 ($R_{\text{int}} = 0.0315$)	
Completeness to $\theta = 30.26^\circ$	100.0 %	
Absorption correction	Semi-empirical from equivalents	
Max. and min. transmission	0.7159	0.4485
Refinement method	Full-matrix least-squares on F^2	
Data / restraints / parameters	240 / 2 / 20	
Goodness-of-fit on F^2	1.207	
Final R indices [$I > 2\sigma(I)$]	$R_1 = 0.0112$	$wR_2 = 0.0282$
R indices (all data)	$R_1 = 0.0112$	$wR_2 = 0.0282$
Largest diff. peak and hole	0.378 eÅ^{-3}	-0.285 eÅ^{-3}

Appendix A

Table A.3.28. Atomic coordinates [$\times 10^4$] and equivalent isotropic displacement parameters [$\text{\AA}^2 \times 10^3$] for 08038_cu_mix, $\text{Zn}_{0.76}\text{Cu}_{3.24}(\text{OH})_6\text{Cl}_2$. U_{eq} is defined as one third of the trace of the orthogonalized U_{ij} tensor.

	x	y	z	U_{eq}
Cu(1)	5000	5000	0	5(1)
Zn(2)	3333	6667	1667	5(1)
Cu(2)	3333	6667	1667	5(1)
Cl(1)	6667	3333	1372(1)	9(1)
O(1)	2058(1)	4115(2)	618(1)	8(1)

Table A.3.29. Bond lengths [\AA] for 08038_cu_mix, $\text{Zn}_{0.76}\text{Cu}_{3.24}(\text{OH})_6\text{Cl}_2$.

Cu(1)-O(1)	1.9913(6)	Zn(2)-Cu(1) ^g	3.0724(3)
Cu(1)-O(1) ^a	1.9913(6)	Zn(2)-Cu(1) ^b	3.0724(4)
Cu(1)-O(1) ^b	1.9913(6)	Zn(2)-Cu(1) ⁱ	3.0724(3)
Cu(1)-O(1) ^c	1.9913(6)	Zn(2)-Cu(1) ^j	3.0724(4)
Cu(1)-Cl(1) ^c	2.7664(6)	Zn(2)-Cu(1) ^k	3.0724(4)
Cu(1)-Cl(1)	2.7664(6)	Cu(2)-O(1) ^e	2.1160(13)
Cu(1)-Zn(2)	3.0724(3)	Cu(2)-O(1) ^f	2.1160(13)
Cu(1)-Zn(2) ^d	3.0725(4)	Cu(2)-O(1) ^g	2.1160(13)
Zn(2)-O(1) ^e	2.1160(13)	Cu(2)-O(1) ^h	2.1160(13)
Zn(2)-O(1) ^f	2.1160(13)	Cu(2)-O(1) ^b	2.1160(13)
Zn(2)-O(1) ^g	2.1160(13)	Cu(2)-O(1)	2.1160(13)
Zn(2)-O(1) ^h	2.1160(13)	Cl(1)-Cu(1) ^l	2.7664(6)
Zn(2)-O(1) ^b	2.1160(13)	Cl(1)-Cu(1) ^m	2.7664(6)
Zn(2)-O(1)	2.1160(13)	O(1)-Cu(1) ^g	1.9913(6)

Symmetry transformations used to generate equivalent atoms:

$$\begin{array}{llll}
 {}^a y, -x + y, -z & {}^b -y + 1, x - y + 1, z & {}^c -x + 1, -y + 1, -z & {}^d x + 1/3, y - 1/3, z - 1/3 \\
 {}^e -x + 2/3, -y + 4/3, -z + 1/3 & & {}^f y - 1/3, -x + y + 1/3, -z + 1/3 & \\
 {}^g -x + y, -x + 1, z & {}^h x - y + 2/3, x + 1/3, -z + 1/3 & & {}^i -x + y + 2/3, -x + 4/3, z + 1/3 \\
 {}^j -y + 2/3, x - y + 1/3, z + 1/3 & & {}^k x - 1/3, y + 1/3, z + 1/3 & {}^l -y + 1, x - y, z \\
 {}^m -x + y + 1, -x + 1, z & & &
 \end{array}$$

Appendix A

Table A.3.30. Bond angles [°] for 08038_cu_mix, Zn_{0.76}Cu_{3.24}(OH)₆Cl₂.

O(1)-Cu(1)-O(1) ^a	97.74(8)	O(1) ^h -Zn(2)-Cu(1)	94.35(4)
O(1)-Cu(1)-O(2) ^a	82.26(8)	O(1) ^b -Zn(2)-Cu(1)	40.059(17)
O(1) ^a -Cu(1)-O(1) ^b	180.00(7)	O(1)-Zn(2)-Cu(1)	40.058(17)
O(1)-Cu(1)-O(1) ^c	180.0	Cu(1) ^f -Zn(2)-Cu(1)	67.691(9)
O(1) ^a -Cu(1)-O(1) ^c	82.26(8)	Cu(1) ^b -Zn(2)-Cu(1)	67.691(9)
O(1) ^b -Cu(1)-O(1) ^c	97.74(8)	O(1) ^e -Zn(2)-Cu(1) ⁱ	40.058(17)
O(1)-Cu(1)-Cl(1) ^c	82.49(3)	O(1) ^f -Zn(2)-Cu(1) ⁱ	85.65(4)
O(1) ^a -Cu(1)-Cl(1) ^c	97.51(3)	O(1) ^g -Zn(2)-Cu(1) ⁱ	139.941(17)
O(1) ^b -Cu(1)-Cl(1) ^c	82.49(3)	O(1) ^h -Zn(2)-Cu(1) ⁱ	40.058(18)
O(1) ^c -Cu(1)-Cl(1) ^c	97.51(3)	O(1) ^b -Zn(2)-Cu(1) ⁱ	94.35(4)
O(1)-Cu(1)-Cl(1)	97.51(3)	O(1)-Zn(2)-Cu(1) ⁱ	139.943(17)
O(1) ^a -Cu(1)-Cl(1)	82.49(3)	Cu(1) ^g -Zn(2)-Cu(1) ⁱ	180.0
O(1) ^b -Cu(1)-Cl(1)	97.51(3)	Cu(1) ^b -Zn(2)-Cu(1) ⁱ	112.309(9)
O(1) ^c -Cu(1)-Cl(1)	82.49(3)	Cu(1)-Zn(2)-Cu(1) ⁱ	112.310(9)
Cl(1) ^c -Cu(1)-Cl(1)	180.0	O(1) ^e -Zn(2)-Cu(1) ^j	85.65(4)
O(1)-Cu(1)-Zn(2)	43.15(4)	O(1) ^f -Zn(2)-Cu(1) ^j	40.058(17)
O(1) ^a -Cu(1)-Zn(2)	136.85(4)	O(1) ^g -Zn(2)-Cu(1) ^j	139.941(17)
O(1) ^b -Cu(1)-Zn(2)	43.15(4)	O(1) ^h -Zn(2)-Cu(1) ^j	40.058(18)
O(1) ^c -Cu(1)-Zn(2)	136.85(4)	O(1) ^b -Zn(2)-Cu(1) ^j	139.942(17)
Cl(1) ^c -Cu(1)-Zn(2)	94.395(16)	O(1)-Zn(2)-Cu(1) ^j	94.35(4)
Cl(1)-Cu(1)-Zn(2)	85.606(15)	Cu(1) ^g -Zn(2)-Cu(1) ^j	112.309(9)
O(1)-Cu(1)-Zn(2) ^d	136.85(4)	Cu(1) ^b -Zn(2)-Cu(1) ^j	180.0
O(1) ^a -Cu(1)-Zn(2) ^d	43.15(4)	Cu(1)-Zn(2)-Cu(1) ^j	112.310(9)
O(1) ^b -Cu(1)-Zn(2) ^d	136.85(4)	Cu(1) ⁱ -Zn(2)-Cu(1) ^j	67.690(9)
O(1) ^c -Cu(1)-Zn(2) ^d	43.15(4)	O(1) ^e -Zn(2)-Cu(1) ^k	40.058(17)
Cl(1) ^c -Cu(1)-Zn(2) ^d	85.605(15)	O(1) ^f -Zn(2)-Cu(1) ^k	40.058(17)
Cl(1)-Cu(1)-Zn(2) ^d	94.394(15)	O(1) ^g -Zn(2)-Cu(1) ^k	94.35(4)
Zn(2)-Cu(1)-Zn(2) ^d	180.0	O(1) ^h -Zn(2)-Cu(1) ^k	85.65(4)
O(1) ^e -Zn(2)-O(1) ^f	76.49(5)	O(1) ^b -Zn(2)-Cu(1) ^k	139.941(17)
O(1) ^e -Zn(2)-O(1) ^g	103.51(5)	O(1)-Zn(2)-Cu(1) ^k	139.942(17)
O(1) ^f -Zn(2)-O(1) ^g	103.51(5)	Cu(1) ^g -Zn(2)-Cu(1) ^k	112.309(9)
O(1) ^e -Zn(2)-O(1) ^h	76.49(5)	Cu(1) ^b -Zn(2)-Cu(1) ^k	112.309(9)
O(1) ^f -Zn(2)-O(1) ^h	76.49(5)	Cu(1)-Zn(2)-Cu(1) ^k	180.0
O(1) ^g -Zn(2)-O(1) ^h	180.0	Cu(1) ⁱ -Zn(2)-Cu(1) ^k	67.690(9)

Appendix A

O(1) ^e -Zn(2)-O(1) ^b	103.51(5)	Cu(1) ^j -Zn(2)-Cu(1) ^k	67.690(9)
O(1) ^f -Zn(2)-O(1) ^b	180.0	O(1) ^e -Cu(2)-O(1) ^f	76.49(5)
O(1) ^g -Zn(2)-O(1) ^b	76.49(5)	O(1) ^e -Cu(2)-O(1) ^g	103.51(5)
O(1) ^h -Zn(2)-O(1) ^b	103.51(5)	O(1) ^f -Cu(2)-O(1) ^g	103.51(5)
O(1) ^e -Zn(2)-O(1)	180.0	O(1) ^e -Cu(2)-O(1) ^h	76.49(5)
O(1) ^f -Zn(2)-O(1)	103.51(5)	O(1) ^f -Cu(2)-O(1) ^h	76.49(5)
O(1) ^g -Zn(2)-O(1)	76.49(5)	O(1) ^g -Cu(2)-O(1) ^h	180.0
O(1) ^h -Zn(2)-O(1)	103.51(5)	O(1) ^e -Cu(2)-O(1) ^b	103.51(5)
O(1) ^b -Zn(2)-O(1)	76.49(5)	O(1) ^f -Cu(2)-O(1) ^b	180.0
O(1) ^e -Zn(2)-Cu(1) ^g	139.942(18)	O(1) ^g -Cu(2)-O(1) ^b	76.49(5)
O(1) ^f -Zn(2)-Cu(1) ^g	94.35(4)	O(1) ^h -Cu(2)-O(1) ^b	103.51(5)
O(1) ^g -Zn(2)-Cu(1) ^g	40.059(18)	O(1) ^e -Cu(2)-O(1)	180.0
O(1) ^h -Zn(2)-Cu(1) ^g	139.942(18)	O(1) ^f -Cu(2)-O(1)	103.51(5)
O(1) ^b -Zn(2)-Cu(1) ^g	85.65(4)	O(1) ^g -Cu(2)-O(1)	76.49(5)
O(1)-Zn(2)-Cu(1) ^g	40.058(18)	O(1) ^h -Cu(2)-O(1)	103.51(5)
O(1) ^e -Zn(2)-Cu(1) ^b	94.35(4)	O(1) ^b -Cu(2)-O(1)	76.49(5)
O(1) ^f -Zn(2)-Cu(1) ^b	139.942(18)	Cu(1) ^l -Cl(1)-Cu(1) ^m	76.421(18)
O(1) ^g -Zn(2)-Cu(1) ^b	40.059(17)	Cu(1) ^l -Cl(1)-Cu(1)	76.421(18)
O(1) ^h -Zn(2)-Cu(1) ^b	139.942(18)	Cu(1) ^m -Cl(1)-Cu(1)	76.421(18)
O(1) ^b -Zn(2)-Cu(1) ^b	40.059(17)	Cu(1) ^g -O(1)-Cu(1)	118.49(6)
O(1)-Zn(2)-Cu(1) ^b	85.65(4)	Cu(1) ^g -O(1)-Zn(2)	96.79(4)
Cu(1) ^g -Zn(2)-Cu(1) ^b	67.691(9)	Cu(1)-O(1)-Zn(2)	96.79(4)
O(1) ^e -Zn(2)-Cu(1)	139.942(18)	Cu(1) ^g -O(1)-Cu(2)	96.79(4)
O(1) ^f -Zn(2)-Cu(1)	139.942(17)	Cu(1)-O(1)-Cu(2)	96.79(4)
O(1) ^g -Zn(2)-Cu(1)	85.65(4)	Zn(2)-O(1)-Cu(2)	0.0

Symmetry transformations used to generate equivalent atoms:

$$\begin{array}{llll}
 a & y, -x + y, -z & b & -y + 1, x - y + 1, z & c & -x + 1, -y + 1, -z & d & x + 1/3, y - 1/3, z - 1/3 \\
 e & -x + 2/3, -y + 4/3, -z + 1/3 & f & y - 1/3, -x + y + 1/3, -z + 1/3 & & & & \\
 g & -x + y, -x + 1, z & h & x - y + 2/3, x + 1/3, -z + 1/3 & i & -x + y + 2/3, -x + 4/3, z + 1/3 & & \\
 j & -y + 2/3, x - y + 1/3, z + 1/3 & k & x - 1/3, y + 1/3, z + 1/3 & l & -y + 1, x - y, z & & \\
 m & -x + y + 1, -x + 1, z & & & & & &
 \end{array}$$

Appendix A

Table A.3.31. Anisotropic displacement parameters [$\text{\AA}^2 \times 10^3$] for 08038_cu_mix, $\text{Zn}_{0.76}\text{Cu}_{3.24}(\text{OH})_6\text{Cl}_2$. The anisotropic displacement factor exponent takes the form: $-2\pi^2[(ha^*)^2U_{11} + \dots + 2hka^*b^*U_{12}]$.

	U_{11}	U_{22}	U_{33}	U_{23}	U_{13}	U_{12}
Cu(1)	5(1)	5(1)	6(1)	-1(1)	1(1)	2(1)
Zn(2)	5(1)	5(1)	4(1)	0	0	3(1)
Cu(2)	5(1)	5(1)	4(1)	0	0	3(1)
Cl(1)	10(1)	10(1)	8(1)	0	0	5(1)
O(1)	7(1)	7(1)	11(1)	3(1)	2(1)	3(1)

Table A.3.32. Hydrogen coordinates [$\times 10^4$] and isotropic displacement parameters [$\text{\AA}^2 \times 10^3$] for 08038_cu_mix, $\text{Zn}_{0.76}\text{Cu}_{3.24}(\text{OH})_6\text{Cl}_2$.

	x	y	z	U_{eq}
H(1)	1419(16)	2840(30)	862(16)	10

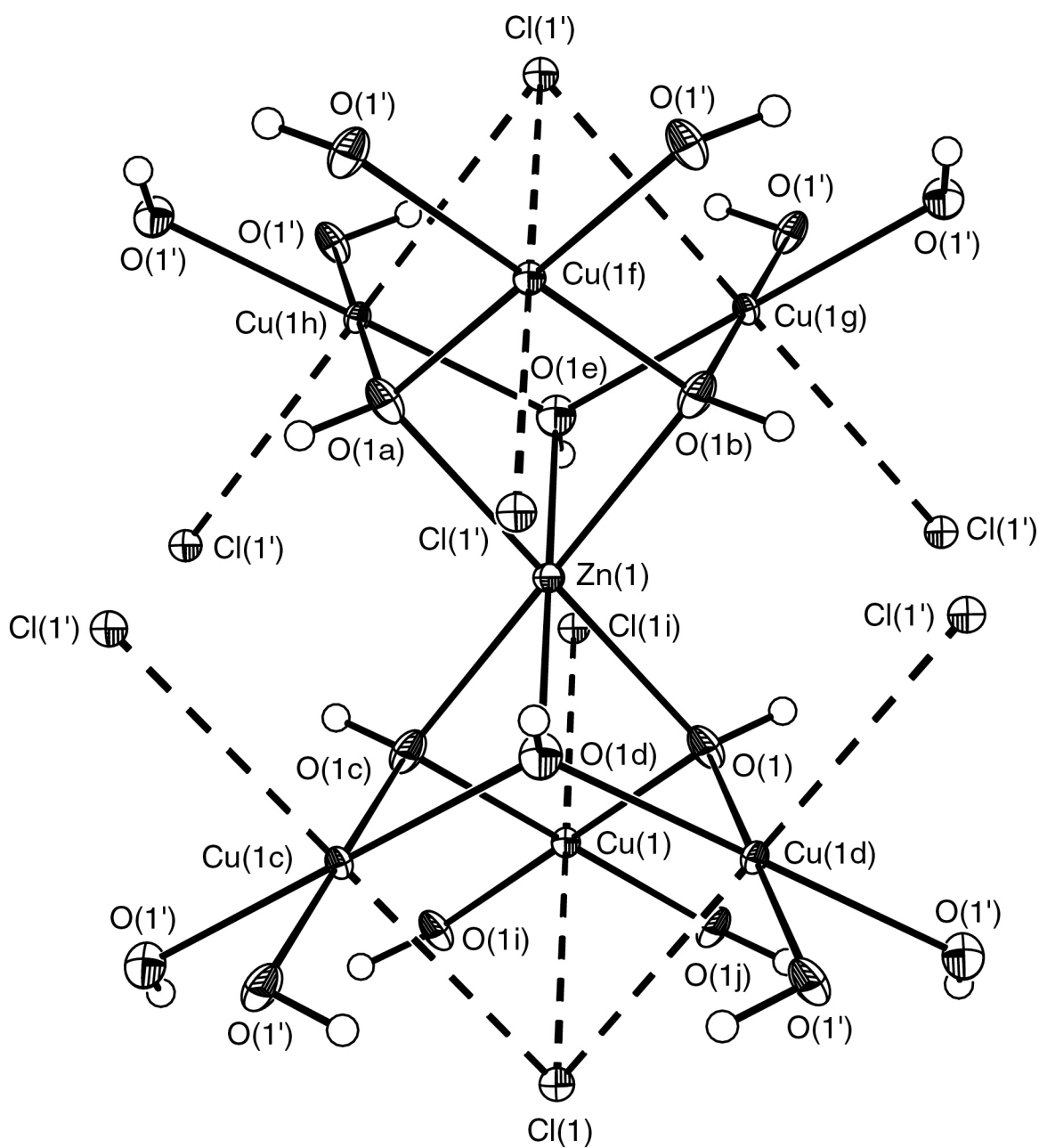


Figure A.3.7. A portion of the crystal structure of c05017a, $\text{ZnCu}_3(\text{OH})_6\text{Cl}_2$. 50% ellipsoids are shown. Atoms labeled with letters correspond to symmetry equivalent atoms as found in Tables A.3.37 and A.3.38. Hydrogen atoms are not labeled.

Table A.3.33. Crystal data and structure refinement for $\text{ZnCu}_3(\text{OH})_6\text{Cl}_2$.

Identification code	c05017a	
Empirical formula	$\text{H}_6\text{Cl}_2\text{Cu}_3\text{O}_6\text{Zn}$	
Formula weight	428.94	
Temperature	130(2) K	
Wavelength	0.71073 Å	
Crystal system	Rhombohedral (obverse)	
Space group	$R\bar{3}m$	
Unit cell dimensions	$a = 6.8342(3)$ Å	$\alpha = 90^\circ$
	$b = 6.8342(3)$ Å	$\beta = 90^\circ$
	$c = 14.0320(12)$ Å	$\gamma = 120^\circ$
Volume, Z	$567.58(6)$ Å ³	3
Density (calculated)	3.765 g/cm ³	
Absorption coefficient	12.133 mm ⁻¹	
F(000)	615	
Crystal size	0.05 × 0.04 × 0.04 mm	
θ range for data collection	3.74 to 24.69°	
Limiting indices	$-7 \leq h \leq 8$ $-7 \leq k \leq 8$ $-16 \leq l \leq 16$	
Reflections collected	1422	
Independent reflections	135 ($R_{\text{int}} = 0.0333$)	
Completeness to $\theta = 24.69^\circ$	97.8 %	
Refinement method	Full-matrix least-squares on F^2	
Data / restraints / parameters	135 / 1 / 19	
Goodness-of-fit on F^2	1.539	
Final R indices [$I > 2\sigma(I)$]	$R_1 = 0.0213$	$wR_2 = 0.0642$
R indices (all data)	$R_1 = 0.0213$	$wR_2 = 0.0642$
Largest diff. peak and hole	0.602 eÅ ⁻³	-0.621 eÅ ⁻³

Appendix A

Table A.3.34. Atomic coordinates [$\times 10^4$] and equivalent isotropic displacement parameters [$\text{\AA}^2 \times 10^3$] for c05017a, $\text{ZnCu}_3(\text{OH})_6\text{Cl}_2$. U_{eq} is defined as one third of the trace of the orthogonalized U_{ij} tensor.

	<i>x</i>	<i>y</i>	<i>z</i>	U_{eq}
Zn(1)	0	0	0	7(1)
Cu(1)	3333	1667	1667	6(1)
O(1)	1265(4)	2529(8)	1050(3)	12(1)
Cl(1)	0	0	3052(2)	9(1)

Table A.3.35. Bond lengths [\AA] for c05017a, $\text{ZnCu}_3(\text{OH})_6\text{Cl}_2$.

Zn(1)-O(1) ^a	2.101(5)	Zn(1)-Cu(1) ^h	3.05971(16)
Zn(1)-O(1)	2.101(5)	Cu(1)-O(1) ⁱ	1.982(2)
Zn(1)-O(1) ^b	2.101(5)	Cu(1)-O(1)	1.982(2)
Zn(1)-O(1) ^c	2.101(5)	Cu(1)-O(1) ^c	1.982(2)
Zn(1)-O(1) ^d	2.101(5)	Cu(1)-O(1) ^j	1.982(2)
Zn(1)-O(1) ^e	2.101(5)	Cu(1)-Cl(1) ⁱ	2.7697(17)
Zn(1)-Cu(1)	3.05967(16)	Cu(1)-Cl(1)	2.7698(17)
Zn(1)-Cu(1) ^d	3.05967(16)	Cu(1)-Zn(1) ^k	3.05968(16)
Zn(1)-Cu(1) ^c	3.05967(16)	O(1)-Cu(1) ^d	1.982(2)
Zn(1)-Cu(1) ^f	3.05968(16)	Cl(1)-Cu(1) ^c	2.7698(17)
Zn(1)-Cu(1) ^g	3.05968(16)	Cl(1)-Cu(1) ^d	2.7698(17)

Symmetry transformations used to generate equivalent atoms:

$$\begin{array}{lllll}
 {}^a -x, -y, -z & {}^b x - y, x, -z & {}^c -x + y, -x, z & {}^d -y, x - y, z & {}^e y, -x + y, -z \\
 {}^f x - 2/3, y - 1/3, z - 1/3 & {}^g -x + y + 1/3, -x + 2/3, z - 1/3 & {}^h -y + 1/3, x - y - 1/3, z - 1/3 & & \\
 {}^i -x + 2/3, -y + 1/3, -z + 1/3 & {}^j x - y + 2/3, x + 1/3, -z + 1/3 & {}^k x + 2/3, y + 1/3, z + 1/3 & &
 \end{array}$$

Table A.3.36. Bond angles [°] for c05017a, $\text{ZnCu}_3(\text{OH})_6\text{Cl}_2$.

$\text{O}(1)^a\text{-Zn}(1)\text{-O}(1)$	180.00(19)	$\text{O}(1)^e\text{-Zn}(1)\text{-Cu}(1)^g$	40.00(6)
$\text{O}(1)^a\text{-Zn}(1)\text{-O}(1)^b$	76.21(18)	$\text{Cu}(1)\text{-Zn}(1)\text{-Cu}(1)^g$	112.108(4)
$\text{O}(1)\text{-Zn}(1)\text{-O}(1)^b$	103.79(18)	$\text{Cu}(1)^d\text{-Zn}(1)\text{-Cu}(1)^g$	112.109(4)
$\text{O}(1)^a\text{-Zn}(1)\text{-O}(1)^c$	103.79(18)	$\text{Cu}(1)^c\text{-Zn}(1)\text{-Cu}(1)^g$	180.0
$\text{O}(1)\text{-Zn}(1)\text{-O}(1)^c$	76.21(18)	$\text{Cu}(1)^f\text{-Zn}(1)\text{-Cu}(1)^g$	67.891(4)
$\text{O}(1)^b\text{-Zn}(1)\text{-O}(1)^c$	180.0(2)	$\text{O}(1)^a\text{-Zn}(1)\text{-Cu}(1)^h$	40.01(6)
$\text{O}(1)^a\text{-Zn}(1)\text{-O}(1)^d$	103.79(18)	$\text{O}(1)\text{-Zn}(1)\text{-Cu}(1)^h$	139.99(6)
$\text{O}(1)\text{-Zn}(1)\text{-O}(1)^d$	76.21(18)	$\text{O}(1)^b\text{-Zn}(1)\text{-Cu}(1)^h$	85.60(12)
$\text{O}(1)^b\text{-Zn}(1)\text{-O}(1)^d$	103.79(18)	$\text{O}(1)^c\text{-Zn}(1)\text{-Cu}(1)^h$	94.40(12)
$\text{O}(1)^c\text{-Zn}(1)\text{-O}(1)^d$	76.21(18)	$\text{O}(1)^d\text{-Zn}(1)\text{-Cu}(1)^h$	139.99(6)
$\text{O}(1)^a\text{-Zn}(1)\text{-O}(1)^e$	76.21(18)	$\text{O}(1)^e\text{-Zn}(1)\text{-Cu}(1)^h$	40.01(6)
$\text{O}(1)\text{-Zn}(1)\text{-O}(1)^e$	103.79(18)	$\text{Cu}(1)\text{-Zn}(1)\text{-Cu}(1)^h$	112.108(4)
$\text{O}(1)^b\text{-Zn}(1)\text{-O}(1)^e$	76.21(18)	$\text{Cu}(1)^d\text{-Zn}(1)\text{-Cu}(1)^h$	180.0
$\text{O}(1)^c\text{-Zn}(1)\text{-O}(1)^e$	103.79(18)	$\text{Cu}(1)^c\text{-Zn}(1)\text{-Cu}(1)^h$	112.108(4)
$\text{O}(1)^d\text{-Zn}(1)\text{-O}(1)^e$	180.0(2)	$\text{Cu}(1)^f\text{-Zn}(1)\text{-Cu}(1)^h$	67.891(4)
$\text{O}(1)^a\text{-Zn}(1)\text{-Cu}(1)$	139.99(6)	$\text{Cu}(1)^g\text{-Zn}(1)\text{-Cu}(1)^h$	67.891(4)
$\text{O}(1)\text{-Zn}(1)\text{-Cu}(1)$	40.01(6)	$\text{O}(1)^i\text{-Cu}(1)\text{-O}(1)$	180.0
$\text{O}(1)^b\text{-Zn}(1)\text{-Cu}(1)$	139.99(6)	$\text{O}(1)^i\text{-Cu}(1)\text{-O}(1)^c$	98.3(3)
$\text{O}(1)^c\text{-Zn}(1)\text{-Cu}(1)$	40.01(6)	$\text{O}(1)\text{-Cu}(1)\text{-O}(1)^c$	81.7(3)
$\text{O}(1)^d\text{-Zn}(1)\text{-Cu}(1)$	85.60(12)	$\text{O}(1)^i\text{-Cu}(1)\text{-O}(1)^j$	81.7(3)
$\text{O}(1)^e\text{-Zn}(1)\text{-Cu}(1)$	94.40(12)	$\text{O}(1)\text{-Cu}(1)\text{-O}(1)^j$	98.3(3)
$\text{O}(1)^a\text{-Zn}(1)\text{-Cu}(1)^d$	139.99(6)	$\text{O}(1)^c\text{-Cu}(1)\text{-O}(1)^j$	180.0
$\text{O}(1)\text{-Zn}(1)\text{-Cu}(1)^d$	40.01(6)	$\text{O}(1)^i\text{-Cu}(1)\text{-Cl}(1)^i$	82.32(11)
$\text{O}(1)^b\text{-Zn}(1)\text{-Cu}(1)^d$	94.40(12)	$\text{O}(1)\text{-Cu}(1)\text{-Cl}(1)^i$	97.69(11)
$\text{O}(1)^c\text{-Zn}(1)\text{-Cu}(1)^d$	85.60(12)	$\text{O}(1)^c\text{-Cu}(1)\text{-Cl}(1)^i$	97.69(11)
$\text{O}(1)^d\text{-Zn}(1)\text{-Cu}(1)^d$	40.01(6)	$\text{O}(1)^j\text{-Cu}(1)\text{-Cl}(1)^i$	82.32(11)
$\text{O}(1)^e\text{-Zn}(1)\text{-Cu}(1)^d$	139.99(6)	$\text{O}(1)^i\text{-Cu}(1)\text{-Cl}(1)$	97.68(11)
$\text{Cu}(1)\text{-Zn}(1)\text{-Cu}(1)^d$	67.892(4)	$\text{O}(1)\text{-Cu}(1)\text{-Cl}(1)$	82.31(11)
$\text{O}(1)^a\text{-Zn}(1)\text{-Cu}(1)^c$	94.40(12)	$\text{O}(1)^c\text{-Cu}(1)\text{-Cl}(1)$	82.31(11)
$\text{O}(1)\text{-Zn}(1)\text{-Cu}(1)^c$	85.60(12)	$\text{O}(1)^j\text{-Cu}(1)\text{-Cl}(1)$	97.68(11)
$\text{O}(1)^b\text{-Zn}(1)\text{-Cu}(1)^c$	139.99(6)	$\text{Cl}(1)^i\text{-Cu}(1)\text{-Cl}(1)$	180.0
$\text{O}(1)^c\text{-Zn}(1)\text{-Cu}(1)^c$	40.01(6)	$\text{O}(1)^i\text{-Cu}(1)\text{-Zn}(1)$	137.05(13)
$\text{O}(1)^d\text{-Zn}(1)\text{-Cu}(1)^c$	40.01(6)	$\text{O}(1)\text{-Cu}(1)\text{-Zn}(1)$	42.95(13)
$\text{O}(1)^e\text{-Zn}(1)\text{-Cu}(1)^c$	139.99(6)	$\text{O}(1)^c\text{-Cu}(1)\text{-Zn}(1)$	42.95(13)

Table A.3.36. Bond angles [°] for c05017a, ZnCu₃(OH)₆Cl₂ (continued).

Cu(1)-Zn(1)-Cu(1) ^c	67.892(4)	O(1) ^j -Cu(1)-Zn(1)	137.05(13)
Cu(1) ^d -Zn(1)-Cu(1) ^c	67.892(4)	Cl(1) ⁱ -Cu(1)-Zn(1)	85.57(4)
O(1) ^a -Zn(1)-Cu(1) ^f	40.00(6)	Cl(1)-Cu(1)-Zn(1)	94.43(4)
O(1)-Zn(1)-Cu(1) ^f	140.00(6)	O(1) ⁱ -Cu(1)-Zn(1) ^k	42.95(13)
O(1) ^b -Zn(1)-Cu(1) ^f	40.01(6)	O(1)-Cu(1)-Zn(1) ^k	137.05(13)
O(1) ^c -Zn(1)-Cu(1) ^f	139.99(6)	O(1) ^e -Cu(1)-Zn(1) ^k	137.05(13)
O(1) ^d -Zn(1)-Cu(1) ^f	94.40(12)	O(1) ^j -Cu(1)-Zn(1) ^k	42.95(13)
O(1) ^e -Zn(1)-Cu(1) ^f	85.60(12)	Cl(1) ⁱ -Cu(1)-Zn(1) ^k	94.43(4)
Cu(1)-Zn(1)-Cu(1) ^f	180.0	Cl(1)-Cu(1)-Zn(1) ^k	85.57(4)
Cu(1) ^d -Zn(1)-Cu(1) ^f	112.109(4)	Zn(1)-Cu(1)-Zn(1) ^k	180.0
Cu(1) ^e -Zn(1)-Cu(1) ^f	112.108(4)	Cu(1)-O(1)-Cu(1) ^d	119.1(2)
O(1) ^a -Zn(1)-Cu(1) ^g	85.60(12)	Cu(1)-O(1)-Zn(1)	97.04(15)
O(1)-Zn(1)-Cu(1) ^g	94.40(12)	Cu(1) ^d -O(1)-Zn(1)	97.04(15)
O(1) ^b -Zn(1)-Cu(1) ^g	40.01(6)	Cu(1) ^e -Cl(1)-Cu(1) ^d	76.17(5)
O(1) ^c -Zn(1)-Cu(1) ^g	139.99(6)	Cu(1) ^e -Cl(1)-Cu(1)	76.17(5)
O(1) ^d -Zn(1)-Cu(1) ^g	140.00(6)	Cu(1) ^d -Cl(1)-Cu(1)	76.17(5)

Symmetry transformations used to generate equivalent atoms:

$$\begin{array}{llll}
 a & -x, -y, -z & b & x - y, x, -z \\
 f & x - 2/3, y - 1/3, z - 1/3 & g & -x + y + 1/3, -x + 2/3, z - 1/3 \\
 i & -x + 2/3, -y + 1/3, -z + 1/3 & j & x - y + 2/3, x + 1/3, -z + 1/3 \\
 c & -x + y, -x, z & d & -y, x - y, z \\
 e & y, -x + y, -z & h & -y + 1/3, x - y - 1/3, z - 1/3 \\
 k & & k & x + 2/3, y + 1/3, z + 1/3
 \end{array}$$

Appendix A

Table A.3.37. Anisotropic displacement parameters [$\text{\AA}^2 \times 10^3$] for c05017a, $\text{ZnCu}_3(\text{OH})_6\text{Cl}_2$. The anisotropic displacement factor exponent takes the form: $-2\pi^2[(ha^*)^2U_{11} + \dots + 2hka^*b^*U_{12}]$.

	U_{11}	U_{22}	U_{33}	U_{23}	U_{13}	U_{12}
Zn(1)	7(1)	7(1)	6(1)	0	0	4(1)
Cu(1)	5(1)	6(1)	7(1)	-1(1)	-1(1)	3(1)
O(1)	12(2)	10(3)	15(2)	6(2)	3(1)	5(1)
Cl(1)	9(1)	9(1)	8(1)	0	0	5(1)

Table A.3.38. Hydrogen coordinates [$\times 10^4$] and isotropic displacement parameters [$\text{\AA}^2 \times 10^3$] for c05017a, $\text{ZnCu}_3(\text{OH})_6\text{Cl}_2$.

	x	y	z	U_{eq}
H(1)	1920(30)	3840(60)	840(60)	40(30)

Table A.3.39. Crystal data and structure refinement for $\text{ZnCu}_3(\text{OH})_6\text{Cl}_2$.

Identification code	07036	
Empirical formula	$\text{H}_6\text{Cl}_2\text{Cu}_6\text{O}_6\text{Zn}$	
Formula weight	428.94	
Temperature	100(2) K	
Wavelength	0.71073 Å	
Crystal system	Rhobohedral	
Space group	$R\bar{3}m$	
Unit cell dimensions	$a = 6.8367(16)$ Å	$\alpha = 90^\circ$
	$b = 6.8367(16)$ Å	$\beta = 90^\circ$
	$c = 14.106(7)$ Å	$\gamma = 120^\circ$
Volume, Z	$571.0(3)$ Å ³	3
Density (calculated)	3.742 g/cm ³	
Absorption coefficient	12.060 mm ⁻¹	
F(000)	615	
Crystal size	$0.10 \times 0.05 \times 0.05$ mm	
θ range for data collection	3.73 to 29.57°	
Limiting indices	$-9 \leq h \leq 9$	
	$-9 \leq k \leq 9$	
	$-19 \leq l \leq 19$	
Reflections collected	4216	
Independent reflections	227 ($R_{\text{int}} = 0.0437$)	
Completeness to $\theta = 29.57^\circ$	100.0 %	
Absorption correction	Semi-empirical from equivalents	
Max. and min. transmission	0.5839	0.3785
Refinement method	Full-matrix least-squares on F^2	
Data / restraints / parameters	227 / 1 / 18	
Goodness-of-fit on F^2	1.286	
Final R indices [$I > 2\sigma(I)$]	$R_1 = 0.0255$	$wR_2 = 0.0662$
R indices (all data)	$R_1 = 0.0263$	$wR_2 = 0.0668$
Largest diff. peak and hole	1.269 eÅ ⁻³	-0.793 eÅ ⁻³

Appendix A

Table A.3.40. Atomic coordinates [$\times 10^4$] and equivalent isotropic displacement parameters [$\text{\AA}^2 \times 10^3$] for 07036, $\text{ZnCu}_3(\text{OH})_6\text{Cl}_2$. U_{eq} is defined as one third of the trace of the orthogonalized U_{ij} tensor.

	x	y	z	U_{eq}
Zn(1)	6667	3333	3333	8(1)
Cu(2)	3333	1667	1667	8(1)
Cl(1)	0	0	3037(1)	12(1)
O(1)	1275(3)	-1275(3)	1049(2)	11(1)

Table A.3.41. Bond lengths [\AA] for 07036, $\text{ZnCu}_3(\text{OH})_6\text{Cl}_2$.

Zn(1)-O(1) ^a	2.114(3)	Cu(2)-O(1)	1.9889(15)
Zn(1)-O(1) ^b	2.114(3)	Cu(2)-O(1) ^a	1.9889(16)
Zn(1)-O(1) ^c	2.114(3)	Cu(2)-O(1) ⁱ	1.9889(15)
Zn(1)-O(1) ^d	2.114(3)	Cu(2)-O(1) ^c	1.9889(16)
Zn(1)-O(1) ^e	2.114(3)	Cu(2)-Cl(1) ^c	2.7629(14)
Zn(1)-O(1) ^f	2.114(3)	Cu(2)-Cl(1)	2.7630(14)
Zn(1)-Cu(2)	3.0696(9)	Cu(2)-Zn(1) ^j	3.0696(9)
Zn(1)-Cu(2) ^d	3.0696(9)	Cl(1)-Cu(2) ⁱ	2.7630(14)
Zn(1)-Cu(2) ^f	3.0696(9)	Cl(1)-Cu(2) ^k	2.7630(14)
Zn(1)-Cu(2) ^e	3.0696(9)	O(1)-Cu(2) ^k	1.9889(16)
Zn(1)-Cu(2) ^g	3.0696(9)	O(1)-Zn(1) ^j	2.114(3)
Zn(1)-Cu(2) ^h	3.0697(9)		

Symmetry transformations used to generate equivalent atoms:

$$^a y + 2/3, -x + y + 1/3, -z + 1/3$$

$$^c -x + 2/3, -y + 1/3, -z + 1/3$$

$$^e -y + 2/3, x - y + 1/3, z + 1/3$$

$$^g -x + y + 1, -x + 1, z$$

$$^i -y, x - y, z$$

$$^k -x + y, -x, z$$

$$^b x - y + 2/3, x + 1/3, -z + 1/3$$

$$^d x + 2/3, y + 1/3, z + 1/3$$

$$^f -x + y + 2/3, -x + 1/3, z + 1/3$$

$$^h -y + 1, x - y, z$$

$$^j x - 2/3, y - 1/3, z - 1/3$$

Appendix A

Table A.3.42. Bond angles [°] for 07036, ZnCu₃(OH)₆Cl₂.

O(1) ^a -Zn(1)-O(1) ^b	76.45(13)	O(1) ^f -Zn(1)-Cu(2) ^g	139.96(4)
O(1) ^a -Zn(1)-O(1) ^c	76.45(13)	Cu(2)-Zn(1)-Cu(2) ^g	67.67(2)
O(1) ^b -Zn(1)-O(1) ^c	76.45(13)	Cu(2) ^d -Zn(1)-Cu(2) ^g	112.33(2)
O(1) ^a -Zn(1)-O(1) ^d	103.55(13)	Cu(2) ^f -Zn(1)-Cu(2) ^g	180.0
O(1) ^b -Zn(1)-O(1) ^d	103.55(13)	Cu(2) ^e -Zn(1)-Cu(2) ^g	112.33(2)
O(1) ^c -Zn(1)-O(1) ^d	180.0	O(1) ^a -Zn(1)-Cu(2) ^h	40.04(4)
O(1) ^a -Zn(1)-O(1) ^e	180.0	O(1) ^b -Zn(1)-Cu(2) ^h	40.04(4)
O(1) ^b -Zn(1)-O(1) ^e	103.55(13)	O(1) ^c -Zn(1)-Cu(2) ^h	85.61(9)
O(1) ^c -Zn(1)-O(1) ^e	103.55(13)	O(1) ^d -Zn(1)-Cu(2) ^h	94.39(9)
O(1) ^d -Zn(1)-O(1) ^e	76.45(13)	O(1) ^e -Zn(1)-Cu(2) ^h	139.96(4)
O(1) ^a -Zn(1)-O(1) ^f	103.55(13)	O(1) ^f -Zn(1)-Cu(2) ^h	139.96(4)
O(1) ^b -Zn(1)-O(1) ^f	180.0	Cu(2)-Zn(1)-Cu(2) ^h	67.67(2)
O(1) ^c -Zn(1)-O(1) ^f	103.55(13)	Cu(2) ^d -Zn(1)-Cu(2) ^h	112.33(2)
O(1) ^d -Zn(1)-O(1) ^f	76.45(13)	Cu(2) ^f -Zn(1)-Cu(2) ^h	112.33(2)
O(1) ^e -Zn(1)-O(1) ^f	76.45(13)	Cu(2) ^e -Zn(1)-Cu(2) ^h	180.0
O(1) ^a -Zn(1)-Cu(2)	40.04(4)	Cu(2) ^g -Zn(1)-Cu(2) ^h	67.67(2)
O(1) ^b -Zn(1)-Cu(2)	85.61(9)	O(1)-Cu(2)-O(1) ^a	97.76(18)
O(1) ^c -Zn(1)-Cu(2)	40.04(4)	O(1)-Cu(2)-O(1) ⁱ	82.24(18)
O(1) ^d -Zn(1)-Cu(2)	139.96(4)	O(1) ^a -Cu(2)-O(1) ⁱ	180.0
O(1) ^e -Zn(1)-Cu(2)	139.96(4)	O(1)-Cu(2)-O(1) ^c	180.0
O(1) ^f -Zn(1)-Cu(2)	94.39(9)	O(1) ^a -Cu(2)-O(1) ^c	82.24(18)
O(1) ^a -Zn(1)-Cu(2) ^d	139.96(4)	O(1) ⁱ -Cu(2)-O(1) ^c	97.76(18)
O(1) ^b -Zn(1)-Cu(2) ^d	94.39(9)	O(1)-Cu(2)-Cl(1) ^c	97.51(8)
O(1) ^c -Zn(1)-Cu(2) ^d	139.96(4)	O(1) ^a -Cu(2)-Cl(1) ^c	82.49(8)
O(1) ^d -Zn(1)-Cu(2) ^d	40.04(4)	O(1) ⁱ -Cu(2)-Cl(1) ^c	97.51(8)
O(1) ^e -Zn(1)-Cu(2) ^d	40.04(4)	O(1) ^c -Cu(2)-Cl(1) ^c	82.49(8)
O(1) ^f -Zn(1)-Cu(2) ^d	85.61(9)	O(1)-Cu(2)-Cl(1)	82.49(8)
Cu(2)-Zn(1)-Cu(2) ^d	180.0	O(1) ^a -Cu(2)-Cl(1)	97.51(8)
O(1) ^a -Zn(1)-Cu(2) ^f	94.39(9)	O(1) ⁱ -Cu(2)-Cl(1)	82.49(8)
O(1) ^b -Zn(1)-Cu(2) ^f	139.96(4)	O(1) ^c -Cu(2)-Cl(1)	97.51(8)
O(1) ^c -Zn(1)-Cu(2) ^f	139.96(4)	Cl(1) ^c -Cu(2)-Cl(1)	180.0
O(1) ^d -Zn(1)-Cu(2) ^f	40.04(4)	O(1)-Cu(2)-Zn(1)	136.86(9)
O(1) ^e -Zn(1)-Cu(2) ^f	85.61(9)	O(1) ^a -Cu(2)-Zn(1)	43.14(9)
O(1) ^f -Zn(1)-Cu(2) ^f	40.04(4)	O(1) ⁱ -Cu(2)-Zn(1)	136.86(9)

Appendix A

Cu(2)-Zn(1)-Cu(2) ^f	112.33(2)	O(1) ^c -Cu(2)-Zn(1)	43.14(9)
Cu(2) ^d -Zn(1)-Cu(2) ^f	67.67(2)	Cl(1) ^c -Cu(2)-Zn(1)	94.40(4)
O(1) ^a -Zn(1)-Cu(2) ^e	139.96(4)	Cl(1)-Cu(2)-Zn(1)	85.60(4)
O(1) ^b -Zn(1)-Cu(2) ^e	139.96(4)	O(1)-Cu(2)-Zn(1) ^j	43.14(9)
O(1) ^c -Zn(1)-Cu(2) ^e	94.39(9)	O(1) ^a -Cu(2)-Zn(1) ^j	136.86(9)
O(1) ^d -Zn(1)-Cu(2) ^e	85.61(9)	O(1) ⁱ -Cu(2)-Zn(1) ^j	43.14(9)
O(1) ^e -Zn(1)-Cu(2) ^e	40.04(4)	O(1) ^c -Cu(2)-Zn(1) ^j	136.86(9)
O(1) ^f -Zn(1)-Cu(2) ^e	40.04(4)	Cl(1) ^c -Cu(2)-Zn(1) ^j	85.60(4)
Cu(2)-Zn(1)-Cu(2) ^e	112.33(2)	Cl(1)-Cu(2)-Zn(1) ^j	94.40(4)
Cu(2) ^d -Zn(1)-Cu(2) ^e	67.67(2)	Zn(1)-Cu(2)-Zn(1) ^j	180.0
Cu(2) ^f -Zn(1)-Cu(2) ^e	67.67(2)	Cu(2)-Cl(1)-Cu(2) ⁱ	76.43(5)
O(1) ^a -Zn(1)-Cu(2)#7	85.61(9)	Cu(2)-Cl(1)-Cu(2) ^k	76.43(5)
O(1) ^b -Zn(1)-Cu(2)#7	40.04(4)	Cu(2) ⁱ -Cl(1)-Cu(2) ^k	76.43(5)
O(1) ^c -Zn(1)-Cu(2)#7	40.04(4)	Cu(2) ^k -O(1)-Cu(2)	118.49(15)
O(1) ^d -Zn(1)-Cu(2)#7	139.96(4)	Cu(2) ^k -O(1)-Zn(1) ^j	96.82(11)
O(1) ^e -Zn(1)-Cu(2)#7	94.39(9)	Cu(2)-O(1)-Zn(1) ^j	96.82(11)

Symmetry transformations used to generate equivalent atoms:

$$^a y + 2/3, -x + y + 1/3, -z + 1/3$$

$$^c -x + 2/3, -y + 1/3, -z + 1/3$$

$$^e -y + 2/3, x - y + 1/3, z + 1/3$$

$$^g -x + y + 1, -x + 1, z$$

$$^i -y, x - y, z$$

$$^k -x + y, -x, z$$

$$^b x - y + 2/3, x + 1/3, -z + 1/3$$

$$^d x + 2/3, y + 1/3, z + 1/3$$

$$^f -x + y + 2/3, -x + 1/3, z + 1/3$$

$$^h -y + 1, x - y, z$$

$$^j x - 2/3, y - 1/3, z - 1/3$$

Table A.3.43. Anisotropic displacement parameters [$\text{\AA}^2 \times 10^3$] for 07036, $\text{ZnCu}_3(\text{OH})_6\text{Cl}_2$. The anisotropic displacement factor exponent takes the form: $-2\pi^2[(ha^*)^2U_{11} + \dots + 2hka^*b^*U_{12}]$.

	U_{11}	U_{22}	U_{33}	U_{23}	U_{13}	U_{12}
Zn(1)	7(1)	7(1)	11(1)	0	0	3(1)
Cu(2)	6(1)	6(1)	13(1)	-1(1)	-1(1)	3(1)
Cl(1)	11(1)	11(1)	14(1)	0	0	5(1)
O(1)	9(1)	9(1)	15(1)	-1(1)	1(1)	4(1)

Appendix A

Table A.3.44. Hydrogen coordinates [$\times 10^4$] and isotropic displacement parameters [$\text{\AA}^2 \times 10^3$] for 07036, $\text{ZnCu}_3(\text{OH})_6\text{Cl}_2$.

	<i>x</i>	<i>y</i>	<i>z</i>	U_{eq}
H(1)	1880(30)	-1880(30)	750(40)	13

Table A.3.45. Hydrogen bond lengths [\AA] and angles [$^\circ$] for 07036, $\text{ZnCu}_3(\text{OH})_6\text{Cl}_2$.

D-H \cdots A	$d(\text{D-H})$	$d(\text{H}\cdots\text{A})$	$d(\text{D}\cdots\text{A})$	$\angle(\text{DHA})$
O(1)-H(1) \cdots Cl(1) ^{<i>l</i>}	0.84(2)	2.26(2)	3.088(3)	170(5)

Symmetry transformations used to generate equivalent atoms:

$$^a y + 2/3, -x + y + 1/3, -z + 1/3$$

$$^c -x + 2/3, -y + 1/3, -z + 1/3$$

$$^e -y + 2/3, x - y + 1/3, z + 1/3$$

$$^g -x + y + 1, -x + 1, z$$

$$^i -y, x - y, z$$

$$^k -x + y, -x, z$$

$$^b x - y + 2/3, x + 1/3, -z + 1/3$$

$$^d x + 2/3, y + 1/3, z + 1/3$$

$$^f -x + y + 2/3, -x + 1/3, z + 1/3$$

$$^h -y + 1, x - y, z$$

$$^j x - 2/3, y - 1/3, z - 1/3$$

$$^l x + 1/3, y - 1/3, z - 1/3$$

Table A.3.46. Crystal data and structure refinement for $\text{ZnCu}_3(\text{OH})_6\text{Cl}_2$.

Identification code	08039	
Empirical formula	$\text{H}_6\text{Cl}_2\text{Cu}_3\text{O}_6\text{Zn}$	
Formula weight	428.94	
Temperature	100(2) K	
Wavelength	0.71073 Å	
Crystal system	Rhombohedral	
Space group	$R\bar{3}m$	
Unit cell dimensions	$a = 6.8447(6)$ Å	$\alpha = 90^\circ$
	$b = 6.8447(6)$ Å	$\beta = 90^\circ$
	$c = 14.116(3)$ Å	$\gamma = 120^\circ$
Volume, Z	$572.75(7)$ Å ³	3
Density (calculated)	3.731 g/cm ³	
Absorption coefficient	12.023 mm ⁻¹	
F(000)	615	
Crystal size	$0.08 \times 0.04 \times 0.03$ mm	
θ range for data collection	3.73 to 29.56°	
Limiting indices	$-9 \leq h \leq 9$	
	$-9 \leq k \leq 9$	
	$-19 \leq l \leq 19$	
Reflections collected	4928	
Independent reflections	228 ($R_{\text{int}} = 0.0400$)	
Completeness to $\theta = 29.56^\circ$	100.0 %	
Absorption correction	Semi-empirical from equivalents	
Max. and min. transmission	0.7143	0.4463
Refinement method	Full-matrix least-squares on F^2	
Data / restraints / parameters	228 / 1 / 18	
Goodness-of-fit on F^2	1.310	
Final R indices [$I > 2\sigma(I)$]	$R_1 = 0.0180$	$wR_2 = 0.0466$
R indices (all data)	$R_1 = 0.0183$	$wR_2 = 0.0466$
Largest diff. peak and hole	0.458 eÅ ⁻³	-0.625 eÅ ⁻³

Appendix A

Table A.3.47. Atomic coordinates [$\times 10^4$] and equivalent isotropic displacement parameters [$\text{\AA}^2 \times 10^3$] for 08039, $\text{ZnCu}_3(\text{OH})_6\text{Cl}_2$. U_{eq} is defined as one third of the trace of the orthogonalized U_{ij} tensor.

	<i>x</i>	<i>y</i>	<i>Z</i>	U_{eq}
Cu(1)	5000	5000	0	7(1)
Zn(2)	3333	6667	1667	7(1)
Cl(1)	6667	3333	1350(1)	13(1)
O(1)	2055(2)	4110(4)	627(2)	10(1)

Table A.3.48. Bond lengths [\AA] for 08039, $\text{ZnCu}_3(\text{OH})_6\text{Cl}_2$.

Cu(1)-O(1)	1.9972(11)	Zn(2)-O(1) ^b	2.110(2)
Cu(1)-O(1) ^a	1.9972(11)	Zn(2)-O(1) ^g	2.110(2)
Cu(1)-O(1) ^b	1.9972(11)	Zn(2)-O(1) ^h	2.110(2)
Cu(1)-O(1) ^c	1.9972(11)	Zn(2)-Cu(1) ^e	3.0724(3)
Cu(1)-Cl(1)	2.7447(9)	Zn(2)-Cu(1) ^b	3.0724(4)
Cu(1)-Cl(1) ^c	2.7447(9)	Zn(2)-Cu(1) ⁱ	3.0724(3)
Cu(1)-Zn(2)	3.0724(3)	Zn(2)-Cu(1) ^j	3.0724(4)
Cu(1)-Zn(2) ^d	3.0725(4)	Zn(2)-Cu(1) ^k	3.0724(4)
Zn(2)-O(1) ^e	2.110(2)	Cl(1)-Cu(1) ^l	2.7447(9)
Zn(2)-O(1) ^f	2.110(2)	Cl(1)-Cu(1) ^m	2.7447(9)
Zn(2)-O(1)	2.110(2)	O(1)-Cu(1) ^e	1.9972(11)

Symmetry transformations used to generate equivalent atoms:

$$^a y, -x + y, -z$$

$$^c -x + 1, -y + 1, -z$$

$$^e -x + y, -x + 1, z$$

$$^g -x + 2/3, -y + 4/3, -z + 1/3$$

$$^i -x + y + 2/3, -x + 4/3, z + 1/3$$

$$^k x - 1/3, y + 1/3, z + 1/3$$

$$^m -x + y + 1, -x + 1, z$$

$$^b -y + 1, x - y + 1, z$$

$$^d x + 1/3, y - 1/3, z - 1/3$$

$$^f x - y + 2/3, x + 1/3, -z + 1/3$$

$$^h y - 1/3, -x + y + 1/3, -z + 1/3$$

$$^j -y + 2/3, x - y + 1/3, z + 1/3$$

$$^l -y + 1, x - y, z$$

Appendix A

Table A.3.49. Bond angles [°] for 08039, ZnCu₃(OH)₆Cl₂.

O(1)-Cu(1)-O(1) ^a	97.85(12)	O(1) ^f -Zn(2)-Cu(1) ^b	139.80(3)
O(1)-Cu(1)-O(1) ^b	82.15(12)	O(1)-Zn(2)-Cu(1) ^b	85.93(6)
O(1) ^a -Cu(1)-O(1) ^b	180.00(15)	O(1) ^b -Zn(2)-Cu(1) ^b	40.20(3)
O(1)-Cu(1)-O(1) ^c	180.0	O(1) ^g -Zn(2)-Cu(1) ^b	94.07(6)
O(1) ^a -Cu(1)-O(1) ^c	82.15(12)	O(1) ^h -Zn(2)-Cu(1) ^b	139.80(3)
O(1) ^b -Cu(1)-O(1) ^c	97.85(12)	Cu(1) ^e -Zn(2)-Cu(1) ^b	67.691(9)
O(1)-Cu(1)-Cl(1)	97.57(5)	O(1) ^e -Zn(2)-Cu(1)	85.93(6)
O(1) ^a -Cu(1)-Cl(1)	82.44(5)	O(1) ^f -Zn(2)-Cu(1)	94.07(6)
O(1) ^b -Cu(1)-Cl(1)	97.56(5)	O(1)-Zn(2)-Cu(1)	40.20(3)
O(1) ^c -Cu(1)-Cl(1)	82.44(5)	O(1) ^b -Zn(2)-Cu(1)	40.20(3)
O(1)-Cu(1)-Cl(1) ^c	82.44(5)	O(1) ^g -Zn(2)-Cu(1)	139.80(3)
O(1) ^a -Cu(1)-Cl(1) ^c	97.56(5)	O(1) ^h -Zn(2)-Cu(1)	139.80(3)
O(1) ^b -Cu(1)-Cl(1) ^c	82.44(5)	Cu(1) ^e -Zn(2)-Cu(1)	67.691(9)
O(1) ^c -Cu(1)-Cl(1) ^c	97.56(5)	Cu(1) ^b -Zn(2)-Cu(1)	67.691(9)
Cl(1)-Cu(1)-Cl(1) ^c	180.0	O(1) ^e -Zn(2)-Cu(1) ⁱ	139.80(3)
O(1)-Cu(1)-Zn(2)	42.99(6)	O(1) ^f -Zn(2)-Cu(1) ⁱ	40.20(3)
O(1) ^a -Cu(1)-Zn(2)	137.01(6)	O(1)-Zn(2)-Cu(1) ⁱ	139.80(3)
O(1) ^b -Cu(1)-Zn(2)	42.99(6)	O(1) ^b -Zn(2)-Cu(1) ⁱ	94.07(6)
O(1) ^c -Cu(1)-Zn(2)	137.01(6)	O(1) ^g -Zn(2)-Cu(1) ⁱ	40.20(3)
Cl(1)-Cu(1)-Zn(2)	86.07(2)	O(1) ^h -Zn(2)-Cu(1) ⁱ	85.93(6)
Cl(1) ^c -Cu(1)-Zn(2)	93.93(2)	Cu(1) ^e -Zn(2)-Cu(1) ⁱ	180.0
O(1)-Cu(1)-Zn(2) ^d	137.01(6)	Cu(1) ^b -Zn(2)-Cu(1) ⁱ	112.309(9)
O(1) ^a -Cu(1)-Zn(2) ^d	42.99(6)	Cu(1)-Zn(2)-Cu(1) ⁱ	112.310(9)
O(1) ^b -Cu(1)-Zn(2) ^d	137.01(6)	O(1) ^e -Zn(2)-Cu(1) ^j	139.80(3)
O(1) ^c -Cu(1)-Zn(2) ^d	42.99(6)	O(1) ^f -Zn(2)-Cu(1) ^j	40.20(3)
Cl(1)-Cu(1)-Zn(2) ^d	93.93(2)	O(1)-Zn(2)-Cu(1) ^j	94.07(6)
Cl(1) ^c -Cu(1)-Zn(2) ^d	86.07(2)	O(1) ^b -Zn(2)-Cu(1) ^j	139.80(3)
Zn(2)-Cu(1)-Zn(2) ^d	180.0	O(1) ^g -Zn(2)-Cu(1) ^j	85.93(6)
O(1) ^e -Zn(2)-O(1) ^f	180.0	O(1) ^h -Zn(2)-Cu(1) ^j	40.20(3)
O(1)-Zn(2)-O(1)	76.92(9)	Cu(1) ^e -Zn(2)-Cu(1) ^j	112.309(9)
O(1) ^f -Zn(2)-O(1)	103.08(9)	Cu(1) ^b -Zn(2)-Cu(1) ^j	180.0
O(1) ^e -Zn(2)-O(1) ^b	76.92(9)	Cu(1)-Zn(2)-Cu(1) ^j	112.310(9)
O(1) ^f -Zn(2)-O(1) ^b	103.08(9)	Cu(1) ⁱ -Zn(2)-Cu(1) ^j	67.690(9)
O(1)-Zn(2)-O(1) ^b	76.92(9)	O(1) ^e -Zn(2)-Cu(1) ^k	94.07(6)

Appendix A

O(1) ^e -Zn(2)-O(1) ^g	103.08(9)	O(1) ^f -Zn(2)-Cu(1) ^k	85.93(6)
O(1) ^f -Zn(2)-O(1) ^g	76.92(9)	O(1)-Zn(2)-Cu(1) ^k	139.80(3)
O(1)-Zn(2)-O(1) ^g	180.0	O(1) ^b -Zn(2)-Cu(1) ^k	139.80(3)
O(1) ^b -Zn(2)-O(1) ^g	103.08(9)	O(1) ^g -Zn(2)-Cu(1) ^k	40.20(3)
O(1) ^e -Zn(2)-O(1) ^h	103.08(9)	O(1) ^h -Zn(2)-Cu(1) ^k	40.20(3)
O(1) ^f -Zn(2)-O(1) ^h	76.92(9)	Cu(1) ^e -Zn(2)-Cu(1) ^k	112.309(9)
O(1)-Zn(2)-O(1) ^h	103.08(9)	Cu(1) ^b -Zn(2)-Cu(1) ^k	112.309(9)
O(1) ^b -Zn(2)-O(1) ^h	180.00(10)	Cu(1)-Zn(2)-Cu(1) ^k	180.0
O(1) ^g -Zn(2)-O(1) ^h	76.92(9)	Cu(1) ⁱ -Zn(2)-Cu(1) ^k	67.690(9)
O(1) ^e -Zn(2)-Cu(1) ^e	40.20(3)	Cu(1)-Zn(2)-Cu(1) ^k	67.690(9)
O(1) ^f -Zn(2)-Cu(1) ^e	139.80(3)	Cu(1) ^l -Cl(1)-Cu(1) ^m	77.14(3)
O(1)-Zn(2)-Cu(1) ^e	40.20(3)	Cu(1) ^l -Cl(1)-Cu(1)	77.14(3)
O(1) ^b -Zn(2)-Cu(1) ^e	85.93(6)	Cu(1) ^m -Cl(1)-Cu(1)	77.14(3)
O(1) ^g -Zn(2)-Cu(1) ^e	139.80(3)	Cu(1) ^e -O(1)-Cu(1)	117.91(10)
O(1) ^h -Zn(2)-Cu(1) ^e	94.07(6)	Cu(1) ^e -O(1)-Zn(2)	96.81(7)
O(1) ^e -Zn(2)-Cu(1) ^b	40.20(3)	Cu(1)-O(1)-Zn(2)	96.81(7)

Symmetry transformations used to generate equivalent atoms:

$$^a y, -x + y, -z$$

$$^c -x + 1, -y + 1, -z$$

$$^e -x + y, -x + 1, z$$

$$^g -x + 2/3, -y + 4/3, -z + 1/3$$

$$^i -x + y + 2/3, -x + 4/3, z + 1/3$$

$$^k x - 1/3, y + 1/3, z + 1/3$$

$$^m -x + y + 1, -x + 1, z$$

$$^b -y + 1, x - y + 1, z$$

$$^d x + 1/3, y - 1/3, z - 1/3$$

$$^f x - y + 2/3, x + 1/3, -z + 1/3$$

$$^h y - 1/3, -x + y + 1/3, -z + 1/3$$

$$^j -y + 2/3, x - y + 1/3, z + 1/3$$

$$^l -y + 1, x - y, z$$

Appendix A

Table A.3.50. Anisotropic displacement parameters [$\text{\AA}^2 \times 10^3$] for 08039, $\text{ZnCu}_3(\text{OH})_6\text{Cl}_2$. The anisotropic displacement factor exponent takes the form: $-2\pi^2[(ha^*)^2U_{11} + \dots + 2hka^*b^*U_{12}]$.

	U_{11}	U_{22}	U_{33}	U_{23}	U_{13}	U_{12}
Cu(1)	5(1)	5(1)	12(1)	-1(1)	1(1)	3(1)
Zn(2)	6(1)	6(1)	10(1)	0	0	3(1)
Cl(1)	13(1)	13(1)	14(1)	0	0	6(1)
O(1)	8(1)	6(1)	15(1)	2(1)	1(1)	3(1)

Table A.3.51. Hydrogen coordinates [$\times 10^4$] and isotropic displacement parameters [$\text{\AA}^2 \times 10^3$] for 08039, $\text{ZnCu}_3(\text{OH})_6\text{Cl}_2$.

	x	y	Z	U_{eq}
H(1)	1420(20)	2850(40)	900(20)	12

Appendix A

Table A.3.52. Hydrogen bond lengths [\AA] and angles [$^\circ$] for 08039, $\text{ZnCu}_3(\text{OH})_6\text{Cl}_2$.

D-H \cdots A	$d(\text{D-H})$	$d(\text{H}\cdots\text{A})$	$d(\text{D}\cdots\text{A})$	$\angle(\text{DHA})$
O(1)-H(1) \cdots Cl(1) ⁿ	0.838(19)	2.28(2)	3.099(2)	165(4)

Symmetry transformations used to generate equivalent atoms:

$$^a y, -x + y, -z$$

$$^c -x + 1, -y + 1, -z$$

$$^e -x + y, -x + 1, z$$

$$^g -x + 2/3, -y + 4/3, -z + 1/3$$

$$^i -x + y + 2/3, -x + 4/3, z + 1/3$$

$$^k x - 1/3, y + 1/3, z + 1/3$$

$$^m -x + y + 1, -x + 1, z$$

$$^b -y + 1, x - y + 1, z$$

$$^d x + 1/3, y - 1/3, z - 1/3$$

$$^f x - y + 2/3, x + 1/3, -z + 1/3$$

$$^h y - 1/3, -x + y + 1/3, -z + 1/3$$

$$^j -y + 2/3, x - y + 1/3, z + 1/3$$

$$^l -y + 1, x - y, z$$

$$^n -x + 2/3, -y + 1/3, -z + 1/3$$

Table A.3.53. Crystal data and structure refinement for $\text{ZnCu}_3(\text{OH})_6\text{Cl}_2$.

Identification code	C04072b	
Empirical formula	$\text{H}_6\text{Cl}_2\text{Cu}_3\text{O}_6\text{Zn}$	
Formula weight	428.94	
Temperature	150(2) K	
Wavelength	0.71073 Å	
Crystal system	Rhombohedral	
Space group	$R\bar{3}m$	
Unit cell dimensions	$a = 6.8373(7)$ Å	$\alpha = 90^\circ$
	$b = 6.8373(7)$ Å	$\beta = 90^\circ$
	$c = 14.061(3)$ Å	$\gamma = 120^\circ$
Volume, Z	$569.25(14)$ Å ³	3
Density (calculated)	3.754 g/cm ³	
Absorption coefficient	12.097 mm ⁻¹	
F(000)	615	
Crystal size	0.09 × 0.04 × 0.02 mm	
θ range for data collection	3.73 to 28.29°	
Limiting indices	$-9 \leq h \leq 8$	
	$-8 \leq k \leq 9$	
	$-17 \leq l \leq 18$	
Reflections collected	1999	
Independent reflections	182 ($R_{\text{int}} = 0.0389$)	
Completeness to $\theta = 28.29^\circ$	91.5 %	
Absorption correction	Semi-empirical from equivalents	
Refinement method	Full-matrix least-squares on F^2	
Data / restraints / parameters	182 / 0 / 19	
Goodness-of-fit on F^2	1.146	
Final R indices [$I > 2\sigma(I)$]	$R_1 = 0.0206$	$wR_2 = 0.0508$
R indices (all data)	$R_1 = 0.0212$	$wR_2 = 0.0512$
Largest diff. peak and hole	$0.519 \text{ e}\text{\AA}^{-3}$	$-0.585 \text{ e}\text{\AA}^{-3}$

Appendix A

Table A.3.54. Atomic coordinates [$\times 10^4$] and equivalent isotropic displacement parameters [$\text{\AA}^2 \times 10^3$] for c04072b, $\text{ZnCu}_3(\text{OH})_6\text{Cl}_2$. U_{eq} is defined as one third of the trace of the orthogonalized U_{ij} tensor.

	x	y	Z	U_{eq}
Cu(1)	1667	8333	3333	8(1)
Zn(2)	3333	6667	1667	8(1)
Cl(1)	3333	6667	4720(1)	10(1)
O(1)	2546(4)	11273(2)	3946(2)	9(1)

Table A.3.55. Bond lengths [\AA] for c04072b, $\text{ZnCu}_3(\text{OH})_6\text{Cl}_2$.

Cu(1)-O(1) ^a	1.9835(11)	Zn(2)-O(1) ^g	2.114(2)
Cu(1)-O(1)	1.9835(11)	Zn(2)-O(1) ^h	2.114(2)
Cu(1)-O(1) ^b	1.9835(11)	Zn(2)-Cu(1) ^g	3.0639(4)
Cu(1)-O(1) ^c	1.9835(11)	Zn(2)-Cu(1) ^f	3.0639(4)
Cu(1)-Zn(2)	3.0639(4)	Zn(2)-Cu(1) ^h	3.0639(4)
Cu(1)-Zn(2) ^d	3.0639(4)	Zn(2)-Cu(1) ⁱ	3.0639(4)
Zn(2)-O(1) ^c	2.114(2)	Zn(2)-Cu(1) ^j	3.0639(4)
Zn(2)-O(1) ^b	2.114(2)	O(1)-Cu(1) ^k	1.9835(11)
Zn(2)-O(1) ^e	2.114(2)	O(1)-Zn(2) ^d	2.114(2)
Zn(2)-O(1) ^f	2.114(2)		

Symmetry transformations used to generate equivalent atoms:

$$^a -x + y - 1, -x + 1, -z$$

$$^c x - y + 4/3, x + 2/3, -z + 2/3$$

$$^e y - 2/3, -x + y - 1/3, -z + 2/3$$

$$^g -x + y - 2/3, -x + 2/3, z - 1/3$$

$$^i -x + y, -x + 1, z$$

$$^k -y + 1, x - y + 2, z$$

$$^b -x + 1/3, -y + 5/3, -z + 2/3$$

$$^d x - 1/3, y + 1/3, z + 1/3$$

$$^f -y + 4/3, x - y + 5/3, z - 1/3$$

$$^h x + 1/3, y - 1/3, z - 1/3$$

$$^j -y + 1, x - y + 1, z$$

Table A.3.56. Bond angles [°] for c04072b, ZnCu₃(OH)₆Cl₂.

O(1) ^a -Cu(1)-O(1)	82.32(13)	Cu(1)-Zn(2)-Cu(1) ^g	112.180(10)
O(1) ^a -Cu(1)-O(1) ^b	97.68(13)	O(1) ^c -Zn(2)-Cu(1) ^f	94.41(6)
O(1)-Cu(1)-O(1) ^b	180.0	O(1) ^b -Zn(2)-Cu(1) ^f	139.99(3)
O(1) ^a -Cu(1)-O(1) ^c	180.0	O(1) ^e -Zn(2)-Cu(1) ^f	139.99(3)
O(1)-Cu(1)-O(1) ^c	97.68(13)	O(1) ^f -Zn(2)-Cu(1) ^f	40.01(3)
O(1) ^b -Cu(1)-O(1) ^c	82.32(13)	O(1) ^g -Zn(2)-Cu(1) ^f	85.59(6)
O(1) ^a -Cu(1)-Zn(2)	136.75(6)	O(1) ^h -Zn(2)-Cu(1) ^f	40.01(3)
O(1)-Cu(1)-Zn(2)	136.74(6)	Cu(1)-Zn(2)-Cu(1) ^f	112.180(10)
O(1) ^b -Cu(1)-Zn(2)	43.25(6)	Cu(1) ^g -Zn(2)-Cu(1) ^f	67.820(10)
O(1) ^c -Cu(1)-Zn(2)	43.25(6)	O(1) ^c -Zn(2)-Cu(1) ^h	139.99(3)
O(1) ^a -Cu(1)-Zn(2) ^d	43.25(6)	O(1) ^b -Zn(2)-Cu(1) ^h	139.99(3)
O(1)-Cu(1)-Zn(2) ^d	43.26(6)	O(1) ^e -Zn(2)-Cu(1) ^h	94.41(6)
O(1) ^b -Cu(1)-Zn(2) ^d	136.75(6)	O(1) ^f -Zn(2)-Cu(1) ^h	85.58(6)
O(1) ^c -Cu(1)-Zn(2) ^d	136.75(6)	O(1) ^g -Zn(2)-Cu(1) ^h	40.01(3)
Zn(2)-Cu(1)-Zn(2) ^d	180.0	O(1) ^h -Zn(2)-Cu(1) ^h	40.01(3)
O(1) ^c -Zn(2)-O(1) ^b	76.27(9)	Cu(1)-Zn(2)-Cu(1) ^h	180.0
O(1) ^c -Zn(2)-O(1) ^e	76.27(9)	Cu(1) ^g -Zn(2)-Cu(1) ^h	67.820(11)
O(1) ^b -Zn(2)-O(1) ^e	76.27(9)	Cu(1) ^f -Zn(2)-Cu(1) ^h	67.820(10)
O(1) ^c -Zn(2)-O(1) ^f	103.74(9)	O(1) ^c -Zn(2)-Cu(1) ⁱ	40.01(3)
O(1) ^b -Zn(2)-O(1) ^f	103.74(9)	O(1) ^b -Zn(2)-Cu(1) ⁱ	85.59(6)
O(1) ^e -Zn(2)-O(1) ^f	180.0	O(1) ^e -Zn(2)-Cu(1) ⁱ	40.01(3)
O(1) ^c -Zn(2)-O(1) ^g	180.0	O(1) ^f -Zn(2)-Cu(1) ⁱ	139.99(3)
O(1) ^b -Zn(2)-O(1) ^g	103.74(9)	O(1) ^g -Zn(2)-Cu(1) ⁱ	139.99(3)
O(1) ^e -Zn(2)-O(1) ^g	103.73(9)	O(1) ^h -Zn(2)-Cu(1) ⁱ	94.42(6)
O(1) ^f -Zn(2)-O(1) ^g	76.26(9)	Cu(1)-Zn(2)-Cu(1) ⁱ	67.819(10)
O(1) ^c -Zn(2)-O(1) ^h	103.74(9)	Cu(1) ^g -Zn(2)-Cu(1) ⁱ	180.0
O(1) ^b -Zn(2)-O(1) ^h	180.0	Cu(1) ^f -Zn(2)-Cu(1) ⁱ	112.180(10)
O(1) ^e -Zn(2)-O(1) ^h	103.73(9)	Cu(1) ^h -Zn(2)-Cu(1) ⁱ	112.181(10)
O(1) ^f -Zn(2)-O(1) ^h	76.26(9)	O(1) ^c -Zn(2)-Cu(1) ^j	85.59(6)
O(1) ^g -Zn(2)-O(1) ^h	76.26(9)	O(1) ^b -Zn(2)-Cu(1) ^j	40.01(3)
O(1) ^c -Zn(2)-Cu(1)	40.01(3)	O(1) ^e -Zn(2)-Cu(1) ^j	40.01(3)
O(1) ^b -Zn(2)-Cu(1)	40.01(3)	O(1) ^f -Zn(2)-Cu(1) ^j	139.99(3)
O(1) ^e -Zn(2)-Cu(1)	85.59(6)	O(1) ^g -Zn(2)-Cu(1) ^j	94.42(6)
O(1) ^f -Zn(2)-Cu(1)	94.42(6)	O(1) ^h -Zn(2)-Cu(1) ^j	139.99(3)

Appendix A

O(1) ^g -Zn(2)-Cu(1)	139.99(3)	Cu(1)-Zn(2)-Cu(1) ^j	67.819(10)
O(1) ^h -Zn(2)-Cu(1)	139.99(3)	Cu(1) ^g -Zn(2)-Cu(1) ^j	112.180(10)
O(1) ^c -Zn(2)-Cu(1) ^g	139.99(3)	Cu(1) ^f -Zn(2)-Cu(1) ^j	180.0
O(1) ^b -Zn(2)-Cu(1) ^g	94.41(6)	Cu(1) ^h -Zn(2)-Cu(1) ^j	112.181(10)
O(1) ^e -Zn(2)-Cu(1) ^g	139.99(3)	Cu(1) ⁱ -Zn(2)-Cu(1) ^j	67.820(10)
O(1) ^f -Zn(2)-Cu(1) ^g	40.01(3)	Cu(1)-O(1)-Cu(1) ^k	119.04(11)
O(1) ^g -Zn(2)-Cu(1) ^g	40.01(3)	Cu(1)-O(1)-Zn(2) ^d	96.74(7)
O(1) ^h -Zn(2)-Cu(1) ^g	85.59(6)	Cu(1) ^k -O(1)-Zn(2) ^d	96.74(7)

Symmetry transformations used to generate equivalent atoms:

$$^a -x + y - 1, -x + 1, -z$$

$$^c x - y + 4/3, x + 2/3, -z + 2/3$$

$$^e y - 2/3, -x + y - 1/3, -z + 2/3$$

$$^g -x + y - 2/3, -x + 2/3, z - 1/3$$

$$^i -x + y, -x + 1, z$$

$$^k -y + 1, x - y + 2, z$$

$$^b -x + 1/3, -y + 5/3, -z + 2/3$$

$$^d x - 1/3, y + 1/3, z + 1/3$$

$$^f -y + 4/3, x - y + 5/3, z - 1/3$$

$$^h x + 1/3, y - 1/3, z - 1/3$$

$$^j -y + 1, x - y + 1, z$$

Appendix A

Table A.3.57. Anisotropic displacement parameters [$\text{\AA}^2 \times 10^3$] for c04072b, $\text{ZnCu}_3(\text{OH})_6\text{Cl}_2$. The anisotropic displacement factor exponent takes the form: $-2\pi^2[(ha^*)^2U_{11} + \dots + 2hka^*b^*U_{12}]$.

	U_{11}	U_{22}	U_{33}	U_{23}	U_{13}	U_{12}
Cu(1)	7(1)	7(1)	8(1)	-1(1)	1(1)	4(1)
Zn(2)	9(1)	9(1)	6(1)	0	0	4(1)
Cl(1)	11(1)	11(1)	9(1)	0	0	6(1)
O(1)	8(1)	9(1)	10(1)	0(1)	-1(1)	4(1)

Table A.3.58. Hydrogen coordinates [$\times 10^4$] and isotropic displacement parameters [$\text{\AA}^2 \times 10^3$] for c04072b, $\text{ZnCu}_3(\text{OH})_6\text{Cl}_2$.

	x	Y	z	U_{eq}
H(1)	3780(110)	11890(50)	4230(40)	50(18)

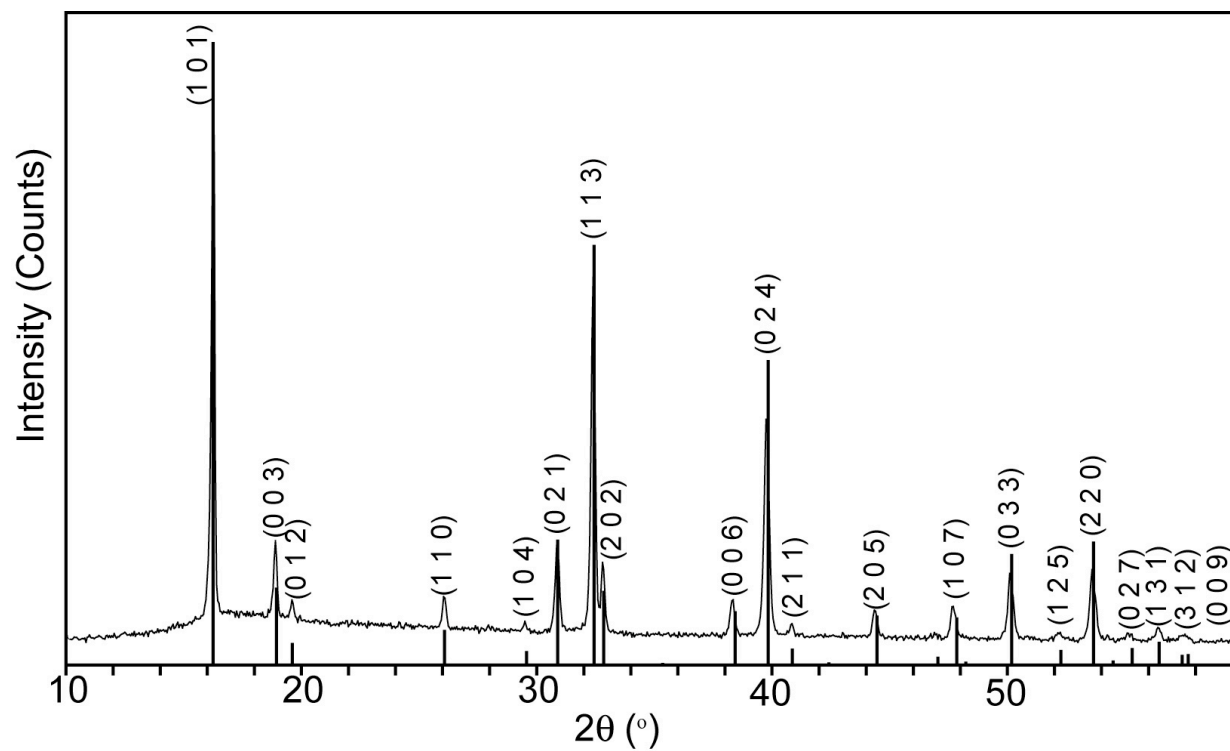


Figure A.3.8. pXRD of herbertsmithite powder sample, matched and indexed to PDF # 01-087-0679.

Appendix A

Table A.3.59. Bragg reflections and Miller indices of pXRD pattern for herbertsmithite, syn. matched to PDF # 01-87-0679.

$2\theta_{\text{obs}}$	d_{obs}	% I_{obs}	$2\theta_{\text{calcd}}$	d_{calcd}	% I_{calcd}	Δd	hkl
16.250	5.4503	100.0	16.254	5.4490	100.0	0.0013	1 0 1
18.900	4.6917	13.1	18.946	4.6803	12.2	0.0114	0 0 3
19.607	4.5239	3.0	19.614	4.5223	3.3	0.0016	0 1 2
26.068	3.4155	5.4	26.084	3.4135	5.4	0.0020	1 1 0
29.498	3.0256	1.7	29.571	3.0184	2.0	0.0072	1 0 4
30.864	2.8948	14.8	30.886	2.8928	19.9	0.0020	0 2 1
32.400	2.7610	61.5	32.437	2.7579	67.4	0.0031	1 1 3
32.809	2.7275	11.8	32.846	2.7245	11.7	0.0030	2 0 2
38.334	2.3462	6.0	38.436	2.3402	8.4	0.0060	0 0 6
39.760	2.2652	37.4	39.835	2.2612	48.8	0.0040	0 2 4
40.845	2.2075	1.8	40.857	2.2069	2.4	0.0006	2 1 1
44.359	2.0404	4.6	44.461	2.0360	7.7	0.0044	2 0 5
47.699	1.9051	5.5	47.848	1.8995	7.4	0.0056	1 0 7
50.112	1.8189	11.3	50.187	1.8163	17.6	0.0026	0 3 3
52.232	1.7499	1.3	52.275	1.7486	2.2	0.0013	1 2 5
53.605	1.7083	12.3	53.657	1.7068	19.6	0.0015	2 2 0
55.116	1.6650	1.3	55.301	1.6598	2.5	0.0052	0 2 7
56.407	1.6299	2.2	56.451	1.6287	3.5	0.0012	1 3 1
57.547	1.6003	1.2	57.422	1.6035	1.4	-0.0032	2 2 3

Appendix A

Table A.3.60. Bragg reflections and Miller indices of pXRD pattern for herbertsmithite, syn. matched to PDF # 00-57-0595. Pattern calculated on Braithwaite *et al.* single-crystal structure, Chapter 4, Ref. [20].

$2\theta_{\text{obs}}$	d_{obs}	% I_{obs}	$2\theta_{\text{calcd}}$	d_{calcd}	% I_{calcd}	Δd	hkl
16.250	5.4503	100.0	16.243	5.4490	55.0	0.0013	1 0 1
18.900	4.6917	13.1	18.898	4.6803	14.0	0.0114	0 0 3
19.607	4.5239	3.0	19.590	4.5223	3.0	0.0016	0 1 2
26.068	3.4155	5.4	26.050	3.4135	5.0	0.0020	1 1 0
29.498	3.0256	1.7	29.515	3.0184	1.0	0.0072	1 0 4
30.864	2.8948	14.8	30.858	2.8928	11.0	0.0020	0 2 1
32.400	2.7610	61.5	32.404	2.7579	100.0	0.0031	1 1 3
32.809	2.7275	11.8	32.818	2.7245	13.0	0.0030	2 0 2
38.334	2.3462	6.0	38.377	2.3402	4.0	0.0060	0 0 6
39.760	2.2652	37.4	39.786	2.2612	36.0	0.0040	0 2 4
40.845	2.2075	1.8	40.837	2.2069	2.0	0.0006	2 1 1
44.359	2.0404	4.6	44.410	2.0360	4.0	0.0044	2 0 5
47.699	1.9051	5.5	47.741	1.8995	5.0	0.0056	1 0 7
50.112	1.8189	11.3	50.119	1.8163	13.0	0.0026	3 0 3
52.232	1.7499	1.3	52.205	1.7486	1.0	0.0013	1 2 5
53.605	1.7083	12.3	53.621	1.7068	18.0	0.0015	2 2 0
55.116	1.6650	1.3	55.191	1.6598	1.0	0.0052	0 2 7
56.407	1.6299	2.2	56.405	1.6287	3.0	0.0012	1 3 1
57.547	1.6003	1.2	57.638	1.6035	1.0	-0.0032	3 1 2

Appendix B.
Thermal and Spectroscopic Characterization of Compounds

Appendix B.1

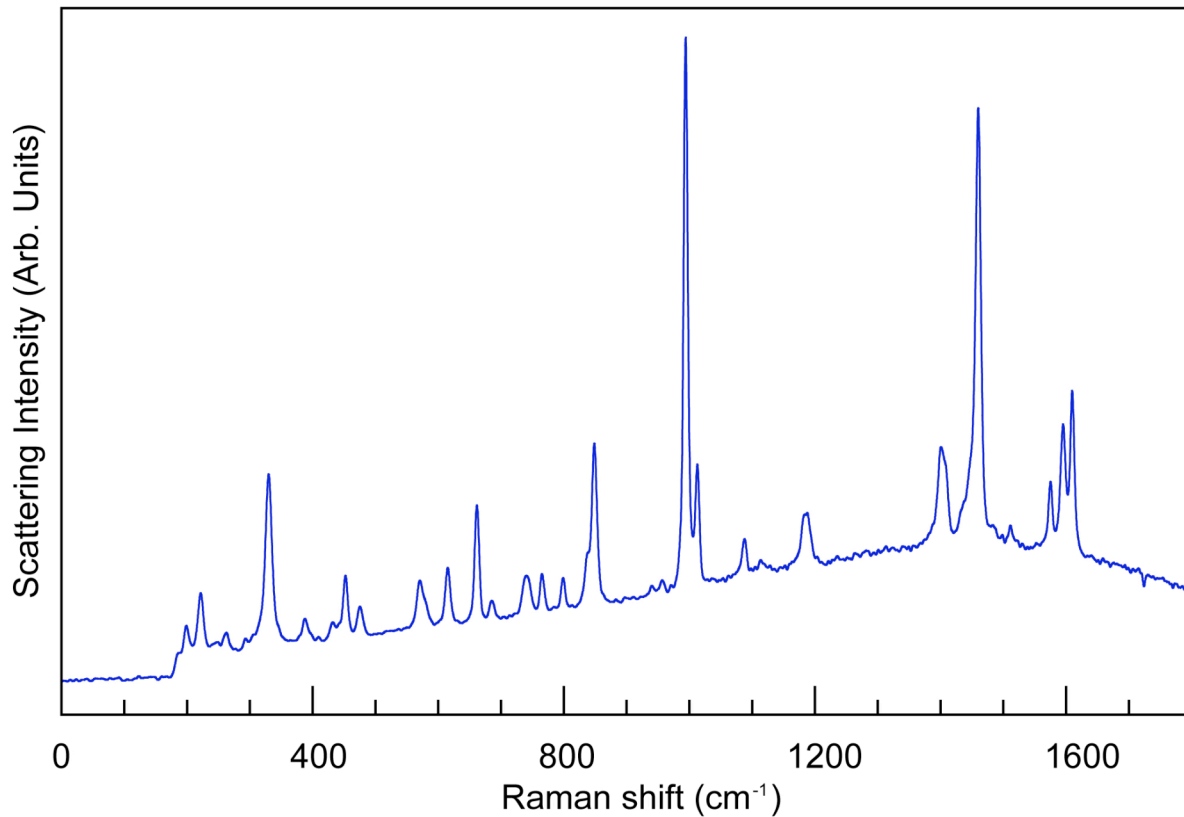


Figure B.1.1. Raman spectrum of $\text{Cu}(1,3\text{-bdc})\cdot 0.11\text{H}_2\text{O}$. Data: 172.3 (sh), 199.6, 222.2, 302.4(sh), 329.4, 388.9, 432.9(sh), 452.2, 475.6, 570.9, 615.7, 662.5, 686.4, 741.4, 765.8, 799.5, 816.9(sh), 848.8, 941.4(vw), 955.8(vw), 994.8, 1012.1, 1087.9, 1113.3(vw), 1184.8, 1401.3, 1444.5(sh), 1459.3, 1493.4, 1511.4, 1575.1, 1594.3, 1609.2. sh = shoulder, v = very, w = weak.

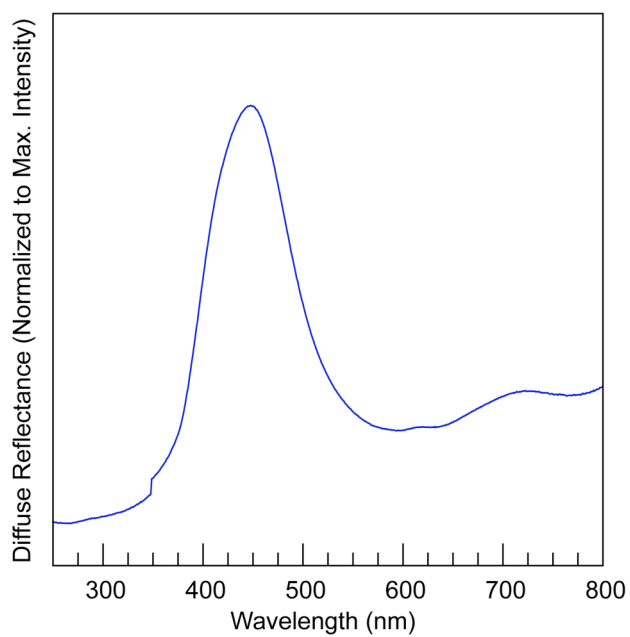


Figure B.1.2. Diffuse reflectance UV-vis spectrum of Cu(1,3-bdc)•0.11H₂O. The compound shows a maximum reflectance at 449 nm with weaker maxima at 613 and 718 nm.

Appendix B.2

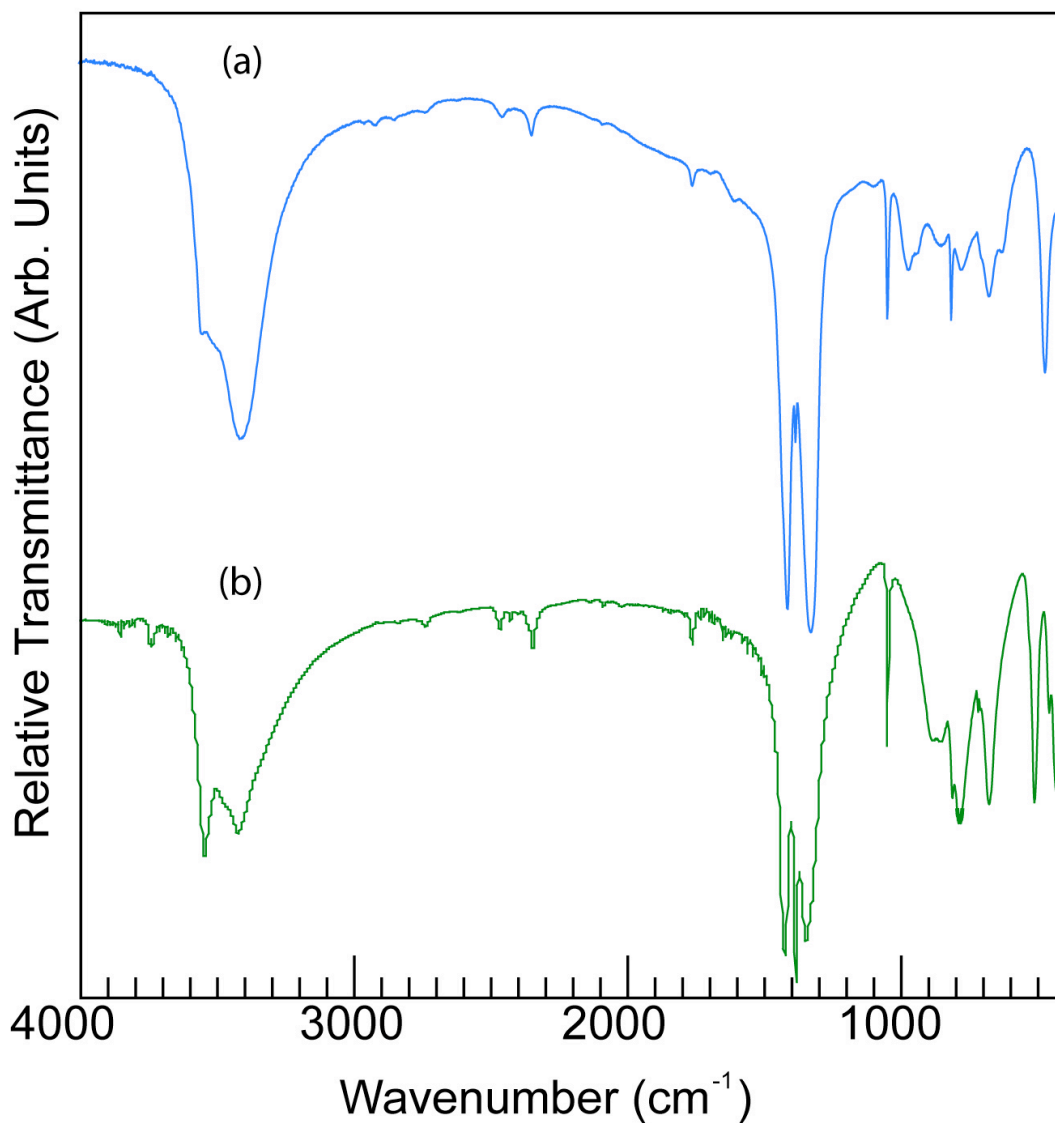


Figure B.2.1. FTIR of samples of (a) $\text{CdCu}_3(\text{OH})_6(\text{NO}_3)_2 \cdot 0.5\text{H}_2\text{O}$ and (b) rouaite. Data for (a): 3543(sh, O–H stretch), 3417(i, br, O–H stretch), 2459(w), 2351(w), 1763(w), 1610(br, w, δ H–O–H), 1413(i), 1384(s, w), 1329(i), 1049(s), 972(w), 945(w), 876(w), 816(s), 779(w), 679(w), 640(w, sh), 472(i). (b): 3743(w), 3545(i, br, O–H stretch), 3421(i, br, O–H stretch), 2464(w), 2426(w), 2343(w), 1763(w), 1421(i), 1384(s, i), 1346(i), 1047(s), 883(w), 852(w), 810(w, sh), 785(i), 717(w, sh), 677(i), 511(i, s), 457(w, sh), 428(i). s = sharp, i = intense, w = weak, sh = shoulder. The data agree with those reported in the literature for these compounds.^{1,2}

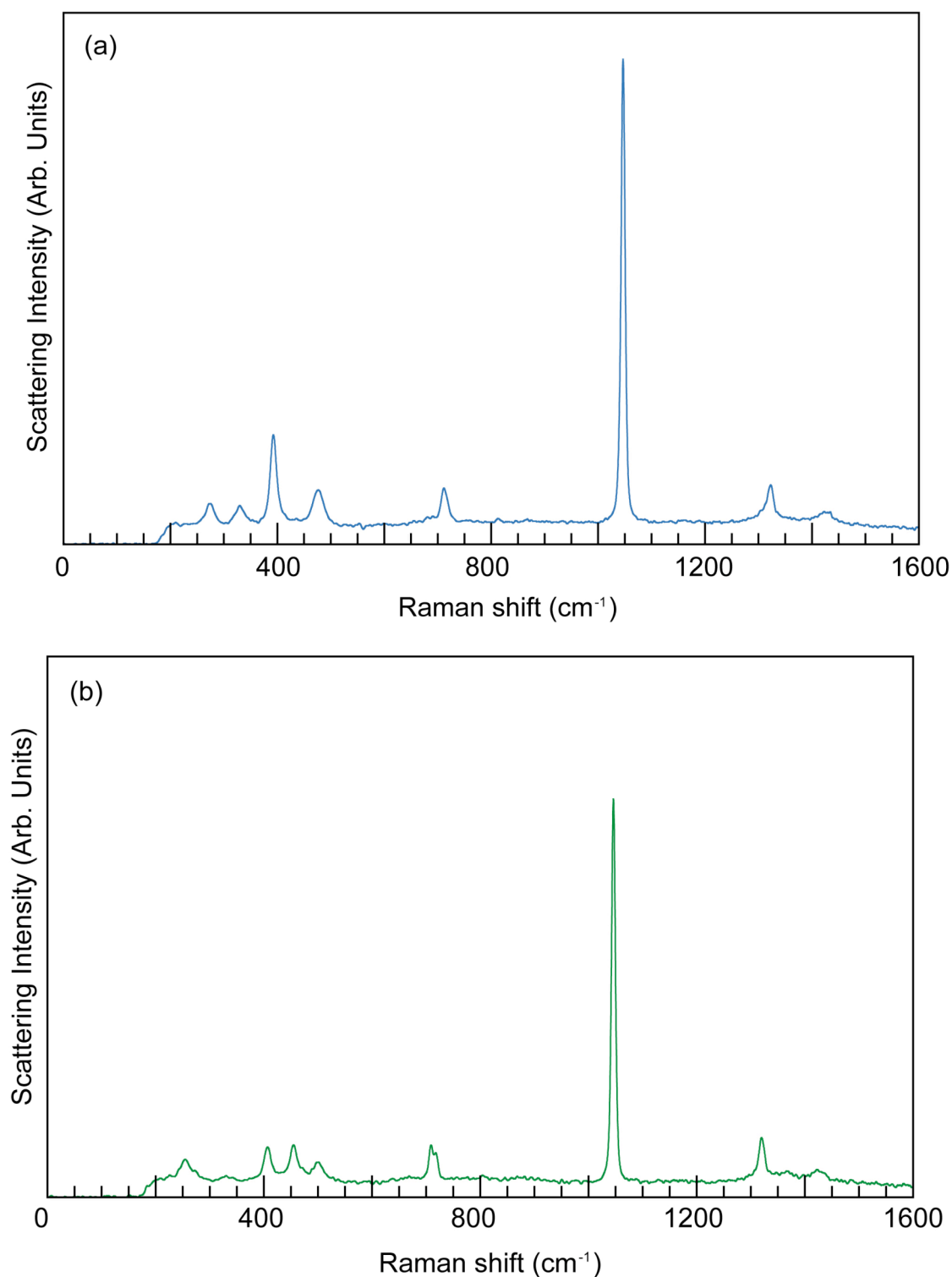


Figure B.2.2. Raman spectra of samples of (a) $\text{CdCu}_3(\text{OH})_6(\text{NO}_3)_2 \cdot 0.5\text{H}_2\text{O}$ and (b) rouaite. Data for (a): 275.2, 330.9, 393.6, 476.9, 713.5, 1047.2(i), 1321.6, 1427.5. (b) 255.3, 331.2, 407.7, 456.0, 500.5, 713.7, 1046.7(i), 1320.7, 1423.2. i = intense.

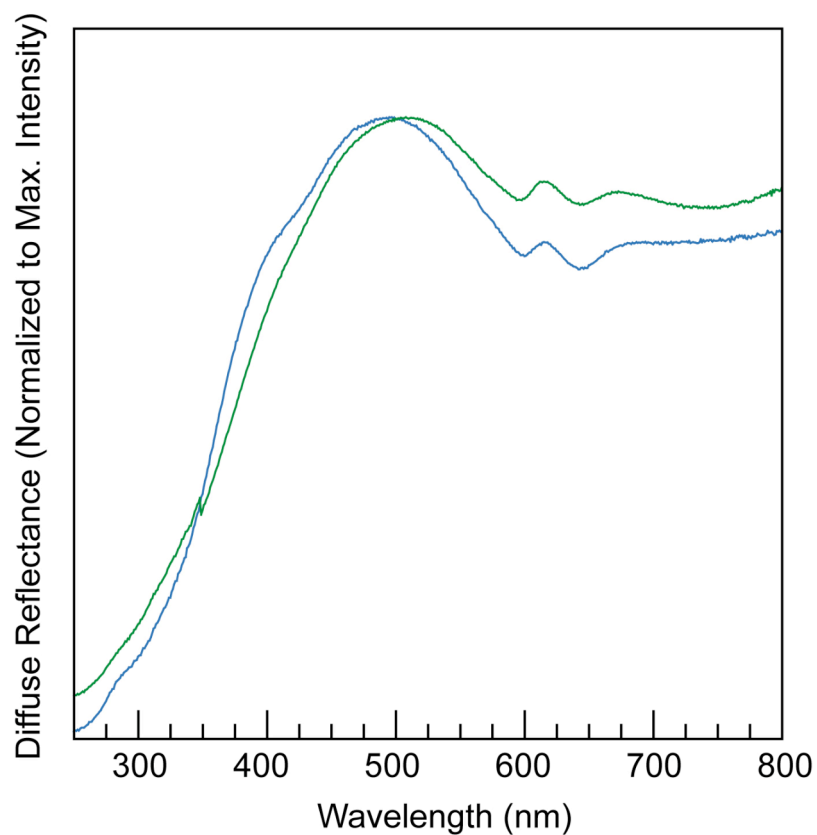


Figure B.2.3. Normalized diffuse reflectance UV-vis spectra of $\text{CdCu}_3(\text{OH})_6(\text{NO}_3)_2 \cdot 0.5\text{H}_2\text{O}$ (pale blue) and rouaite (pale green). Data were normalized on the maximum intensity of reflectance for each. The title compound has a maximum reflectance at 497, with weaker maxima at 615 and 687, and a shoulder at 410 nm. Rouaite has a maximum reflectance at 508, with weaker maxima at 615 and 673 nm. $\text{CdCu}_3(\text{OH})_6(\text{NO}_3)_2 \cdot 0.5\text{H}_2\text{O}$ is a pale blue powder, and rouaite is a pale green powder.

Appendix B.3

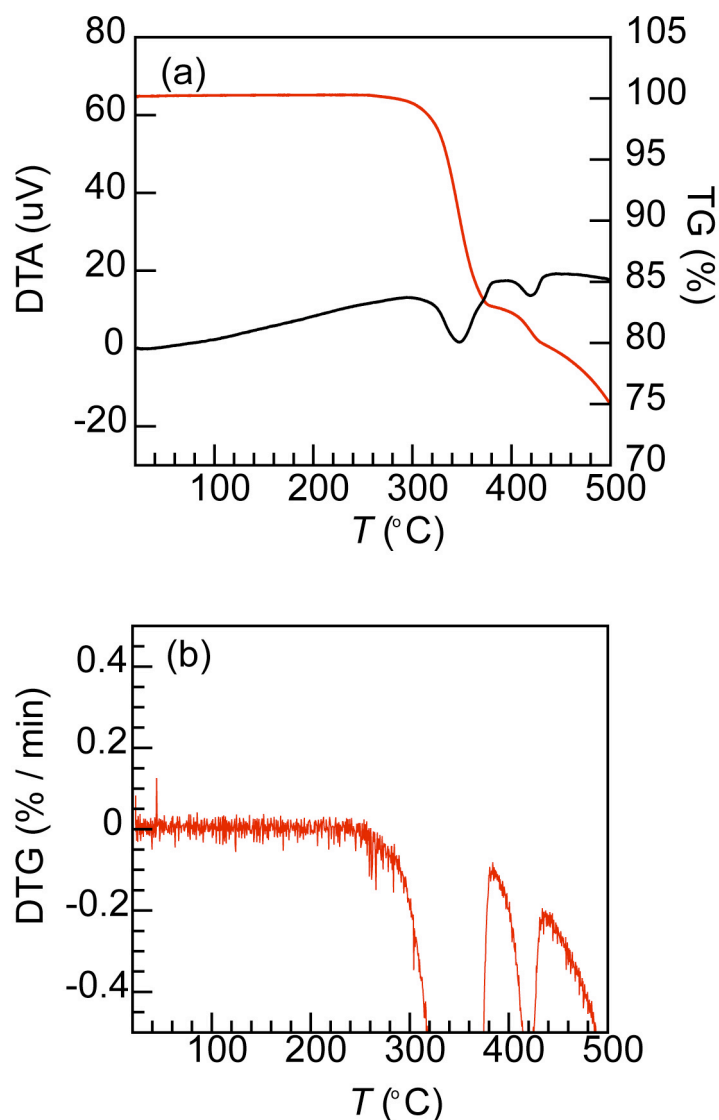


Figure B.3.1. (a) TGDTA of claringbulite. The compound loses 13.9% of its mass between 260 °C and 360 °C, leaving 86.1%. (The calculated value for loss of $3\text{H}_2\text{O}$ from $\text{Cu}_4(\text{OH})_6\text{Cl}_2$ is 87.35% and from $\text{Cu}_4(\text{OH})_6\text{ClF}$ is 86.84%.) What upon initial examination appears to be a continuous loss of mass from 260 and 390 °C, upon closer examination of the endotherm in the DTA data is actually shown to be two different events (one from 260 to 360 °C and the other from 360 to 390 °C). Further decompositions occur at 390 °C and 440 °C. (b) A differential plot shows the loss of mass more clearly.

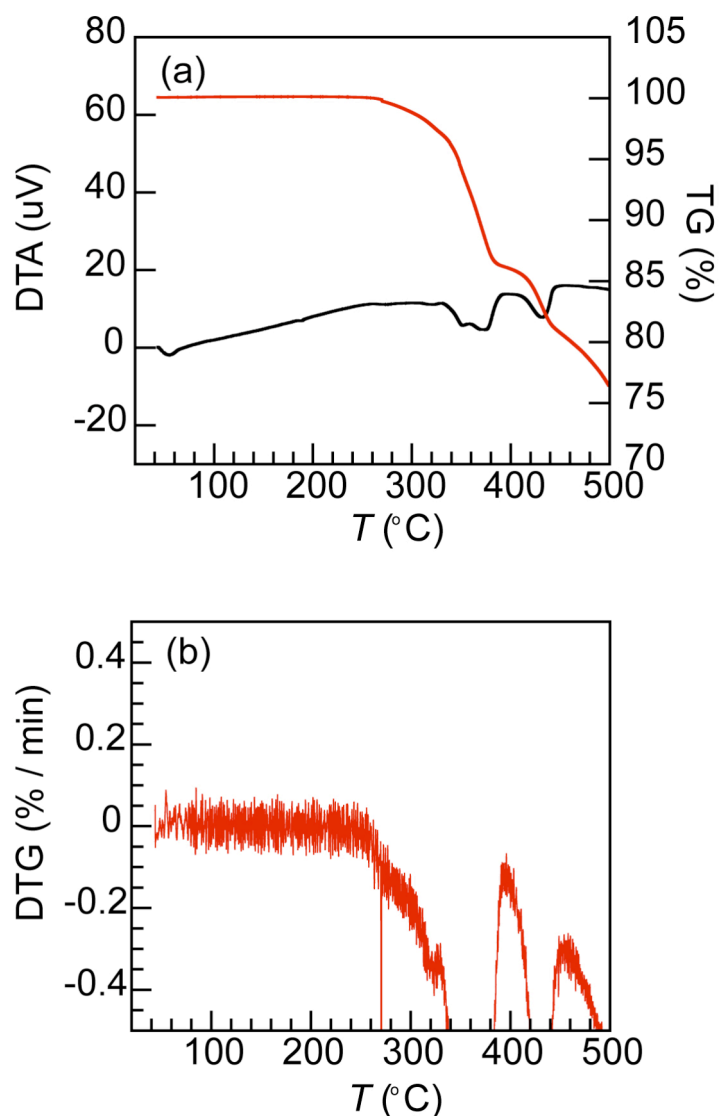


Figure B.3.2. (a) TGDTA of clinoatacamite. The compound loses 12.65% of its mass between 270 $^{\circ}\text{C}$ and 380 $^{\circ}\text{C}$, leaving 87.35% of the initial mass. (This value is theoretically expected for loss of $3\text{H}_2\text{O}$. Similarly to claringbullite, what initially appears as one loss of mass in the TGA is actually shown to be two in the DTA: one from 270 to 380 $^{\circ}\text{C}$, another from 380 to 400 $^{\circ}\text{C}$. At 400 $^{\circ}\text{C}$ another decomposition starts, and a final one starts at around 460 $^{\circ}\text{C}$. (b) A differential plot shows the loss of mass more clearly.

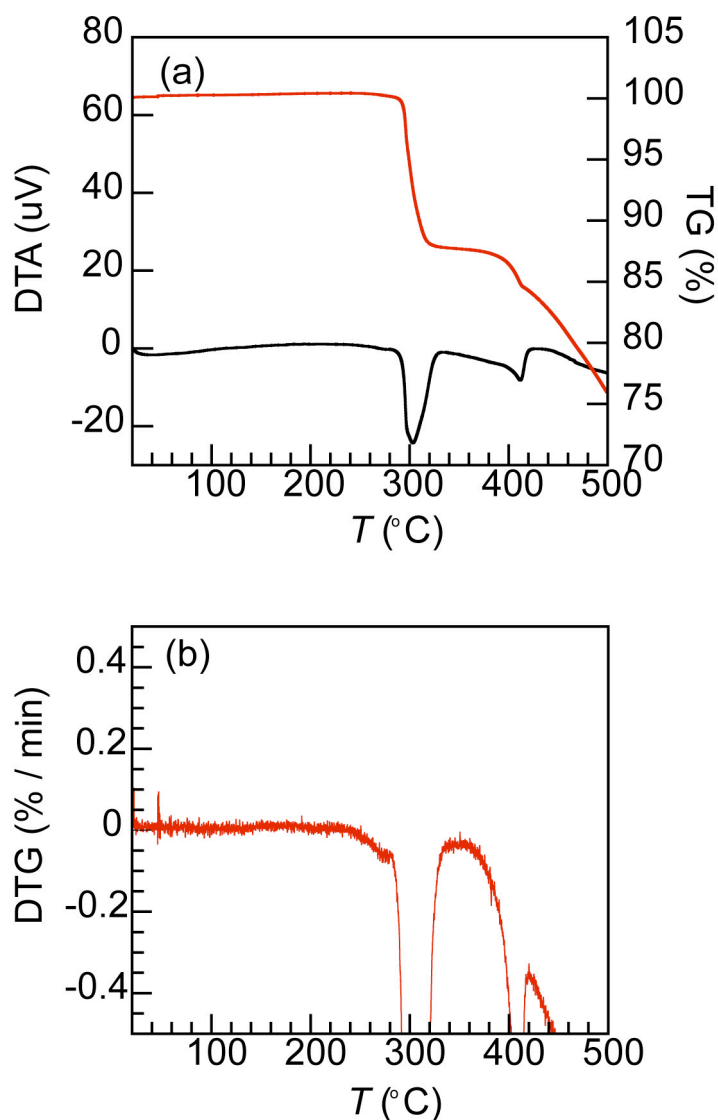


Figure B.3.3. (a) TGDTA of herbertsmithite. The compound loses 12.75% of its mass between 290 °C and 340 °C, leaving 87.25% of the initial mass. (12.6% mass loss is theoretically expected for loss of $3\text{H}_2\text{O}$.) Further mass losses occur at 375 °C and 425 °C, to leave a residue after heating to 550 °C of ZnO , CuO , CuCl , and $\text{Zn}_5(\text{OH})_8\text{Cl}_2 \cdot \text{H}_2\text{O}$ by pXRD. (b) A differential plot shows the loss of mass more clearly. Braithwaite *et al.* also performed TGA but heated the compound to higher temperatures. They report similar results with a loss of 12.5% from 300 – 340 °C, followed by gradual weight loss that is complete by 620 °C leaving 50.0 % of the original mass (Cu_2O and ZnO by pXRD.)³

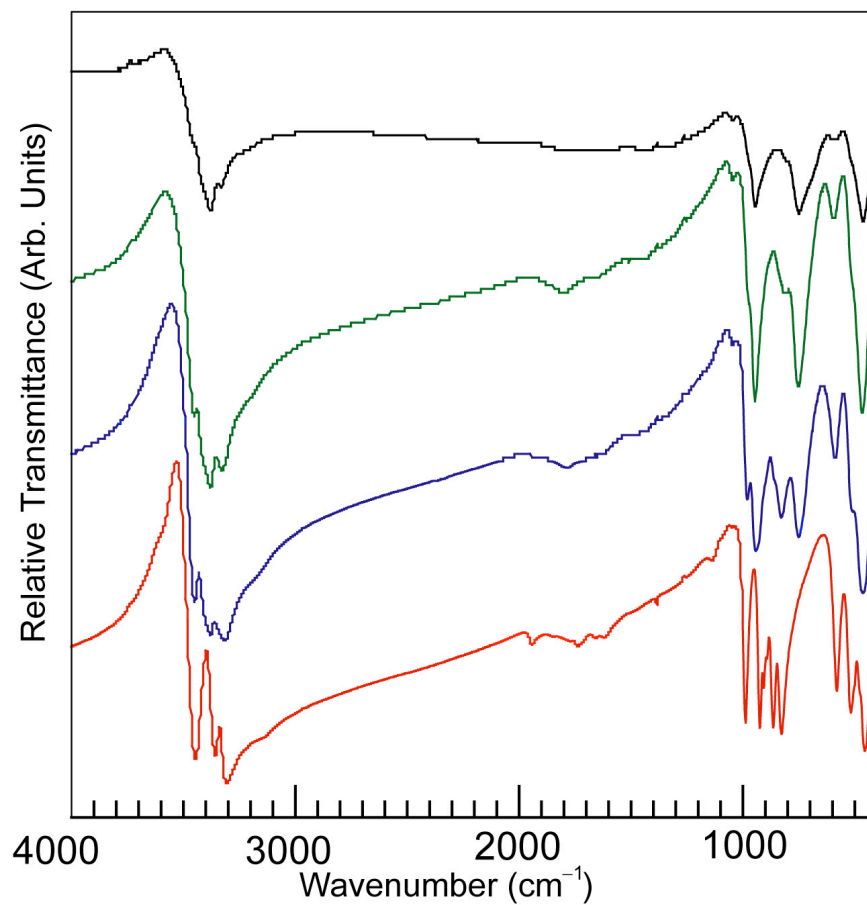


Figure B.3.4. FTIR spectra of, from top to bottom: herbertsmithite (black), Zn_{0.66}-paratacamite (green), Zn_{0.50}-paratacamite (blue), and clinoatacamite (red).

Appendix B

Table B.3.1. Frequency (in wavenumbers) of FTIR absorption maxima for (a) $\text{Cu}\{\text{Cu}_3(\text{OH})_6\}\text{Cl}_2$ (b) $\text{Zn}_{0.50}\text{Cu}_{3.50}(\text{OH})_6\text{Cl}_2$ (c) $\text{Zn}_{0.66}\text{Cu}_{3.34}(\text{OH})_6\text{Cl}_2$ and (d) $\text{ZnCu}_3(\text{OH})_6\text{Cl}_2$. Data agree with those reported by Braithwaite³ and Martens⁴ for naturally occurring samples.

a	b	c	d
3441 s	3441 s	3441 w	3451 sh
3353 s	3372 s	3372 s	3372 s
3303 s, br	3312 s, br	3322 s, br	3322 s
987 s, sp	979 w	972 w, sh	946 s
923 s, sp	941 s, br	945 s, sp	871 sh
906 w	876 w, sh	819 w	749 s
892 w	828 s	752 s	
863 s, sp	750 s		
826 s, sp			
579 s	590 s, sp	599 s	607 w
516 s	509 w, sh	540 vw, sh	464 s
474 w, sh	462 s	468 s	
454 s	407 s		
409 s			

s=strong, w= weak, sp=sharp, br=broad, sh=shoulder, v=very

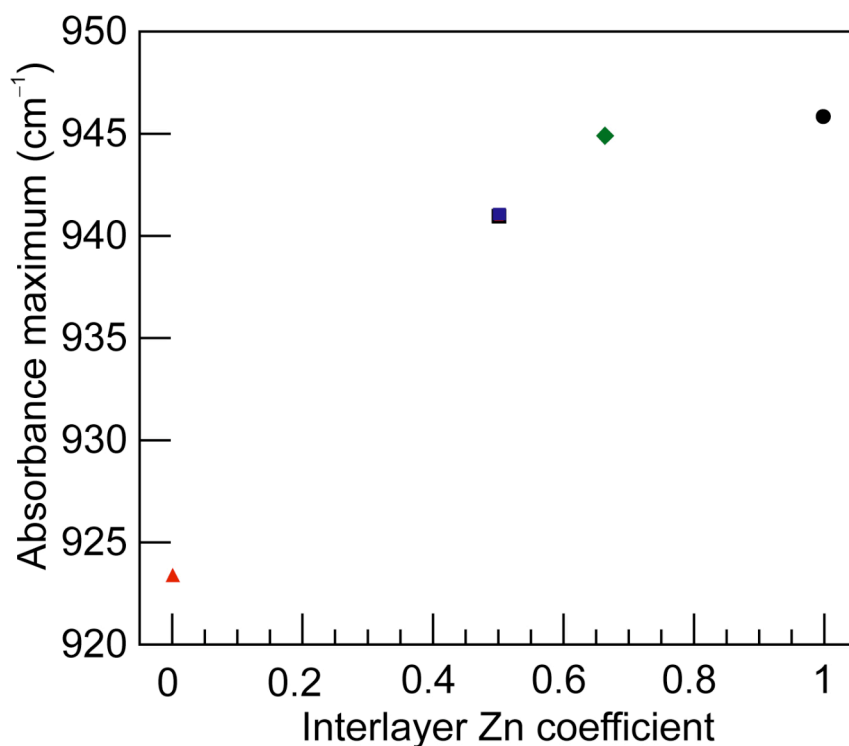


Figure B.3.5. FTIR absorbance maximum in the 930 cm⁻¹ region for synthetic samples of herbertsmithite (black ●), Zn_{0.66}-paratacamite (green ◆), Zn_{0.50}-paratacamite (blue ■), and clinoatacamite (red ▲). Braithwaite *et al.* proposed that the position of this maximum (which is probably due to an in-plane M–OH deformation) can be used to assess the approximate composition of a sample in the paratacamite series.³ The change, however, is very subtle near the herbertsmithite end member, and therefore this method is only very useful near the clinoatacamite-paratacamite phase boundary.

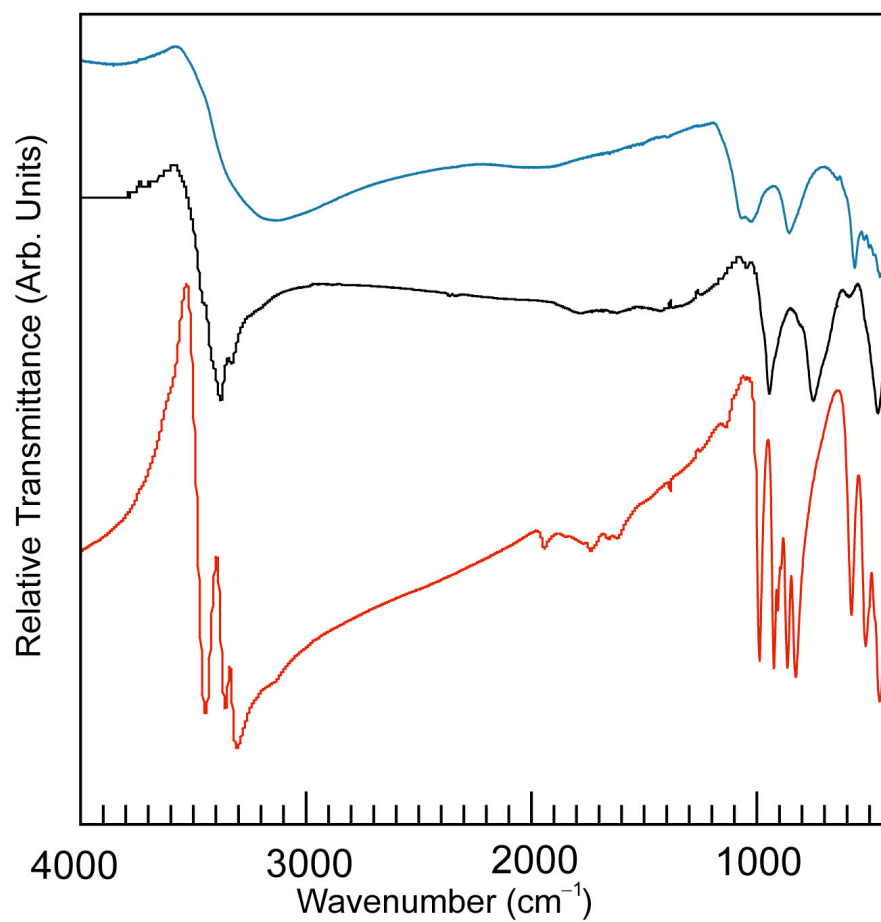


Figure B.3.6. FTIR spectra of, from top to bottom: claringbullite (blue), herbertsmithite (black), and clinoatacamite (red). Peak listing for claringbullite: 3133 br; 1067 sh; 1022; 855 s; 642 vw, sh; 565 s; 523 vw; 500 vw; 480 vw, sh; 453; 444 cm⁻¹ sh. . s = sharp, br = broad, w = weak, v = very sh = shoulder.

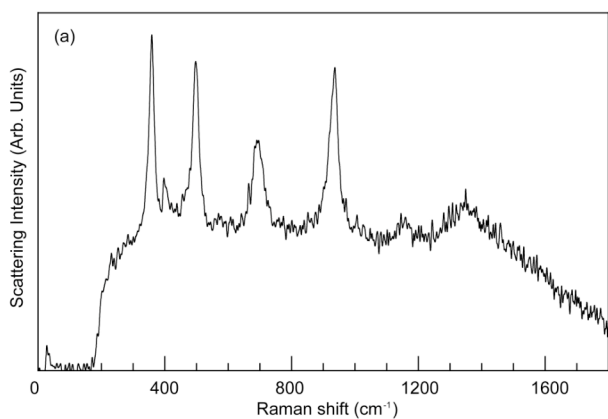
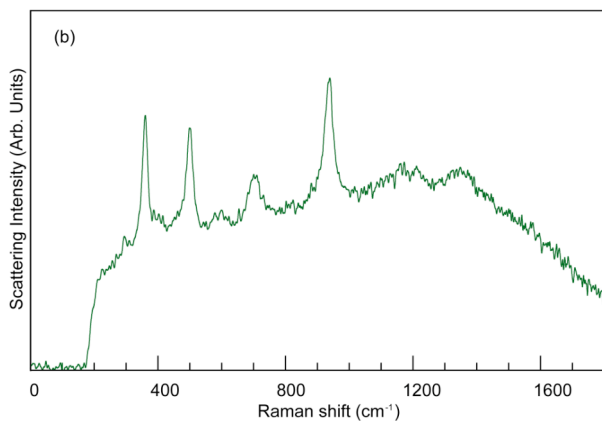
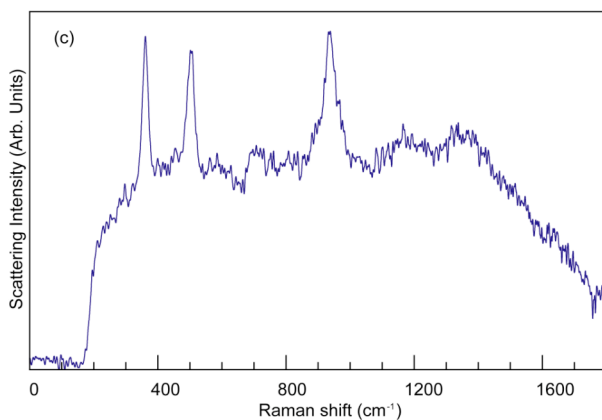


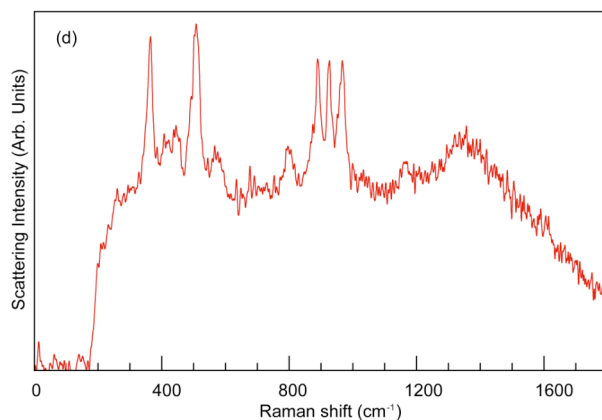
Figure B.3.7. Raman spectra for copper hydroxychloride minerals. Data are in agreement with those reported for naturally occurring samples.³⁻⁵ Data for (a), herbertsmithite: 360, 398, 498; 691, 937, 1146; 1350 cm^{-1} .



(b), $\text{Zn}_{0.66}$ -paratacamite: 296, 361, 388, 500, 600; 701, 825, 940, 1173, 1212, 1349 cm^{-1} .



(c), $\text{Zn}_{0.50}$ -paratacamite: 298, 362, 400, 455, 502, 585, 708, 762, 869, 939, 1166, 1338 cm^{-1} .



(d), clinoatacamite: 261, 365, 408, 446, 509, 567, 678, 797, 875, 890, 927, 968, 1167, 1357 cm^{-1} .

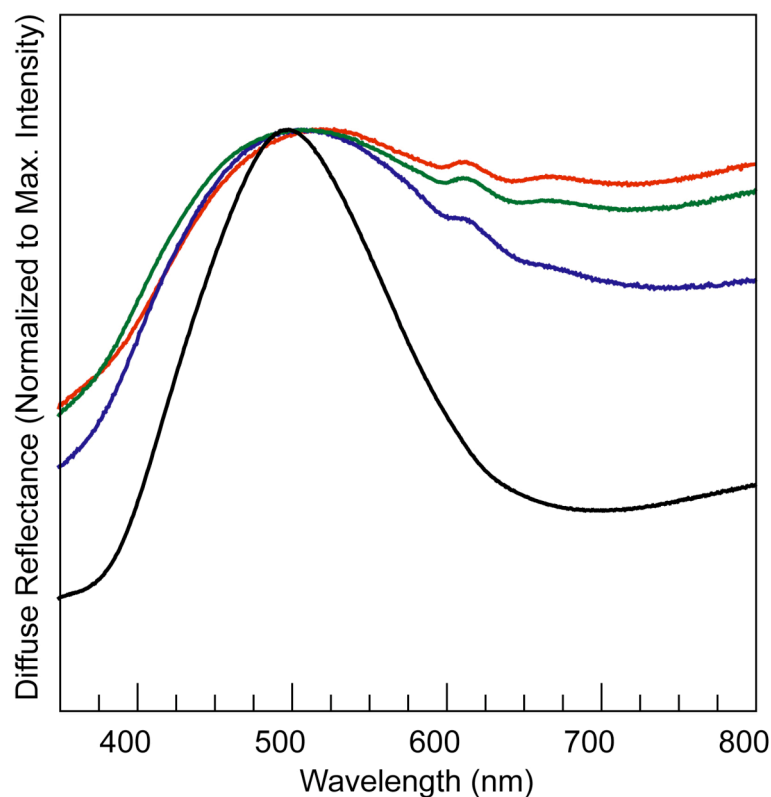


Figure B.3.8. Normalized Diffuse Reflectance UV-vis Spectra of herbertsmithite (black, bottom), $Zn_{0.66}$ -paratacamite (green, second from top), $Zn_{0.50}$ -paratacamite (blue, second from bottom), and clinoatacamite (red, top). Max. intensities for herbertsmithite: 499 nm. $Zn_{0.66}$ -paratacamite: 508, 611, 662 nm. $Zn_{0.50}$ -paratacamite: 507, 612, 667 nm. Clinoatacamite: 528, 613, 665 nm. We observe, like Jambor *et al.*, that the color of the compounds shifts from green to blue-green with increasing zinc substitution.⁶ Qualitatively, the peak at around 500 nm generally follows this trend (though $Zn_{0.50}$ and $Zn_{0.66}$ do not follow it monotonically), with herbertsmithite showing maximum intensity at the shortest wavelength of any of the compounds. Herbertsmithite shows no additional bands at longer wavelengths, unlike the other compounds.

References

1. Oswald, H. R. *Helv. Chim. Acta* **1969**, *52*, 2369-2380.
2. Newman, S. P.; Jones, W. J. *Solid State Chem.* **1999**, *148*, 26-40.
3. Braithwaite, R. S. W.; Mereiter, K.; Paar, W. H.; Clark, A. M. *Mineral. Mag.* **2004**, *68*, 527-539.
4. Martens, W.; Frost, R. L.; Williams, P. A. *Neues Jahrb. Mineral., Abh.* **2003**, *178*, 197-215.
5. Frost, R. L. *Spectrochim. Acta, Part A* **2003**, *59A*, 1195-1204.
6. Jambor, J. L.; Dutrizac, J. E.; Roberts, A. C.; Grice, J. D.; Szymanski, J. T. *Can. Mineral.* **1996**, *34*, 61-72.

EDUCATION

Massachusetts Institute of Technology Cambridge, MA
Ph.D. in Inorganic Chemistry, September 2008 2003–2008
Thesis: "Synthesis, Structure, and Magnetic Properties of Spin- $\frac{1}{2}$ Kagomé Antiferromagnets"
Advisor: Professor Daniel G. Nocera

Dartmouth College Hanover, NH
A.B. Chemistry with Honors, 2001 · *magna cum laude* · GPA: 3.78/4.00 1997–2001
Thesis: "Synthesis of Bis-dimesitylphosphineplatinum(II) Complexes"
Advisor: Professor David S. Glueck

AWARDS AND AFFILIATIONS

National Science Foundation Graduate Research Fellowship (2004–2007), MIT Presidential Graduate Fellowship (2003), American Chemical Society, Phi Beta Kappa Society

RESEARCH EXPERIENCE

Massachusetts Institute of Technology Cambridge, MA
Graduate Research Assistant 2003–present

- Developed the first pure structurally perfect materials for magnetic studies of spin frustration on $S = \frac{1}{2}$ kagomé (triangle-based) lattices.
- Optimized formation of a series of copper(II) minerals using hydrothermal synthesis.
- Discovered a novel coordination polymer of copper(II).
- Characterized systems through structural studies and magnetometry measurements.
- Collaborated with condensed matter physicists in the U.S., Canada, and Israel to publish neutron scattering, muon scattering, and NMR measurements.

Beth Israel Deaconess Medical Center, Harvard Medical School Boston, MA
Research Assistant 2001–2002
Principal Investigator: Dr. Sam W. Lee

- Utilized molecular biology techniques to study the synergy between tumor suppressor proteins in response to DNA damage induced by gamma-irradiation.
- Prepared cell samples for fluorescence-activated cell sorting (FACS) and isolated total RNA from cells for cDNA microarray analysis.
- Discovered that BRCA1 is involved in p53-mediated growth suppression rather than apoptosis.

Dartmouth College Hanover, NH
Undergraduate Research Assistant 2001

- Studied reactions relevant to olefin hydrophosphination catalysis.
- Synthesized and characterized platinum(II) phosphine ethyl complexes to look for β -hydrogen elimination and phosphine cleavage.
- Discovered a novel platinum(II) diphosphine complex and characterized its isomerization.

Undergraduate Research Assistant 2000
Advisor: Professor Charles L. Braun

- Measured kinetics of photo-induced electron transfer for a series of electron donors and an acceptor molecule to study the behavior of ion pairs in solution.

TEACHING EXPERIENCE

Massachusetts Institute of Technology

Cambridge, MA

Teaching Assistant

2003

- Taught recitation component of Principles of Chemical Science.
- Reviewed lecture material and problem-solving methods with students.
- Assisted professors in development of exam questions. Graded homework and exams.

The Gunnery School

Washington, CT

High School Science Teacher

2002-2003

- Developed entire classroom and laboratory curriculum for both a chemistry class and an exploratory physical science class.
- Focused on teaching students the fundamentals of the scientific method, recording and reporting data, and laboratory safety.

Dartmouth College

Hanover, NH

Chemistry Department Laboratory Teaching Assistant

1999

- Taught general chemistry students laboratory and instrumental techniques. Graded labs.

SKILLS

Experimental techniques: hydrothermal synthesis, glove box and Schlenk techniques, tissue culture, Western blotting, restriction-ligation cloning, DNA gel electrophoresis

Instrumentation: powder X-ray diffraction, SQUID magnetometry, TGDTA, FTIR, NMR (small molecules), X-band EPR, AA, some familiarity with single crystal X-ray diffraction, fluorescence spectroscopy, and time-correlated single photon counting

Computer skills: Bruker AXS, HTML, JavaScript, some experience with ASP.Net/VB.Net

ACTIVITIES

MIT Women in Chemistry Committee Member, 2006–present. MIT Chemical Hygiene and Safety Committee Member, 2003–present. MIT Nocera Group Webmaster, 2005–2008. MIT Chemistry Department Mentor to New Teaching Assistants, Fall 2005, 2006. MIT Nocera Group Environmental Health and Safety Representative, 2004–2005. The Gunnery School Webmaster, 2002–2003.

SCIENTIFIC PUBLICATIONS AND PRESENTATIONS

Publications

Ofer, O.; Keren, A.; **Nytko, E. A.**; Shores, M. P.; Bartlett, B. M.; Nocera, D. G.; Baines, C.; Amato, A. Ground State and Excitation Properties of the Quantum Kagomé System $\text{ZnCu}_3(\text{OH})_6\text{Cl}_2$ Investigated by Local Probes. Manuscript submitted to *Nat. Phys.*; arXiv:cond-mat/0610540.

Nytko, E. A.; Helton, J. S.; Müller, P.; Nocera, D. G. A Structurally Perfect $S = \frac{1}{2}$ Metal-Organic Hybrid Kagomé Antiferromagnet. *J. Am. Chem. Soc.* **2008**, *130*, 2922-2923.

Imai, T.; **Nytko, E. A.**; Shores, M. P.; Nocera, D. G. ^{63}Cu and ^{35}Cl NMR Investigation of the Kagomé Lattice System $\text{ZnCu}_3(\text{OH})_6\text{Cl}_2$. *Phys. Rev. Lett.* **2008**, *100*, 077203/1-4.

Helton, J. S.; Matan, K.; Shores, M. P.; **Nytko, E. A.**; Bartlett, B. M.; Yoshida, Y.; Takano, Y.; Suslov, A.; Qiu, Y.; Chung, J.-H.; Nocera, D. G.; Lee, Y. S. Spin Dynamics of the Spin-1/2 Kagomé Lattice Antiferromagnet $\text{ZnCu}_3(\text{OH})_6\text{Cl}_2$. *Phys. Rev. Lett.* **2007**, *98*, 107204/1-4.

Shores, M. P.; **Nytko, E. A.**; Bartlett, B. M.; Nocera, D. G. A Structurally Perfect $S = \frac{1}{2}$ Kagomé Antiferromagnet. *J. Am. Chem. Soc.* **2005**, *127*, 13462-3.

Ongusaha, P. P.; Ouchi, T.; Kim, K.; **Nytko, E.**; Kwak, J. C.; Duda, R. B.; Deng, C.-X.; Lee, S. W. BRCA1 Shifts p53-mediated Cellular Outcomes Towards Irreversible Growth Arrest. *Oncogene* **2003**, *22*, 3749–3758.

Pelczar, E. M.; **Nytko, E. A.**; Zhuravel, M. A.; Smith, J. M.; Glueck, D. S.; Sommer, R.; Incarvito, C. D.; Rheingold, A. L. Synthesis and Structure of Platinum and Palladium Complexes of Dimesitylphosphine. *Polyhedron* **2002**, *21*, 2409–2419.

Zhou, J.; Findley, B. R.; Francis, T. M.; **Nytko, E. A.**; Braun, C. L. The Solution Dynamics of Photoinduced Geminate Radical Ion Pairs: Free Ion Formation. *Chem. Phys. Lett.* **2002**, *362*, 63–71.

Nytko, E. A.; Shores, M. P.; Helton, J. S.; Nocera, D. G. $\text{CdCu}_3(\text{OH})_6(\text{NO}_3)_2$, An $S = \frac{1}{2}$ Kagomé Antiferromagnet System with Hydrogen-Bonded Layers. *Manuscript in preparation*.

Nytko, E. A.; Müller, P.; Shores, M. P.; Chu, S.; Bartlett, B. M.; Nocera, D. G. A Statistical Study of Antisite Disorder: Single-Crystal Structures of Synthetic Atacamite Minerals. *Manuscript in preparation*.

Nytko, E. A.; Shores, M. P.; Bartlett, B. M.; Nocera, D. G. Structural Evolution of $S = \frac{1}{2}$ Kagomé Antiferromagnets. *Manuscript in preparation*.

Helton, J. S.; Matan, K.; Chung, J.-H.; Shores, M. P.; Bartlett, B. M.; **Nytko, E. A.**; Chen, Y.; Huang, Q.; Lynn, J. W.; Nocera, D. G.; Lee, Y. S. Magnetic Order and Spin Fluctuations in the Spin-1/2 Three-Dimensional Frustrated Magnet Clinoatacamite, $\text{Cu}_2(\text{OH})_3\text{Cl}$. *Manuscript in preparation*.

Talks

Nytko, E. A.; Shores, M. P.; Bartlett, B. M.; Nocera, D. G. Spin Frustration on $S = \frac{1}{2}$ Kagomé Antiferromagnets. Abstract of Papers, 233rd ACS National Meeting, Chicago, IL U.S.A.; March 2007.

Posters

Nytko, E. A.; Shores, M. P.; Bartlett, B. M.; Nocera, D. G. Spin Frustration on $S = \frac{1}{2}$ Kagomé Antiferromagnets. Gordon Research Conference: Solid State Chemistry for Advanced Materials, Oxford, UK; September 2007.

REFERENCES

Professor Daniel G. Nocera
MIT Department of Chemistry
77 Massachusetts Avenue (6-333)
Cambridge, MA 02139
nocera@mit.edu/617.253.5537

Professor Stephen J. Lippard
MIT Department of Chemistry
77 Massachusetts Avenue (18-498)
Cambridge, MA 02139
lippard@mit.edu/617.253.1848

Professor Young S. Lee
MIT Department of Physics
77 Massachusetts Avenue (13-2153)
Cambridge, MA 02139
younglee@mit.edu/617.253.7834

Professor David S. Glueck
Dartmouth College Chemistry Department
Burke Laboratory HB 6128
Hanover, NH 03755
glueck@dartmouth.edu/603.646.1568

Autobiographical Note

Emily Anne Nytko was born on November 2, 1979 in Cold Spring, NY[†] to Elizabeth (Treacy) Nytko and Frederick Nytko. She and her younger brother, Fred, were raised in Fort Montgomery and Highland Falls, NY. Her early interest in chemistry was spurred by experimenting with baking soda and vinegar volcanoes, cornstarch and water goo, and nail polish and its removal. Early science experiments included a study of the effects of microwaves and focused solar radiation on her brother's Sergeant Slaughter G.I. Joe. Both radiation sources caused Sergeant Slaughter to melt and deform, and Emily learned a valuable lesson in the importance of funding to science when hers was withdrawn...she lost her allowance that week.

She graduated from James I. O'Neill High School in 1997, where chemistry and physics were her favorite subjects. She then attended Dartmouth College, where she found herself further fascinated by brightly colored inorganic compounds in undergraduate labs. She worked in the labs of Professors Charles Braun (studying photoinduced charge transfer kinetics in solution) and David Glueck (studying platinum(II) bisphosphine complexes) in the chemistry department before graduating with a bachelor's degree in chemistry in 2001. After college, Emily taught high school chemistry at The Gunnery School in Washington, CT. In 2003, she began attending MIT, where she did doctoral research on synthesis of inorganic compounds for studying spin frustration in the labs of Daniel Nocera.

She married John Lutz on July 22, 2006. They live with their cat, Black Mamba, a.k.a., "the Meat Puck Assassin". In her spare time, Emily enjoys scuba diving, lifting weights, and running, and hopes to finish a second marathon in the near future.

[†]N.B. Despite living in New England for most of her adult life, as a native New Yorker, Emily will always hate the Red Sox.

